Measurement of the Polarised Quark Distributions of the Nucleon at HERMES

Michael Ruh

FAKULTÄT FÜR PHYSIK
ALBERT-LUDWIGS-UNIVERSITÄT FREIBURG

Measurement of the Polarised Quark Distributions of the Nucleon at HERMES

INAUGURAL-DISSERTATION
zur
Erlangung des Doktorgrades
der
Fakultät für Physik
der
Albert-Ludwigs-Universität Freiburg i. Brsg.

vorgelegt von
Michael Ruh
aus Freiburg

1999

Dekan:	Prof. Dr. K. Königsmann
Leiter der Arbeit:	Prof. Dr. K. Königsmann
Referent:	Prof. Dr. K. Königsmann
Korreferent:	Prof. Dr. K. Runge
Tag der Verkündigung des Prüfungsergebnisses:	29. Oktober 1999

Contents

1. Introduction **1**

2. Deep inelastic scattering **3**
2.1. Deep inelastic scattering kinematics 3
2.2. Inclusive deep inelastic scattering 5
2.2.1. Unpolarised cross section 5
2.2.2. Polarised cross section 7
2.2.3. Cross section asymmetries 10
2.3. The quark parton model 11
2.4. Structure functions and parton distributions in QCD 13
2.5. Sum rules 16
2.5.1. Bjørken sum rule 17
2.5.2. Ellis-Jaffe sum rule 18
2.6. Semi-inclusive deep inelastic scattering 19
2.6.1. Semi-inclusive cross section and asymmetries 19
2.6.2. Fragmentation functions 20
2.6.3. Fragmentation models 22

3. The HERMES Experiment **27**
3.1. The polarised positron beam 28
3.1.1. Self-polarisation of the positron beam 28
3.1.2. Beam polarimetry 29
3.2. The polarised gas targets 31
3.2.1. The polarised ^{3}He target 32
3.2.2. The polarised ^{1}H target 33
3.3. The HERMES spectrometer 34
3.3.1. Tracking system 36
3.3.2. Particle identification detectors 36
3.3.3. Luminosity monitor 40
3.3.4. Trigger 40

4. Extraction of spin asymmetries **43**
4.1. Data quality selection . . . 43
4.2. Event selection . . . 44
4.2.1. Track selection . . . 45
4.2.2. Particle identification . . . 46
4.2.3. Kinematical cuts . . . 48
4.3. Extraction of the asymmetry $A_{\parallel}^{(h)}$ . . . 49
4.4. The ^{3}He and proton asymmetries $A_{\parallel}^{(h)}$ . . . 51
4.5. Corrections to $A_{\parallel}^{(h)}$ . . . 51
4.5.1. Background corrections . . . 53
4.5.2. Corrections for acceptance and kinematical smearing . . . 53
4.5.3. QED radiative corrections . . . 55
4.6. The ^{3}He and proton asymmetries $A_1^{(h)}$ . . . 57
4.6.1. Systematic error of the ^{3}He and proton asymmetries $A_1^{(h)}$ . . . 60

5. Extraction of polarised quark distributions **67**
5.1. The extraction formalism . . . 67
5.1.1. Assumptions on the polarisation of sea quarks . . . 69
5.1.2. Different options to separate quark flavours . . . 70
5.2. Generation of fragmentation functions . . . 70
5.3. Test of the extraction formalism with Monte Carlo . . . 75
5.4. Nuclear corrections to calculate A_1^{He} from A_1^{n} and A_1^{p} . . . 77
5.5. Results on polarised quark distributions . . . 78
5.5.1. Flavour decomposition . . . 78
5.5.2. Valence decomposition . . . 83
5.5.3. Systematic error of polarised quark distributions . . . 85
5.5.4. Moments of polarised quark distributions . . . 87
5.6. Comparison of results . . . 90
5.6.1. Results from semi-inclusive measurements . . . 90
5.6.2. Constituent and relativistic quark models . . . 91
5.6.3. Baryon decays and inclusive spin structure functions . . . 93
5.6.4. Lattice QCD calculations . . . 95

6. Summary **97**

A. Formalism of the analysis **99**
A.1. Extraction formalism for polarisation symmetric sea distributions . . . 99
A.2. Extraction formalism for SU(3)$_f$ symmetric sea distributions . . . 100
A.3. Parametrisations of unpolarised quark distributions and A_1 . . . 101
A.4. Parametrisations of polarised quark distributions . . . 103
A.5. Construction of the covariance matrix $\mathcal{V}_{\boldsymbol{A}}$ . . . 105
A.6. Systematic error calculation . . . 107

A.7. QCD corrections 110

B. Tables of results **113**

List of Figures **125**

List of Tables **127**

Bibliography **129**

Acknowledgements **137**

1. Introduction

The spin of the nucleon can be decomposed into contributions from quarks, gluons and orbital angular momenta

$$s_z^{\mathrm{N}}/\hbar = \frac{1}{2} = \frac{1}{2}\Delta\Sigma + \Delta g + L_z^q + L_z^g \,, \tag{1.1}$$

where, neglecting heavy quarks,

$$\Delta\Sigma = \Delta u + \Delta\bar{u} + \Delta d + \Delta\bar{d} + \Delta s + \Delta\bar{s} \tag{1.2}$$

is the contribution from quark spins, Δg is the gluon spin contribution, and L_z^q and L_z^g are those from orbital angular momenta carried by quarks and gluons [Jaf 90].

Over the last decade several experiments on polarised deep inelastic lepton-nucleon scattering provided accurate data on the spin structure functions $g_1(x, Q^2)$ of the proton and neutron as a function of the Bjørken scaling variable x and the squared four-momentum transfer $-Q^2$ of the exchanged virtual boson. These experiments were based on *inclusive* deep inelastic processes, where only the scattered lepton is detected. When the results for g_1 are combined with experimental information from weak baryon decays, values can be extracted for $\Delta\Sigma$ and for the contributions of the individual quark flavours assuming SU(3) flavour symmetry. From these analyses one obtains a value of $\Delta\Sigma \simeq 0.3$ which amounts to about 40% of the value expected from relativistic quark models. Furthermore, the contributions of the individual quark flavours are found to be $\Delta u + \Delta\bar{u} \simeq 0.8$, $\Delta d + \Delta\bar{d} \simeq -0.4$ and $\Delta s + \Delta\bar{s} \simeq -0.1$. Until now, little is experimentally known about Δg and no measurements exist for L_z^q and L_z^g.

The HERMES experiment at HERA/DESY started data taking in 1995 with the aim to determine the spin contributions of the various quark flavours to the spin of the nucleon using *semi-inclusive* deep inelastic scattering involving the detection of hadrons in coincidence with the scattered lepton. The experiment is based on two novel techniques: an internal gas target of polarised atomic hydrogen, deuterium or ^{3}He, and a high current longitudinally polarised positron beam circulating in a high-energy storage ring. Semi-inclusive measurements offer a means of *flavour-tagging* the struck quark which allows to extract the x-dependence of the polarised quark distributions $\Delta q_f(x)$ for each quark and anti-quark flavour. This way, the contributions of each quark flavour to the nucleon spin can be investigated in different x-regions. Furthermore, the flavour tagging method does not rely on the assumption of flavour symmetry to extract the polarised quark distributions. The SMC experiment at CERN presented first results on the

polarised valence and sea quark distributions from semi-inclusive measurements in the kinematic range $0.003 < x < 0.7$ and $1\ \text{GeV}^2 \leq Q^2 \leq 56\ \text{GeV}^2$ [Ade 98a]. In this work polarised quark distributions from HERMES are extracted for the up $[\Delta u(x) + \Delta\bar{u}(x)]$ and down $[\Delta d(x) + \Delta\bar{d}(x)]$ flavours, and for valence and sea quarks in the kinematic range $0.023 \leq x \leq 0.6$ and $1\ \text{GeV}^2 \leq Q^2 \leq 10\ \text{GeV}^2$. The results represent the most precise measurement of polarised quark distributions currently existing.

The outline of this work is as follows. Chapter 2 gives an introduction to polarised deep inelastic scattering and provides the formalism used to extract the quark spin distributions from inclusive and semi-inclusive spin-dependent cross section asymmetries. In chapter 3 the HERMES experimental apparatus is introduced. The analysis of inclusive and semi-inclusive charged hadron asymmetries is presented in chapter 4 and the extraction of the polarised quark distributions from the measured cross section asymmetries is described in chapter 5. The HERMES results on the polarised quark distributions are discussed and compared to existing experimental results and to predictions from quark models and lattice QCD.

2. Deep inelastic scattering

2.1. Deep inelastic scattering kinematics

Fig. 2.1 shows the lowest order Feynman diagram for deep inelastic lepton-nucleon scattering (DIS). The incoming lepton emits a boson which is absorbed by the nucleon target. For electromagnetic interactions the exchanged boson is a virtual photon while in weak interactions it is the intermediate vector boson $W^{\pm}$ or Z^0, for the charged and the neutral current interaction, respectively. In the kinematic region of the HERMES experiment with a 27.5 GeV positron beam incident on a stationary target the contributions from weak currents can be neglected.

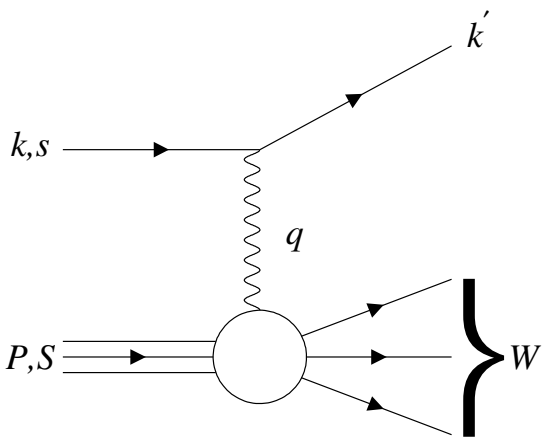

Figure 2.1.: Feynman diagram of deep inelastic lepton-nucleon scattering in the one-photon exchange approximation.

The incoming lepton is characterised by its four-momentum k and polarisation four-vector s. The four-momenta of the outgoing lepton and the exchanged virtual photon are denoted by k' and q, respectively. The target nucleon with rest mass M carries four-momentum P and its polarisation four-vector is S. In the HERMES experiment the polarisation states of the scattered lepton and of the hadronic final state are not recorded.

The negative square of the four-momentum of the exchanged virtual photon is defined as

$$Q^2 \equiv -q^2 = -(k - k')^2 > 0 \; . \tag{2.1}$$

Since the exchanged photon is virtual ($q^2 < 0$) it can be longitudinally or transversely polarised. In contrast, real photons have zero mass and pure transverse polarisation. The wavelength of the virtual photon depends on the reference frame. In the Breit frame which

is defined by $q = (0, \boldsymbol{q})$ one has[1]

$$\lambda = \frac{2\pi}{|\boldsymbol{q}|} = \frac{2\pi}{\sqrt{Q^2}} \tag{2.2}$$

so that the transverse size of the nucleon structure revealed decreases with increasing Q^2. The Lorentz invariant dimensionless Bjørken scaling variable x is defined by

$$x \equiv \frac{Q^2}{2M\nu} \,, \tag{2.3}$$

where $\nu \equiv P \cdot q/M$. The kinematically allowed range for x is $0 \leq x \leq 1$. In the Quark Parton Model (see section 2.3), where deep inelastic lepton-nucleon scattering is described as scattering from free partons, the variable x can be interpreted as the fraction of the nucleon's momentum carried by the interacting quark. The squared invariant mass of the hadronic final state is given by

$$W^2 = (q + P)^2 = M^2 + Q^2\,(1/x - 1) \ . \tag{2.4}$$

In the limit of elastic scattering one has $W^2 = M^2$ and consequently $x = 1$.

In the laboratory system (lab) of the HERMES experiment the target nucleon is at rest so that $P = (M, \mathbf{0})$. The variables x, Q^2 and W^2 are determined from the laboratory scattering angle θ between the three momenta of the incoming and outgoing lepton with respective energies E and E'

$$Q^2 \stackrel{\text{lab}}{\simeq} 4EE'\sin^2(\theta/2) \,, \tag{2.5}$$

$$\nu \stackrel{\text{lab}}{=} E - E' \,. \tag{2.6}$$

In the laboratory frame ν gives the energy transfer from the lepton to the virtual photon. In Eq. (2.5) the lepton mass has been neglected compared to its energy.

For studies of a final state hadron h (four-momentum $p_h = (E_h, \boldsymbol{p}_h)$) in coincidence with the scattered lepton the hadron momentum $\boldsymbol{p}_h$ is resolved into its three momentum component p_h^{L} along the virtual photon momentum $\boldsymbol{q}$ and component p_h^{T} perpendicular to $\boldsymbol{q}$. The Feynman variable x_{F} is defined in the virtual photon-nucleon centre of mass frame and scales the longitudinal hadron momentum to its maximum possible value

$$x_{\mathrm{F}} = \frac{2\,p_h^{\mathrm{L}}}{W} \,. \tag{2.7}$$

Further, the Lorentz invariant variable

$$z = \frac{p_h \cdot P}{q \cdot P} \stackrel{\text{lab}}{=} \frac{E_h}{\nu} \tag{2.8}$$

is introduced which relates the hadron energy E_h in the laboratory system to the maximum possible energy ν. The kinematically allowed ranges of x_{F} and z are $-1 \leq x_{\mathrm{F}} \leq 1$ and $0 \leq z \leq 1$. For $W \gg M$, the kinematic correlation between z and x_{F} is such that backward going hadrons ($x_{\mathrm{F}} < 0$) have small z values, whereas for large and positive values of x_{F} the two variables x_{F} and z are roughly equal.

[1] Throughout this text $\hbar = c = 1$ is used.

2.2. Inclusive deep inelastic scattering

Assuming one-photon exchange the inclusive differential DIS cross section for scattering a lepton (four-momentum k, spin four-vector s) from a target nucleon (four-momentum P, spin four-vector S) can be written in the laboratory frame as [Ans 95]

$$\frac{\mathrm{d}^2\sigma^{s,S}}{\mathrm{d}\Omega\ \mathrm{d}E'} = \frac{\alpha^2}{MQ^4}\frac{E'}{E}L_{\mu\nu}W^{\mu\nu}\ , \tag{2.9}$$

where the final state lepton is detected in the differential solid angle $\mathrm{d}\Omega$ and in the energy range $[E', E' + \mathrm{d}E']$. The quantity α denotes the electro-magnetic coupling constant and $L_{\mu\nu}$ is the lepton tensor calculable in quantum electrodynamics. The lepton tensor can be expressed as the sum

$$L_{\mu\nu} = L^{(\mathrm{S})}_{\mu\nu} + iL^{(\mathrm{A})}_{\mu\nu} \tag{2.10}$$

of a polarisation-independent part

$$L^{(\mathrm{S})}_{\mu\nu}(k;k') = 2\left[k'_\mu k_\nu + k_\mu k'_\nu - g_{\mu\nu}\left(k\cdot k' - m^2\right)\right]\ , \tag{2.11}$$

which is symmetric under μ, ν interchange, and a polarisation-dependent part

$$L^{(\mathrm{A})}_{\mu\nu}(k,s;k') = 2m\ \varepsilon_{\mu\nu\alpha\beta}\ s^\alpha\ (k-k')^\beta\ , \tag{2.12}$$

which is anti-symmetric under μ, ν interchange. Here, m is the lepton mass, $g_{\mu\nu}$ is the metric tensor and $\varepsilon_{\mu\nu\alpha\beta}$ is the totally anti-symmetric Levi-Civita tensor. The expressions for the symmetric and anti-symmetric parts, Eqs. (2.11) and (2.12), are given after summation over the polarisation states of the outgoing lepton. The unknown hadron tensor $W^{\mu\nu}$ which describes the interaction at the photon-nucleon vertex can be similarly expressed as the sum

$$W_{\mu\nu} = W^{(\mathrm{S})}_{\mu\nu} + iW^{(\mathrm{A})}_{\mu\nu} \tag{2.13}$$

of a polarisation-independent symmetric part $W^{(\mathrm{S})}_{\mu\nu}$ and a polarisation-dependent anti-symmetric part $W^{(\mathrm{A})}_{\mu\nu}$.

2.2.1. Unpolarised cross section

Using Lorentz covariance, gauge invariance, parity conservation in electro-magnetism and standard discrete symmetries of the strong interactions the spin-independent term $W^{(\mathrm{S})}_{\mu\nu}$ can be parameterised in terms of two dimensionless *spin-independent structure functions*, $F_1(x,Q^2)$ and $F_2(x,Q^2)$, which depend on only two invariants x and Q^2:

$$W^{(\mathrm{S})}_{\mu\nu}(q;P) = \left(-g_{\mu\nu} + \frac{q_\mu q_\nu}{q^2}\right)\ F_1 + \left[\left(P_\mu - \frac{\nu}{q^2}q_\mu\right)\left(P_\nu - \frac{\nu}{q^2}q_\nu\right)\right]\frac{F_2}{\nu}\ . \tag{2.14}$$

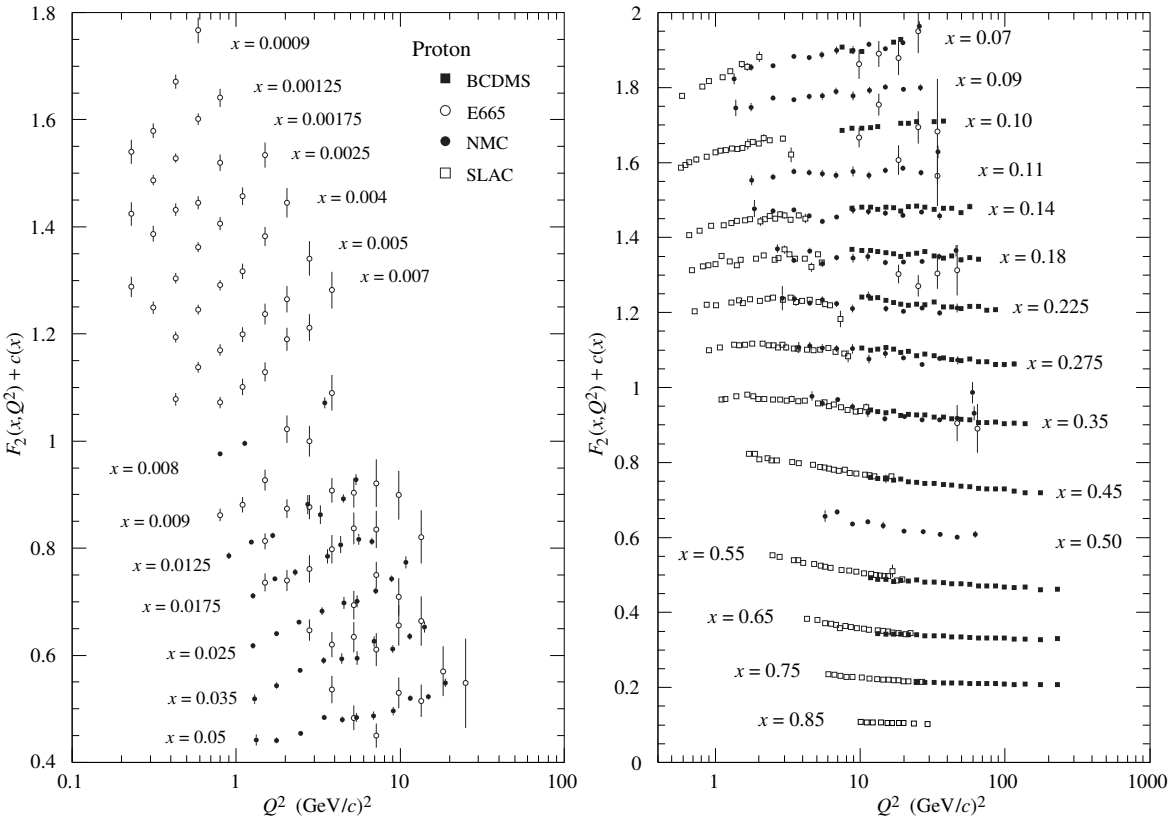

Figure 2.2.: The proton structure function F_2^{p} measured in deep inelastic scattering of electrons (SLAC) and muons (BCDMS, E665, NMC), shown as a function of Q^2 for fixed x [Cas 98]. Only statistical errors are shown. For the purpose of plotting, a constant $c(x) = 0.1\ i_x$ is added to F_2^{p} where i_x is the number of the x-bin, ranging from 1 $(x = 0.05)$ to 14 $(x = 0.0009)$ on the left-hand figure and from 1 $(x = 0.85)$ to 15 $(x = 0.07)$ on the right-hand figure. For HERA data in the kinematic range of this figure, see [Cas 98].

The unpolarised differential cross section is calculated by contracting the lepton tensor $L_{\mu\nu}^{(\mathrm{S})}$ with the hadron tensor $W_{\mu\nu}^{(\mathrm{S})}$ averaging over initial spin states and summing over final spin states

$$\frac{\mathrm{d}^2\sigma}{\mathrm{d}\Omega\,\mathrm{d}E'} = \frac{4\alpha^2\,(E')^2}{Q^4}\left[\frac{1}{\nu}\,F_2(x,Q^2)\,\cos^2\left(\frac{\theta}{2}\right) + \frac{2}{M}\,F_1(x,Q^2)\,\sin^2\left(\frac{\theta}{2}\right)\right]. \quad (2.15)$$

Precise measurements of the structure functions F_2^{p} and F_2^{d} for the proton and deuteron have been performed by BCDMS, NMC, SLAC, E665, ZEUS and H1 covering a wide kinematic range of $10^{-6} \leq x \leq 0.9$ and $0.1\ \mathrm{GeV}^2 \leq Q^2 \leq 5 \cdot 10^3\ \mathrm{GeV}^2$. Fig. 2.2 gives a compilation of the world data on F_2^{p} from fixed target experiments. Measurements with similar accuracy exist for the deuteron. Fig. 2.2 shows that the structure function F_2 is approximately independent of Q^2 at fixed x. This behaviour is known as *Bjørken*

scaling or *scale invariance* and can be explained by the existence of point-like scattering centres in the nucleon. However, scale invariance is only exact for $x \simeq 0.2$. For $x \gtrsim 0.2$ the structure function F_2 decreases with increasing values of Q^2 whereas the opposite behaviour is observed for $x \lesssim 0.2$. The issue of scaling violations will be addressed in more detail in section 2.4.

The unpolarised DIS cross section can be related to the absorption cross sections for transversely (σ_{T}) and longitudinally (σ_{L}) polarised photons

$$\frac{\mathrm{d}^2\sigma}{\mathrm{d}\Omega\ \mathrm{d}E'} = \Gamma\left[\sigma_{\mathrm{T}}(x,Q^2) + \varepsilon\sigma_{\mathrm{L}}(x,Q^2)\right]\ , \tag{2.16}$$

where Γ represents the flux of virtual photons and ε is their degree of longitudinal polarisation,

$$\varepsilon = \frac{4(1-y) - \gamma^2 y^2}{4(1-y) + 2y^2 + \gamma^2 y^2}\ , \tag{2.17}$$

with $\gamma = 2Mx/\sqrt{Q^2}$ and $y = \nu/E$. The ratio $R = \sigma_{\mathrm{L}}/\sigma_{\mathrm{T}}$ of the longitudinal to transverse cross section relates the structure function F_1 with F_2 by

$$R(x,Q^2) = \frac{F_2(x,Q^2)}{2xF_1(x,Q^2)}\left(1+\gamma^2\right) - 1\ . \tag{2.18}$$

The cross section ratio R has been determined from DIS experiments at SLAC [Abe 99, Whi 90] in a kinematical range which covers the HERMES kinematical range. Within the experimental uncertainties R was found to be identical for proton and neutron targets. At the average $Q^2 = 2.5$ GeV^2 of the HERMES experiment the value of R decreases from 0.32 at $x = 0.02$ to 0.19 at $x = 0.7$. In the limit of $Q^2 \to \infty$ the cross section σ_{L} vanishes so that $R = 0$ and consequently $2xF_1 = F_2$.

2.2.2. Polarised cross section

The cross section for polarised DIS (Eq. (2.9)) depends on both the symmetric and antisymmetric parts of the lepton and hadron tensors. In the *cross section difference* for scattering polarised leptons from polarised nucleons with spin four-vector S and $-S$ the symmetric parts cancel so that this cross section difference can be used to isolate the antisymmetric parts of the lepton and hadron tensors. Using the same symmetry arguments as for the spin-independent tensor $W_{\mu\nu}^{(\mathrm{S})}$ the spin-dependent tensor $W_{\mu\nu}^{(\mathrm{A})}$ can be expressed in terms of two dimensionless *spin-dependent structure functions*, $g_1(x,Q^2)$ and $g_2(x,Q^2)$:

$$W_{\mu\nu}^{(\mathrm{A})}(q;P,S) = 2\,\varepsilon_{\mu\nu\alpha\beta}\,q^\alpha\,\frac{1}{\nu}\left\{S^\beta g_1 + \left[S^\beta - \frac{(S\cdot q)P^\beta}{P\cdot q}\right]g_2\right\}\ . \tag{2.19}$$

In the laboratory frame, in which the target nucleon is at rest, the spin four-vector of the target nucleon reads $S^\beta = (0,\hat{\boldsymbol{S}})$ with $S^2 = -1$. For *longitudinally* polarised leptons the

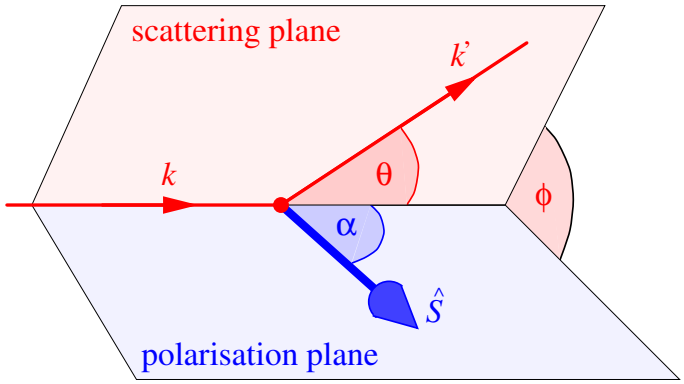

Figure 2.3.: Definition of scattering angles in polarised deep inelastic scattering in the laboratory frame. The four-vectors of the incident and scattered lepton are denoted by $k = (E, \boldsymbol{k})$ and $k' = (E', \boldsymbol{k'})$. The lepton scattering angle is called θ. $\hat{\boldsymbol{S}}$ gives the target spin direction and ϕ is the angle between the polarisation plane (defined by $\boldsymbol{k}$ and $\hat{\boldsymbol{S}}$) and the scattering plane (defined by $\boldsymbol{k}$ and $\boldsymbol{k'}$). α is the angle between the beam momentum $\boldsymbol{k}$ and the target spin direction $\hat{\boldsymbol{S}}$.

cross section difference for the target spin aligned parallel or anti-parallel with respect to some arbitrary direction $\hat{\boldsymbol{S}}$ is given by

$$\frac{\mathrm{d}^2\left[\sigma(\alpha+\pi)-\sigma(\alpha)\right]}{\mathrm{d}\Omega\,\mathrm{d}E'} = \frac{4\alpha^2}{Q^2}\frac{E'}{E} \times\frac{1}{M\nu}\left\{\left[E\cos\alpha + E'\cos\Theta\right]g_1 + 2EE'\left[\cos\Theta-\cos\alpha\right]\frac{1}{\nu}\,g_2\right\}, \tag{2.20}$$

where $\cos\Theta = \sin\theta\sin\alpha\cos\phi + \cos\theta\cos\alpha$ and the angles α and ϕ are defined in Fig. 2.3. The cross section difference for beam and target spins aligned parallel ($\overrightarrow{\Rightarrow}$) or anti-parallel ($\overrightarrow{\Leftarrow}$) corresponds to $\alpha = 0$ and simplifies to

$$\frac{\mathrm{d}^2(\sigma^{\overrightarrow{\Leftarrow}} - \sigma^{\overrightarrow{\Rightarrow}})}{\mathrm{d}\Omega\,\mathrm{d}E'} = \frac{4\alpha^2}{Q^2}\frac{E'}{E}\frac{1}{M\nu}\left\{\left(E + E'\cos\theta\right)g_1 - \frac{Q^2}{\nu}\,g_2\right\}. \tag{2.21}$$

Polarising the target transverse to the lepton beam ($\alpha = \pi/2$) yields another combination of g_1 and g_2

$$\frac{\mathrm{d}^2(\sigma^{\rightarrow\Downarrow} - \sigma^{\rightarrow\Uparrow})}{\mathrm{d}\Omega\,\mathrm{d}E'} = \frac{4\alpha^2}{Q^2}\frac{E'}{E}\frac{1}{M\nu}\left\{g_1 + \frac{2E}{\nu}\,g_2\right\}E'\sin\theta\cos\phi. \tag{2.22}$$

Fig. 2.4 shows the world data on the spin-dependent structure function g_1^{p} of the proton as measured in polarised DIS. The structure function is shown as a function of x for a fixed value of $Q^2 = 5$ GeV^2. Measurements with similar accuracy exist for the

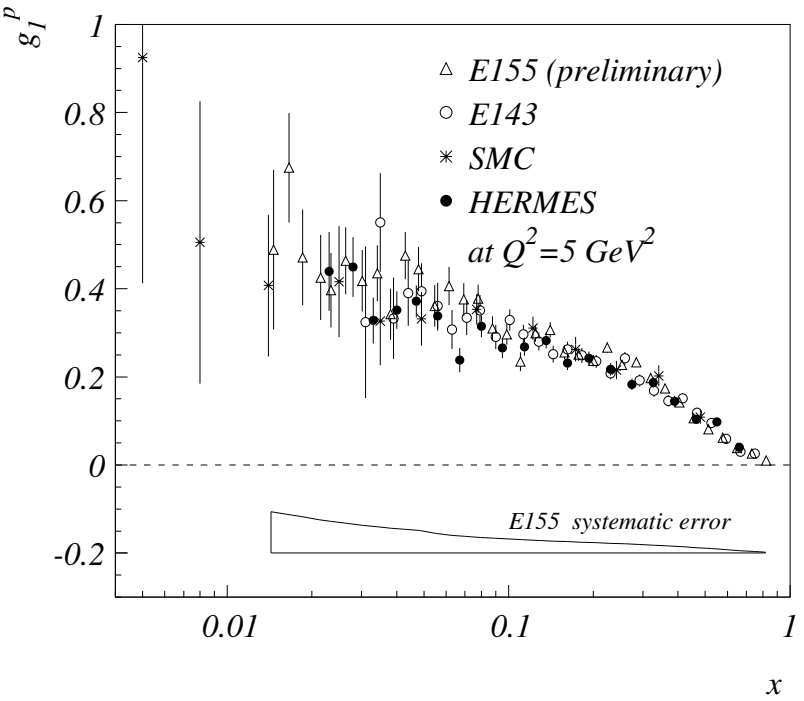

Figure 2.4.: The spin-dependent structure function g_1^{p} of the proton measured in deep inelastic scattering of polarised electrons or positrons (E155 [Hug 99], E143 [Abe 98], HERMES [Air 98]) and muons (SMC [Ade 98b]), shown as a function of x for a fixed value of $Q^2 = 5$ GeV^2. Only statistical errors are shown with the data points. As an example, the E155 systematic uncertainty is indicated by the error band.

deuteron [Ada 97, Abe 95b] and for the neutron [Hug 99, Ack 97, Abe 97b]. The combined data of the different experiments cover a kinematical range of $0.003 \leq x \leq 0.8$ for 1 GeV$^2 \leq Q^2 \leq 60$ GeV^2. The interpretation of g_1 in the quark parton model will be discussed in section 2.3.

The spin structure function g_2 can be decomposed as [Wan 77]

$$g_2(x, Q^2) = g_2^{\mathrm{WW}}(x, Q^2) + \hat{g}_2(x, Q^2) \tag{2.23}$$

with g_2^{WW} given as a function of g_1

$$g_2^{\mathrm{WW}}(x, Q^2) = -g_1(x, Q^2) + \int_x^1 g_1(t, Q^2)\frac{\mathrm{d}t}{t}\,. \tag{2.24}$$

The term $\hat{g}_2$ is due to a twist-3 contribution in the operator product expansion [Ans 95] and is a measure of long distance, non-perturbative effects like quark-quark or quark-gluon correlations in the nucleon. Experimental data on g_2 [Abe 98, Ant 99, Abe 97a] cover a kinematical range of $0.03 \leq x \leq 0.8$ for 1 GeV$^2 \leq Q^2 \leq 30$ GeV^2 and have significantly larger experimental uncertainties than the measurements of g_1. The data are

consistent with the leading twist formula Eq. (2.24) and are close to the quark parton model prediction of $g_2(x) = 0$. Furthermore, the measurements are compatible with the Burkhardt-Cottingham sum rule [Bur 70]

$$\int_0^1 g_2(x, Q^2)\,\mathrm{d}x = 0\,, \tag{2.25}$$

which has been verified to leading order in perturbative QCD [Alt 94, Kod 95].

2.2.3. Cross section asymmetries

In the previous section the spin structure functions g_1 and g_2 were related to the cross section difference for scattering polarised leptons from polarised targets with opposite spin orientation. Rather than measuring a cross section difference, experimentally, a cross section asymmetry is determined. For a longitudinally polarised beam g_1 and g_2 are derived from the cross section asymmetry $A_\parallel$ measured for the target spin parallel and anti-parallel to the beam spin,

$$A_\parallel = \frac{\sigma^{\rightleftarrows} - \sigma^{\rightrightarrows}}{\sigma^{\rightleftarrows} + \sigma^{\rightrightarrows}}\,, \tag{2.26}$$

and the asymmetry $A_\perp$, which corresponds to the target polarisation perpendicular to the longitudinally polarised beam,

$$A_\perp = \frac{\sigma^{\rightarrow\Downarrow} - \sigma^{\rightarrow\Uparrow}}{\sigma^{\rightarrow\Downarrow} + \sigma^{\rightarrow\Uparrow}}\,. \tag{2.27}$$

The measured lepton asymmetries can be rewritten in terms of the virtual photon asymmetries A_1 and A_2:

$$A_1 = \frac{\sigma^{\frac{1}{2}} - \sigma^{\frac{3}{2}}}{\sigma^{\frac{1}{2}} + \sigma^{\frac{3}{2}}}\,, \tag{2.28}$$

$$A_2 = \frac{2\sigma_{\mathrm{I}}}{\sigma^{\frac{1}{2}} + \sigma^{\frac{3}{2}}}\,, \tag{2.29}$$

where $\sigma^{\frac{1}{2}}$ ($\sigma^{\frac{3}{2}}$) are the photon-nucleon absorption cross sections for transversely polarised virtual photons with projection $\frac{1}{2}$ ($\frac{3}{2}$) of the total photon and nucleon spin along the direction of the photon momentum, and σ_{I} is the interference cross section between the transverse and the longitudinal polarisations of the virtual photon. The asymmetries $A_{1,2}$ are subject to the following positivity constraints

$$|A_1| \leq 1\,, \qquad |A_2| = \frac{\sigma_{\mathrm{I}}}{\sigma_{\mathrm{T}}} \leq \sqrt{\frac{\sigma_{\mathrm{L}}\sigma_{\mathrm{T}}}{(\sigma_{\mathrm{T}})^2}} = \sqrt{R}\,, \tag{2.30}$$

where $\sigma_{\mathrm{T}} = (\sigma^{\frac{1}{2}} + \sigma^{\frac{3}{2}})/2$. In terms of $A_{1,2}$ the measured lepton asymmetries are given by

$$A_\parallel = D(A_1 + \eta A_2)\,, \tag{2.31}$$

$$A_\perp = d(A_2 - \xi A_1)\,, \tag{2.32}$$

where the virtual photon depolarisation factor D and the kinematical factors are

$$D = \frac{1-(1-y)\varepsilon}{1+\varepsilon R}\,, \tag{2.33}$$

$$\eta = \varepsilon\gamma y/[1-\varepsilon(1-y)]\,, \tag{2.34}$$

$$d = D\sqrt{\frac{2\varepsilon}{1+\varepsilon}}\,, \tag{2.35}$$

$$\xi = \eta\,\frac{1+\varepsilon}{2\varepsilon}\,. \tag{2.36}$$

Eventually, the asymmetries $A_{1,2}$ can be expressed in terms of the structure functions $g_{1,2}$ and the unpolarised structure function F_1 by

$$A_1 = \frac{g_1-\gamma^2 g_2}{F_1}\,, \tag{2.37}$$

$$A_2 = \gamma\,\frac{g_1+g_2}{F_1}\,. \tag{2.38}$$

As mentioned before, g_2 was measured to be close to zero for the proton and the neutron in the kinematic region of the HERMES experiment. Additionally, its contribution to A_1 is suppressed by the kinematical factor γ^2 which is small ($0.003 \lesssim \gamma^2 \lesssim 0.15$) in the kinematical region of the HERMES experiment. Neglecting contributions from $\gamma^2 g_2$ in Eq. (2.37) one obtains $A_1 = g_1/F_1$.

2.3. The quark parton model

The experimental observation that the structure functions for fixed x exhibit only a relatively small dependence on Q^2 was the basis of the quark parton model (QPM) of Feynman [Fey 72] and Bjørken [Bjø 69], where the nucleons probed in a hard scattering process appear to consist of point-like scattering centres called *partons*. The partons active in lepton-nucleon scattering are identified with the fractionally charged spin-1/2 quarks postulated to explain symmetries in hadron spectroscopy.

Under the assumption that in the Bjørken limit ($\nu, Q^2 \to \infty$) *deep inelastic* lepton-nucleon scattering can be described as incoherent *elastic* scattering from non-interacting point-like charged spin-1/2 constituents one can predict the structure functions $F_{1,2}$ by comparing the unpolarised DIS cross section, Eq. (2.15), with the cross section for elastic electron-muon scattering [Hal 84]. For scattering from point-like constituents the structure functions $F_{1,2}$ are independent of Q^2 at fixed x

$$F_{1,2}(x,Q^2) \overset{(\nu,Q^2\to\infty)}{\longrightarrow} F_{1,2}(x)\,, \tag{2.39}$$

and, as a consequence of the assumption that the charged partons carry spin 1/2, the structure functions obey the Callan-Gross relation [Cal 68]

$$2xF_1(x) = F_2(x)\,, \tag{2.40}$$

which was experimentally confirmed. Furthermore, by substituting this result in Eq. (2.18) one obtains $R = \sigma_{\rm L}/\sigma_{\rm T} = 0$ and consequently $\sigma_{\rm L} = 0$ in the Bjørken limit.

The QPM model is formulated in the *infinite momentum frame*, in which the proton is moving with infinite momentum so that the nucleon and parton rest masses and the transverse momentum components of the partons inside the nucleon can be neglected compared to the longitudinal momenta. In this frame the four-momentum of the nucleon is given by $P = (P, 0, 0, P)$ and the four-momentum of a parton inside the nucleon writes $\zeta P = (\zeta P, 0, 0, \zeta P)$, where ζ is the fraction of the nucleon momentum carried by the parton. For elastic photon-quark scattering four-momentum conservation at the photon-quark vertex implies $0 \simeq m_q^2 = (\zeta P + q)^2$, where m_q is the quark rest mass. In the limit $\zeta^2 P^2 = \zeta^2 M^2 \ll Q^2$ one obtains

$$\zeta = \frac{Q^2}{2M\nu}\,, \tag{2.41}$$

so that the fractional momentum ζ carried by the struck quark is identical to the kinematical variable $x = Q^2/(2M\nu)$ of the virtual photon. Further, if the DIS process can be described as the incoherent sum of elastic scattering from non-interacting quarks, the structure functions $F_{1,2}$ are obtained by summing over all quark and anti-quark flavours f and integrating over all fractional quark momenta ζ

$$2xF_1(x) = F_2(x) = \sum_f \int_0^1 {\rm d}\zeta\; e_f^2\; \zeta\; q_f(\zeta)\; \delta(\zeta - x) = \sum_f e_f^2\; x\; q_f(x)\,. \tag{2.42}$$

Here, $q_f(\zeta){\rm d}\zeta$ is defined as the probability of finding a quark or anti-quark with flavour f and fractional momentum in the range $[\zeta, \zeta + {\rm d}\zeta]$ and e_f is the quark charge in units of the elementary charge e.

If the proton consisted only of charged constituents, their momenta would be expected to add up to the proton momentum $\sum_f \int_0^1 {\rm d}x\; x\; q_f(x) = 1$. However, experimentally a value of $\simeq 0.54$ was found which implies that about half of the nucleons momentum is carried by partons interacting neither electro-magnetically nor weakly. These partons are identified with the gluons, the field quanta of the strong interactions.

To interpret the spin structure function g_1 in the QPM one considers a photon-quark interaction in the infinite momentum frame with the quark moving along the z-axis. In this frame the photon-quark collision is collinear and a transversely polarised photon will necessarily flip the spin S_z^q of the quark (since $L_z^q = 0$ for a collinear collision). Consequently, the virtual photon can only be absorbed by a quark whose spin is aligned anti-parallel to the spin of the virtual photon. The unpolarised quark distributions can be decomposed as $q_f(x) = q_f^+(x) + q_f^-(x)$, where $q_f^{+(-)}(x)\,{\rm d}x$ is defined as the probability of finding a quark or anti-quark with fractional momentum in the range $[x, x + {\rm d}x]$ and spin aligned parallel (anti-parallel) to the nucleon spin. The photon-nucleon absorption cross sections $\sigma^{\frac{1}{2}}$ ($\sigma^{\frac{3}{2}}$) for anti-parallel (parallel) orientations of the photon and nucleon spins are thus given by $\sigma^{\frac{1}{2}} \propto \sum_f e_f^2\; q^+$ and $\sigma^{\frac{3}{2}} \propto \sum_f e_f^2\; q^-$. It follows for the spin structure function

g_1 which is proportional to the cross section difference $\sigma^{\frac{1}{2}} - \sigma^{\frac{3}{2}}$:

$$g_1(x) = \frac{1}{2} \sum_f e_f^2 \, \Delta q_f(x) \, , \tag{2.43}$$

where the polarised quark distributions Δq_f have been defined as

$$\Delta q_f(x) = q_f^+(x) - q_f^-(x) \, . \tag{2.44}$$

Eq. (2.43) for g_1 represents the polarised counterpart to Eq. (2.42) for $F_1(x)$. The spin structure function g_2 does not have an equally transparent probabilistic interpretation but can be understood from the spin-flip amplitude that gives rise to the interference asymmetry $A_2 \propto g_1 + g_2$ caused by the absorption of a longitudinally polarised photon by the nucleon [Ji 95]. In the QPM the second spin structure function $g_2(x)$ vanishes [Ans 95].

2.4. Structure functions and parton distributions in quantum chromodynamics

The parton model predicts that the structure functions should be scale invariant. However, one can see from Fig. 2.2 that scaling is only approximately fulfilled, i.e. that the structure functions exhibit a small Q^2-dependence which is not consistent with the QPM picture that the nucleon consists of non-interacting Dirac particles. In quantum chromodynamics (QCD) the scaling violations of the structure functions can be explained by the interaction between quarks and gluons, the field quanta of the strong interaction, which are exchanged between particles carrying colour charge. In addition to the emission and absorption of gluons by quarks, three or four gluons can couple to each other with a coupling strength which in first order perturbative QCD calculation is given by

$$\alpha_{\mathrm{s}}(Q^2) = \frac{4\pi}{\beta_0 \ln\left(Q^2/\Lambda^2\right)} \tag{2.45}$$

with $\beta_0 = 11 - \frac{2}{3} n_f$ and n_f the number of active quark flavours. The QCD scale parameter Λ gives the limit where perturbative QCD can be applied and is about 300 MeV. The Q^2-dependence of α_{s} corresponds to a dependence on spatial separation since the wavelength λ of the virtual photon in the laboratory frame is proportional to $1/Q^2$. For small distances and corresponding high values of Q^2, the quark-quark coupling decreases logarithmically and vanishes in the limit $Q^2 \to \infty$ (asymptotic freedom). For this reason, at high enough values of Q^2, DIS can be described as scattering from free constituents.

A common way to schematically represent the Q^2-dependence of the quark distributions is shown in Fig. 2.5. At a certain value of $Q^2 = Q_0^2$ one measures a quark distribution $q_f(x, Q_0^2)$. If one increases the resolution of the virtual photon by going to higher values of $Q^2 > Q_0^2$, one can resolve that the quark momentum has changed by gluon radiation. A quark with momentum fraction x can originate from a parent quark

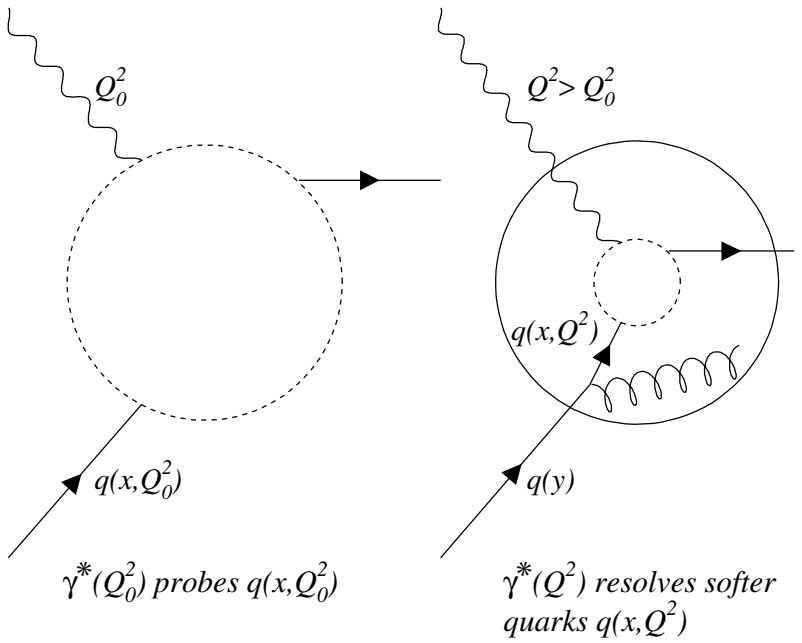

Figure 2.5.: Schematical representation of the Q^2-dependence of quark distributions due to the increasing resolving power of the virtual photon [Hal 84].

with higher momentum fraction y. Similarly, the virtual photon can couple to a quark which arose from a gluon splitting into a quark anti-quark pair. These processes lead to the observed behaviour (see Fig. 2.2) that the structure functions decrease at high values of x with increasing values of Q^2 whereas they rise at low values of x.

The evolution of the parton distributions and structure functions as a function of Q^2 can be described quantitatively by QCD. With the definitions

$$t \equiv \ln(Q^2/\Lambda^2)\,, \tag{2.46}$$

$$\langle e^2 \rangle \equiv \frac{1}{n_f}\sum_f e_f^2\,, \tag{2.47}$$

$$[f \otimes h](x,t) \equiv \int_x^1 \frac{\mathrm{d}y}{y} f\left(\frac{x}{y},t\right) h(y,t)\,, \tag{2.48}$$

the unpolarised and polarised structure functions F_1 and g_1 are in perturbative QCD given by [Alt 82]

$$F_1(x,t) = \frac{1}{2}\langle e^2\rangle \left\{c^{\mathrm{NS}} \otimes q^{\mathrm{NS}} + c^{\mathrm{S}} \otimes \Sigma + 2n_f\, c^g \otimes g\right\}\,, \tag{2.49}$$

$$g_1(x,t) = \frac{1}{2}\langle e^2\rangle \left\{\Delta c^{\mathrm{NS}} \otimes \Delta q^{\mathrm{NS}} + \Delta c^{\mathrm{S}} \otimes \Delta\Sigma + 2n_f\, \Delta c^g \otimes \Delta g\right\}\,. \tag{2.50}$$

Here, $c^{\mathrm{S,NS},g}$ ($\Delta c^{\mathrm{S,NS},g}$) denote the so-called unpolarised (polarised) flavour singlet (S), non-singlet (NS) and gluon (g) coefficient functions. The unpolarised (polarised) gluon

distribution is denoted by g (Δg), and Σ ($\Delta\Sigma$) and $q^{\rm NS}$ ($\Delta q^{\rm NS}$) are the unpolarised (polarised) singlet and non-singlet combinations of the quark and anti-quark distributions. The unpolarised singlet and non-singlet combinations are defined as

$$\Sigma(x,t) = \sum_f q_f(x,t)\,, \tag{2.51}$$

$$q^{\rm NS}(x,t) = \sum_f \left[\frac{e_f^2}{\langle e^2\rangle} - 1\right] q_f(x,t)\,, \tag{2.52}$$

and the polarised ones $\Delta\Sigma$ and $\Delta q^{\rm NS}$ are obtained from Eqs. (2.51) and (2.52) by replacing q_f with Δq_f.

The Q^2-dependence of the unpolarised parton distributions follows the Gribov-Lipatov-Altarelli-Parisi (GLAP) equations [Gri 72, Alt 77]

$$\frac{\rm d}{{\rm d}t}\, q^{\rm NS}(x,t) = \frac{\alpha_{\rm s}(t)}{2\pi}\left[P_{qq}^{\rm NS}\otimes q^{\rm NS}\right](x,t)\,, \tag{2.53}$$

$$\frac{\rm d}{{\rm d}t}\begin{bmatrix}\Sigma\\ g\end{bmatrix}(x,t) = \frac{\alpha_{\rm s}(t)}{2\pi}\begin{bmatrix}P_{qq}^{\rm S} & P_{qg}\\ 2n_f P_{gq} & P_{gg}\end{bmatrix}\otimes\begin{bmatrix}\Sigma\\ g\end{bmatrix}(x,t)\,, \tag{2.54}$$

where P_{ij} are the QCD splitting functions for the unpolarised parton distributions. The probability that a quark with momentum fraction x originates from a parent quark with momentum fraction y ($> x$) is given by $\alpha_{\rm s}(t)P_{qq}(x/y)$. The probability that a quark with momentum fraction x is the result of a $\bar{q}q$ pair creation from a gluon with higher momentum y is $\alpha_{\rm s}(t)P_{qg}(x/y)$, and similarly for P_{gq}. The splitting function P_{gg} accounts for the three gluon vertex. Note that $q^{\rm NS}$ evolves independently from the gluon distribution, while Σ is coupled to the gluon distribution.

Given the splitting functions for polarised parton distributions $\Delta P_{qq}^{\rm NS}$, $\Delta P_{qq}^{\rm S}$, ΔP_{qg}, ΔP_{gq} and ΔP_{gg} the polarised non-singlet, singlet and gluon distributions evolve formally equivalent to the unpolarised ones and are calculated from Eqs. (2.53) and (2.54) with the replacements $q^{\rm NS}\to\Delta q^{\rm NS}$, $\Sigma\to\Delta\Sigma$, $g\to\Delta g$ and $P_{ij}\to\Delta P_{ij}$.

The expressions (2.49) to (2.54) are valid in all orders of perturbative QCD. The splitting and coefficient functions can be expanded as a power series in $\alpha_{\rm s}$. At order $\alpha_{\rm s}^1$ (leading order (LO)) the polarised and unpolarised singlet and non-singlet coefficient functions are given by $\delta(1-x/y)$ while the gluon coefficient function vanishes. Consequently, F_1 (g_1) decouples from g (Δg) in LO and Eqs. (2.49) and (2.50) become

$$F_1(x,t) = \frac{1}{2}\sum_f e_f^2\; q_f(x,t)\,, \tag{2.55}$$

$$g_1(x,t) = \frac{1}{2}\sum_f e_f^2\; \Delta q_f(x,t)\,. \tag{2.56}$$

Therefore, in LO, the parton model quark distributions $q_f(x)$ introduced in section 2.3 are replaced by an effective Q^2-dependent quark distribution $q_f(x,t)$. Beyond LO, the coefficient functions and the splitting functions are not uniquely defined, but depend on the

renormalisation scheme (see e.g. [Rob 90]). All coefficient and splitting functions have been computed at next-to-leading order (NLO), the polarised calculations being completed only recently [Zij 94, Mer 96, Vog 96]. The formalism described above allows a complete NLO QCD analysis of the scaling violations of g_1 and F_1.

In QCD, the ratio g_1/F_1 is Q^2-dependent because the splitting functions, with the exception of ΔP_{qq} and P_{qq}, are different for polarised and unpolarised parton distributions. However, in kinematic regions dominated by valence quarks, the Q^2-dependence of g_1/F_1 is expected to be small [Ger 95] which is consistent with existing measurements (see e.g. [You 97, Air 98]).

2.5. Sum rules

Important information on the nucleon spin structure can be gained from the integrals of the spin structure functions. The first moment of g_1 is defined as

$$\Gamma_1(Q^2) \equiv \int_0^1 g_1(x,Q^2)\,\mathrm{d}x \tag{2.57}$$

and can be expressed as [Ans 95]

$$\Gamma_1^{\mathrm{p(n)}}(Q^2) = \frac{1}{12}\left[+(-)a_3 + \frac{1}{3}a_8\right]\,\Delta C^{\mathrm{NS}}(Q^2) + \frac{1}{9}a_0(Q^2)\,\Delta C^{\mathrm{S}}(Q^2)\,. \tag{2.58}$$

Here, a_j are the proton expectation values of the axial-vector currents

$$J_\mu^j = \overline{\boldsymbol{\psi}}\gamma_\mu\gamma_5\left(\frac{\boldsymbol{\lambda}_j}{2}\right)\boldsymbol{\psi}\,, \qquad j = 0,\ldots,8 \tag{2.59}$$

where the matrices $\boldsymbol{\lambda}_j$ $(j = 1,\ldots,8)$ are the generators of SU(3)$_f$ in the Gell-Mann notation, $\boldsymbol{\lambda}_0 = 2\boldsymbol{I}$ and $\boldsymbol{\psi}$ is a column vector in flavour space. Note that a_3 and a_8 are independent of Q^2 whereas a_0 depends upon Q^2. In Eq. (2.58) the flavour non-singlet and singlet coefficient functions denote the first moments

$$\Delta C^{\mathrm{NS(S)}}(Q^2) = \int_0^1 \mathrm{d}x\;\Delta c^{\mathrm{NS(S)}}(x,Q^2) \tag{2.60}$$

of the corresponding coefficient functions introduced in the previous section. They depend on the number of flavours and have been calculated to $\mathcal{O}(\alpha_{\mathrm{s}}^4)$ and $\mathcal{O}(\alpha_{\mathrm{s}}^3)$ for the non-singlet and singlet coefficient function, respectively [Lar 91, Lar 94, Kat 95]. For $n_f = 3$ they are given by

$$\Delta C^{\mathrm{NS}}(Q^2) = 1 - \frac{\alpha_{\mathrm{s}}}{\pi} - 3.583\left(\frac{\alpha_{\mathrm{s}}}{\pi}\right)^2 - 20.22\left(\frac{\alpha_{\mathrm{s}}}{\pi}\right)^3 - \mathcal{O}(130)\left(\frac{\alpha_{\mathrm{s}}}{\pi}\right)^4, \tag{2.61}$$

$$\Delta C^{\mathrm{S}}(Q^2) = 1 - \frac{\alpha_{\mathrm{s}}}{\pi} - 1.096\left(\frac{\alpha_{\mathrm{s}}}{\pi}\right)^2 - \mathcal{O}(3.7)\left(\frac{\alpha_{\mathrm{s}}}{\pi}\right)^3, \tag{2.62}$$

where $\alpha_s = \alpha_s(Q^2)$.

Assuming isospin symmetry the matrix element a_3 equals the ratio $|g_A/g_V| = 1.2573 \pm 0.0028$ [Cas 98] of axial vector (g_A) to vector coupling (g_V). Further, by assuming SU(3)$_f$ symmetry for the axial-vector flavour octet current, a_3 and a_8 can be expressed in terms of the decay constants $F = 0.459 \pm 0.008$ and $D = 0.798 \pm 0.008$ [Cas 98] obtained from neutron and hyperon β-decays:

$$a_3 = F + D, \;\; a_8 = 3F - D \,. \tag{2.63}$$

The matrix element a_0 cannot be calculated from the decay constants, but can be determined from Eq. (2.58) using the measured values of $\Gamma_1^{p(n)}$ together with Eq. (2.63).

In the QPM the axial-vector current matrix elements are related to the first moments $\Delta q_f = \int_0^1 \mathrm{d}x \; \Delta q_f(x)$ of the polarised quark and anti-quark distributions by

$$a_0 = \Delta\Sigma \equiv \Delta u + \Delta\bar{u} + \Delta d + \Delta\bar{d} + \Delta s + \Delta\bar{s} \,, \tag{2.64}$$

$$a_3 = \Delta q_3 \equiv \Delta u + \Delta\bar{u} - \Delta d - \Delta\bar{d} \,, \tag{2.65}$$

$$a_8 = \Delta q_8 \equiv \Delta u + \Delta\bar{u} + \Delta d + \Delta\bar{d} - 2(\Delta s + \Delta\bar{s}) \,. \tag{2.66}$$

Thus, in the QPM, a_0 equals the fraction $\Delta\Sigma$ of the nucleon spin carried by quark spins. In QCD the Adler-Bell-Jackiw anomaly [Adl 69a, Bel 69] causes a gluon contribution to $a_0(Q^2)$ [Alt 88, Car 88, Efr 88] which makes $\Delta\Sigma$ dependent on the factorisation scheme, while a_0 is not. In the Adler-Bardeen [Adl 69b] factorisation scheme [Bal 95]

$$a_0(Q^2) = \Delta\Sigma - n_f \frac{\alpha_s(Q^2)}{2\pi} \Delta g(Q^2). \tag{2.67}$$

In this scheme $\Delta\Sigma$ is independent of Q^2, but cannot be obtained from the measured $a_0(Q^2)$ without an input value for Δg. In the $\overline{\mathrm{MS}}$ scheme $\Delta\Sigma$ is equal to $a_0(Q^2)$ but then $\Delta\Sigma$ depends on Q^2 [Che 96]. The differences between the two schemes do not vanish in the limit $Q^2 \to \infty$ since $\alpha_s(Q^2)\Delta g(Q^2)$ remains finite for $Q^2 \to \infty$ [Alt 88].

2.5.1. Bjørken sum rule

The Bjørken sum rule [Bjø 66] derived from current algebra relates the difference $\Gamma_1^p - \Gamma_1^n$ of the integrals of the proton and neutron spin structure functions g_1 to the neutron β-decay constant g_A/g_V:

$$\Gamma_1^p(Q^2) - \Gamma_1^n(Q^2) = \frac{1}{6} \left| \frac{g_A}{g_V} \right| \; \Delta C^{NS}(Q^2) \,, \tag{2.68}$$

where ΔC^{NS} is given by Eq. (2.61). At $Q^2 = 5$ GeV^2 and with $\alpha_s(m_Z) = 0.118 \pm 0.003$ (where m_Z is the Z^0 mass) one obtains $\Gamma_1^p - \Gamma_1^n = 0.182 \pm 0.003$ in comparison with the experimental world average of 0.170 ± 0.012 [Abe 98]. It follows that the Bjørken sum rule is experimentally confirmed with a precision of about 10%.

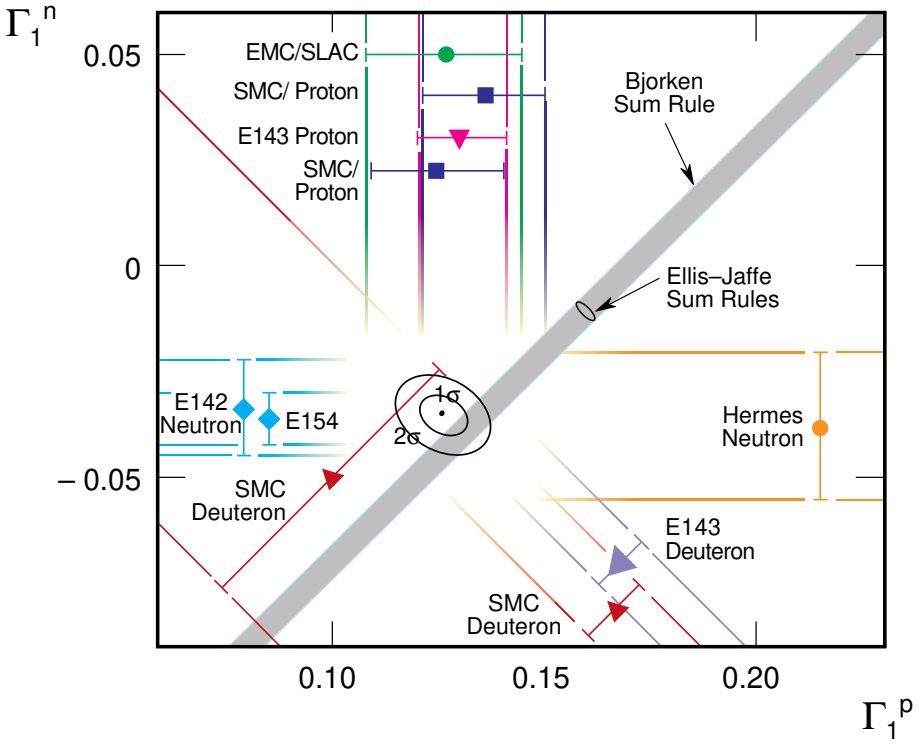

Figure 2.6.: Summary of experimental tests of the Bjørken and Ellis-Jaffe sum rules [Hug 99]. The horizontal (vertical) axis is the integral Γ_1^p (Γ_1^n). The prediction of the Bjørken sum rule is shown by the $45°$ band and the Ellis-Jaffe sum rule predictions are indicated by the small ellipse. The overall best fit to the experimental data and the 1σ and 2σ contours are shown.

2.5.2. Ellis-Jaffe sum rule

Separate sum rules for Γ_1^p and Γ_1^n can only be derived when assumptions about a_0 are made. In the QPM the first moments ΔC^{NS} and ΔC^S of the coefficient functions are equal to unity. Assuming isospin symmetry and SU(3)$_f$ symmetry (Eq. (2.63)) the expression (2.58) can be written

$$\Gamma_1^{p(n)} = \frac{1}{12}\left[+(-)\left|\frac{g_A}{g_V}\right| + \frac{5}{3}(3F - D)\right] + \frac{1}{3}(\Delta s + \Delta\bar{s}). \tag{2.69}$$

This relation was first derived by Ellis and Jaffe [Ell 74]. With the additional assumption that $\Delta s + \Delta\bar{s} = 0$ they obtained numerical predictions for $\Gamma_1^{p(n)}$. Since $\Delta\Sigma = a_8 + 3(\Delta s + \Delta\bar{s})$, the assumption $\Delta s + \Delta\bar{s} = 0$ is equivalent to $\Delta\Sigma = a_8 = 3F - D$. The QCD-corrected Ellis-Jaffe prediction for $\Delta s + \Delta\bar{s} = 0$ becomes

$$\Gamma_1^{p(n)}(Q^2) = \frac{1}{12}\left[+(-)\left|\frac{g_A}{g_V}\right| + \frac{1}{3}(3F - D)\right]\ \Delta C^{NS}(Q^2) + \frac{1}{9}(3F - D)\,\Delta C^S(Q^2)\,. \tag{2.70}$$

With $\alpha_s(m_Z) = 0.118 \pm 0.003$ it follows from Eq. (2.70) that $\Gamma_1^p = 0.164 \pm 0.005$ and $\Gamma_1^n = -0.018 \pm 0.004$ at $Q^2 = 5$ GeV^2 compared to the experimental world average of $\Gamma_1^p = 0.130 \pm 0.006$ and $\Gamma_1^n = -0.040 \pm 0.008$ [Abe 98] at the same scale, so that this sum rule is significantly violated. Fig. 2.6 summarises the results on Γ_1 for the proton, neutron and deuteron from various experiments and compares the experimental results with the expectations from the Ellis-Jaffe and Bjørken sum rules. The integral Γ_1^d for the deuteron is related to Γ_1^p and Γ_1^n by $\Gamma_1^p + \Gamma_1^n = 2\Gamma_1^d / \left(1 - \frac{3}{2}\omega_D\right)$ where $\omega_D = 0.05 \pm 0.01$ is the probability of the deuteron to be in a D-state.

2.6. Semi-inclusive deep inelastic scattering

2.6.1. Semi-inclusive cross section and asymmetries

In semi-inclusive DIS, $lN \to l'hX$, a final state hadron h is detected in coincidence with the scattered lepton. Applying the quark parton model outlined in section 2.3, the hadron fragments are produced following the ejection of a quark by the virtual photon probe. The quark is ejected along the direction of the virtual photon in the laboratory frame and its energy is of the same order of magnitude as the energy of the photon [Alt 82]. If quarks could be liberated, then, for sufficiently large Q^2, a free quark would emerge from the target. However, due to the confinement property of QCD the struck quark and the target remnant will fragment into hadrons. Hadrons produced from the fragmentation of the struck quark are defined as *current fragments* while those produced from the fragmentation of the target remnant are called *target fragments*. Since the fragmentation process involves long distance (small Q^2) processes the fragmentation functions cannot be calculated by perturbative QCD.

The process of the fragmentation of the struck quark is parameterised by fragmentation functions $D_f^h(x, Q^2, z)$ which are defined as the probability density that a struck quark q_f, probed at a particular x and Q^2, fragments into a hadron h with energy fraction z. In order to study the fragmentation functions $D_f^h(x, Q^2, z)$ the current fragments must be selected. To achieve this several methods are used in literature. These include selecting hadrons which are (a) forward in the $\gamma^* N$ centre of mass system ($x_F > 0$), (b) forward in the Breit frame, or (c) fast in the laboratory system (e.g. $z > 0.2$). These kinematical cuts cannot unambiguously identify the current fragments, but allow a significant enhancement of the correlation of the detected hadron with the struck quark. The separation of the two fragmentation regions improves with increasing values of W.

In LO QCD the differential cross section $\mathrm{d}\sigma^h/\mathrm{d}z$ for the production of a particular hadron h from the current fragmentation region can be expressed in terms of fragmentation functions and unpolarised quark distributions

$$\frac{1}{\sigma_{\mathrm{INCL}}} \frac{\mathrm{d}\sigma^h}{\mathrm{d}z}(x, Q^2, z) = \frac{\sum_f e_f^2 \; q_f(x, Q^2) \; D_f^h(x, Q^2, z)}{\sum_f e_f^2 \; q_f(x, Q^2)} \,, \tag{2.71}$$

where σ_{INCL} denotes the inclusive DIS cross section. Further, based on Eqs. (2.55) and (2.71), the LO semi-inclusive structure function F_1^h is defined as

$$F_1^h(x, Q^2, z) = \frac{1}{2} \sum_f e_f^2 \; q_f(x, Q^2) \; D_f^h(x, Q^2, z) \; . \tag{2.72}$$

Under the assumption that the fragmentation process is spin-independent, i.e. that the probability to produce a hadron of type h by scattering from a quark q_f is independent of the relative orientations of the quark spin and the nucleon spin, the LO semi-inclusive spin structure function g_1^h can similarly be written as

$$g_1^h(x, Q^2, z) = \frac{1}{2} \sum_f e_f^2 \; \Delta q_f(x, Q^2) \; D_f^h(x, Q^2, z) \; . \tag{2.73}$$

Assuming $g_2^h = 0$ it follows for the z-integrated semi-inclusive spin asymmetries

$$\begin{aligned} A_1^h(x, Q^2) &\overset{g_2^h=0}{=} \frac{\int \mathrm{d}z \; g_1^h(x, Q^2, z)}{\int \mathrm{d}z \; F_1^h(x, Q^2, z)} \\ &= \frac{\sum_f e_f^2 \; \Delta q_f(x, Q^2) \; \int \mathrm{d}z \; D_f^h(x, Q^2, z)}{\sum_f e_f^2 \; q_f(x, Q^2) \; \int \mathrm{d}z \; D_f^h(x, Q^2, z)} \; . \end{aligned} \tag{2.74}$$

Eq. (2.74) relates the measured spin asymmetries A_1^h to the polarised and unpolarised quark distributions and fragmentation functions. The region over which z is integrated is determined by cuts on the hadron kinematics to select hadrons from the current fragmentation region. Given the fragmentation functions D_f^h and the unpolarised quark distributions q_f, Eq. (2.74) together with the corresponding expression for the inclusive asymmetry

$$A_1(x, Q^2) \overset{g_2=0}{=} \frac{g_1(x, Q^2)}{F_1(x, Q^2)} = \frac{\sum_f e_f^2 \; \Delta q_f(x, Q^2)}{\sum_f e_f^2 \; q_f(x, Q^2)} \tag{2.75}$$

can be used to extract the polarised quark distributions Δq_f from a set of measured inclusive and semi-inclusive asymmetries.

2.6.2. Fragmentation functions

The fragmentation functions are subject to constraints imposed by momentum and probability conservation. The total energy of all hadrons emerging from the struck quark q_f must be that of q_f

$$\sum_h \int_0^1 \mathrm{d}z \; z \; D_f^h(z) = 1 \; , \tag{2.76}$$

and the mean multiplicity of hadrons of type h emerging from the parent quark q_f with $z > z_{\min}$ is given as the integral

$$\int_{z_{\min}}^1 \mathrm{d}z \; D_f^h(z) \; . \tag{2.77}$$

Since the fragmentation proceeds by strong interactions, the number of independent fragmentation functions is reduced by isospin and charge conjugation invariance. In particular the fragmentation functions of u and d quarks into charged pions can be expressed by two independent fragmentation functions called *favoured* (D^+) and *unfavoured* (D^-)

$$D^+ \equiv D_u^{\pi^+} = D_d^{\pi^-} = D_{\bar{u}}^{\pi^-} = D_{\bar{d}}^{\pi^+} , \tag{2.78}$$

$$D^- \equiv D_d^{\pi^+} = D_u^{\pi^-} = D_{\bar{d}}^{\pi^-} = D_{\bar{u}}^{\pi^+} . \tag{2.79}$$

The fragmentation functions D^+ and D^- have been measured in charged lepton DIS from identified pions in the forward region [Gei 98a, Arn 89]. This was achieved by taking the sum and difference of the measured scaled energy distributions $N_e^{-1}\mathrm{d}N^{\pi^+}/\mathrm{d}z$ and $N_e^{-1}\mathrm{d}N^{\pi^-}/\mathrm{d}z$ from a deuterium target, where N_e is the number of DIS events and N^π is the number of coincident pions. At large values of x, where sea quarks can be neglected, a simple expression for D^+ and D^- follows

$$D^\pm = \frac{1}{3N_e}\left[4\,\frac{\mathrm{d}N^{\pi^\pm}}{\mathrm{d}z} - \frac{\mathrm{d}N^{\pi^\mp}}{\mathrm{d}z}\right] . \tag{2.80}$$

The data show that with increasing values of z the u quark preferentially fragments into a π^+ rather than into a π^-, as expected from charge conservation. As z decreases D^+ and D^- become nearly equal since current fragment hadrons are more and more diluted by target fragments.

As discussed in section 2.4 gluonic radiation in QCD introduces a logarithmic Q^2-dependence in the quark distributions q_f. Similarly, processes such as gluon bremsstrahlung from the final quark line as shown schematically in Fig. 2.7 (a) introduce a Q^2-dependence in the fragmentation functions. Such scale breaking effects have been experimentally verified (see e.g. [Arn 85b, Arn 86, Jon 91]). Given the z-dependence of the fragmentation functions at some initial scale Q_0^2, the evolution of the fragmentation functions can be calculated by perturbative QCD. If the fragmentation functions are combined with the cross section for the inclusive production of each parton type in a given physical process, predictions can be made for scaling violations, expressed as the Q^2-evolution of final state hadron multiplicities. LO and NLO QCD expressions for the scale dependence of fragmentation functions into light mesons are presented e.g. in [Bin 95] and [Rol 96]. Predictions based on these fragmentation functions are in excellent agreement with experimental data at different scales. An overview of the analysis of the scaling violations of hadron multiplicities and fragmentation functions can be found in [Cow 94].

The assumption of *factorisation* states that the quark fragmentation should be independent of photon-quark scattering process and thus should be independent of x. The factorisation property can be broken by processes such as gluon exchange between the initial and final quark lines as shown in Fig. 2.7 (b). Tests of factorisation utilise precise measurements of the total hadron multiplicity $\sigma_{\mathrm{INCL}}^{-1}\,\mathrm{d}\sigma^h/\mathrm{d}z$. Within small bins in W a rise of the charged hadron multiplicity with increasing values of x is observed [Arn 85a, Arn 86]. However, since the variables x, Q^2 and W are correlated $(W^2 = M^2 + Q^2[1/x - 1])$,

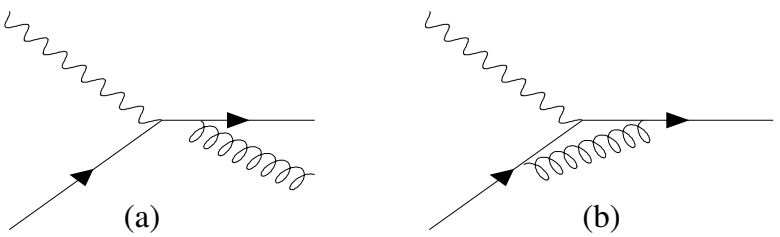

Figure 2.7.: Example of a QCD effect which produces scaling violations (a), and an effect which causes factorisation violation (b).

a variation of the multiplicity as a function of x for fixed W can also be interpreted as a variation with Q^2 for fixed W, so that it is experimentally difficult to distinguish between scaling violations (Q^2-dependence of D_f^h) and a breakdown of factorisation (x-dependence of D_f^h). Alternatively, factorisation breaking can be investigated by comparing the observed dependence of the multiplicity on x to the expectation from the QPM (with exact factorisation) and to predictions based on QCD calculations including higher order effects which lead to factorisation breaking. While the QPM expectation of $\sigma_{\mathrm{INCL}}^{-1}\ \mathrm{d}\sigma^h/\mathrm{d}z\ =\ \sum_f\ e_f^2\ q_f(x)D_f^h(z)/\sum_f e_f^2\ q_f(x)$ does not provide a satisfactory description of the data, the experimental results show the same qualitative behaviour than the QCD calculation [Aub 82].

If the fragmentation of quarks is independent of their formation, the fragmentation functions measured in neutral current lepto-production should be the same as those measured in charged current neutrino-nucleon scattering or in e^+e^- annihilation (*environmental independence*). Experimentally, the multiplicity distributions measured in e^+e^- annihilation are consistent with those measured in DIS processes [Bre 99, Adl 97], showing that the integrals of the fragmentation functions are the same. The data thus support the environmental independence of quark fragmentation in charged and neutral current lepto-production and in e^+e^- annihilation.

2.6.3. Fragmentation models

As mentioned before perturbative QCD fails to calculate the fragmentation functions. Instead, phenomenological models have been developed to predict the fragmentation functions. This section summarises two of the most important models, the independent fragmentation model [Fie 78] and the string fragmentation model [And 83]. Both models are implemented into the JETSET-7.4 Monte Carlo generator [Sjö 94]. Based on these models fragmentation functions have been calculated which were then used in the extraction of the polarised quark distributions from the measured spin asymmetries. The LUND model has been extensively tested in e^+e^- annihilation and in DIS. The model contains free parameters which have to be adapted to the experimental conditions. These param-

eters are determined from tuning the model to particle production rates and event shape data. For a review on the tuning and test of the LUND model in e^+e^- annihilation see e.g. [Abr 96]. A comparison of the model with event shapes measured in DIS at HERA is given in [Adl 97]. The LUND model is found to give a good description of the data. Both the LUND and the independent fragmentation model have been tuned to HERMES data. The tuning procedure is described in [Gei 98a, Tal 98] and summarised at the end of this section. In the following a brief description of both fragmentation models is given. For a complete description of both models as realized in the JETSET generator see [Sjö 94].

Independent Fragmentation

The independent fragmentation (IF) model is based on a hierarchical process in which each parton is assumed to fragment independently from the others. In the model, the struck quark q_0 combines with the anti-quark $\bar{q}_1$ of a quark anti-quark pair $q_1\bar{q}_1$ created out of the vacuum to form the so-called first-rank primary meson with energy fraction z_0. The remaining energy fraction ($1 - z_0 = z_1$) is assigned to q_1. The next anti-quark is produced when the colour field breaks again creating the pair $q_2\bar{q}_2$, and $\bar{q}_2$ combines with q_1 to form a rank-2 primary meson. This process continues down to a certain energy cut-off $E_{\min}$, when the last remaining quark is neglected. The primary mesons may be unstable and decay into long-lived secondary particles.

The model contains a number of parameters which have to be determined in order to make quantitative predictions[2]. The first one concerns the sharing of the energy of the quark: Independent of the rank, the probability $f(\xi)$ that a meson carries a fraction ξ of the remaining energy plus longitudinal momentum $E + p_{\mathrm{L}}$ is always the same. The form of $f(\xi)$ is based on theoretical models or chosen to give agreement with data. In the IF model $f(\xi) = 1 - a + 3a(1 - \xi)^2$ with the normalisation $\int_0^1 f(\xi)\,\mathrm{d}\xi = 1$, and a to be determined from fits to data. A second parameter γ_q describes the relative probability for creating a quark pair $u\bar{u},\ d\bar{d}$ or $s\bar{s}$ as the colour field breaks. Neglecting heavier quarks one has $\gamma_u + \gamma_d + \gamma_s = 1$ and by isospin symmetry $u\bar{u}$ and $d\bar{d}$ pairs will be created equally (probability $\gamma \equiv \gamma_u = \gamma_d$) leaving the probability of creating an $s\bar{s}$ pair $\gamma_s = 1 - 2\gamma$. The parameter γ_s has been measured [Arn 84] and is set to 0.3γ. A third parameter, α_{ps}, is the fraction of primary mesons that are pseudo-scalar. The assumption is made that the only other primary mesons are vector mesons so that their fraction is $1 - \alpha_{\mathrm{ps}}$. The IF model uses $\alpha_{\mathrm{ps}} = 0.5$. The parameter r controls the suppression of diquark-antidiquark pair production in the colour field, compared with quark-antiquark production and is $r = 0.1$ determined from data. This ratio controls the relative meson and baryon multiplicities. Another parameter concerns the transverse momentum. The IF model assumes that the members of each $\bar{q}q$ pair created in the colour field have equal and opposite transverse momenta with a Gaussian distribution. Any primary meson will have a transverse momentum equal to the vector sum of the transverse momenta of the quark and anti-quark the meson is made of. This leads to primary mesons with a Gaussian

[2] All values given for model parameters in this section refer to the JETSET default values.

distribution of transverse momenta. The width of the transverse momentum distribution can be adjusted in the model.

Many properties of fragmentation functions are described successfully by the IF model. The most serious conceptual weakness of the model is its lack of Lorentz invariance. The fragmentation process is explicitly carried out in the hadronic centre of mass frame and the transformation into a different reference frame affects the results of the fragmentation procedure. Furthermore, since the quark of highest rank is neglected, the colour and flavour quantum numbers are not conserved.

String Fragmentation

In QCD a linear confinement is expected at large distances. This provides the starting point for the string fragmentation (SF) model, which is the most successful model nowadays to match the experimental data. The SF model is most easily illustrated for the production of a back-to-back $\bar{q}q$ pair. As the partons move apart, the physical picture is that of a colour flux tube being stretched between the $\bar{q}$ and the q. If the tube is assumed to have a constant field energy κ per unit length, this leads to a confinement picture with a linearly rising potential, $V(r) = \kappa r$. From hadron mass spectroscopy, the string constant κ is known to be $\kappa \approx 1$ GeV/fm. At a certain distance the field energy is sufficiently large to produce a quark-antiquark pair $\bar{q}_1 q_1$ so that the original string is divided into two substrings, which now fragment independently from each other. For each string, this iterative procedure continues until a string-connected quark-antiquark pair is close to the mass shell of a hadron.

A number of parameters are shared between the IF model and the SF model. These are the flavour production ratios ($\gamma_u,\ \gamma_d$ and γ_s), the ratio between pseudo-scalar and vector meson production ($\alpha_{\rm ps}$) and the ratio between quark and diquark production (r).

In the SF model the production of a $\bar{q}q$ pair is governed by a quantum mechanical tunnelling mechanism and the production probability for this tunnelling process is proportional to

$$\exp\left(-\frac{\pi m_\perp^2}{\kappa}\right) , \tag{2.81}$$

where $m_\perp^2 \equiv m^2 + p_\perp^2$, m is the quark mass and $p_\perp$ is the transverse momentum of the quark with respect to the string. The string itself has no transverse momentum, so $p_\perp$ of each quark produced in a pair is balanced by its partner. The resultant hadrons receive their $p_\perp$ from the vector sum of the transverse momenta of their constituent quarks. The width $\langle p_\perp \rangle$ of the $p_\perp$ distribution can be adjusted in the JETSET code. The fraction ζ of the disposable energy plus longitudinal momentum $E + p_{\rm L}$ assigned to a hadron is controlled by the so-called LUND symmetric fragmentation function

$$f(\zeta) = \frac{(1-\zeta)^a}{\zeta} \exp\left(\frac{-bm_\perp^2}{\zeta}\right) , \tag{2.82}$$

where a and b are free parameters.

The SF model contains several features which distinguish it from the IF model. In particular, the use of a relativistic string model for fragmentation, whereas the IF model does not give any dynamical picture of the fragmentation process. The treatment of several jets is relativistic in SF and the model avoids problems related to matching quantum numbers of different jets. It also allows for the possibility of gluon radiation and $\bar{q}q$ pair production, leading to extra jets. The probability of gluon radiation is taken from QCD, and the problem of divergences in the cross section is circumvented by using cut-off parameters such that soft or collinear gluons are absorbed into the single quark fragmentation. A weakness of both models is that they do not naturally accommodate baryon production, in particular for a target fragment jet.

Tuning of fragmentation parameters

The default free parameters of the JETSET LUND model are the constants a and b of the LUND symmetric fragmentation function given in Eq. (2.82) and the width $\langle p_\perp \rangle$ of the transverse momentum distribution of the produced hadrons. The default parameters were determined by tuning the model to high energy e^+e^- annihilation data which require the simulation of jet and multi-jet events [Ing 97]. While the fragmentation process is experimentally found to be equivalent for both e^+e^- and DIS interactions, these parameters refer to the simulation of QCD effects which are included in the Monte Carlo. As HERMES does not have high enough energy to produce jets, it is necessary to adjust the free parameters such that the simulation gives an accurate description of the experimental data. The procedure for fitting the parameters to the experimental data is described in [Gei 98a, Tal 98]. An iterative fitting procedure was used whereby the event generator was run for a particular set of parameters and the difference between the generated and the measured z and $p_\perp$ distributions was minimised. The optimum parameters found after this tuning procedure were $\langle p_\perp \rangle = 0.34\ (0.36)$ GeV, $a = 0.82\ (0.32)$ and $b = 0.58\ (0.24)$ GeV^{-2} compared to the default values given in parenthesis [Gei 98a]. The result of the tuning procedure is to create more low energy string breaks, resulting in more low energy hadrons produced in the fragmentation process. A comparison of the experimentally measured z distribution of charged hadrons with the prediction from the tuned and from the default JETSET generator can be found in [Gei 98a]. The tuned JETSET model successfully describes the measured z distributions.

3. The HERMES Experiment

The HERMES experiment [HER 93] is located at the HERA positron-proton collider[1] at DESY in Hamburg, Germany. The experiment is arranged such that the 27.5 GeV longitudinally polarised positron beam interacts with polarised pure atomic gas targets internal to the HERA positron ring without interference from the proton beam. The positron beam is self-polarised transverse to the beam plane by the emission of synchrotron radiation. Spin rotators provide longitudinal beam polarisation at the HERMES interaction region. Positron polarisations exceeding 50% are routinely achieved and measured using two independent Compton backscattering polarimeters. In 1995 an optically pumped po-

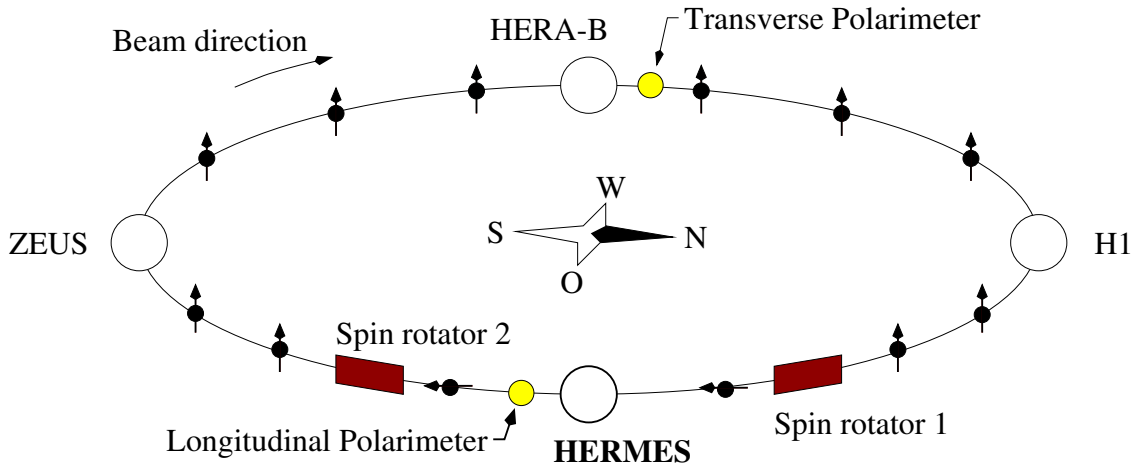

Figure 3.1.: The HERA storage ring with its four experiments ZEUS, HERA-B, H1 and HERMES. The locations of the positron beam polarimeters are shown. The arrows indicate the transverse or longitudinal polarisation direction of the positron beam.

larised ^{3}He target was used. In 1996/97 the experiment was performed with an atomic beam source of polarised hydrogen. The typical nuclear polarisation was 90% (50%) for the hydrogen (^{3}He) source. In addition, various unpolarised gas targets have been used with the maximum target thickness limited only by the impact on the lifetime of the stored

[1] HERA has been operated with positrons in 1995 to 1997. Sine 1998 HERA was also running with electrons.

positron beam. The HERMES spectrometer is a forward angle detector and was designed for measuring both inclusive and semi-inclusive processes. It contains a dipole magnet and tracking chambers upstream of the magnet, in the magnetic field and downstream of the magnet providing charged particle tracking and momentum reconstruction. Particle identification is accomplished using a lead-glass calorimeter, a pre-shower counter, six transition radiation detector modules and a N_2/C_4F_{10} threshold gas Čerenkov counter[2]. The kinematic range accessible is $0.004 < x < 1$ and $0.2 < Q^2 < 20$ GeV^2. The luminosities obtained with polarised targets are in the range of $0.5 - 5 \times 10^{32}$ nucleons/(cm$^2\cdot$ sec).

3.1. The polarised positron beam

3.1.1. Self-polarisation of the positron beam

The HERA positron beam becomes polarised transverse to the beam plane through the emission of synchrotron radiation (Sokolov-Ternov mechanism) [Sok 64]. For positrons moving in a plane perpendicular to a constant magnetic field B_y, the polarisation P_y increases in time according to [Cha 81]

$$P_y(t) = P_{\max}\left[1 - e^{-t/\tau}\right], \tag{3.1}$$

where τ is the polarisation build up time and $P_{\max}$ the equilibrium polarisation. For positrons (electrons) the polarisation direction is anti-parallel (parallel) to the guide field. In a planar storage ring, in the absence of depolarising effects, the equilibrium polarisation is $P_{\rm ST} = 92.4\%$. The build up time $\tau_{\rm ST}$ is a strong function of the beam energy and of the bending radius ρ in the magnetic field and is 40 min for a beam energy of 27 GeV. In HERA the magnetic field seen by the positrons is more complicated than a simple homogeneous vertical field and the polarisation mechanisms can be counteracted by depolarising effects. The build-up of polarisation can be divided into two separated processes, namely the Sokolov-Ternov mechanism and the depolarisation due to spin diffusion, resulting from the classical stochastical motion of the stored positrons [Bar 94]. In the presence of depolarising effects the value of the asymptotic polarisation and the build-up time are determined by the relative strength of both processes

$$P_{\max} = P_{\rm ST} \cdot \frac{\tau_{\rm dep}}{\tau_{\rm dep} + \tau_{\rm ST}}, \tag{3.2}$$

$$\tau = \tau_{\rm ST} \cdot \frac{\tau_{\rm dep}}{\tau_{\rm dep} + \tau_{\rm ST}}, \tag{3.3}$$

where the strength of the depolarisation is described by the time constant $\tau_{\rm dep}$. The measurement of the build-up time τ allows one to calibrate the polarimeter since the equilibrium polarisation $P_{\max}$ can be calculated from the measured time constant (*rise time*

[2]The description of the HERMES apparatus refers to the setup used in 1995 to 1997. In 1998 the threshold Čerenkov counter has been replaced by a ring-imaging Čerenkov counter.

calibration)

$$P_{\max} = \tau \cdot \frac{P_{\mathrm{ST}}}{\tau_{\mathrm{ST}}} \,. \tag{3.4}$$

This value can then be compared to the measured polarisation. As the HERMES experiment requires longitudinal polarisation a pair of spin rotators [Bar 95] has been installed which rotates the spin from the vertical into the longitudinal direction upstream of the HERMES interaction region and back to the vertical direction downstream of the interaction region. The average positron beam polarisation was about 55% in 1995 to 1997.

3.1.2. Beam polarimetry

In order to maximise the positron beam polarisation, the orbit of the positron beam is optimised empirically which requires a reasonably fast polarimeter. Furthermore, the polarisation measurement has to be done in parallel to the running experiments and without affecting these. A common method to achieve this is through the use of a Compton-laser polarimeter. In this technique, a circularly polarised photon beam is scattered off the polarised positron beam. The polarisation of the positron beam can be determined by measuring the asymmetry in the spin-dependent Compton cross section for left and right circularly polarised laser light. For transversely polarised positrons a spatial asymmetry is measured with respect to the orbital plane of the positrons, while for longitudinally polarised positrons the asymmetry is measured in the energy-dependent cross section.

In the rest frame of the positron the Compton cross section for scattering circularly polarised photons from polarised positrons can be written as a function of the initial positron and photon polarisations $\boldsymbol{P}$ and $\boldsymbol{S}$

$$\frac{\mathrm{d}\sigma}{\mathrm{d}\Omega}(\boldsymbol{P}, \boldsymbol{S}) = \Sigma_0 + S_1(0)\Sigma_1' + S_3 \left[P_y \Sigma_{2y} + P_z \Sigma_{2z}\right], \tag{3.5}$$

where the positron polarisation direction is specified in Cartesian coordinates $\boldsymbol{P} = P_e \hat{\boldsymbol{P}} = (P_x, P_y, P_z)$ and that of the incident photon by the Stokes vector $\boldsymbol{S} = (S_0, S_1, S_2, S_3)$ [Fan 49]. The magnitude of linear light polarisation is given by $S_{\mathrm{lin}} = \sqrt{S_1^2 + S_2^2}$ and that of circular light polarisation by $S_{\mathrm{circ}} = |S_3|$. A positive (negative) value of S_3 indicates left-handed (right-handed) helicity $S_{3\mathrm{L}}$ $(S_{3\mathrm{R}})$. For normalisation of the Stokes vector $S_0 = 1$. The functions Σ_0, Σ_1', Σ_{2y} and Σ_{2z} are functions of the initial and final photon momenta and the scattering angles and can be found in [Bar 93]. The quantity $S_1(0)$ is calculated from S_{lin} and the azimuthal orientation of the linear polarisation ϕ_{lin} with respect to the scattering plane defined by the momenta of the incoming and outgoing photon. From Eq. (3.5) on can derive the cross section asymmetry measured by switching the helicity of the laser light

$$A(y, E_\gamma) = \frac{\sigma(y, E_\gamma)_{\mathrm{L}} - \sigma(y, E_\gamma)_{\mathrm{R}}}{\sigma(y, E_\gamma)_{\mathrm{L}} + \sigma(y, E_\gamma)_{\mathrm{R}}} = \Delta S_1 \frac{\Sigma_1'}{\Sigma_0} + \Delta S_3 \left[P_y \frac{\Sigma_{2y}}{\Sigma_0} + P_z \frac{\Sigma_{2z}}{\Sigma_0}\right] \,, \tag{3.6}$$

where $\Delta S_3 = (S_{3\mathrm{L}} - S_{3\mathrm{R}})/2$ and similarly for ΔS_1. In the following Eq. (3.6) will be explored to measure the transverse and longitudinal positron polarisation.

The Transverse Polarimeter

The Transverse Polarimeter [Bar 93] measures the degree of transverse positron polarisation using the spatial asymmetry of the spin-dependent Compton cross section for scattering circularly polarised photons from transversely polarised positrons. Light from a continuous argon ion laser with a wavelength of 514 nm is directed against the positron beam and the energy E_γ and vertical position y of the backscattered photons are measured. A Pockels cell switches the circular polarisation direction with a frequency of 83.8 Hz. From Eq. (3.6) the cross section asymmetry for scattering circularly polarised photons from transversely polarised positrons ($P_z = 0$) can be written as

$$A(y, E_\gamma) = \Delta S_1 \frac{\Sigma_1'}{\Sigma_0} + \Delta S_3 P_y \frac{\Sigma_{2y}}{\Sigma_0} \,. \tag{3.7}$$

The transverse positron polarisation P_y is obtained from the difference Δy in the mean vertical positions $\langle y \rangle$ of the distributions measured with left and right circularly polarised light:

$$\Delta y(E_\gamma) = \frac{\langle y \rangle_{\mathrm{L}} - \langle y \rangle_{\mathrm{R}}}{2} = \Delta S_3 P_y \, \Pi_y(E_\gamma) \,. \tag{3.8}$$

The analysing power $\Pi_y(E_\gamma)$ is derived from the spin-dependent Compton cross section and is equal to the shift of means Δy for $\Delta S_3 P_y = 1$. The analysing power has a maximum value of 180 μm at $E_\gamma = 8$ GeV.

The energy E_γ and the vertical position y of the backscattered Compton photons are measured using a tungsten-scintillator sandwich calorimeter. Conceptually, the calorimeter can be considered to consists of two identical halves, one on top of the other. The scintillator plates of the upper and lower calorimeter halves are separated by a thin aluminium foil to provide light isolation. The scintillation light from each half is collected with wavelength shifters along the top and the bottom of the detector (channels T and B). The energy of an incoming photon is derived from the sum of the energies in the two halves $E_\gamma = E_{\mathrm{T}} + E_{\mathrm{B}}$ and the vertical position is measured using the energy asymmetry

$$\eta_{\mathrm{V}}(y) = \frac{E_{\mathrm{T}} - E_{\mathrm{B}}}{E_{\mathrm{T}} + E_{\mathrm{B}}} \,. \tag{3.9}$$

The energy resolution of the calorimeter is dominated by sampling fluctuations and photoelectron statistics leading to $\sigma(E)/E = P_1/\sqrt{E/\mathrm{GeV}} \oplus P_2$ with $P_1 = (22.7 \pm 0.5)\%$ and $P_2 = (3.4 \pm 0.2)\%$ [Ruh 97]. The vertical position resolution depends on the energy and the vertical impact point and is $\sigma_y = 0.5$ mm at $E_\gamma = 3$ GeV in the centre of the calorimeter and approximately scales according to $1/\sqrt{E_\gamma}$. The positron polarisation is measured every minute with an absolute statistical error of typically $(1-2)\%$ depending on the beam current. The fractional systematic error of the beam polarisation measurement is dominated by the rise time calibration error and was $\delta P_y/P_y = 4.0\%$ in 1995 and 3.4% in 1996/97.

The Longitudinal Polarimeter

For scattering circularly polarised photons from longitudinally polarised positrons, the integrals over Σ_1' and Σ_{2y} vanish in Eq. (3.6) so that the general form of the asymmetry integrated over y is given by

$$A(E_\gamma) = \frac{\sigma(E_\gamma)_{\mathrm{L}} - \sigma(E_\gamma)_{\mathrm{R}}}{\sigma(E_\gamma)_{\mathrm{L}} + \sigma(E_\gamma)_{\mathrm{R}}} = \Delta S_3 P_z \, \Sigma_{2z/0}(E_\gamma) \, , \tag{3.10}$$

where $\Sigma_{2z/0}(E_\gamma) \equiv \int \mathrm{d}y \, [\Sigma_{2z}(y, E_\gamma)/\Sigma_0(y, E_\gamma)]$. Eq. (3.10) shows that the longitudinal beam polarisation P_z is proportional to an energy dependent count rate asymmetry $A(E_\gamma)$ measured for switching the sign of S_3. The analysing power $\Sigma_{2z/0}(E_\gamma)$ can be found in [Bar 93]. It has a maximum value of about -0.6 at the highest possible Compton photon energy $E_{\gamma,\mathrm{max}} = 13.6$ GeV for the given beam energy of 27.5 GeV.

The setup of the Longitudinal Polarimeter is similar to the Transverse Polarimeter and is described in [Bec 99]. The light of a pulsed YAG laser with a wavelength of 532 nm and a pulse length of 3 ns is steered onto the positron beam by means of a computer controlled mirror system. The laser light is switched between the helicity states by a Pockels cell at a rate of about 100 Hz and hits the positron beam at about 53 m downstream of the HERMES target with a crossing angle of 9 mrad. When the intense laser pulse crosses a positron bunch several thousand Compton photons are backscattered. The energy sum of these Compton photons is measured in a radiation hard calorimeter which consists of an array of four (2.2×2.2) cm^2 NaBi(WO)$_2$ crystals with a length of 20 cm (19.4 radiation lengths). The energy resolution of the calorimeter improves with the deposited energy according to $\sigma(E)/E = P_1/\sqrt{E/\mathrm{GeV}} \oplus P_2$ with $P_1 = (24.5 \pm 0.5)\%$ and $P_2 = (12.3 \pm 0.5)\%$ [Men 99]. The calorimeter measures the energy weighted integrated asymmetry

$$A_{\mathrm{exp}} = \int \mathrm{d}E_\gamma \; E_\gamma \; A(E_\gamma) = \Delta S_3 P_z \int \mathrm{d}E_\gamma \; E_\gamma \; \Sigma_{2z/0}(E_\gamma) \, . \tag{3.11}$$

The analysing power $\int \mathrm{d}E_\gamma \; E_\gamma \; \Sigma_{2z/0}(E_\gamma)$ can be calculated from the spin-dependent Compton cross section and is -0.184 [HER 95] for the given photon and positron energies. The fractional systematic error of the polarisation measurement was $\delta P_z/P_z = 4.3\%$ in 1997.

3.2. The polarised gas targets

At HERMES a thin-walled cryogenically-cooled storage cell is placed in the HERA storage ring [Kra 95] through which the circulating positron beam passes. The cell is embedded in a vacuum chamber (see Fig. 3.2) and consists of an open-ended elliptical tube, with a feed tube intersecting at the centre. It is constructed from ultra-pure aluminium with a uniform wall thickness of about 100 μm and the cell walls are cooled in order to increase the target density by reducing the velocity of the target atoms. To avoid heating of the storage cell and particle shower development at the cell walls, the target region is

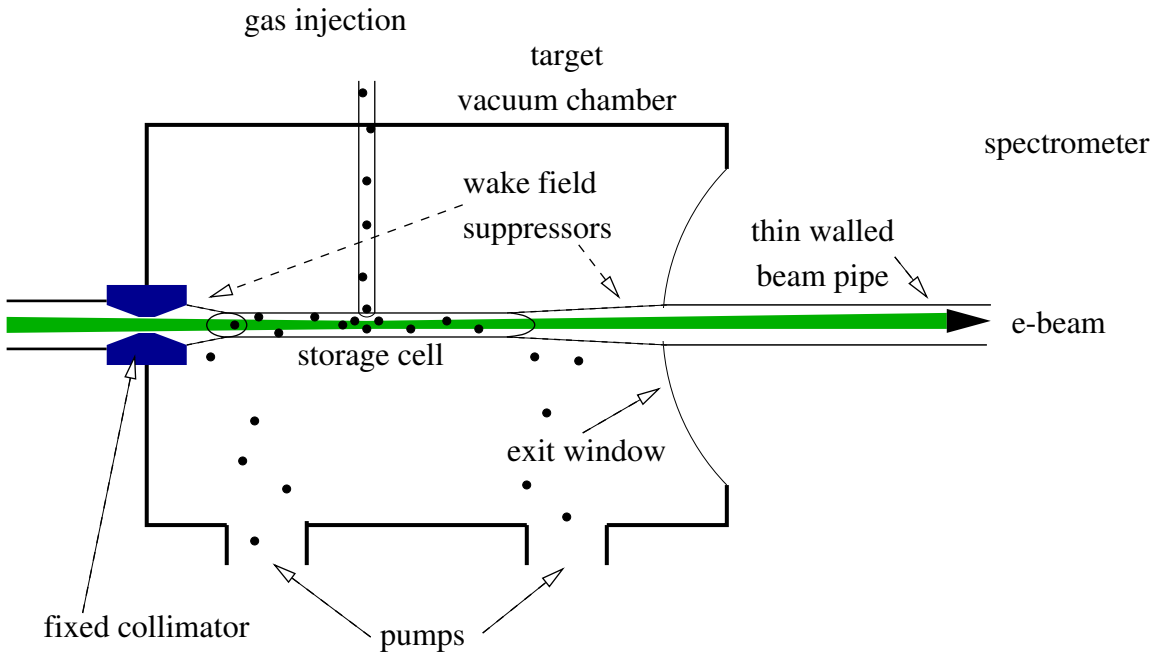

Figure 3.2.: Schematic diagram of the target region. See text for further explanation.

shielded by collimators against synchrotron light and beam halo particles. The cell is fed by polarised pure atomic gas from an optically pumped ^{3}He source, or from an atomic beam source of polarised hydrogen. Compared to a free atomic beam the storage cell increases the areal target density by about two orders of magnitude. The areal target densities are about 7.5×10^{13} nucleons/cm^2 for hydrogen and 1.2×10^{15}nucleons/cm^2 for ^{3}He. To maintain the ultra-high vacuum within the accelerator beam line the leaking gas atoms are pumped at both ends of the storage cell by a differential pumping system. Both target setups are equipped with a target magnet generating a longitudinal holding field for the nuclearly polarised gas atoms.

3.2.1. The polarised ^{3}He target

In 1995 a polarised ^{3}He target was installed in the HERMES experiment. In this section the principle of operation of the target is discussed. A detailed description can be found elsewhere [Lee 93, DeS 98]. The ^{3}He target uses an infrared laser to polarise ^{3}He atoms by meta-stability exchange optical pumping in a glass cell. Inside the glass cell a small fraction ($\simeq 10^{-6}$) of the atoms is excited from the ground state to the meta-stable state 2^3S_1 using a low intensity radio-frequency discharge. The meta-stable atoms are polarised by the absorption of angular momentum from circularly polarised laser light incident upon the sample and are excited to the 2^3P_0 state. Hyperfine interactions in the exited state transfer the polarisation of the electronic cloud to the nucleus so that the meta-stable sample gets nuclearly polarised. The nuclear polarisation of the 2^3P_0 state is transfered

to the ground state through meta-stability exchange collisions. The nuclearly polarised atoms exit the pumping cell through a capillary and are directed to the target storage cell. To maintain the polarisation of the target atoms, the whole target area is kept in a longitudinal holding field of 3.2 mT provided by a pair of large Helmholtz coils. During data taking the target polarisation direction is reversed every 10 minutes by inverting the circular polarisation direction of the laser light. In order to increase the target density the storage cell is cooled down to about 25 K.

The nuclear polarisation of the ^{3}He atoms is determined in two ways. The pumping cell polarimeter (PCP) measures the degree of circular polarisation of the 667 nm ^{3}He transition. This transition occurs as the electronic states of the ^{3}He atoms de-excite, having been excited by the radio-frequency discharge. The nuclear polarisation of the ^{3}He atoms is obtained from the measured circular light polarisation by a calibration relation. An independent measurement of the polarisation of the ^{3}He atoms inside the storage cell is provided by the target optical monitor (TOM). The gas atoms inside the target cell are excited by Coulomb interaction with the passing HERA positron beam and emit light at characteristic wavelength as they de-excite. The circularly polarised light is collected by a mirror located upstream in the beam pipe and analysed, yielding a measure for the target polarisation. The main principle difference between the TOM and the PCP lies in the excitation mechanism of the target atoms. The average nuclear ^{3}He polarisation was 55% with a fractional systematic error of the polarisation measurement of 5%.

3.2.2. The polarised ^{1}H target

In 1996 and 1997 the experiment employed an Atomic Beam Source (ABS) of polarised hydrogen (see Figure 3.3). A detailed description of the ABS is given in [Sto 94, Bra 97]. The ABS is based on the Stern-Gerlach separation of electron spin in an inhomogeneous magnetic field. Molecular hydrogen is dissociated by radio frequency discharge into hydrogen atoms and an unpolarised beam is formed by a cooled nozzle and skimmers. The atomic beam leaving the dissociator is directed into an inhomogeneous magnetic field generated by a sequence of sextupole magnets. Atoms with electronic spin along the local magnetic field direction are focused while other states are defocused and subsequently pumped. The selected atomic beam consist of two hyperfine states with opposite nuclear spin direction. Using high frequency transitions the population of one of the hyperfine states can be exchanged by a state with opposite nuclear spin direction to form an atomic beam consisting of two hyperfine states with parallel nuclear spin. Since 1998 the ABS is used to realize a polarised deuterium target.

The polarisation of the hydrogen atoms inside the target cell is measured by a Breit-Rabi Polarimeter (BRP). A small fraction of the target gas is extracted from the storage cell into the BRP to measure the relative populations of the hyperfine states and thus the nuclear polarisation of the sample. In order to suppress the recombination of hydrogen atoms the cell is coated by Dri-film or a layer of ice. The cell is operated at a temperature of about 100 K. A target gas analyser measures the fraction $1 - \alpha_{\mathrm{r}}$ of atoms that recom-

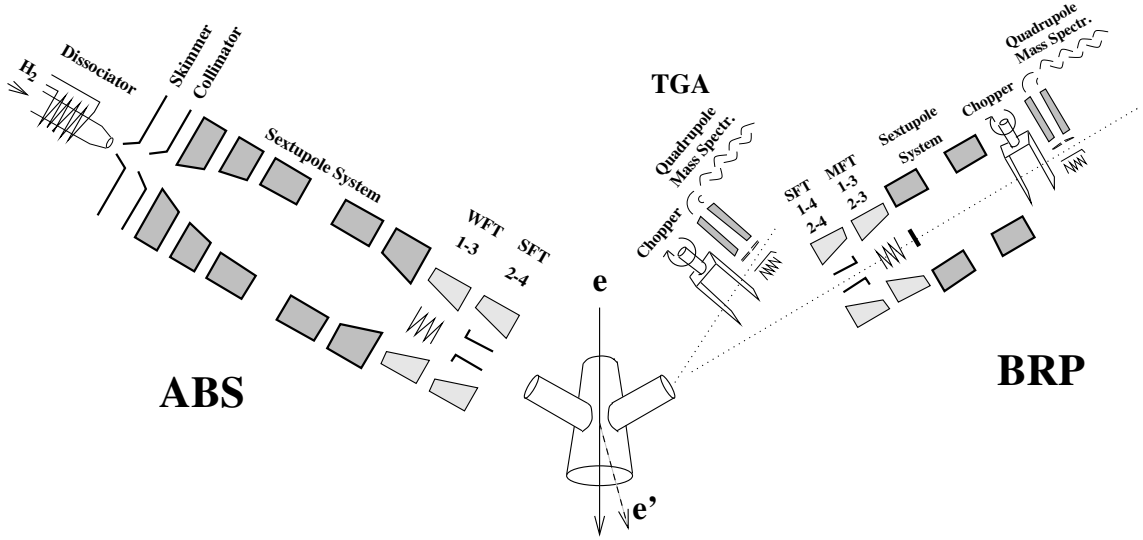

Figure 3.3.: Schematic diagram of the HERMES hydrogen target. The left side shows the Atomic Beam Source (ABS) used to inject nuclearly polarised hydrogen atoms into the storage cell. The right side shows the Breit-Rabi Polarimeter (BRP) to measure the nuclear polarisation of the hydrogen atoms and the Target Gas Analyser (TGA) to measure the composition of the target gas.

bined in molecules. The value of $\alpha_{\rm r}$ was 0.93 ± 0.04 (0.88 ± 0.03) in 1997 (1996). The target proton polarisation $p_{\rm T}$ inside the cell is calculated from the polarisation $p_{\rm BRP}$ of the hydrogen atoms analysed in the BRP according to

$$p_{\rm T} = \alpha_0 \left[\alpha_{\rm r} + (1-\alpha_{\rm r})\beta\right] \cdot c_{\rm p} \cdot p_{\rm BRP} \ , \tag{3.12}$$

where $1-\alpha_0 = 0.01 \pm 0.01$ is the fraction of protons entering the cell in molecules and $c_{\rm p}$ is a correction for sampling efficiencies of the BRP and TGA. The quantity β is defined as the ratio of the polarisation of protons in molecules from recombination to the polarisation of protons in atoms and is in the range $0.2 \leq \beta \leq 1.0$. During data taking the nuclear polarisation direction has been reversed every 45 s. The average proton polarisation was 88 $(82)\%$ in 1997 (1996) with a fractional systematic error of 4.5 $(6.3)\%$.

3.3. The HERMES spectrometer

The HERMES spectrometer is a forward angle detector, which consists of two identical halves above and below the positron ring plane. At low angles the spectrometer acceptance is limited by a pair of iron plates above and below the beam plane, which shield the positron and proton beams from the magnetic field of the spectrometer magnet. The scattering angle acceptance is 40 mrad $\leq |\theta_y| \leq 140$ mrad vertically and $|\theta_x| \leq 170$ mrad horizontally so that the total range of scattering angles is 40 mrad $\leq \theta \leq 220$ mrad.

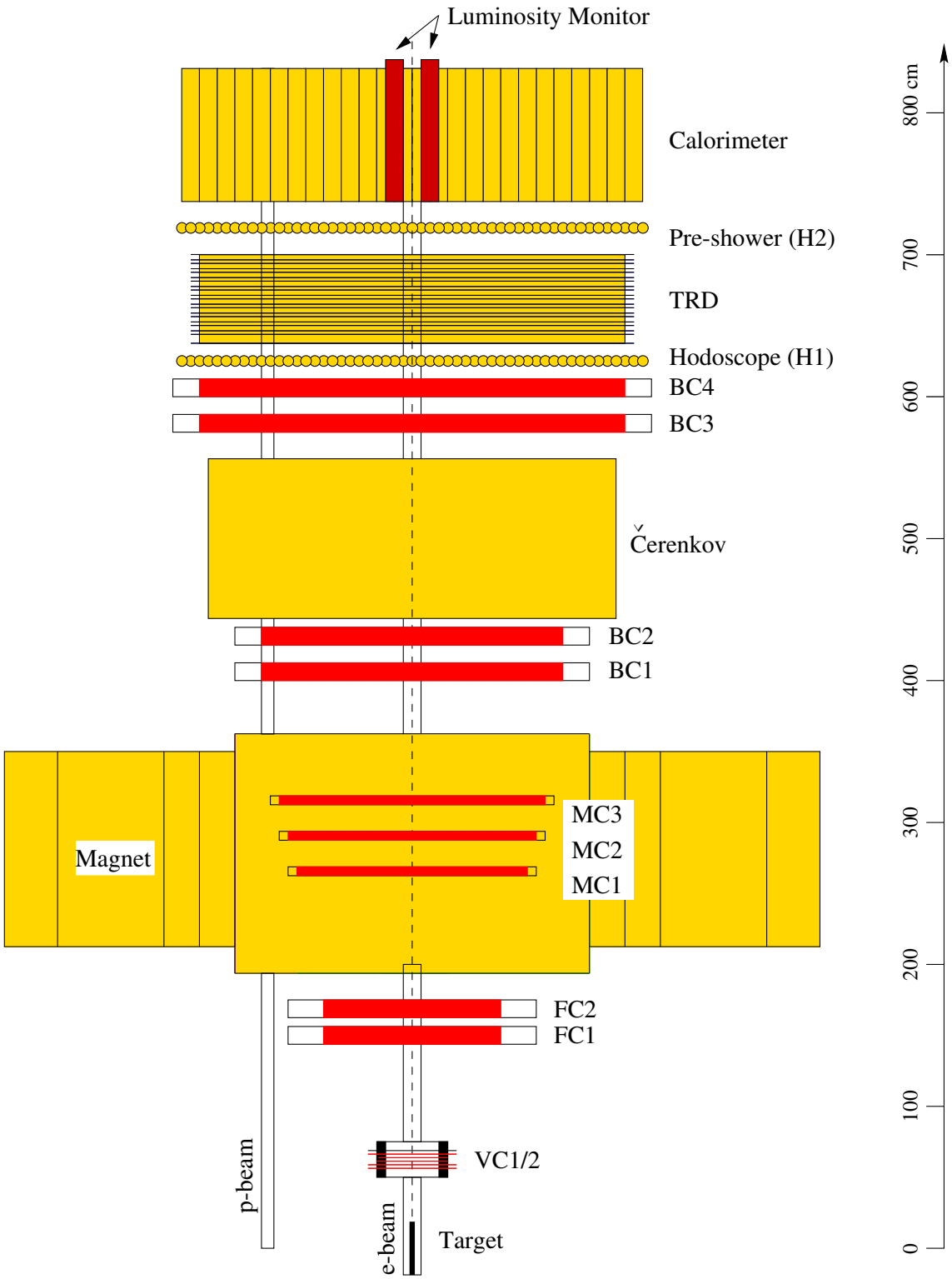

Figure 3.4.: Schematic diagram of the experimental apparatus (top view). See text for the meaning of the labels.

Fig. 3.4 shows a schematic diagram of the experimental apparatus[3]. A detailed description of the spectrometer is presented in [Ack 98]. In the following an overview of the individual detector components is given.

3.3.1. Tracking system

The tracking system consists of micro-strip gas chambers (referred to as vertex chambers (VC1/2)) and drift chambers (DVCs, FC1/2) upstream of the magnet, three proportional chambers in the magnetic field (MC1/3) and two sets of drift chambers downstream of the magnet (BC1/2 and BC3/4) (see Fig. 3.4). In total, the tracking system includes 57 tracking chamber planes per detector half with a number of 46880 readout channels. The initial trajectory of charged particles and the reconstruction of the scattering angle is provided by the tracking devices upstream of the magnet. To determine the particle momentum, charged tracks are deflected in the main spectrometer magnet with an integrated field of 1.3 Tm. A positron momentum resolution $\delta p/p$ of $(0.7 - 1.25)\%$, depending on the kinematics, and a scattering angle resolution of $(0.3 - 0.6)$ mrad are achieved. The resolution in the kinematical variables x-Bjørken and Q^2 is $\delta x/x = (4 - 8)\%$ and $\delta Q^2/Q^2 = (1.4-2.2)\%$. The track reconstruction is based on a fast pattern recognition algorithm and a look-up table for fast momentum determination. For a detailed description of the underlying tracking algorithms see [Wan 96].

3.3.2. Particle identification detectors

Particle identification (PID) is accomplished using a threshold gas Čerenkov counter, six transition radiation detector (TRD) modules, a pre-shower counter (a scintillator hodoscope preceded by 2 radiation lengths of lead) and a lead-glass calorimeter (see Fig. 3.4). This system provides clean positron hadron separation and additional pion identification. A hadron rejection factor of better than 10^4 is achieved to keep the contamination of the positron sample with hadrons below 1% over the entire kinematic range. The PID scheme is described in detail in [Kai 97]. In the following a short description of the individual PID detectors is given.

Calorimeter

Each half of the calorimeter [Ava 98] is build out of 420 radiation resistant F101 lead-glass blocks [Ava 96] attached to photo-multiplier tubes (PMTs). The blocks are arranged in an array of 42×10 modules in horizontal and vertical direction. The cross section of each module is (9×9) cm^2 with a length of 50 cm. The calorimeter provides a first-level trigger for scattered positrons and is used to separate leptons from hadrons.

[3] HERMES uses a right-handed coordinate system where the z-axis points along the direction of the incoming positron beam, the x-axis points to the left and the y-axis points upwards. The origin of the coordinate system is located in the centre of the target cell.

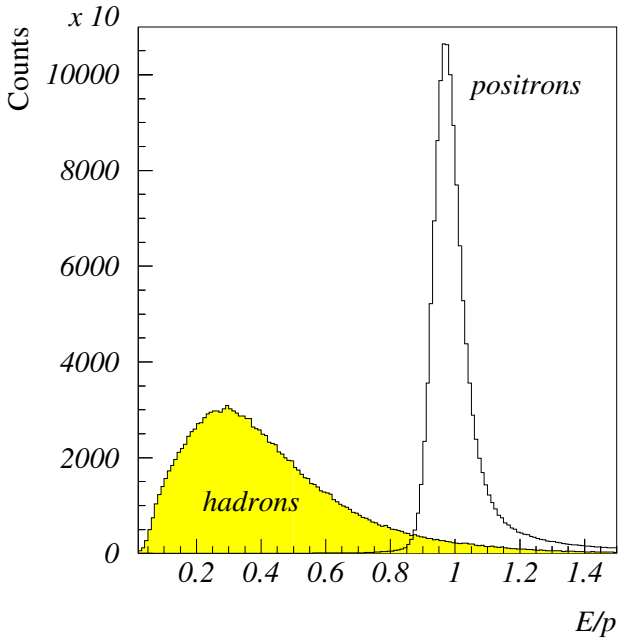

Figure 3.5.: The ratio of the energy deposit E in the calorimeter over the reconstructed particle momentum p is shown for positrons and hadrons (1997 data).

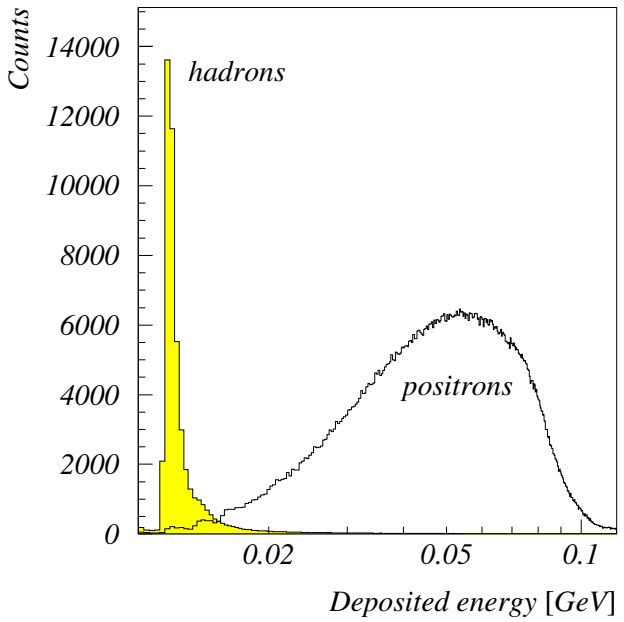

Figure 3.6.: Response of the pre-shower detector to hadrons and positrons (1997 data).

Lepton hadron separation can be accomplished by measuring the ratio of the deposited energy E over the particle momentum p. The depth of each lead-glass block corresponds to about 18 radiation lengths, so that the electro-magnetic shower is fully contained in the calorimeter. In contrast, hadrons will deposit only a fraction of their energy in the calorimeter due to their large nuclear interaction length. Consequently, the ratio of the energy deposit in the calorimeter (added to the energy loss in the pre-shower counter) divided by the reconstructed momentum p will be close to 1 for positrons whereas $E/p \leq 1$ for hadrons (see Fig. 3.5). The energy resolution of the calorimeter for positrons is $\sigma(E)/E = (5.1 \pm 1.1)\%/\sqrt{E/\mathrm{GeV}} + (1.5 \pm 0.5)\%$. The asymmetric tail of the positron distribution shown in Fig. 3.5 towards high values of E/p is due to events where a bremsstrahlungs photon is emitted by the positron in material upstream of the spectrometer magnet and the energies of both the bremsstrahlungs-photon and the positron are summed in the calorimeter.

Hodoscopes

At HERMES two hodoscopes are available to provide trigger signals and particle identification information. The hodoscope H1 (see Fig. 3.4) is used for trigger purposes only and consists of 42 vertical plastic scintillator paddles per detector

half connected to PMTs. H1 is mounted upstream of the TRD. The hodoscope H2 is installed downstream of the TRD and is designed as a pre-shower counter. It consists of a layer of 11 mm (2 radiation lengths) of lead in front of a scintillator plane identical to H1. Due to their large nuclear interaction length hadrons produce little energy deposit in the pre-shower counter while positrons start to develop an electro-magnetic shower and deposit a larger fraction of their energy. Fig. 3.6 shows the energy deposit in the pre-shower counter for positrons and hadrons. One can see a clear distinction between the two particle types.

Transition radiation detector

Transition radiation is emitted if a charged particle crosses the boundary of materials with different dielectric constants. The emission angle of the radiated photons is $\theta \simeq 1/\gamma$ where γ is the Lorentz factor. In the ultra-relativistic case ($\gamma > 1000$) the photons are radiated in a narrow cone in forward direction and have energies above several keV. Since a 5 GeV positron has a γ-factor of 10^4 compared to 36 for a pion of the same energy, transition radiation can be used very efficiently to distinguish positrons from hadrons. The TRD is able to provide a pion rejection factor of better than 100 for a positron efficiency of 90%. It consists of six identical modules per detector half, each one build of a 6.35 cm thick radiator and a 2.54 cm thick X-ray detector. The radiating volume is filled with polyethylene/polypropylene fibres with a diameter of $17-20$ μm surrounded by air, which corresponds to an average of 267 dielectric layers per particle track. A multi-wire proportional chamber filled with Xe/CH_4 is used to detect the generated photons and allows to assign the measured X-ray clusters to the reconstructed tracks. Fig. 3.7 shows the truncated mean value[4] of the energy deposit in the 6 TRD modules.

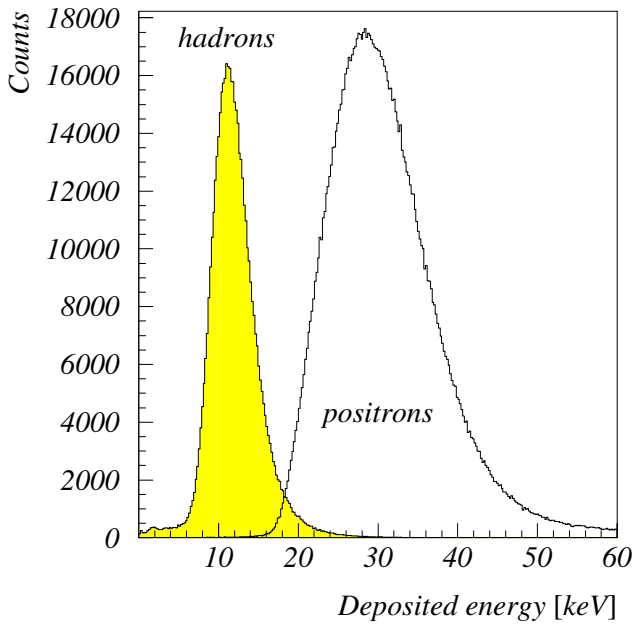

Figure 3.7.: Truncated mean value of the TRD for hadrons and positrons (1997 data).

[4]The *truncated mean value* of the TRD is defined as the average value of the five lowest module responses.

Threshold Čerenkov counter

Čerenkov light is emitted if a particle passes through a medium (refractive index n) with a velocity v faster than the speed of light in this medium c/n. The light is emitted along a cone with half opening angle $\theta_c = \arccos(1/\beta n)$ with respect to the particle momentum where $\beta = v/c$. The number of emitted photons is proportional to $\sin^2\theta_c$. The threshold Čerenkov counter can be used to identify particles above a certain threshold velocity $v_t > c/n$. Since $p = \gamma m_0 v$ with the Lorentz factor $\gamma = (1-\beta^2)^{-1/2}$ the threshold velocity is related to a threshold momentum p_t which depends on the particle rest mass m_0.

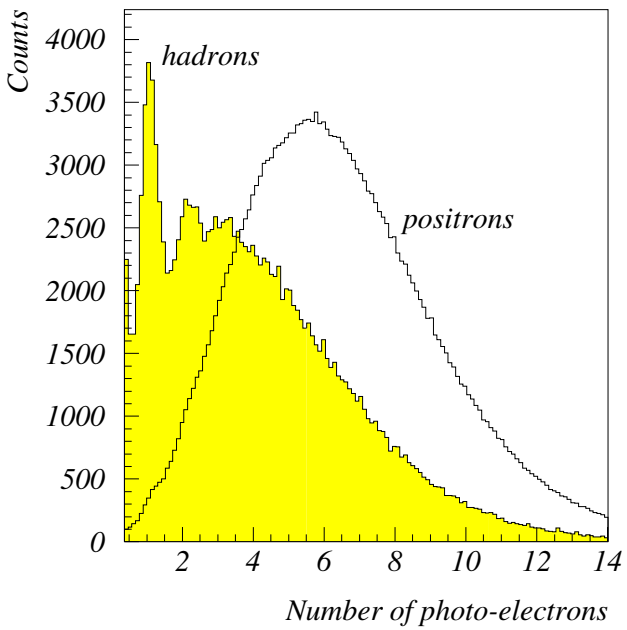

Figure 3.8.: Response of the Čerenkov counter to positrons and hadrons (1997 data). Note that events below 0.35 photo-electrons have been suppressed.

The threshold momentum can be controlled by varying the composition of the radiator gas which is kept at atmospheric pressure. The counter was operated with pure nitrogen in 1995 while in 1996/97 a mixture of 70% N_2 and 30% C_4F_{10} was used. The resulting threshold momenta for pions, kaons and protons to trigger the Čerenkov counter were 5.6, 19.8 and 37.6 GeV in 1995, while they were lowered to 3.8, 13.6 and 25.8 GeV in 1996/97. The counter was mainly used to unambiguously distinguish pions with momenta in the range of 5.6 (3.8) GeV $< p_\pi <$ 19.8 (13.6) GeV in 1995 (1996/97) from other hadrons. The Čerenkov light is reflected onto PMTs by an array of 20 mirrors per detector half and the observed Čerenkov signals are assigned to the reconstructed tracks. Fig. 3.8 shows the response of the Čerenkov counter to positrons and hadrons. For a given momentum a positron ($m_0 = 511$ keV) is much faster than a hadron. Consequently, the Čerenkov cone for positrons has on average a larger opening angle and the average number of photo-electrons $N_p \propto \sin^2\theta_c$ exceeds the number of photo-electrons measured for hadrons. In the hadron spectrum one can see the single and higher photo-electron peaks. The average number of photo-electrons is about 3 (6.5) for hadrons (positrons).

In 1998 the threshold Čerenkov counter was replaced by a ring-imaging Čerenkov counter which provides a measurement of the particle velocity by measuring the opening angle of the Čerenkov cone. Given its velocity, the particle rest mass can then be calculated from the reconstructed momentum according to $m_0 = p/(\gamma n)$.

3.3.3. Luminosity monitor

The luminosity is measured by detecting Bhabha scattering of the beam positrons from the electrons of the target atoms ($e^+e^- \rightarrow e^+e^-$) and electron positron annihilation into photons ($e^+e^- \rightarrow \gamma\gamma$). The cross section of both processes is known from QED and is 1.73 μbarn for $e^+e^- \rightarrow e^+e^-$ and 0.398 μbarn for $e^+e^- \rightarrow \gamma\gamma$ for the given beam energy of 27.5 GeV and integrated over the acceptance of the luminosity monitor. The symmetric scattering angle of the final state leptons is 6.1 mrad with respect to the beam axis and both particles in the final state carry half of the beam energy. The scattered particles exit the beam pipe through an exit window about 7.2 m downstream of the target and are detected in two radiation hard calorimeter modules each build of 12 NaBi(WO_4) crystals connected to PMTs. The modules fit into the horizontal gap of the main calorimeter and are moved close to the beam when stable HERA running conditions are established. Fig. 3.9 shows a schematic diagram of the luminosity monitor which shows the hit distribution in the two calorimeters. The coincidence rate is about 130 Hz for a beam current of 20 mA and a ^{3}He target density of 1×10^{15} nucleons/cm^2 which provides a luminosity measurement with a statistical accuracy of 1% within about 100 s.

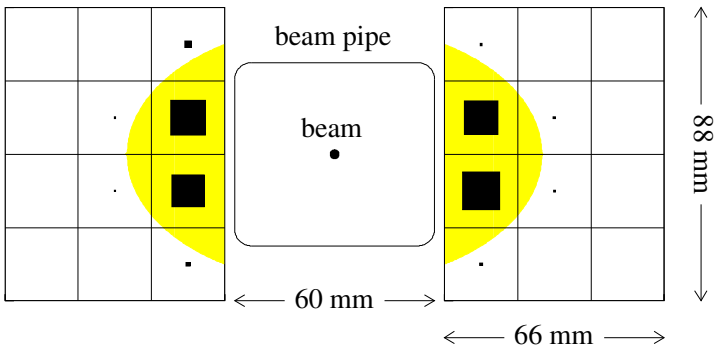

Figure 3.9.: Schematic diagram of the luminosity monitor (front view). The hit distribution is indicated by size of the boxes, which is proportional to the number of hits per channel. The shaded area indicates the limitation in the Bhabha scattering angle acceptance due to the dimensions of the exit window of the beam pipe.

3.3.4. Trigger

The trigger system induces the readout of all detector components if an event of physical interest is detected. The trigger requirement for DIS events is the detection of a scattered positron in the fast detectors and makes use of the signals derived from a small scintillator H0 (installed upstream of FC1), the hodoscope H1, the pre-shower (H2) and column-wise summed calorimeter signals. The following coincidence of all three conditions is required to trigger the data acquisition: (a) a signal in the hodoscopes H0 and H1, (b) a pre-shower signal above the minimum ionising level, and (c) an energy cluster of above 3.5 GeV in the calorimeter. The readout decision is made up within about 400 ns. Besides trigger

conditions for the detection of DIS events a number of technical triggers are necessary to study trigger efficiencies and background conditions. Typical trigger rates are on the order of 50 Hz for a luminosity of 5×10^{32} nucleons/(cm^2 sec).

4. Extraction of spin asymmetries

This section describes the extraction of the inclusive and semi-inclusive photon-nucleon spin asymmetries $A_1^{(h)}$ on the ^{3}He and proton target. After a summary of the data quality selection, the selection of deep inelastic scattering events is described and the lepton-nucleon asymmetries $A_{\parallel}^{(h)}$ are extracted. Corrections are applied to $A_{\parallel}^{(h)}$ for charge-symmetric background processes, detector effects and radiative events. The photon-nucleon asymmetries $A_1^{(h)}$ are then determined and the results are compared to results from other experiments. A discussion of the systematic uncertainty of $A_1^{(h)}$ is given.

In this analysis spin asymmetries were extracted for the 1996 and 1997 measurements with a hydrogen target. The 1995 ^{3}He asymmetries, which enter into the extraction of the polarised quark distributions, had already been analysed and were taken from [Tal 98]. Nevertheless, the extraction of the helium asymmetries is described for completeness.

4.1. Data quality selection

The spin asymmetries are extracted from the measured count rates, the values of the beam and target polarisations and the luminosity. In the data quality selection an event sample is selected where the spectrometer, the beam and target polarimeters and the luminosity monitor were fully operational. In addition, selection cuts are imposed to ensure high polarisation.

The data quality selection applied in this semi-inclusive analysis corresponds to the data selection used for the extraction of the spin structure functions g_1^{n} and g_1^{p} which were published in [Ack 97] and [Air 98], respectively. The complete list of data quality criteria can be found in [Ako 97, Tal 98] for the helium data and in [Gut 99a, Has 99] for the proton data. In the following the most important selection criteria are summarised.

The data quality was determined for each burst[1] which corresponds to a time interval of about 10 seconds. Most of the quality criteria were identical for the different years of data taking. Differences were caused by changes in machine performance, the spectrometer setup and the use of different targets.

Target performance The target polarisation direction was flipped on a short time scale. Bursts were excluded from the analysis if the target spin state was undefined due

[1] A *burst* is a technical term related to the data acquisition system.

to the spin flip. In addition to a reliable polarisation measurement the target polarisation value was required to be in the range $30\ (80)\% \leq p_{\mathrm{T}} \leq 60\ (99)\%$ in 1995 (1996/97).

Beam current and polarimeter performance The positron beam current was required to be in the range $8\ (5) \leq I_e \leq 32\ (50)$ mA in 1995 (1996/97). For each fill a fit was made to the minute by minute measurements to smooth the statistical fluctuations [Bel 96]. In addition to the requirement for a reliable polarisation measurement a cut was imposed on the fitted beam polarisation value to be in the range $40\ (30)\% \leq p_{\mathrm{B}} \leq 70\ (80)\%$ in 1995 (1996/97).

Luminosity measurement The event rate measured by the luminosity monitor was required to be in the range $40\ (5)$ Hz $\leq R_{\mathrm{LUMI}} \leq 210\ (60)$ Hz in 1995 (1996/97).

Tracking system High voltage trips of tracking chambers and PID detectors were recorded and checked. Alternatively, cuts were imposed on the plane efficiencies and track reconstruction efficiencies separately for front- and back-chambers. In 1995 bursts were included in the data sample with tracking efficiencies inside the range $80\ (94)\% \leq \varepsilon_{\mathrm{FRONT}}\ (\varepsilon_{\mathrm{BACK}}) \leq 100\ (100)\%$. In 1996/97 the high voltage monitoring was included into the data stream and used to decide on the performance of the tracking chambers.

Trigger and PID detectors Since the DIS trigger is based on the hodoscope H1, the pre-shower detector and the calorimeter, the functionality of these detectors has to be guaranteed. Furthermore, these detectors are used for PID together with the threshold Čerenkov counter and the TRD. The gains of the pre-shower detector and the calorimeter were continuously recorded with a laser gain-monitoring system. Furthermore, the PID detectors were included into the high voltage monitoring. Efficiency cuts were imposed on the TRD and the Čerenkov detector.

In addition to the cuts described above both detector halves were required to be simultaneously operational for the analysis of semi-inclusive events. The selected data set was checked against the time stability of various kinematical distributions and of the yield of inclusive and semi-inclusive DIS events. After the data quality selection approximately the same number of bursts was available for the parallel and anti-parallel beam and target spin states in each year.

4.2. Event selection

This section describes the selection of deep inelastic scattering events from bursts which passed the data quality cuts. The track selection and the kinematical cuts were identical for the helium and the hydrogen asymmetries. Due to improvements in the PID scheme the particle identification was slightly different in 1995 and 1996/97. The event selection is summarised in table 4.1.

Table 4.1.: Overview of the event selection. The table shows the cuts which were used for the track selection and particle identification. In addition, the table comprises the cuts imposed on the kinematics of identified positrons and hadrons (see text for explanation).

Track selection		
Quantity	Range	Unit
$\lvert\theta_x\rvert$	$[0, 170]$	mrad
$\lvert\theta_y\rvert$	$[40, 140]$	mrad
Horizontal position at calorimeter	$[-175, 175]$	cm
Vertical position at calorimeter	$[30, 100]$	cm
Longitudinal vertex position	$[-18, +18]$	cm
Lateral vertex position	$[0, 0.75]$	cm
Momentum	≥ 0.5	GeV
Particle identification		
Quantity	Hadrons	Leptons
PID 1995 (1996/97)	≤ -1 (0)	≥ 2 (2)
Positron kinematics		
Quantity	Range	Unit
Q^2	≥ 1	GeV^2
W^2 (semi-incl. events)	≥ 4 (10)	GeV^2
y	$[0, 0.85]$	
E Calorimeter	≥ 3.5	GeV
Hadron kinematics		
Quantity	Range	Unit
z	$[0.2, 1]$	
x_{F}	$[0.1, 1]$	

4.2.1. Track selection

A cut was imposed on the horizontal and vertical projection of the scattering angle $\theta_x = \arctan(p_x/p_z)$ and $\theta_y = \arctan(p_y/p_z)$ according to $|\theta_x| \leq 170$ mrad and 40 mrad $\leq |\theta_x| \leq 140$ mrad. Here, p_x, p_y and p_z denote the horizontal, vertical and longitudinal projections of the particle momentum p. The cuts on θ_x and θ_y ensure that each track is well separated from the detector edges, so that the track reconstruction efficiency and the efficiency of the PID detectors is high. The cut on the horizontal (-175 cm $\leq x \leq 175$ cm) and vertical calorimeter position (30 cm $\leq |y| \leq 100$ cm) ensures that there is no transverse shower leakage in the upper or lower half of the calorimeter. The cut on the longitudinal (-18 cm $\leq z_{\mathrm{V}} \leq 18$ cm) and transverse vertex position ($\sqrt{x_{\mathrm{V}}^2 + y_{\mathrm{V}}^2} \leq 0.75$ cm) selects events with vertices inside the target cell and well separated from the cell wall. Finally, the track momentum was required to be ≥ 0.5 GeV.

4.2.2. Particle identification

For the particle identification (PID) the responses of all four PID detectors are combined. Rather than imposing hard cuts on the individual detector signals, the responses are converted into a *conditional probability* $\mathcal{L}^i_{\mathrm{D}}$ which is defined as the probability that a given signal is recorded by detector D when a particle of type i passes the detector. These conditional probabilities can be derived by comparing the detector response functions for leptons and hadrons generated from either test beam data or from clean particle samples obtained from restrictive hard cuts on the other PID detectors in the HERMES experiment. The conditional probabilities from a number of n detectors can be combined into an overall conditional probability

$$\mathcal{L}^i = \prod_{\mathrm{D}=1}^{n} \mathcal{L}^i_{\mathrm{D}} \,. \tag{4.1}$$

The probability $\mathcal{P}^i$ that a particle is of type i is related to the conditional probabilities $\mathcal{L}$ by the incident particle fluxes ϕ :

$$\mathcal{P}^i = \frac{\phi^i \mathcal{L}^i}{\sum_j \phi^j \mathcal{L}^j} \,, \tag{4.2}$$

where j runs over all incident particle types.

For the separation of leptons from hadrons the quantity PID is introduced as the logarithm of the ratio of conditional probabilities $\mathcal{L}$ that the particle is a lepton (l) or a hadron (h)

$$PID \equiv \log_{10} \frac{\mathcal{L}^l}{\mathcal{L}^h} \,. \tag{4.3}$$

This quantity is related to the true probabilities $\mathcal{P}^l$ and $\mathcal{P}^h$ by

$$PID = \log_{10} \frac{\mathcal{P}^l}{\mathcal{P}^h} + \log_{10} \frac{\phi^h}{\phi^l} \,. \tag{4.4}$$

Since the ratio ϕ^h/ϕ^l is approximately independent of the kinematics E' and θ, the effect of the flux factor is to introduce a global shift of the $\log_{10}\left[\mathcal{P}^l/\mathcal{P}^h\right]$ distribution against the PID distribution by $\log_{10}[\phi^h/\phi^l]$.

The signals of the threshold Čerenkov detector, the pre-shower counter and the calorimeter are combined into a logarithmic likelihood called PID_3 which is defined as

$$PID_3 \equiv \log_{10} \frac{\mathcal{L}^l_{\mathrm{CER}} \cdot \mathcal{L}^l_{\mathrm{PRE}} \cdot \mathcal{L}^l_{\mathrm{CAL}}}{\mathcal{L}^h_{\mathrm{CER}} \cdot \mathcal{L}^h_{\mathrm{PRE}} \cdot \mathcal{L}^h_{\mathrm{CAL}}} \,. \tag{4.5}$$

For the analysis of the 1996/97 proton data the responses of the six individual TRD modules were combined into a logarithmic likelihood

$$PID_{\mathrm{TRD}} \equiv \log_{10} \frac{\prod_{m=1}^{6} \mathcal{L}^l_{\mathrm{TRD},m}}{\prod_{m=1}^{6} \mathcal{L}^h_{\mathrm{TRD},m}} \,, \tag{4.6}$$

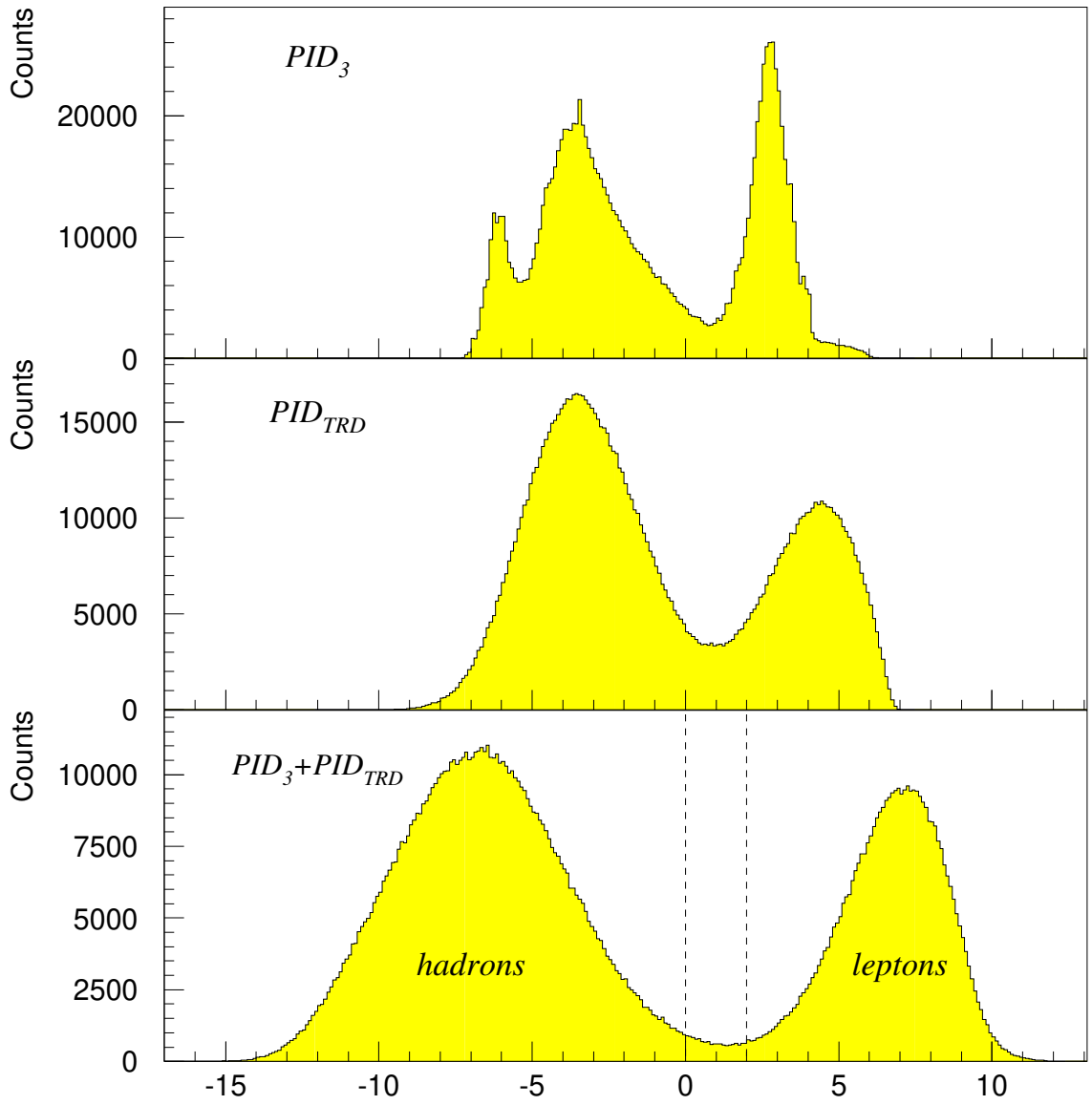

Figure 4.1.: PID likelihood distributions of particle tracks (1997 data). From the top to the bottom the figure shows the likelihood distributions PID_3, PID_{TRD} and $PID_3 + PID_{\mathrm{TRD}}$. The dashed lines shown in the bottom plot for $PID_3 + PID_{\mathrm{TRD}}$ indicate the cuts which were used to separate hadrons ($PID_3 + PID_{\mathrm{TRD}} < 0$) from leptons ($PID_3 + PID_{\mathrm{TRD}} > 2$).

and a cut has been applied to the $PID_3 + PID_{\mathrm{TRD}}$ distribution. Fig. 4.1 shows the likelihood distributions PID_3, PID_{TRD} and the sum of both quantities. The dashed lines shown in the bottom plot for $PID_3 + PID_{\mathrm{TRD}}$ indicate the cuts used to separate leptons from hadrons. Particles with $PID_3 + PID_{\mathrm{TRD}} > 2$ were identified as leptons while those for $PID_3 + PID_{\mathrm{TRD}} < 0$ were identified as hadrons. The positron cut efficiency

and hadron contamination was determined by fitting the sum of two Gaussians to the tails of the positron and hadron distributions in the region around the cuts. For a cut of $PID_3 + PID_{\mathrm{TRD}} > 2$ the positron identification efficiency was larger than 97% for a hadron contamination of less than 1.1% over the entire range in x [Has 99].

For the analysis of the 1995 helium data the TRD has been treated in a different way. The standard particle identification cut used in the analysis of the helium data is a *valley cut* in the PID_3 versus S_{TRD} plane, where S_{TRD} denotes the truncated mean signal of the TRD. Due to initial problems with the TRD in 1995 a PID down-shifting scheme had to be used depending on whether the TRD was operational or not. This lead to the following re-definition of the PID value [Ako 97]:

$$PID \;=\; \begin{cases} PID_3 + 0.31 \cdot S_{\mathrm{TRD}} - 5.48 & \text{if the TRD was operational,} \\ PID_3 & \text{if either half of the TRD was bad,} \end{cases}$$

where the truncated mean value S_{TRD} is given in units of keV. Particles with $PID > 2$ were identified as leptons while those with $PID < -1$ were identified as hadrons. The cut efficiencies and contaminations of the positron and hadron samples were determined by fitting the sum of two Gaussians to the tails of the PID distributions of leptons and hadrons in the valley around the cut. For the applied cuts the average contamination of both the positron and hadron samples was found to be less than 1.2% with an efficiency greater than 97% over the entire range of x [Kai 97, Men 98].

As discussed in section 3.3.2 the threshold Čerenkov counter allows to identify pions in a limited momentum range. Using different gas radiators this momentum window was set to $5.6\ (3.8)$ GeV $\leq p \leq\ 19.8\ (13.6)$ GeV in 1995 (1996/97). A hadron was identified as a pion if its momentum was inside the above limits and at least one Čerenkov photon was detected. Due to the width of response function of the Čerenkov counter (see Fig. 3.8) the requirement for one Čerenkov photon was realized by a cut on the Čerenkov signal of ≥ 0.25.

4.2.3. Kinematical cuts

The inclusive event kinematics was calculated from the energy E' and scattering angle θ of the final state positron (see section 2.1) which was defined as the highest energetic positively charged particle with lepton PID and energy $E' \geq 3.5$ GeV. Deep inelastic scattering events were selected by imposing a cut on the negative four momentum transfer squared $Q^2 \geq 1$ GeV^2. To avoid events where the nucleus is exited to a resonant state, the invariant mass squared of the hadronic final state was required to be $W^2 \geq 4$ GeV^2. In a region with high fractional energy transfer y from the lepton to the virtual photon, radiative corrections become large. In order to exclude this region a cut of $y \leq 0.85$ was applied. Fig. 4.2 shows the resulting distribution of inclusive DIS events in the x versus Q^2 plane.

In semi-inclusive events, where a final state hadron is detected in coincidence with the DIS positron, a cut of $z > 0.2$ and $x_{\mathrm{F}} > 0.1$ was imposed to select hadrons with a high

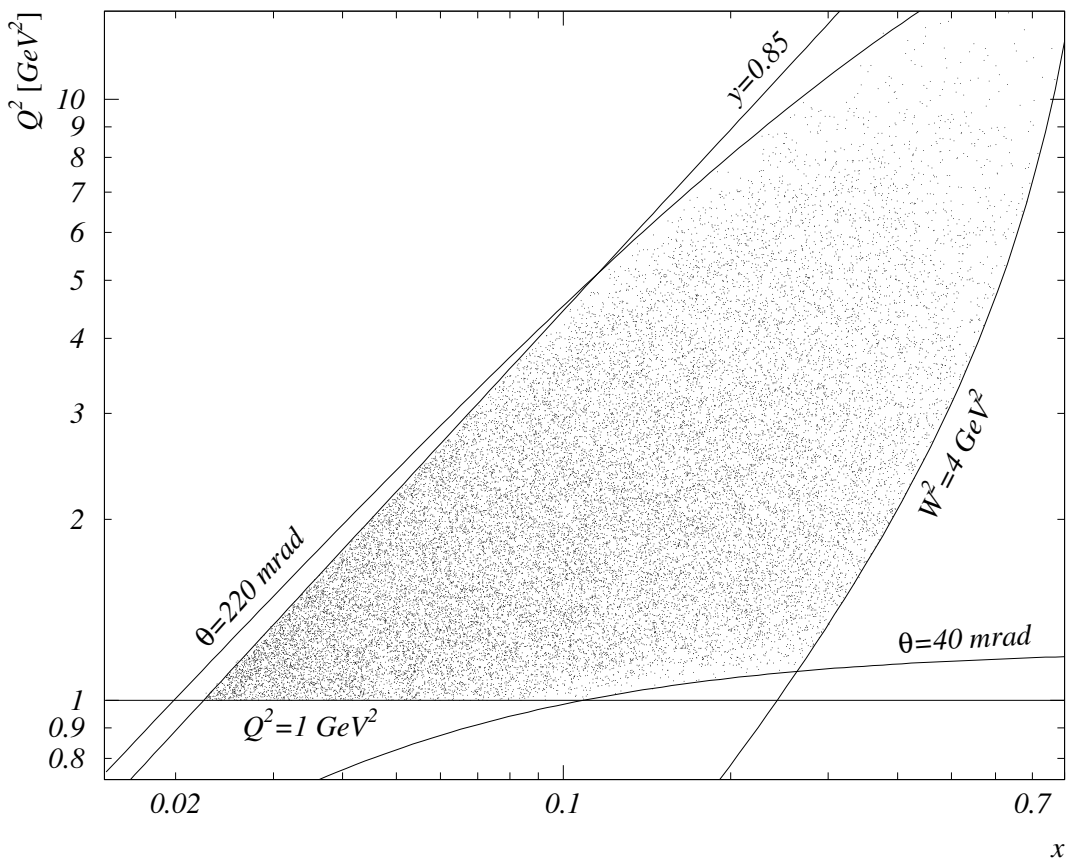

Figure 4.2.: Distribution of inclusive DIS events in the x versus Q^2 plane after cuts on the variables $Q^2 \geq 1$ GeV^2, $W^2 \geq 4$ GeV^2 and $y \leq 0.85$. The lines labeled with $\theta = 40$ mrad and $\theta = 220$ mrad indicate the limitations in the kinematical plane due to the scattering angle acceptance of the spectrometer.

probability of coming from the current fragmentation region. To calculate x_{F} the mass of the hadron has to be known. For the Lorentz transformation from the laboratory system to the photon-nucleon centre of mass system, a pion mass was assumed for all hadrons since most unidentified hadrons are pions as can be proven with Monte Carlo simulations. In order to improve the separation of the current from the target fragmentation region it was additionally required that $W^2 > 10$ GeV^2 for semi-inclusive events.

4.3. Extraction of the asymmetry $A_{\parallel}^{(h)}$

The unpolarised cross section σ_0 is related to the time integrated count rate N_0 by

$$N_0(x, Q^2) = \sigma_0 \int \mathrm{d}t \; a(t, x, Q^2) \; \mathcal{E}(t, x, Q^2) \; \mathcal{L}(t) \; , \tag{4.7}$$

where a is the detector acceptance, $\mathcal{E}$ is the event reconstruction efficiency and $\mathcal{L}$ is the luminosity. The asymmetry $A_{\parallel}(x,Q^2)$ was defined in Eq. (2.26) as the cross section asymmetry for parallel and anti-parallel orientations of beam and target spins. Since $\sigma_0 = (\sigma^{\rightleftarrows} + \sigma^{\rightrightarrows})/2$ the polarised cross section can be written as

$$\sigma^{\rightleftarrows(\rightrightarrows)} = \sigma_0 \left[1 + (-)p\, A_{\parallel}\right] \,, \tag{4.8}$$

where $p = p_{\mathrm{B}} \cdot p_{\mathrm{T}}$ is the product of beam and target polarisations. The count rates for the two spin states can then be expressed by

$$N^{\rightleftarrows}(x,Q^2) = \sigma_0 \int_{\rightleftarrows} \mathrm{d}t\; a(t,x,Q^2)\; \mathcal{E}(t,x,Q^2)\; \mathcal{L}(t) \left[1 + p(t)\; A_{\parallel}(x,Q^2)\right], \tag{4.9}$$

$$N^{\rightrightarrows}(x,Q^2) = \sigma_0 \int_{\rightrightarrows} \mathrm{d}t\; a(t,x,Q^2)\; \mathcal{E}(t,x,Q^2)\; \mathcal{L}(t) \left[1 - \; p(t)\; A_{\parallel}(x,Q^2)\right]. \tag{4.10}$$

The detector acceptance a is independent of time and of the relative orientation of target and beam spin. Likewise the reconstruction efficiency is independent of the relative spin orientation. Variations of the reconstruction efficiency $\mathcal{E}$ are small and happen on a time scale which is much larger than the spin flip period. The effect of these small variations in $\mathcal{E}$ on the extracted asymmetries has been investigated in [Lac 98] and was found to be negligible. Consequently, the count rate n_i for burst number i can be written as

$$n_i^{\rightrightarrows(\rightleftarrows)} = \sigma_0\; a\; \mathcal{E} l_i^{\rightrightarrows(\rightleftarrows)} \left[1 - (+)\; p_i^{\rightrightarrows(\rightleftarrows)}\; A_{\parallel}\right], \tag{4.11}$$

where l_i is the measured luminosity and p_i the measured polarisation. The integrated count rates are obtained by summing over all bursts. With the definitions

$$N^{\rightrightarrows(\rightleftarrows)} \equiv \sum_i n_i^{\rightrightarrows(\rightleftarrows)} \,, \tag{4.12}$$

$$L^{\rightrightarrows(\rightleftarrows)} \equiv \sum_i l_i^{\rightrightarrows(\rightleftarrows)} \,, \tag{4.13}$$

$$L_P^{\rightrightarrows(\rightleftarrows)} \equiv \sum_i \left(l_i \cdot p_i\right)^{\rightrightarrows(\rightleftarrows)} \,, \tag{4.14}$$

the time integrated asymmetry $A_{\parallel}$ is given by

$$A_{\parallel} = \frac{N^{\rightleftarrows} L^{\rightrightarrows} - N^{\rightrightarrows} L^{\rightleftarrows}}{N^{\rightleftarrows} L_P^{\rightrightarrows} + N^{\rightrightarrows} L_P^{\rightleftarrows}} \,. \tag{4.15}$$

The statistical error $\delta A_{\parallel}$ of $A_{\parallel}$ is calculated from the statistical uncertainty of the count rate δN which is taken to be $\sqrt{N}$ since the number of scattering events is Poisson distributed. It follows

$$\begin{aligned} \delta A_{\parallel} &= \sqrt{\left(\frac{\partial A_{\parallel}}{\partial N^{\rightrightarrows}}\, \delta N^{\rightrightarrows}\right)^2 + \left(\frac{\partial A_{\parallel}}{\partial N^{\rightleftarrows}}\, \delta N^{\rightleftarrows}\right)^2} \\ &= \frac{L^{\rightrightarrows} L_P^{\rightleftarrows} + L^{\rightleftarrows} L_P^{\rightrightarrows}}{\left(N^{\rightleftarrows} L_P^{\rightrightarrows} + N^{\rightrightarrows} L_P^{\rightleftarrows}\right)^2} \sqrt{(N^{\rightrightarrows})^2\; N^{\rightleftarrows} + (N^{\rightleftarrows})^2\; N^{\rightrightarrows}} \,. \end{aligned} \tag{4.16}$$

The semi-inclusive asymmetries $A_{\parallel}^{h}$ are technically extracted in the same way as the inclusive asymmetry $A_{\parallel}$. In the semi-inclusive case the count rate $N^{h}_{\overrightarrow{\Leftarrow}(\overrightarrow{\Rightarrow})}$ refers to the number of events where in addition to the DIS positron a hadron h from the current fragmentation region is detected. The asymmetries $A_{\parallel}^{(h)}$ are extracted as a function of x. The binning in x consists of 9 bins with the boundaries 0.023, 0.040, 0.055, 0.075, 0.1, 0.14, 0.2, 0.3, 0.4 and 0.6 and was chosen such that the number of events is about the same in each bin. Within each x-bin the asymmetries are integrated over Q^2 (and z in case of the semi-inclusive asymmetries).

4.4. The ^{3}He and proton asymmetries $A_{\parallel}^{(h)}$

Fig. 4.3 shows the results for the inclusive and semi-inclusive charged hadron and pion asymmetries $A_{\parallel}^{(h)}$ for the ^{3}He [Tal 98] and the proton target[2,3]. The asymmetries shown in the figure were corrected for charge-symmetric background processes, but not for acceptance effects, kinematical smearing or radiative events (see section 4.5). The HERMES data represent the first measurement of semi-inclusive pion asymmetries on ^{3}He and proton targets and of semi-inclusive hadron asymmetries on ^{3}He.

The proton asymmetries are shown separately for the 1996 and 1997 data set. One can see from Fig. 4.3 that in the range $0.075 < x < 0.3$ the asymmetries for negatively charged hadrons and pions measured in 1997 seem to be lower than the respective asymmetries measured in 1996. Detailed studies have been performed in order to investigate this observation [Bai 99]. In the end, no reason could been identified which would prove that the fluctuation is non-statistical. The total χ^2/NDF calculated from the inclusive and the charged hadron asymmetries for a total of 27 measured bins is $\chi^2/27 = 1.0$. If the same quantity is calculated for the h^- asymmetry alone, one obtains $\chi^2/9 = 1.6$. The deviation of the 1996 and 1997 asymmetries $A_{\parallel}^{h^-}$ in bin number 4 corresponds to 2.5 standard deviations.

4.5. Corrections to $A_{\parallel}^{(h)}$

In this section the corrections are discussed which were applied to the measured raw asymmetries $A_{\parallel}^{(h)}$. The asymmetries were corrected for misidentified positrons from charge-symmetric background processes, for acceptance effects and kinematical smearing in the variable x and for contributions to the asymmetry from radiative events.

[2]The 1997 and 1996 proton asymmetries are based on the HERMES data productions 97b2 and 96c1, respectively, and the ^{3}He asymmetries are based on the data production 95e5.

[3]The helium asymmetries shown in the plot were calculated from the values of $A_{\parallel}/D$ from Ref. [Tal 98] by multiplying with the depolarisation factor $D(x, Q^2)$ which was evaluated at the mean value of x and Q^2 in each x-bin.

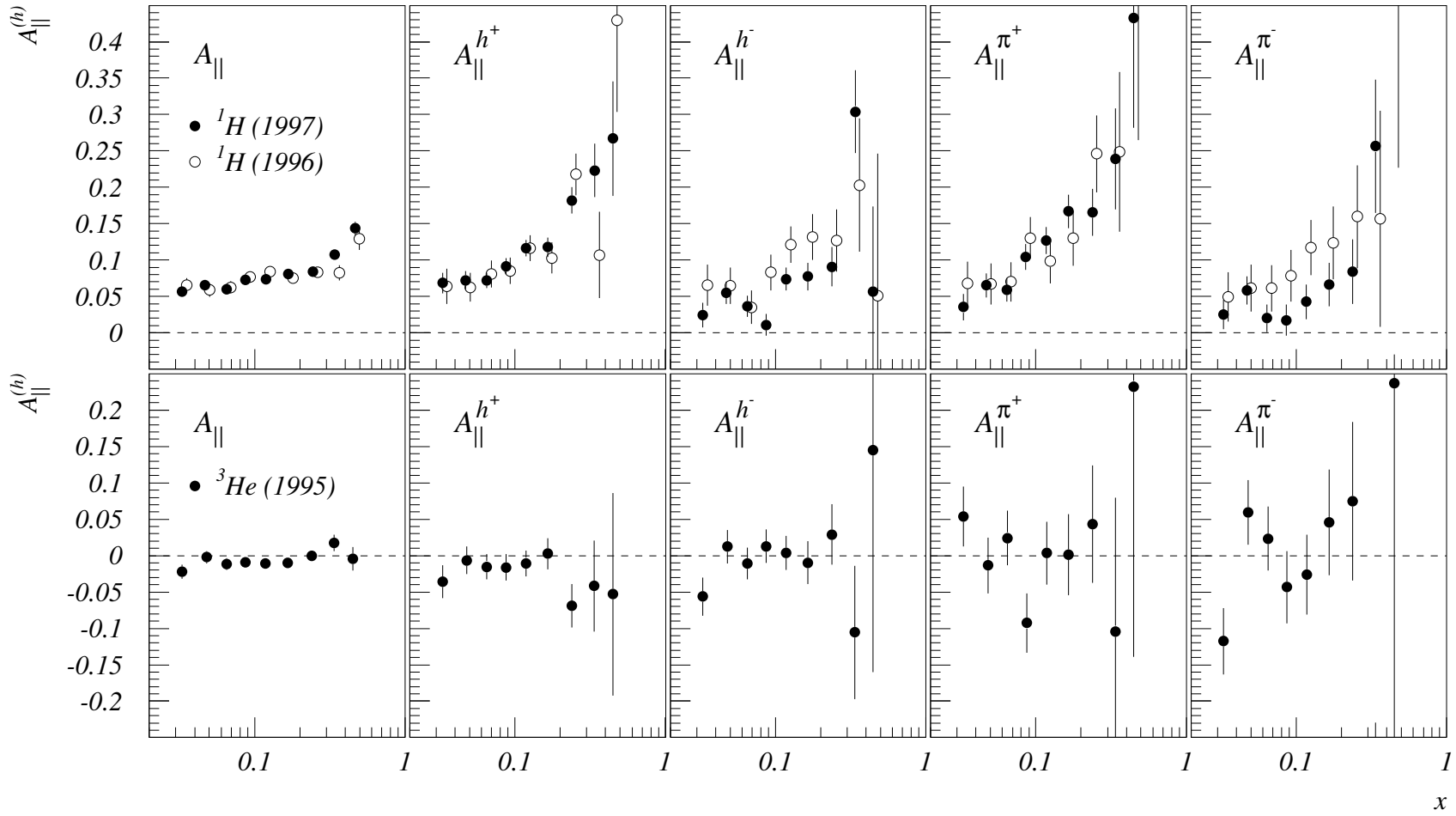

Figure 4.3.: The top panel shows the inclusive $(A_{\parallel})$ and semi-inclusive charged hadron $(A_{\parallel}^{h^+}, A_{\parallel}^{h^-})$ and charged pion $(A_{\parallel}^{\pi^+}, A_{\parallel}^{\pi^-})$ asymmetries on the proton, separately for the 1996 and 1997 data set. The bottom panel shows the same set of asymmetries on ^{3}He. The error bars represent the statistical uncertainties. The asymmetries shown in the figure were corrected for charge-symmetric background processes but not for acceptance effects, kinematical smearing or radiative events.

4.5.1. Background corrections

The asymmetries $A_{\parallel}$ were corrected for misidentified positrons from charge-symmetric processes such as e^+e^- pair production. Photo-production is a potentially large source of background to the DIS process. While for this process the scattered positron will usually be scattered through small angles and will escape into the acceptance gap of the spectrometer, the production of a π^0 and its subsequent decay through $\pi^0 \rightarrow \gamma\gamma$, $\gamma \rightarrow e^+e^-$ may lead to a misidentified DIS positron event. Similarly, a high energy bremsstrahlungs photon may convert into an e^+e^- pair and the positron may be misidentified as a DIS positron.

Assuming equal probabilities of identifying positrons and electrons from these charge-symmetric background processes, the misidentified positrons can be removed from the data sample by subtracting events where the leading lepton is an electron instead of a positron. The correction was done such that if an electron passed all the cuts for a DIS positron (other than the requirement of positive charge), then one DIS positron event, with identical kinematics as the electron event, was subtracted from the event sample. For a positively (negatively) charged hadron in coincidence with the electron, a negatively (positively) charged hadron was subtracted. The ratio of the number of electrons to positrons passing the DIS cuts depends on x and decreases rapidly from about 6% for the lowest x-bin to zero for the highest x-bin. For $x \geq 0.1$ the ratio is already below 0.5%.

The size of the correction to the asymmetry $A_{\parallel}$ is about 5% for the lowest x-bin and decreases towards higher values of x. In the region of $x \geq 0.1$ the correction is below 0.5%.

The correction arising from the contamination of the positron sample with hadrons is small compared to the correction from the background of charge-symmetric processes [Has 99] and was therefore neglected.

4.5.2. Corrections for acceptance and kinematical smearing

Apparatus effects can lead to a systematical difference between the reconstructed and the true asymmetry. This systematical difference is mainly caused by the limited spectrometer acceptance and differences between the true and the reconstructed event kinematics, which is called kinematical smearing. The main source of kinematical smearing is multiple scattering of final state particles inside the spectrometer. Additional sources of kinematical smearing are miscalibrations and alignment offsets of the tracking devices as well as the track reconstruction algorithm itself.

The extracted inclusive and semi-inclusive proton asymmetries $A_{\parallel}^{(h)}$ have been corrected for acceptance effects and for kinematical smearing in the variable x. It was shown in [Fer 97] that acceptance and smearing effects in x are negligible for the helium asymmetries, since $A_{\parallel}^{\mathrm{He}}$ is small and nearly constant as a function of x. Therefore, no corrections were applied to the helium asymmetries.

Corrections for acceptance and kinematical smearing were derived from Monte Carlo

simulations where both the generated and the reconstructed event kinematics are known. Polarised deep inelastic scattering events were generated with the PEPSI Monte Carlo generator [Vel 92]. The inclusive proton asymmetry A_1^{p} used as input to the Monte Carlo generator was taken from a fit to the measurement by [Abe 98]. The scattered positron was reconstructed with the HERMES Monte Carlo (HMC) which includes a complete detector simulation based on the GEANT package [GEA 94]. The angular acceptance and kinematical cuts used in the reconstruction were identical to those used in the analysis from experimental data. For each x-bin, an acceptance correction factor

$$\eta_{\mathrm{ACC}} = \frac{A_{\parallel}^{4\pi}}{A_{\parallel}^{\mathrm{ACC}}} \tag{4.17}$$

was calculated from the comparison of the asymmetry $A_{\parallel}^{4\pi}$ obtained from all generated events with the asymmetry $A_{\parallel}^{\mathrm{ACC}}$ extracted from all accepted events. Here, both asymmetries $A_{\parallel}^{4\pi}$ and $A_{\parallel}^{\mathrm{ACC}}$ were determined from the generated positron kinematics. The smearing correction factor

$$\eta_{\mathrm{SM}} = \frac{A_{\parallel}^{\mathrm{ACC}}}{A_{\parallel}^{\mathrm{ACC,R}}} \tag{4.18}$$

was derived from comparing the asymmetry $A_{\parallel}^{\mathrm{ACC}}$ with the asymmetry $A_{\parallel}^{\mathrm{ACC,R}}$ extracted for all accepted events from the reconstructed kinematics. The product of both correction factors $\eta_{\mathrm{MC}} = \eta_{\mathrm{SM}}\ \eta_{\mathrm{ACC}}$ relates the true asymmetry $A_{\parallel}^{4\pi}$ to the reconstructed asymmetry $A_{\parallel}^{\mathrm{ACC,R}}$ by

$$A_{\parallel}^{4\pi} = \eta_{\mathrm{MC}}\ A_{\parallel}^{\mathrm{ACC,R}}\ . \tag{4.19}$$

To derive the acceptance and smearing corrections in the variable x to the semi-inclusive asymmetries, the multiplicities $n^{h^+}(x)$ and $n^{h^-}(x)$ of positively and negatively charged hadrons in coincidence with the DIS positron have been determined from PEPSI using the tuned LUND string fragmentation model. Based on these multiplicities the subsample of semi-inclusive DIS events was selected from the sample of inclusive DIS events and the acceptance and smearing corrections were calculated for the respective semi-inclusive asymmetry.

The smearing corrections to the measured asymmetries were calculated separately for the 1997 and 1996 data set, since different tracking methods had been used in the two years. In 1997 the vertex chambers and drift vertex chambers were included into the track reconstruction (STD reconstruction) while they were not considered in 1996 (NOVC reconstruction).

Table 4.2 shows the smearing correction factors $\eta_{\mathrm{MC}}^{(h)}(x)$ for the inclusive asymmetry and the semi-inclusive charged hadron asymmetries on the proton [Gut 99b], which were obtained for the STD reconstruction method. The correction factors $\eta_{\mathrm{MC}}^{(h)}$ vary between 0.91 and 1.03. Most of the correction is due to kinematical smearing. The acceptance

Table 4.2.: Corrections to inclusive and semi-inclusive asymmetries for detector acceptance and kinematical smearing for the STD reconstruction method [Gut 99b]. The combined acceptance and smearing correction factor $\eta_{\rm MC}^{(h)}$ is shown for each x-bin. All errors are statistical.

x	$\eta_{\rm MC} \pm$ stat.	$\eta_{\rm MC}^{h^+} \pm$ stat.	$\eta_{\rm MC}^{h^-} \pm$ stat.
0.033	0.946 ± 0.009	0.913 ± 0.011	0.981 ± 0.027
0.047	0.975 ± 0.009	0.931 ± 0.011	0.967 ± 0.025
0.065	0.967 ± 0.009	0.930 ± 0.010	0.944 ± 0.022
0.087	0.955 ± 0.009	0.925 ± 0.009	0.930 ± 0.018
0.119	0.937 ± 0.009	0.929 ± 0.007	0.931 ± 0.011
0.168	0.931 ± 0.008	0.960 ± 0.005	0.961 ± 0.007
0.245	0.934 ± 0.007	0.996 ± 0.004	1.000 ± 0.005
0.342	0.966 ± 0.008	1.019 ± 0.004	1.019 ± 0.005
0.465	0.989 ± 0.005	1.026 ± 0.004	1.023 ± 0.005

correction is small and in the range $0.98 \leq \eta_{\rm ACC}^{(h)}(x) \leq 1.02$. The differences between the correction factors obtained for the NOVC and STD reconstruction methods are typically less than 0.5% and thus smaller or of the same size than the statistical error of the correction factor.

4.5.3. QED radiative corrections

In chapter 2 polarised deep inelastic scattering was discussed in the one-photon exchange approximation (Born approximation). The measured deep inelastic scattering cross section includes contributions from higher order electro-magnetic and electro-weak processes in addition to the one-photon exchange. In order to derive the Born asymmetry these contributions have to be subtracted from the measured asymmetry. Fig. 4.4 shows

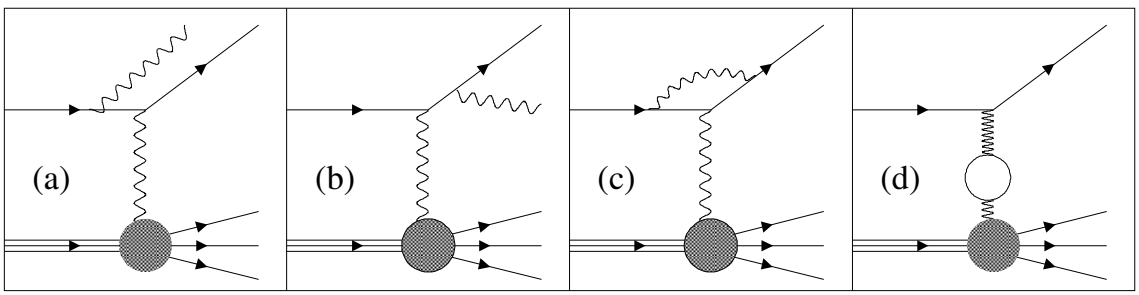

Figure 4.4.: Higher order Feynman diagrams for deep inelastic lepton-nucleon scattering: (a) bremsstrahlung from the initial lepton line, (b) bremsstrahlung from the final lepton line, (c) vertex correction and (d) vacuum polarisation.

Table 4.3.: QED radiative corrections $\Delta A_{\parallel}^{\mathrm{RC}}$ to the inclusive ^{3}He [Ryc 96] and proton [Aku 98b] asymmetries $A_{\parallel}$ with associated systematic uncertainties.

	Helium-3	**Proton**
x	$\Delta A_{\parallel}^{\mathrm{RC}} \pm$ syst.	$\Delta A_{\parallel}^{\mathrm{RC}} \pm$ syst.
0.033	0.0043 ± 0.0021	-0.00088 ± 0.00004
0.047	0.0031 ± 0.0008	-0.00071 ± 0.00002
0.065	0.0024 ± 0.0003	-0.00059 ± 0.00002
0.087	0.0019 ± 0.0001	-0.00042 ± 0.00002
0.119	0.0015 ± 0.0002	-0.00018 ± 0.00001
0.168	0.0012 ± 0.0003	0.00011 ± 0.00001
0.245	0.0010 ± 0.0003	0.00031 ± 0.00002
0.342	0.0009 ± 0.0004	0.00044 ± 0.00001
0.465	0.0009 ± 0.0004	0.00049 ± 0.00003

the Feynman diagrams of the most important higher order QED contributions to the one-photon exchange at HERMES energies. These are processes with the emission of a bremsstrahlungs photon from the initial or final lepton line, lepton vertex correction and vacuum-polarisation.

The formalism to calculate the radiative corrections to the spin-dependent cross section was developed in [Kuc 83, Aku 94] and implemented into the program POLRAD 2.0 [Aku 97]. In the calculation the Born asymmetry is obtained from the measured one according to

$$A_{\parallel}^{\mathrm{BORN}} = A_{\parallel}^{\mathrm{MEAS}} - \Delta A_{\parallel}^{\mathrm{RC}} \ , \tag{4.20}$$

where $\Delta A_{\parallel}^{\mathrm{RC}}$ represents the contribution to the measured asymmetry from radiative events. The correction term $\Delta A_{\parallel}^{\mathrm{RC}}$ is obtained from comparing the one-photon exchange cross section with the fully radiated cross section. Since the polarised part of the inelastic scattering cross section depends on g_1 an iterative correction procedure is required. In the first step of the iterative procedure, a fit to the experimental asymmetry $A_{\parallel}^{\mathrm{MEAS}}$ is used to build the polarised structure function $g_1^{(0)}$. Based on $g_1^{(0)}$ the contributions to the spin-dependent cross section are constructed and used to evaluate the radiative correction $\Delta A_{\parallel}^{\mathrm{RC}}(g_1^{(0)})$. From this result a new model for g_1 is calculated according to

$$g_1^{(1)} = \frac{F_2}{2x\,(1+R)} \frac{1}{D} \left[A_{\parallel}^{\mathrm{MEAS}} - \Delta A_{\parallel}^{\mathrm{RC}}(g_1^{(0)}) \right] \ , \tag{4.21}$$

and $g_1^{(1)}$ serves to calculate the more accurate correction term $\Delta A_{\parallel}^{\mathrm{RC}}(g_1^{(1)})$. This process is repeated until convergence is reached, which already occurs within about four iterations.

The results for the radiative corrections $\Delta A_{\parallel}^{\mathrm{RC}}$ to the inclusive proton and ^{3}He asymmetries are presented in table 4.3. The correction term $\Delta A_{\parallel}^{\mathrm{RC}}$ is relatively small and

varies between 0.0043 (-0.0009) at $x = 0.033$ and 0.0009 (0.0005) at $x = 0.46$ for the helium (proton) asymmetry. The dominating sources of systematic uncertainties of the radiative correction procedure are the uncertainties in the parametrisations of the structure functions and of the elastic and quasi-elastic form-factors. Electro-weak processes were neglected in the radiative correction procedure, but their contribution to $A_{\parallel}^{\mathrm{MEAS}}$ was estimated using POLRAD 2.0 and was included in the total systematic uncertainty of $\Delta A_{\parallel}^{\mathrm{RC}}$. A detailed discussion of the systematical uncertainties of the radiative correction procedure is given in [Aku 98a]. In this analysis, radiative corrections were applied to the inclusive asymmetries but not to the semi-inclusive asymmetries. The corrections to the semi-inclusive asymmetries are significantly smaller than for the inclusive asymmetries and are thus negligible [Aku 94].

4.6. The ^{3}He and proton asymmetries $A_1^{(h)}$

Based on Eqs. (2.31), (2.37) and (2.38) the virtual photon-nucleon asymmetry $A_1^{(h)}$ can be expressed in terms of the measured asymmetry $A_{\parallel}^{(h)}$ and a contribution from the structure function $g_2^{(h)}$:

$$A_1^{(h)} = \frac{1}{1+\eta\gamma}\left[\frac{A_{\parallel}^{(h)}}{D} - \eta\gamma(1+\gamma^2)\,\frac{g_2^{(h)}}{F_1^{(h)}}\right] . \tag{4.22}$$

Assuming $g_2^{(h)} = 0$, it follows

$$A_1^{(h)} = A_{\parallel}^{(h)} / \left[D(1+\eta\gamma)\right] , \tag{4.23}$$

which was used to calculate $A_1^{(h)}$ from $A_{\parallel}^{(h)}$ after applying the corrections discussed in the previous section. The uncertainty in the measured values of $g_2(x)$ was included in the systematic uncertainty of $A_1^{(h)}$. The depolarisation factor $D(x,Q^2)$ and the kinematical factors $\eta(x,Q^2)$ and $\gamma(x,Q^2)$ were calculated from their average values for the two spin states. While the kinematical factor $\eta\gamma$ is relatively small $(0.001 \leq \eta\gamma \leq 0.13)$, the depolarisation factor D is rather large and is a steep function of x. The depolarisation factor is shown in Fig. 4.5 for inclusive and semi-inclusive DIS events at the average value of x and Q^2 in each x-bin. The figure compares the depolarisation factors $D^{\vec{\Leftarrow}}$ and $D^{\vec{\Rightarrow}}$ for each spin state with the average depolarisation factor $D = (D^{\vec{\Leftarrow}} + D^{\vec{\Rightarrow}})/2$. The deviation of $D^{\vec{\Leftarrow}}$ or $D^{\vec{\Rightarrow}}$ from D is below 2% over the entire x-range and smaller than the systematic error of D related to the uncertainty of R. Note that due to the different kinematics of inclusive and semi-inclusive events the values of D, η and γ are different for the inclusive and semi-inclusive asymmetries even though they are not explicitly labeled with the superscript (h).

Fig. 4.6 shows the inclusive asymmetries A_1 and the semi-inclusive asymmetries A_1^h for positively and negatively charged hadrons on both targets. The inclusive asymmetries

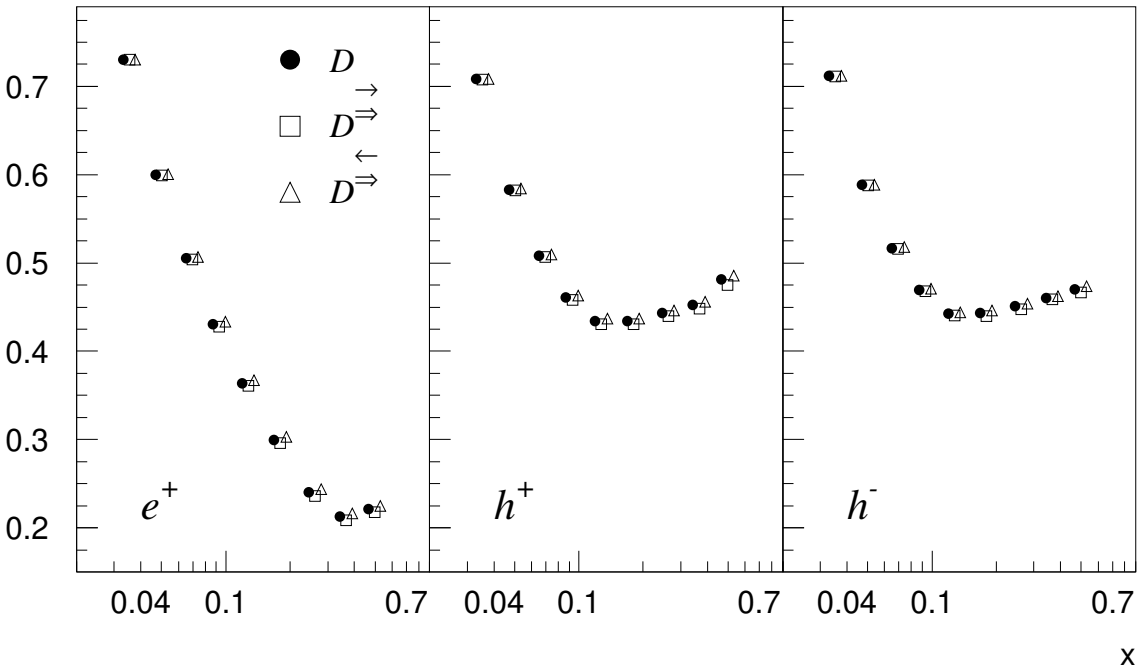

Figure 4.5.: The virtual photon depolarisation factor D for inclusive (e^+) and semi-inclusive DIS events with positively (h^+) and negatively (h^-) charged hadrons given at the mean value of x and Q^2 of each x-bin. The figure shows the depolarisation factors $D^{\rightleftarrows}$ and $D^{\rightrightarrows}$ for each spin state and the average depolarisation factor $D = (D^{\rightleftarrows} + D^{\rightrightarrows})/2$. The depolarisation factors $D^{\rightleftarrows}$ and $D^{\rightrightarrows}$ are shifted slightly in x to make them clearly visible.

are based on 2.2×10^6 (2.3×10^6) deep inelastic scattering events with 284×10^3 (306×10^3) positively and 178×10^3 (175×10^3) negatively charged hadrons in coincidence with the scattered lepton for the ^{3}He (^{1}H) target. The proton asymmetries are given separately for the 1997 and 1996 data set in tables B.2 and B.4, and the helium asymmetries are presented in table B.6. Fig. 4.6 includes the inclusive results measured at similar energy at SLAC [Kol 99, Abe 98, Abe 97b, Abe 95a] and the hadron asymmetries on the proton measured by SMC [Ade 98a]. The experimental error of the world data on the charged hadron asymmetries on the proton has been significantly reduced by the addition of the HERMES data. The SMC asymmetries were extracted under the assumption $A_2^{(h)} = 0$ instead of $g_2^{(h)} = 0$ used in this analysis. The asymmetries of both experiments are in good agreement. The HERMES data represent the first measurement of semi-inclusive hadron asymmetries on ^{3}He.

As can be seen from Fig. 4.6 the proton asymmetries are positive and increase steeply as a function of x, while the helium asymmetries are slightly negative and close to zero over the measured range of x. As the wave function for ^{3}He is dominated by the configuration with the two protons paired to zero spin, most of the asymmetry from ^{3}He is due to the neutron [Fri 90]. In LO QCD (and assuming $g_2 = 0$) the inclusive asym-

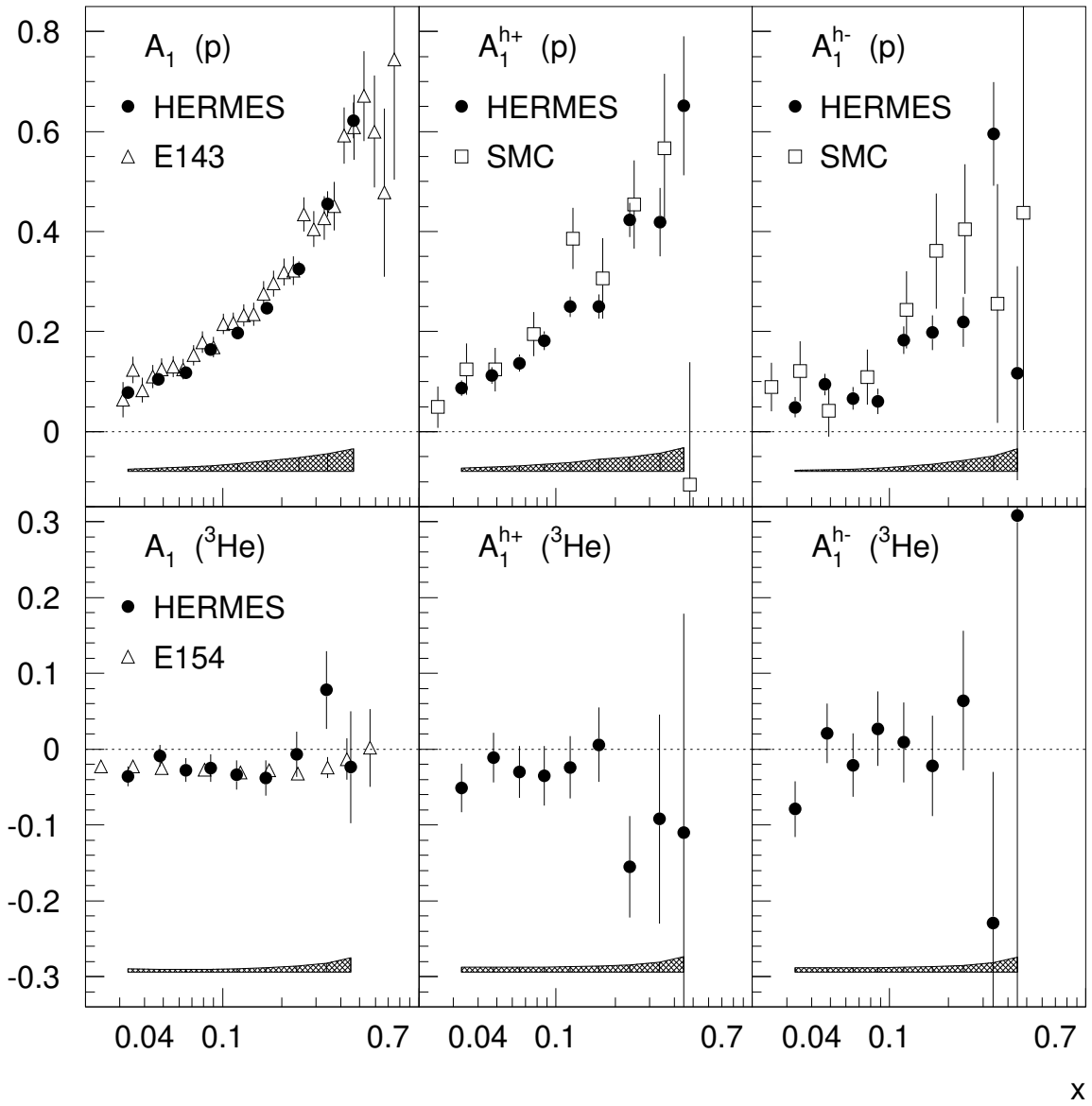

Figure 4.6.: The inclusive and semi-inclusive asymmetries for positively and negatively charged hadrons on the proton (top) and ^{3}He (bottom) target. The inclusive asymmetries are compared to the SLAC results for g_1/F_1 (open triangles). The hadron asymmetries on the proton are compared to SMC results (open squares). The error bars represent the statistical uncertainties and the bands the systematic uncertainties of the HERMES data. The error bars shown for the SLAC and SMC data indicate the total uncertainty.

metry A_1 is related to the polarised and unpolarised quark distributions by $A_1(x,Q^2) = \sum_f e_f^2\ \Delta q_f(x,Q^2) / \sum_f e_f^2\ q_f(x,Q^2)$. Since the proton asymmetry is dominated by the contribution from $(\Delta u + \Delta\bar{u})/(u+\bar{u})$ a positive value of A_1^{p} together with the small and

slightly negative value of A_1^{He} is a first indication for a positive u quark polarisation and a negative d quark polarisation.

4.6.1. Systematic error of the ^{3}He and proton asymmetries $A_1^{(h)}$

The systematic error contributions to A_1 can be subdivided into two classes. First, there are systematic errors which are related to the HERMES experiment. These comprise the systematic uncertainties of the beam and target polarisation measurements, those of radiative and smearing corrections, and the systematic error assigned to A_1^{He} due to the small non-statistical fluctuations of the yield of deep inelastic scattering events in the 1995 helium data. Second, there are systematic error contributions to A_1 which are related to external quantities. These are the uncertainties in the measurements of R and g_2.

In the following the contributions from the different systematic error sources are quantified. Unless explicitly stated otherwise, all formulae given for the inclusive asymmetries hold in the same way also for the semi-inclusive asymmetries.

Beam polarisation The beam polarimeters were calibrated using the rise time calibration method (see section 3.1.1). The fractional systematic error of the beam polarisation measurement as determined from the rise time calibration was $(\delta p_{\mathrm{B}}/p_{\mathrm{B}})_{\mathrm{RISE}} = 3.3\%$ [Tip 97] for the years 1995 to 1997. In addition there were systematic error contributions from a number of corrections which had to be applied to the measured raw polarisation. These contributions added up to a fractional error of 2.2% in 1995 [Bar 96, Ruh 96] and 0.9% in 1996 and 1997 [Tip 97], which was added quadratically to the rise time calibration error resulting in a total fractional error $\delta p_{\mathrm{B}}/p_{\mathrm{B}}$ of 4.0 (3.4)% in 1995 (1996/97). The systematic error of A_1 due to δp_{B} is given by

$$[\delta A_1]_{p_{\mathrm{B}}} = \sqrt{\left(\frac{\partial A_1}{\partial p_{\mathrm{B}}}\right)^2 (\delta p_{\mathrm{B}})^2} = A_1 \cdot \frac{\delta p_{\mathrm{B}}}{p_{\mathrm{B}}} \,. \tag{4.24}$$

Target polarisation The fractional systematic error $\delta p_{\mathrm{T}}/p_{\mathrm{T}}$ of the target polarisation measurement was 5% [Ack 97] for the helium target and 4.5% for the 1997 hydrogen target [Air 98]. In 1996 the fraction $1 - \alpha_{\mathrm{r}}$ of atoms that recombined in molecules was measured to be $(12 \pm 3)\%$ [Tal 98]. Since the polarisation of protons bound in hydrogen molecules is not well known, this lead to a relatively large systematic uncertainty in the polarisation of the target protons. To reduce this systematic uncertainty, the asymmetries measured in 1996 were normalised to the high statistics proton asymmetries measured in 1997, where the molecular fraction was small and did not dominate the systematic error of the measured target polarisation. For the 1996 asymmetries a scale error of 4.3% was introduced from the statistical uncertainty of the normalisation factor obtained from the fit to the 1997 asymmetries. The scale error was added quadratically to the 1997 target polarisation error

of 4.5% which yields a total fractional error of 6.3% for the 1996 measurement. For each year the systematic error of the asymmetries was then calculated according to

$$[\delta A_1]_{p_T} = A_1 \cdot \frac{\delta p_T}{p_T} \,. \tag{4.25}$$

Cross section ratio R The systematic error contribution of R arises from the depolarisation factor D which is a function of R. From $A_1 = A_{||}/[D(1+\eta\gamma)]$ it follows with Eq. (2.33)

$$[\delta A_1]_R = \frac{\varepsilon}{1+\varepsilon R} A_1 \, \delta R \,. \tag{4.26}$$

The value of R and its uncertainty δR were taken from the parametrisation of [Whi 90].

Yield fluctuations In 1995 the yield of deep inelastic scattering events exhibited small non-statistical fluctuations. The size of these fluctuations and their contribution to the systematic uncertainty of $A_1^{(h)}$ is discussed in [Ako 97, Tal 98]. For the inclusive and semi-inclusive charged hadron asymmetries on ^{3}He the systematic error $[\delta A_1]_{\mathrm{YIELD}}$ due to the observed yield fluctuations is given by

$$\left[\delta A_1 \right]_{\mathrm{YIELD}} = 0.00256 \,, \tag{4.27}$$

$$\left[\delta A_1^{h^+}\right]_{\mathrm{YIELD}} = 0.00575 \,, \tag{4.28}$$

$$\left[\delta A_1^{h^-}\right]_{\mathrm{YIELD}} = 0.00547 \,. \tag{4.29}$$

Non-statistical yield fluctuations have not been observed for measurements with the hydrogen target.

Radiative corrections The radiative corrections to the measured asymmetries were discussed in section 4.5.3 and the correction factors are given in table 4.3 together with the associated systematic uncertainties. Radiative corrections have been applied to the inclusive asymmetries but not to the semi-inclusive asymmetries where the corrections are negligible. For the inclusive proton asymmetry the systematic error of the correction term $\Delta A_{||}^{\mathrm{RC}}$ was taken from [Aku 98b]. For the helium asymmetries the systematic error from [Ryc 96] was used.

Acceptance and smearing corrections The statistical uncertainty $\delta\eta_{\mathrm{MC}}$ of the combined acceptance and smearing correction factor η_{MC} was taken as its systematic error. Consequently,

$$[\delta A_1]_{\eta_{\mathrm{MC}}} = A_1 \delta\eta_{\mathrm{MC}} \,. \tag{4.30}$$

Spin structure function g_2 The systematic error of A_1 due to non-zero values of g_2 was estimated from the uncertainty of the measurement of g_2. Fig. 4.7 shows the SLAC results for $xg_2^{\mathrm{p}}(x)$ [Abe 98, Ant 99] and $xg_2^{\mathrm{n}}(x)$ [Abe 97a] which were obtained in a similar x and Q^2-range than the HERMES data. Within their experimental uncertainties the SLAC results are compatible with the QPM prediction of $g_2(x) = 0$ the region $x \lesssim 0.5$. It has been shown in [Ade 98a] that the data for g_2^{p} seem to favour the twist-2 Wandzura-Wilczek calculation $g_2^{\mathrm{WW}}(x) = -g_1(x) + \int_x^1 \mathrm{d}y\ g_1(y)/y$ at high values of x [Ade 98a] whereas for g_2^{n} the experimental error is too large to draw any conclusion about the validity of the Wandzura-Wilczek parametrisation. Each of the figures for xg_2^{p} and xg_2^{n} shows two lines drawn symmetrically around $xg_2(x) = 0$ which were used to parametrise the experimental uncertainty $x\delta g_2$ of xg_2 in order to estimate the systematic uncertainty of A_1. For $x \to 1$ these parametrisations follow the behaviour of the Wandzura-Wilczek term $g_2^{\mathrm{WW}}(x)$ which approaches zero in this limit. Following Eq. (4.22) the systematic error of A_1 due to δg_2 is given by

$$\left[\delta A_1\right]_{g_2} = \frac{\eta\gamma(1+\gamma^2)}{1+\eta\gamma} \cdot \frac{\delta g_2}{F_1} \tag{4.31}$$

for the proton and the neutron asymmetries. To transform $\left[\delta A_1^{\mathrm{n}}\right]_{g_2}$ and $\left[\delta A_1^{\mathrm{p}}\right]_{g_2}$into the uncertainty $\left[\delta A_1^{\mathrm{He}}\right]_{g_2}$ of the helium asymmetry, the latter is split into proton and neutron contributions according to Eq. (5.16). The systematic error of the helium asymmetry due to δg_2 is then given by

$$\left[\delta A_1^{\mathrm{He}}\right]_{g_2} = \sqrt{f_{\mathrm{n}}^2\ p_{\mathrm{n}}^2\ \left[\delta A_1^{\mathrm{n}}\right]_{g_2}^2 + f_{\mathrm{p}}^2\ p_{\mathrm{p}}^2\ \left[\delta A_1^{\mathrm{p}}\right]_{g_2}^2}\,, \tag{4.32}$$

where f_{n} (f_{p}) is the neutron (proton) dilution factor and p_{n} (p_{p}) is the effective neutron (proton) polarisation in the ^{3}He nucleus. No measurements exist for g_2^h. For the error calculation it was assumed that $\delta g_2^h(x) = \delta g_2(x)$. Under the additional assumption that $f_{\mathrm{n}}^h = f_{\mathrm{n}}$ and $f_{\mathrm{p}}^h = f_{\mathrm{p}}$ [Fun 98] the systematic errors of the semi-inclusive hadron asymmetries are identical to those of the inclusive asymmetries.

The inclusive and semi-inclusive asymmetries generated with PEPSI using the parametrisation of [Glu 96] for the polarised quark distributions and the tuned LUND fragmentation model agree well with the measured asymmetries. Therefore, in the systematic error calculation (e.g.: $\left[\delta A_1\right]_{p_{\mathrm{B}}} = (\delta p_{\mathrm{B}}/p_{\mathrm{B}})\ A_1$) the high statistics PEPSI generated asymmetries were used as input for A_1 instead of the measured asymmetries. This was done so in order to avoid fluctuations of the systematic error due to the statistical fluctuations of the measured asymmetries. The Monte Carlo generated asymmetries have been used as input to the systematic error calculation for the following sources of systematic errors: beam and target polarisations, cross section ratio R and the combined acceptance and smearing correction.

Fig. 4.8 gives an overview of the relative size of the various systematic error contributions to A_1. The plot shows the fractional error contributions $\delta_i^2 \equiv (\delta A_1^i/\delta A_1^{\mathrm{TOT}})^2$ for

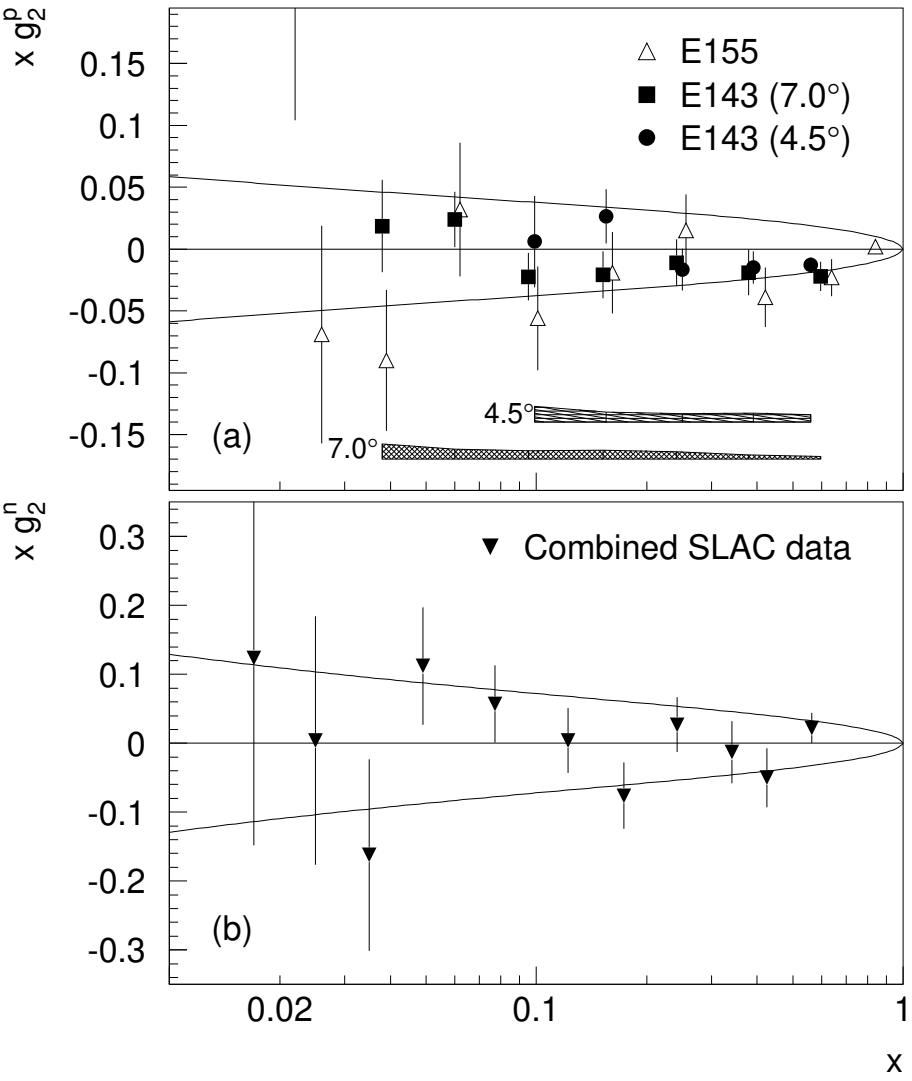

Figure 4.7.: Spin structure function measurements for (a) xg_2^{p} [Abe 98, Ant 99] and (b) xg_2^{n} [Abe 97a] shown as a function of x. The points are displayed at the average measured Q^2 of each x-bin. Overlapping data have been shifted slightly in x to make errors clearly visible. The proton data refer to the results of the experiments E143 (results are shown separately for the 4.5° and 7.0° spectrometer) and E155. The average Q^2 of the proton data set is 3 (5) GeV^2 for E143 (E155). The errors bars give the statistical and the bands the systematic uncertainties of the E143 measurement. The systematic error of E155 is negligible and not shown. The neutron data refer to the combined SLAC results of the experiments E142, E143 and E154. The average Q^2 for the combined neutron data is 3 GeV^2 and the errors bars shown are statistical. The systematic errors of the neutron data are negligible and not shown. The lines drawn symmetrically around $xg_2(x) = 0$ were used to parametrise the uncertainty $x\delta g_2(x)$ of the measurement of $xg_2(x)$.

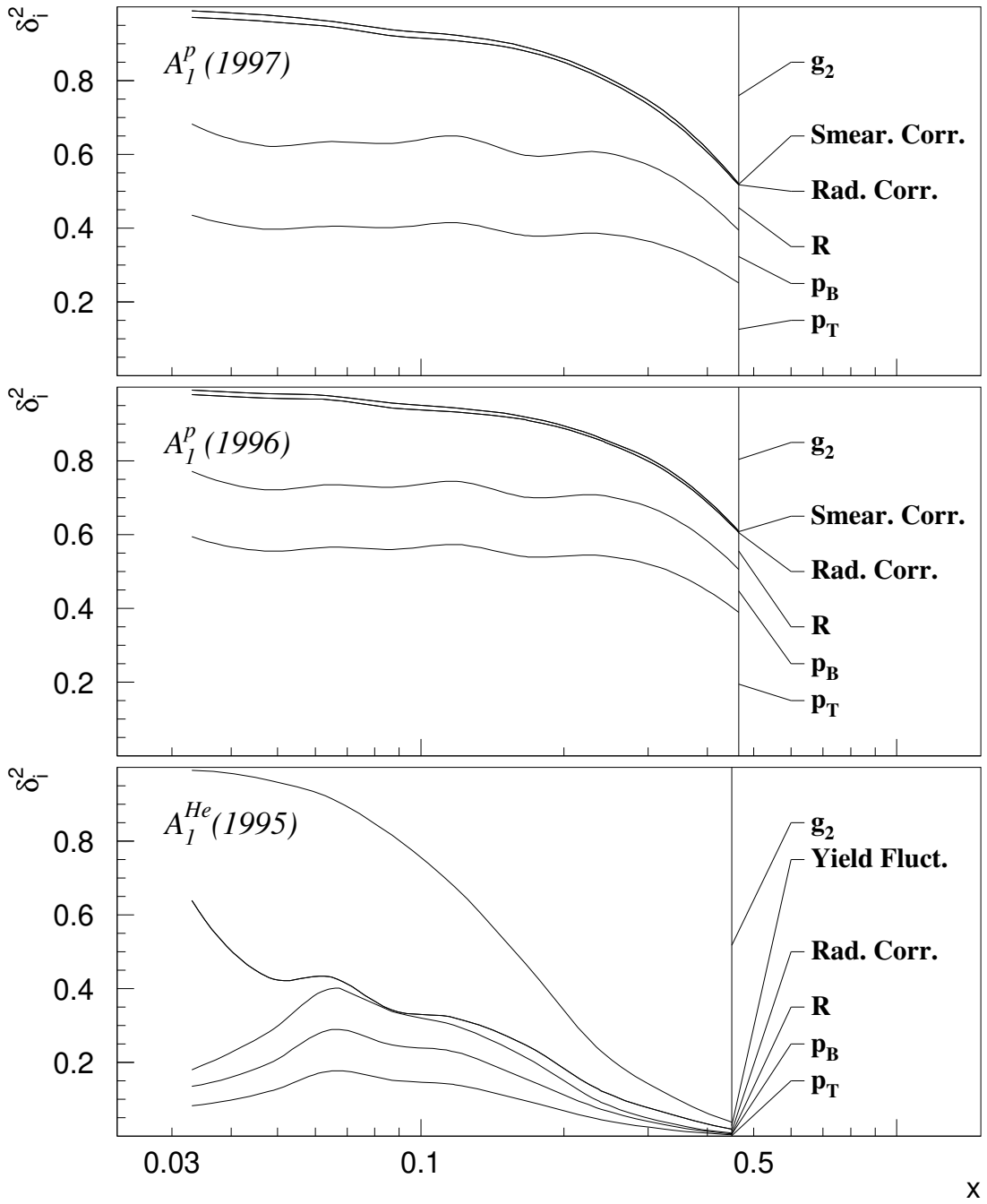

Figure 4.8.: Decomposition of the systematic error of the inclusive asymmetries A_1^{p} (separately for 1997 and 1996) and A_1^{He}, shown as a function of x. In each plot, the vertical distance between two adjacent lines represents the fractional systematic error contribution $\delta_i^2 \equiv (\delta A_1^i / \delta A_1^{\mathrm{TOT}})^2$, where δA_1^i is the systematic error related to a given source i and $\delta A_1^{\mathrm{TOT}} = \sqrt{\sum_i (\delta A_1^i)^2}$ is the total systematic error. By definition of δ_i^2 the different contributions add up to one: $\sum_i \delta_i^2 = 1$.

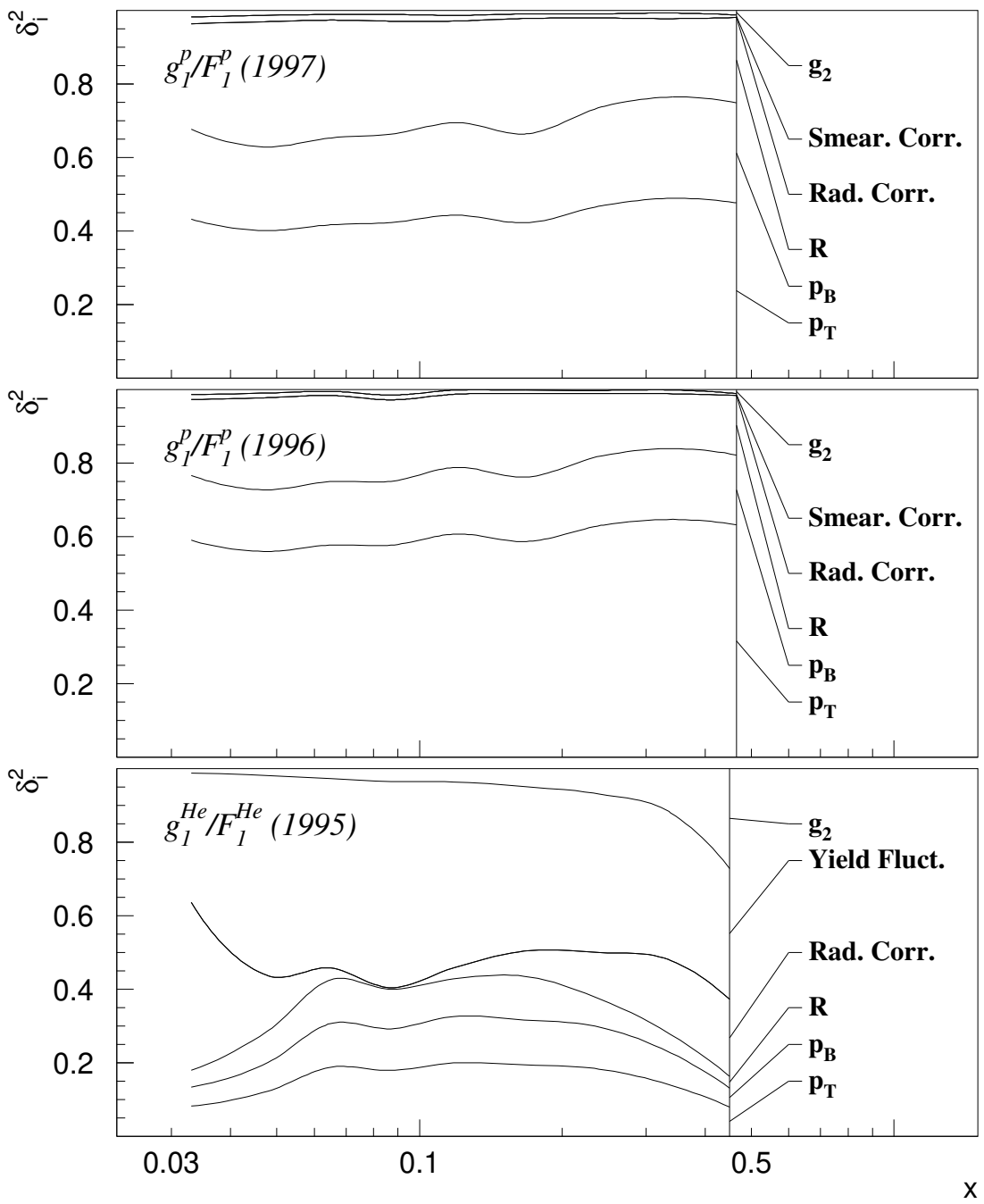

Figure 4.9.: Decomposition of the systematic error of the inclusive structure function ratios $g_1^{\rm p}/F_1^{\rm p}$ (separately for 1997 and 1996) and $g_1^{\rm He}/F_1^{\rm He}$, shown as a function of x. In each plot, the vertical distance between two adjacent lines represents the fractional systematic error contribution $\delta_i^2 \equiv [\delta(g_1/F_1)^i/\delta(g_1/F_1)^{\rm TOT}]^2$, where $\delta(g_1/F_1)^i$ is the systematic error related to a given source i and $\delta(g_1/F_1)^{\rm TOT} = \sqrt{\sum_i [\delta(g_1/F_1)^i]^2}$ is the total systematic error. By definition of δ_i^2 the different contributions add up to one: $\sum_i \delta_i^2 = 1$.

the inclusive helium and proton asymmetries, where δA_1^i is the systematic error related to a given source i and $\delta A_1^{\mathrm{TOT}} = \sqrt{\sum_i (\delta A_1^i)^2}$ is the total systematic error. Due to different systematic errors of the target polarisation measurements in 1996 and 1997, the systematic error decomposition is shown separately for the proton asymmetries of each year. For A_1^{p} (1997) the dominating sources of systematic errors are those of the target and beam polarisation measurements and the uncertainty of R. The same holds for A_1^{p} (1996) with the only difference that the target polarisation error is larger as compared to 1997. For low values of x the systematic uncertainty of A_1^{p} due to $\delta g_2^{\mathrm{p}}(x)$ is suppressed by the kinematical factor $\eta\gamma(1+\gamma^2)$ (see Eq. (4.31)) whereas its error contribution becomes important for high values of x. Since the helium asymmetry is anyway small this effect is even more important for A_1^{He}. For the helium asymmetry the dominating source of the systematic error is the yield fluctuation for low values of x while it is the uncertainty of g_2^{n} for high values of x.

The decomposition of the systematic error of the semi-inclusive asymmetries is similar to the inclusive asymmetries since the dominating sources of systematic uncertainties $[\delta A_1/A_1]^{(h)}_{p_{\mathrm{T}}} = \delta p_{\mathrm{T}}/p_{\mathrm{T}}$, $[\delta A_1/A_1]^{(h)}_{p_{\mathrm{B}}} = \delta p_{\mathrm{B}}/p_{\mathrm{B}}$, $[\delta A_1/A_1]^{(h)}_{R} = \delta R\ \varepsilon/(1+\varepsilon R)$ and the uncertainty assigned to g_2 are identical for the inclusive and semi-inclusive asymmetries. Therefore, the systematic uncertainties of the semi-inclusive asymmetries are not shown separately.

The extraction of the polarised quark distributions is based on Eq. (2.74) for the ratio g_1^h/F_1^h and Eq. (2.75) for g_1/F_1. Although the asymmetry A_1 equals the ratio g_1/F_1 for $g_2 = 0$, the systematic error of both quantities due to the uncertainty in g_2 is different. While A_1 is related to $A_{\parallel}$ and g_2 by Eq. (4.22), the ratio g_1/F_1 writes

$$\frac{g_1}{F_1} = \frac{1}{1+\eta\gamma}\left[\frac{A_{\parallel}}{D} + \gamma(\gamma-\eta)\frac{g_2}{F_1}\right] . \tag{4.33}$$

For high values of x the kinematical factor $\gamma(\gamma-\eta)$, which controls the systematic error

$$\delta\left(g_1/F_1\right)_{g_2} = \frac{\gamma(\gamma-\eta)}{1+\eta\gamma}\cdot\frac{\delta g_2}{F_1} , \tag{4.34}$$

is significantly smaller than the corresponding factor $\eta\gamma(1+\gamma^2)$ for A_1 (see Eq. (4.22)). Therefore, in the systematic error decomposition of g_1/F_1 as shown in Fig. 4.9, the uncertainty of g_2 is less important than in the case of A_1. The same argument holds for the systematic error of g_1^h/F_1^h.

5. Extraction of polarised quark distributions

This section describes the analysis procedure for the extraction of polarised quark distributions from a combination of inclusive and semi-inclusive asymmetry data on ^{3}He and hydrogen. Polarised quark distributions are extracted as a function of x for up $(u+\bar{u})$ and down $(d+\bar{d})$ flavours, and for valence and sea quarks. The first and second moments of the polarised quark distributions are computed and are compared to predictions from the constituent quark model, predictions based on SU(3)$_f$ symmetry and to a prediction from lattice QCD.

5.1. The extraction formalism

The extraction of the polarised quark distributions Δq_f is based on the LO QCD expressions (2.74) and (2.75), which relate the photon-nucleon asymmetries $A_1^{(h)}$ to the polarised and unpolarised quark distributions and fragmentation functions. The extraction formalism makes use of the asymmetries $A_1^{(h)}$ as extracted from the measured count rates of inclusive and semi-inclusive DIS events. Due to the limited acceptance of the HERMES spectrometer not all DIS events are detected. We therefore introduce $\tilde{D}_f(x,Q^2)$ as the probability density that a given inclusive DIS event is detected when the virtual photon scattered from a quark with flavour f. Similarly, we define $\tilde{D}_f^h(x,Q^2,z)$ as the probability density that a particular hadron h with energy fraction z is detected in the same process. With these definitions of $\tilde{D}_f(x,Q^2)$ and $\tilde{D}_f^h(x,Q^2,z)$ the measured inclusive asymmetries A_1 and semi-inclusive asymmetries A_1^h can be related to the quark distributions and fragmentation functions by

$$A_1^{(h)}(x,Q^2,z) = C_R(x,Q^2)\,\frac{\sum_f\, e_f^2\,\Delta q_f(x,Q^2)\,\tilde{D}_f^{(h)}(x,Q^2,z)}{\sum_f\, e_f^2\, q_f(x,Q^2)\,\tilde{D}_f^{(h)}(x,Q^2,z)}\,. \tag{5.1}$$

Compared to Eqs. (2.74) and (2.75) a factor $C_R = [1+R(x,Q^2)]\,/\,[1+\gamma^2]$ appears in this formula since the parametrisations of unpolarised quark distributions q_f used in Eq. (5.1) were extracted from fits to F_2 and not to F_1. A derivation of the correction term C_R is given in appendix A.3. The measured asymmetries $A_1^{(h)}(x,Q^2,z)$ were integrated in each x-bin over the corresponding Q^2-range and the z-range from 0.2 to 1 to

yield $A_1^{(h)}(x)$. In terms of quark distributions and fragmentation functions the measured asymmetries then write

$$A_1^{(h)}(x) \propto \sum_f e_f^2 \left[\iint \Delta q_f(x,Q^2)\, \tilde{D}_f^{(h)}(x,Q^2,z)\, \mathrm{d}Q^2\, \mathrm{d}z \right] . \tag{5.2}$$

As will be discussed in section 5.2 the fragmentation functions $\tilde{D}_f^{(h)}(x,Q^2,z)$ were taken from the LEPTO generator using the LUND string fragmentation model and were calculated on a 3-dimensional grid in x, Q^2 and z where the binning in x was identical to the binning of the asymmetries. If x_i denotes the central x value of bin i, the asymmetry $A_1^{(h)}(x_i)$ is proportional to

$$A_1^{(h)}(x_i) \propto \sum_f e_f^2 \left[\sum_{j,k} \Delta q_f(x_i,Q_j^2)\, \tilde{D}_f^{(h)}(x_i,Q_j^2,z_k)\, \Delta Q_j^2\, \Delta z_k \right] \tag{5.3}$$

where, compared to Eq. (5.2), the integration has been replaced by a summation to account for the finite grid size. For the extraction of the polarised quark distributions it has been assumed that the quark polarisations $\Delta q_f/q_f$ are independent of Q^2 within the limited x and Q^2-range of the experiment:

$$\Delta q_f(x_i,Q_j^2) \;=\; \frac{\Delta q_f(x_i,Q_j^2)}{q_f(x_i,Q_j^2)} \cdot q_f(x_i,Q_j^2) \approx \frac{\Delta q_f}{q_f}(x_i) \cdot q_f(x_i,Q_j^2) . \tag{5.4}$$

This assumption is justified by the weak Q^2-dependence predicted by QCD in the given x and Q^2-range and by the experimental result that there is no significant Q^2-dependence observed in the inclusive asymmetries. Based on Eq. (5.4) it follows with Eq. (5.3)

$$A_1^{(h)}(x_i) = C_R(x_i)\, \frac{\sum_f e_f^2\, \Delta q_f/q_f(x_i) \left[\sum_{j,k} q_f(x_i,Q_j^2)\;\; \tilde{D}_f^{(h)}(x_i,Q_j^2,z_k)\, \Delta Q_j^2\, \Delta z_k \right]}{\sum_f e_f^2 \left[\sum_{j,k} q_f(x_i,Q_j^2)\;\; \tilde{D}_f^{(h)}(x_i,Q_j^2,z_k)\, \Delta Q_j^2\, \Delta z_k \right]} . \tag{5.5}$$

Eq. (5.5) gives the formula used to relate the quark polarisations $\Delta q_f/q_f(x_i)$ to the measured inclusive and semi-inclusive asymmetries for positively or negatively charged hadrons on the proton or neutron. In each x-bin, the quark polarisations $\Delta q_f/q_f$ were extracted by minimising

$$\chi^2 = (\boldsymbol{A}_\mathrm{m} - \boldsymbol{A})^\mathrm{T}\, \mathcal{V}_{\boldsymbol{A}_\mathrm{m}}^{-1}\, (\boldsymbol{A}_\mathrm{m} - \boldsymbol{A}) , \tag{5.6}$$

where the vector $\boldsymbol{A}_\mathrm{m} = (A_{\mathrm{1p},97}, A_{\mathrm{1p},97}^{h^+}, A_{\mathrm{1p},97}^{h^-}, A_{\mathrm{1p},96}, A_{\mathrm{1p},96}^{h^+}, A_{\mathrm{1p},96}^{h^-}, A_{\mathrm{1He}}, A_{\mathrm{1He}}^{h^+}, A_{\mathrm{1He}}^{h^-})$ contains as elements the measured asymmetries[1], $\mathcal{V}_{\boldsymbol{A}_\mathrm{m}}$ is the covariance matrix of the

[1] Due to different systematic uncertainties of the proton asymmetries measured in 1996 and 1997 the two sets of asymmetries were treated separately in the fit procedure.

asymmetry vector $\boldsymbol{A}_{\rm m}$, and $\boldsymbol{A}$ contains the asymmetries computed from Eq. (5.5) as a function of the fit parameters $\Delta q_f/q_f$ (see appendix A.1 for details). The nuclear corrections which were applied to construct the helium asymmetries $A_{^3{\rm He}}^{(h)}$ from the proton and neutron asymmetries are discussed in section 5.4 and the statistical correlations between the different types of asymmetries which enter into the covariance matrix $\mathcal{V}_{\boldsymbol{A}_{\rm m}}$ are given in appendix A.5. In the fit procedure no boundary conditions have been applied to the fitted quark polarisations. The known unpolarised quark distributions $q_f(x,Q^2)$ were taken from a parametrisation of Ref. [Lai 97] (*CTEQ4LQ, Low* Q_0).

The measured set of inclusive and semi-inclusive asymmetries does not allow to determine the polarisation of each sea quark distribution $u_{\rm s}, \bar{u}, d_{\rm s}, \bar{d}, s, \bar{s}$ separately. In particular those of the strange quark sea and light quark sea cannot be independently resolved with an accuracy better than the positivity constraint. To improve statistical significance, all sea contributions have been expressed in terms of one single function. In view of rather ambiguous theoretical model predictions [Dia 96, Fri 98], two different assumptions on the polarised sea quark distributions were considered which are discussed in the following section.

5.1.1. Assumptions on the polarisation of sea quarks

In various parametrisations of polarised quark distributions (e.g. [Flo 98, Ger 96, Glu 96]) the spin distributions of the different sea quark and anti-quark flavours are assumed to be SU(3)$_f$ symmetric:

$$\Delta u_{\rm s} = \Delta d_{\rm s} = \Delta s = \Delta\bar{u} = \Delta\bar{d} = \Delta\bar{s}\,. \tag{5.7}$$

Since the SU(3)$_f$ symmetry of the sea distributions is known to be broken in the unpolarised case [Haw 98], there is no strong reason that the assumption (5.7) is strictly true. Furthermore, as the amount of strange quarks in the nucleon is small compared to the amount of up and down sea quarks, the ansatz of a SU(3)$_f$ symmetric sea may lead to a result which violates the positivity limit $|\Delta s/s| \leq C_R^{-1}$. This problem is not present in an ansatz which assumes that the *polarisation* of sea quarks is independent of flavour:

$$\frac{\Delta q_s}{q_s} \equiv \frac{\Delta u_{\rm s}}{u_{\rm s}} = \frac{\Delta d_{\rm s}}{d_{\rm s}} = \frac{\Delta s}{s} = \frac{\Delta\bar{u}}{\bar{u}} = \frac{\Delta\bar{d}}{\bar{d}} = \frac{\Delta\bar{s}}{\bar{s}}. \tag{5.8}$$

This ansatz can be motivated by the idea that the sea consists of an equilibrium of $q\bar{q}$ pairs, which are continuously created and destroyed by helicity-conserving processes.

The assumption given in Eq. (5.8) was used for all calculations unless explicitely stated otherwise. The sensitivity of the extracted quark polarisations to the assumption about the sea distributions was derived by comparing the results obtained when assumption Eq. (5.8) was replaced by Eq. (5.7). (See appendix A.2 for details on the formalism.) As will be shown in section 5.5.1 the sensitivity of the extracted quark polarisations to the assumption about the sea polarisation is small.

5.1.2. Different options to separate quark flavours

Two ways to separate the polarisations of the different quark flavours have been studied.

In the *valence decomposition* the quark polarisations have been decomposed into the polarisations of valence up and down quarks and the remaining sea polarisation which includes all quarks and anti-quarks from the sea. In this case the three fit parameters were

$$\frac{\Delta u_{\rm v}}{u_{\rm v}}, \quad \frac{\Delta d_{\rm v}}{d_{\rm v}}, \quad \frac{\Delta q_{\rm s}}{q_{\rm s}}\,, \tag{5.9}$$

where Eq. (5.8) was used to express the polarisations of the individual sea quark flavours in terms of a single function $\Delta q_{\rm s}/q_{\rm s}$. In Eq. (5.9) the unpolarised valence quark distributions are defined as $u_{\rm v} = u - \bar{u}$ and $d_{\rm v} = d - \bar{d}$, and similarly for the polarised ones. The unpolarised sea quark distributions are assumed to be charge-symmetric in this analysis, i.e. $\bar{u} = u_{\rm s}$, $\bar{d} = d_{\rm s}$ and $\bar{s} = s$.

In the *flavour decomposition* the quark polarisations were decomposed into the polarisations of quarks and anti-quarks of the same flavour. Here, the fit parameters were

$$\frac{\Delta u + \Delta\bar{u}}{u + \bar{u}}, \quad \frac{\Delta d + \Delta\bar{d}}{d + \bar{d}}, \quad \frac{\Delta s + \Delta\bar{s}}{s + \bar{s}}\,, \tag{5.10}$$

where due to the assumption given in Eq. (5.8) the strange quark polarisation equals the polarisation of the non-strange sea-quarks: $(\Delta s + \Delta\bar{s})/(s + \bar{s}) = \Delta q_{\rm s}/q_{\rm s}$.

The first and second moments of the valence spin distributions are predicted by lattice QCD calculations whereas the first moments of the flavour spin distributions can be derived from inclusive structure function measurements in combination with results from weak baryon decays. The results will be compared in section 5.6.

5.2. Generation of fragmentation functions

Measurements of fragmentation functions are part of the HERMES unpolarised physics programme and results exist for the fragmentation functions of u and d quarks into charged pions [Gei 98a]. However, the fragmentation functions $\tilde{D}_f^h(x, Q^2, z)$ for all quark and anti-quark flavours $f = u, \bar{u}, d, \bar{d}, s, \bar{s}$ and for positively and negatively charged hadrons $h = h^+, h^-$ are not yet available. Resting upon detailed comparison with world data the LUND string fragmentation model was found to be applicable in the HERMES regime [Gei 98a, Tal 98] and has been used to calculate the fragmentation functions. As described in section 2.6.3 the free parameters of the LUND model have been tuned to fit the measured HERMES hadron distributions. The parameters obtained from the tuning procedure were taken from Ref. [Gei 98a] and are given in table B.14.

The LUND model is implemented into the JETSET-7.4 code [Sjö 94] which is part of the unpolarised DIS generator LEPTO-6.5 [Ing 97]. The LEPTO generator consists out of two parts. First, a point in the kinematical plane is selected according to the lepton-nucleon scattering cross section $\sigma(x, Q^2)$, and the unpolarised quark densities are used to

decide on which quark the scattering is performed. Second, the kinematics of the struck quark as well as the structure of the target remnant is passed to JETSET which generates the hadronic final state.

The measured asymmetries which enter into Eq. (5.6) for the extraction of the polarised quark distributions are corrected for kinematical smearing using a detailed model of the HERMES detector (see section 4.5.2). Consequently, the fragmentation functions $\tilde{D}_f^{(h)}$ have to be extracted from the generated event kinematics. The track selection cuts and the kinematical cuts used for the extraction of the fragmentation functions from LEPTO are given in table 4.1 and are identical to the cuts applied for extraction of the spin asymmetries from experimental data.

The fragmentation functions $\tilde{D}_f^{(h)}$ were constructed on a 3-dimensional grid in x, Q^2 and z. The binning in x was identical to the binning of the asymmetries. For technical reasons the binning in Q^2 was replaced by a binning in y since the latter is restricted to the range $0 \leq y \leq 0.85$. The binning in y consisted of 6 bins with the boundaries 0, 0.1, 0.2, 0.3, 0.45, 0.65 and 0.85, and the binning in z of 8 bins from 0.2 to 1 in steps of 0.1. The fragmentation functions $\tilde{D}_f^h(x, Q^2, z)$ which appear in Eq. (5.5) were calculated from the ratio[2]

$$\tilde{D}_f^h(x, Q^2, z) = \frac{N_{\mathrm{A}} : [l(N, q_f) \longrightarrow l' h X](x, Q^2, z)}{N_{\mathrm{G}} : [l(N, q_f) \longrightarrow l' X](x, Q^2)} \,, \tag{5.11}$$

where $N_{\mathrm{G}} : [l(N, q_f) \longrightarrow l' X](x, Q^2)$ is the number of generated inclusive DIS events where the lepton l scattered from a quark q_f in the nucleon N, and $N_{\mathrm{A}} : [l(N, q_f) \longrightarrow l' h X](x, Q^2, z)$ is the number of accepted hadrons h with $z > 0.2$ and $x_{\mathrm{F}} > 0.1$ in the same process. The functions $\tilde{D}_f(x, Q^2)$ were similarly determined from the ratio of accepted to generated inclusive DIS events for scattering from a quark q_f.

The systematic uncertainty of the fragmentation functions was derived from comparing different fragmentation models and varying the model parameters in JETSET. Two sets of alternative fragmentation functions were calculated. The first one was again based on the LUND string model, but this time the JETSET parameters have been tuned to the kinematic distributions of pions instead of all hadrons [Gei 98b]. The second set of fragmentation functions was constructed using the independent fragmentation model tuned to HERMES hadron distributions [Gei 98b]. The JETSET parameters used to generate both sets of fragmentation functions are given in table B.14.

By generating large event samples the statistical uncertainties of the extracted fragmentation functions can be suppressed compared to their systematical uncertainties. It has been verified that the statistical uncertainties of the generated fragmentation functions were small compared to their systematical uncertainties related to the use of a specific fragmentation model. For this reason the statistical errors of the fragmentation functions were neglected.

[2]Since for each value of x and y the value of $Q^2 = 2ME xy$ is fixed we keep the notation $\tilde{D}_f^h(x, Q^2, z)$ instead of $\tilde{D}_f^h(x, y, z)$.

The sensitivity of the inclusive and semi-inclusive hadron asymmetries to the polarisations $\Delta q_f/q_f$ of the different quark and anti-quark flavours is quantified by the so-called *quark flavour purity*:

$$P_f^{(h)}(x,Q^2,z) = \frac{e_f^2\; q_f(x,Q^2)\; \tilde{D}_f^{(h)}(x,Q^2,z)}{\sum_{f'} e_{f'}^2\; q_{f'}(x,Q^2)\; \tilde{D}_{f'}^{(h)}(x,Q^2,z)}\,. \tag{5.12}$$

For each kinematical point (x,Q^2,z) the purity $P_f^{(h)}(x,Q^2,z)$ describes the probability density that a quark of flavour f was probed by the virtual photon when a given inclusive or semi-inclusive DIS event is recorded. By definition of $P_f^{(h)}$ the different quark flavour purities add up to one for any final state: $\sum_f P_f^{(h)}(x,Q^2,z) = 1$. In terms of quark flavour purities the spin asymmetries given in Eq. (5.1) can be written as

$$A_1^{(h)}(x,Q^2,z) = C_R(x,Q^2)\; \sum_f P_f^{(h)}(x,Q^2,z)\; \frac{\Delta q_f(x,Q^2)}{q_f(x,Q^2)}\,. \tag{5.13}$$

Owing to their physically meaningful interpretation the purities are presented rather than the fragmentation functions themselves. Figs. 5.1 and 5.2 show the purities $P_f^{(h)}(x)$ integrated over the Q^2-range and z-range from 0.2 to 1 for a proton and neutron target, respectively. Each figure shows the purities $P_f(x)$ for inclusive events and the purities $P_f^h(x)$ for semi-inclusive events with positively and negatively charged hadrons as obtained from tuned LUND string fragmentation model [Gei 98a] and the *CTEQ4LQ* parametrisations of unpolarised quark distributions. In the figures these purities are referred to as SF1. In addition, the purities are shown for the tuned independent fragmentation model (IF) and the alternative fit of the string fragmentation model (SF2), which were used to estimate the systematic error of SF1. Note that in the plot some of the purities have been multiplied by a scale factor greater than 1 to make them clearly visible.

Since the functions $\tilde{D}_f(x,Q^2)$ for inclusive DIS events are to a very good approximation independent of the quark flavour it follows from Eq. (5.12) that the inclusive purities $P_f(x,Q^2)$ are a function of the unpolarised quark distributions alone:

$$P_f(x,Q^2) = \frac{e_f^2\; q_f(x,Q^2)}{\sum_{f'}\; e_{f'}^2\; q_{f'}(x,Q^2)}\,. \tag{5.14}$$

The inclusive purities calculated from the unpolarised quark distributions according to Eq. (5.14) are shown as the solid lines in Figs. 5.1 and 5.2 and are found to be in very good agreement with the results obtained from the Monte Carlo generated values for $\tilde{D}_f(x,Q^2)$ and Eq. (5.12).

The results obtained for $P_f^{(h)}(x)$ allow to draw the following conclusions. The purities show a strong dependence on x which is mainly introduced by the x-dependence of the unpolarised parton distributions. For a *proton* target, inclusive events as well as semi-inclusive events with positively and negatively charged hadrons are primarily sensitive to the u quark ($0.5 \lesssim P_u^{(h)} \lesssim 1$). For $x < 0.1$ the $\bar{u}$ quark purities become important.

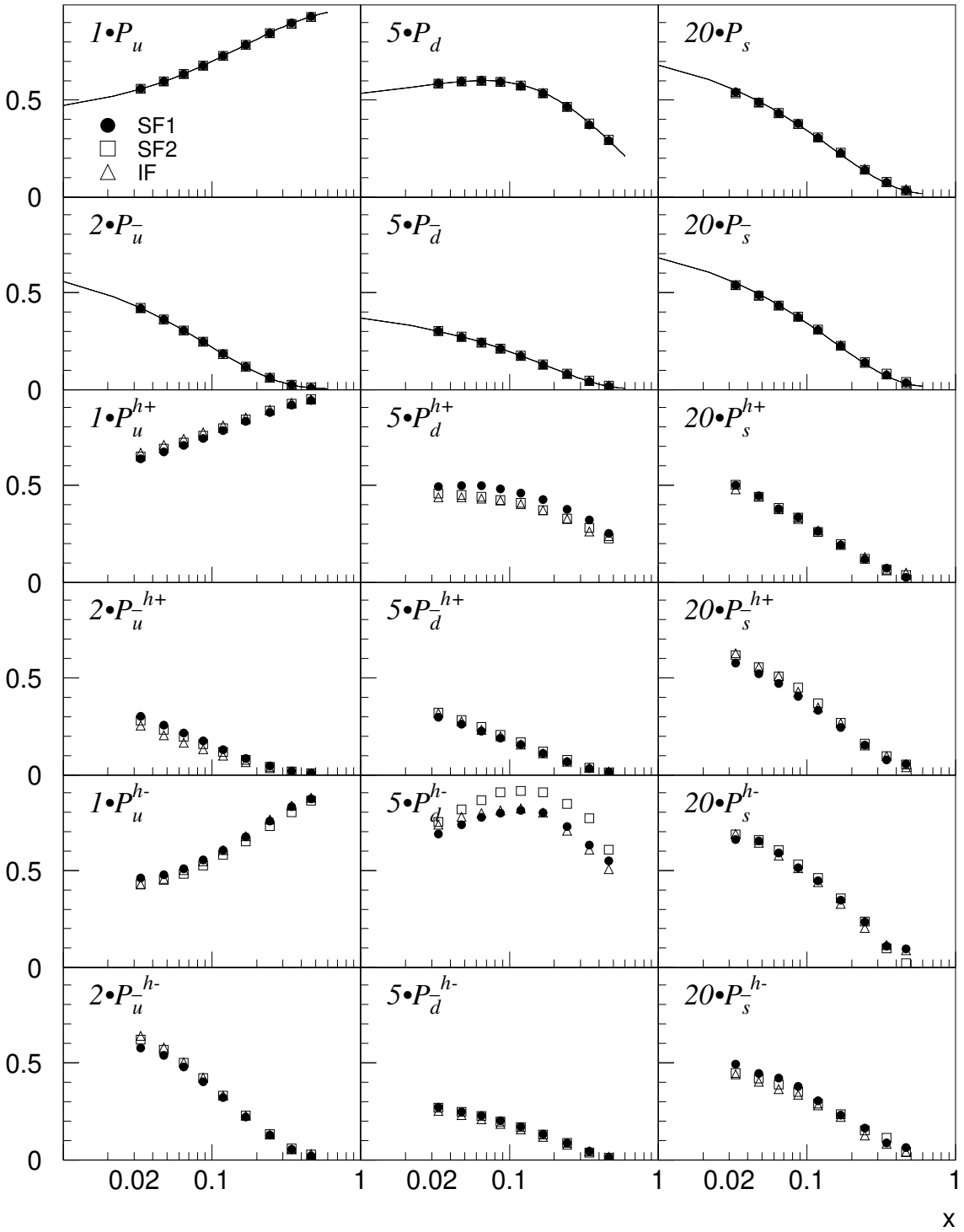

Figure 5.1.: Quark flavour purities $P_f^{(h)}$ on a **proton** target as a function of x for inclusive DIS events and for semi-inclusive DIS events with positively and negatively charged hadrons $h = h^+, h^-$ and for $f = u, \bar{u}, d, \bar{d}, s, \bar{s}$ as extracted from the tuned LUND fragmentation model (SF1) and the *CTEQ4LQ* parametrisations of unpolarised quark distributions. The purities shown as SF2 and IF were used to estimate the systematic error of SF1 (see text).

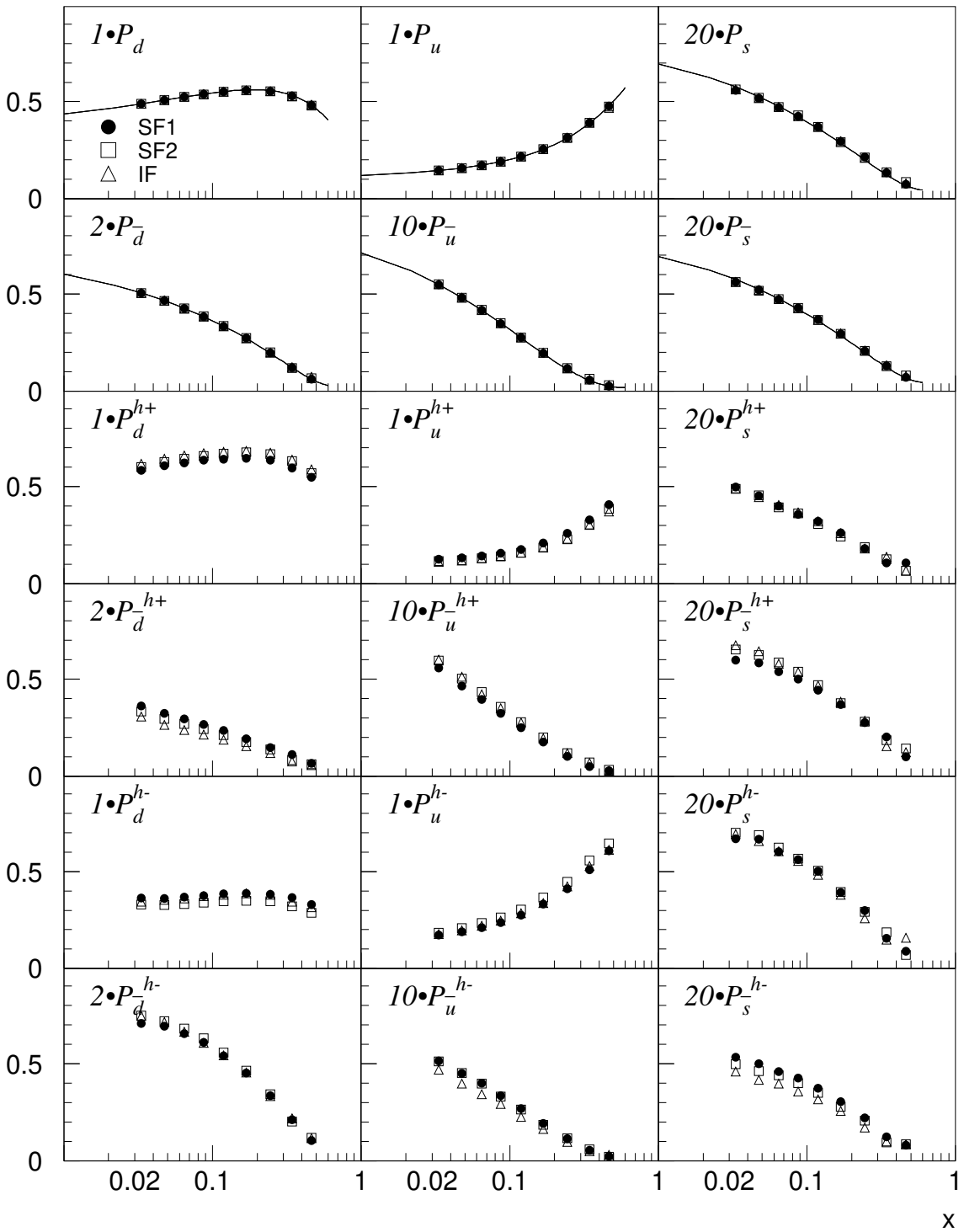

Figure 5.2.: Same as in Fig. 5.1 but for a **neutron** target. All quark flavour labels refer to the proton, using isospin symmetry. Note that some sea quark purities have been multiplied by a scale factor greater than one to make them clearly visible. The purities shown as SF2 and IF were used to estimate the systematic error of SF1.

Scattering from d quarks is typically suppressed by a factor of about 5 to 10 compared to u quarks, depending on x. For the light sea quarks the $\bar{d}$ quark purities are typically lower by a factor of about 2 to 4 compared to the $\bar{u}$ quark purities. In case of a *neutron* target the scattering from $d \equiv u_n$ quarks dominates at low values of x, while $P_u^{(h)} \approx P_d^{(h)}$ at high values of x. The anti-quark purities $P_{\bar{u}}^h (P_{\bar{d}}^h)$ are ≈ 0.2 in the region of $x < 0.2$ for a proton (neutron) target and are different for different final states h^+ or h^-. For both targets the strange and anti-strange quark purities are small ($\lesssim 0.03$) and are significantly suppressed compared to the purities of the light sea quarks.

These results for the quark flavour purities imply that inclusive and semi-inclusive polarised DIS on a proton target is suited to measure the polarisation of the u quarks, while a neutron target is appropriate to measure the polarisation of d quarks. Since for both targets the sea quark purities are small the statistical precision of a measurement of the individual sea quark polarisations for the given final states is limited.

5.3. Test of the extraction formalism with Monte Carlo

The PEPSI Monte Carlo [Vel 92] generator is an extension of the unpolarised DIS generator LEPTO and can be used to simulate *polarised* lepto-production. In addition to the unpolarised parton distributions PEPSI uses parametrisations of polarised parton distributions to decide to which quark flavour the virtual photon couples in a polarised scattering event. Both PEPSI-4.19 and LEPTO-6.5 use JETSET-7.4 to simulate the fragmentation process.

The PEPSI generator was used to perform a consistency check of the formalism for the extraction of polarised quark distributions from a set of inclusive and semi-inclusive spin asymmetries. The parametrisation of polarised parton distributions from *Glück et al.* (Standard Scenario, LO) [Glu 96] was selected together with the tuned LUND string fragmentation model (SF1) to generate inclusive asymmetries and semi-inclusive charged hadron asymmetries $A_1^{(h)}$ on a proton and neutron target. Based on the same fragmentation model, the fragmentation functions $\tilde{D}_f^{(h)}(x, Q^2, z)$ were constructed with LEPTO. Identical cuts were imposed on the particle kinematics and the detector acceptance for generating the spin asymmetries and the fragmentation functions. Using the generated fragmentation functions, Eq. (5.6) was solved for the polarised quark distributions Δq_f, where the asymmetry vector $\boldsymbol{A}_{\mathrm{m}} = (A_{1\mathrm{p}}, A_{1\mathrm{p}}^{h^+}, A_{1\mathrm{p}}^{h^-}, A_{1\mathrm{n}}, A_{1\mathrm{n}}^{h^+}, A_{1\mathrm{n}}^{h^-})$ contained as elements the Monte Carlo generated inclusive and semi-inclusive asymmetries on a proton and neutron target which were calculated from 10^7 generated inclusive DIS events per spin state and target. Since the polarised sea distributions are flavour symmetric (Eq. (5.7)) in the parametrisation from *Glück*, the formalism described in appendix A.2 was used. Furthermore, since $A_2^{(h)} = 0$ in PEPSI, the asymmetries $A_1^{(h)}$ were obtained from the generated lepton-nucleon asymmetries $A_{\|}^{(h)}$ according to $A_1^{(h)} \overset{A_2^{(h)}=0}{=} A_{\|}^{(h)}/D$. Note that for $A_2^{(h)} = 0$

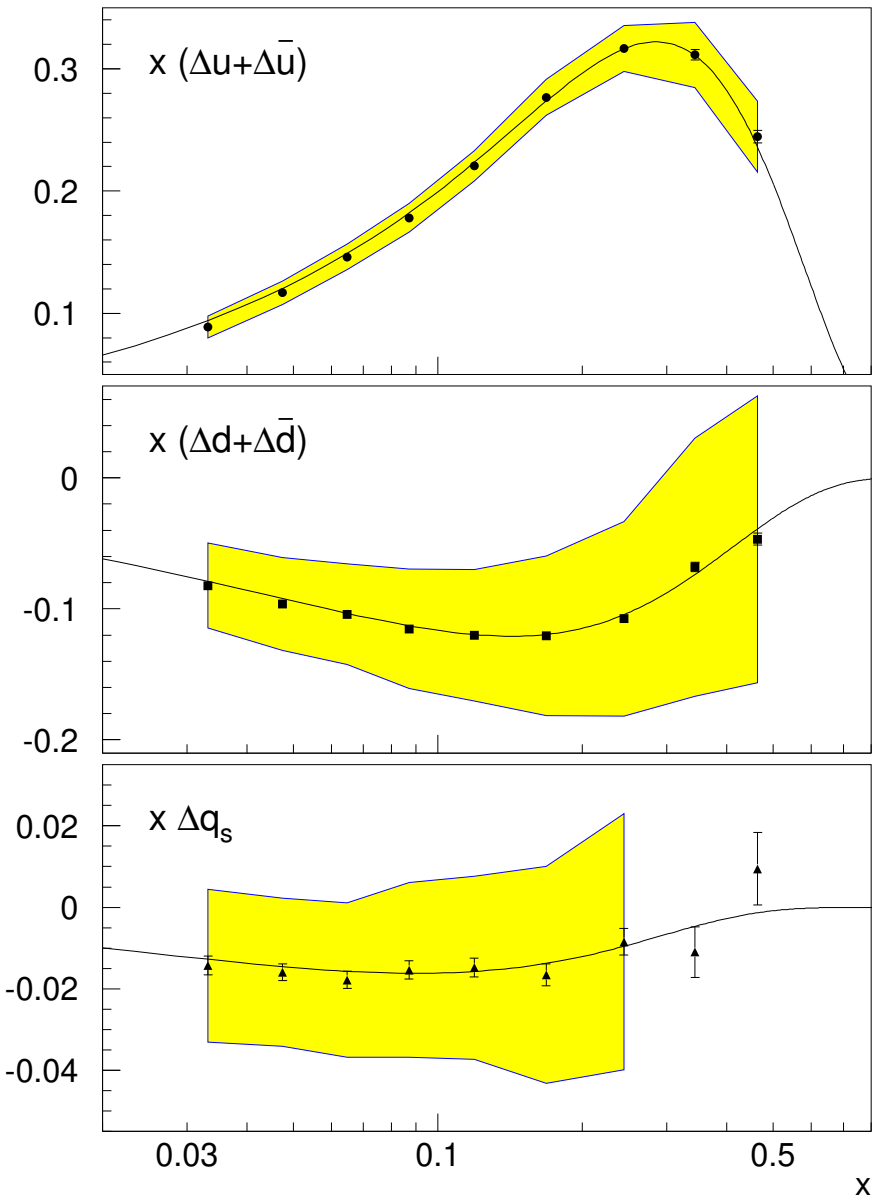

Figure 5.3.: Comparison of the PEPSI input polarised quark distributions $x[\Delta u(x) + \Delta\bar{u}(x)]$, $x[\Delta d(x) + \Delta\bar{d}(x)]$ and $x\Delta q_{\mathrm{s}}(x)$ with those extracted from the generated particle asymmetries. The solid lines indicate the input distributions and the full points refer to the polarised distributions as extracted from the generated asymmetries and fragmentation functions. For comparison, the statistical error of the quark distributions as extracted from *data* is indicated by the shaded bands. All distributions are shown at $Q^2 = 2.5\,\mathrm{GeV}^2$.

the $(1+\gamma^2)$ factor does not appear in Eq. (5.1) since then $A_1^{(h)} = (1+\gamma^2)\, g_1^{(h)}/F_1^{(h)}$ (instead of $A_1^{(h)} = g_1^{(h)}/F_1^{(h)}$ for $g_2^{(h)} = 0$) so that the $1+\gamma^2$ factor cancels. Further, the $(1+R)$ correction vanishes since $R = 0$ in PEPSI.

Fig. 5.3 compares the results for the extracted polarised quark distributions $x(\Delta u + \Delta\bar{u})$, $x(\Delta d + \Delta\bar{d})$ and $x\Delta q_s$ with the PEPSI input parametrisations. Both distributions are found to be in good agreement. For comparison, the statistical error of the quark polarisations as extracted from data is shown in Fig. 5.3 as the shaded bands[3]. The systematic uncertainty of the extraction procedure can be defined as the difference between the extracted and the input distributions. As can be seen from Fig. 5.3 this systematic uncertainty is small compared to the statistical (and systematical) error of the polarised quark distributions extracted from experiment and has therefore been neglected.

In Eq. (A.6) the unpolarised quark distributions $q_f(x_i)$ are evaluated at the central x value of bin i, which is determined by averaging x over collected events within each bin. To calculate the x-weighted polarised quark distributions $x\Delta q(x)$ from $\Delta q(x)$ the quark distributions were multiplied by the central value $x = x_i$.

When the extraction formalism is applied to the decomposition into valence and sea quarks the same level of agreement with the input distributions is achieved.

5.4. Nuclear corrections to calculate A_1^{He} from A_1^{n} and A_1^{p}

In Eq. (5.1) the polarised quark distributions $\Delta q_f(x, Q^2)$ were related to the measured asymmetries $A^{(h)}(x, Q^2, z)$ by[4]

$$A^{(h)}(x,Q^2,z) = C_R(x,Q^2)\,\frac{\sum_f\ e_f^2\ \Delta q_f(x,Q^2)\ \tilde{D}_f^{(h)}(x,Q^2,z)}{\sum_f\ e_f^2\ q_f(x,Q^2)\ \tilde{D}_f^{(h)}(x,Q^2,z)} \equiv \frac{\mathcal{B}^{(h)}(x,Q^2,z)}{\mathcal{C}^{(h)}(x,Q^2,z)}\,. \tag{5.15}$$

This formula holds for scattering from a bare proton or neutron target. In case of a ^{3}He target the summation has to take care of all target nucleons. Taking into account the effective proton and neutron polarisations in the ^{3}He-nucleus, $p_{\mathrm{p}} = -0.028 \pm 0.004$ and $p_{\mathrm{n}} = 0.86 \pm 0.02$ [Fri 90], the helium asymmetry can be split in the following way into a proton and a neutron contribution:

$$A_{\mathrm{He}}^{(h)} \;=\; f_{\mathrm{p}}^{(h)}\,p_{\mathrm{p}}\,A_{\mathrm{p}}^{(h)} + f_{\mathrm{n}}^{(h)}\,p_{\mathrm{n}}\,A_{\mathrm{n}}^{(h)}\,, \tag{5.16}$$

where $A_{\mathrm{p}}^{(h)}$ and $A_{\mathrm{n}}^{(h)}$ are the asymmetries as they would be measured in scattering off bare protons and neutrons. The dilution factors $f_{\mathrm{p}}^{(h)}(x,Q^2)$ and $f_{\mathrm{n}}^{(h)}(x,Q^2)$ give the probability that the reaction took place on one of the two protons or the neutron. Under the assumption that the unpolarised cross section for scattering from ^{3}He is given as the sum

[3] In the extraction of polarised quark distributions from experimental data the polarised sea distribution is extracted in the region $x \leq 0.3$ (see section 5.5.1). Therefore, the error band which represents the statistical error of the sea quark distribution extracted from data is shown only for $x \leq 0.3$.

[4] To reduce the number of subscripts, in this section the notation A is used for the virtual photon-nucleon asymmetry instead of A_1.

of the proton and the neutron cross sections, $\sigma_{\mathrm{He}}^{(h)}(x,Q^2) = 2\sigma_{\mathrm{p}}^{(h)}(x,Q^2) + \sigma_{\mathrm{n}}^{(h)}(x,Q^2)$, the dilution factors can be written as

$$f_{\mathrm{p}}^{(h)} = \frac{2\sigma_{\mathrm{p}}^{(h)}}{2\sigma_{\mathrm{p}}^{(h)} + \sigma_{\mathrm{n}}^{(h)}}\,, \qquad f_{\mathrm{n}}^{(h)} = \frac{\sigma_{\mathrm{n}}^{(h)}}{2\sigma_{\mathrm{p}}^{(h)} + \sigma_{\mathrm{n}}^{(h)}} = 1 - f_{\mathrm{p}}^{(h)}\,, \tag{5.17}$$

and it follows from Eq. (5.16)

$$A_{\mathrm{He}}^{(h)} = \frac{2\sigma_{\mathrm{p}}^{(h)}\; p_{\mathrm{p}}\; A_{\mathrm{p}}^{(h)} + \sigma_{\mathrm{n}}^{(h)}\; p_{\mathrm{n}}\; A_{\mathrm{n}}^{(h)}}{2\sigma_{\mathrm{p}}^{(h)} + \sigma_{\mathrm{n}}^{(h)}}\,. \tag{5.18}$$

The cross section $\sigma^{(h)}$ can be expressed in terms of $F_2^{(h)}$ and R following Eqs. (2.15) and (2.18) for a proton and neutron target. Since $R_{\mathrm{p}} = R_{\mathrm{n}}$ within experimental errors and $F_2^{(h)} = \sum_f e_f^2\; x\; q_f\; \tilde{D}_f^{(h)}$ it follows with the definitions of $\mathcal{B}^{(h)}$ and $\mathcal{C}^{(h)}$:

$$A_{\mathrm{He}}^{(h)} = \frac{2p_{\mathrm{p}}\; \mathcal{C}_{\mathrm{p}}^{(h)}\; A_{\mathrm{p}}^{(h)} + p_{\mathrm{n}}\; \mathcal{C}_{\mathrm{n}}^{(h)}\; A_{\mathrm{n}}^{(h)}}{2\mathcal{C}_{\mathrm{p}}^{(h)} + \mathcal{C}_{\mathrm{n}}^{(h)}} = \frac{2p_{\mathrm{p}}\; \mathcal{B}_{\mathrm{p}}^{(h)} + p_{\mathrm{n}}\; \mathcal{B}_{\mathrm{n}}^{(h)}}{2\mathcal{C}_{\mathrm{p}}^{(h)} + \mathcal{C}_{\mathrm{n}}^{(h)}}\,, \tag{5.19}$$

which relates the asymmetry $A_{\mathrm{He}}^{(h)}$ to the polarised and unpolarised quark distributions and fragmentation functions. Note that this ansatz neglects nuclear binding effects in ^{3}He which lead to small variations of the quark distributions for nucleons embedded in a nuclear environment (Nuclear shadowing, anti-shadowing and EMC Effect).

5.5. Results on polarised quark distributions

5.5.1. Flavour decomposition

The flavour decomposition was obtained by solving Eq. (5.6) for the quark polarisations $(\Delta u + \Delta\bar{u})/(u+\bar{u})$, $(\Delta d + \Delta\bar{d})/(d+\bar{d})$ and $(\Delta s + \Delta\bar{s})/(s+\bar{s})$, where due to assumption (5.8) the strange sea polarisation $(\Delta s + \Delta\bar{s})/(s+\bar{s})$ equals the polarisation of the non-strange sea quarks. For $x > 0.3$ the statistical error of the extracted sea polarisation $\Delta q_{\mathrm{s}}/q_{\mathrm{s}}$ is larger than the positivity limit $|\Delta q_{\mathrm{s}}/q_{\mathrm{s}}| \leq C_R^{-1}$. Therefore, in the region $x > 0.3$, the sea polarisation was set to zero and the corresponding effect on the results for the non-sea polarisations was included in their systematical uncertainties.

The result for the flavour decomposition is shown in Fig. 5.4 and the values are presented in table B.8. The up quark polarisation is positive and the down quark polarisation is negative over the measured range of x. Their absolute values increase with increasing values of x and remain different from zero within the full x-range of the measurement. The sea polarisation is compatible with zero over the measured range of x.

Table B.9 shows the goodness of the fit and the correlation coefficients of the three fit parameters $(\Delta u + \Delta\bar{u})/(u+\bar{u})$, $(\Delta d + \Delta\bar{d})/(d+\bar{d})$ and $(\Delta s + \Delta\bar{s})/(s+\bar{s})$. The correlation coefficients between the up and down quark polarisations are typically -0.7 so that these distributions are strongly anti-correlated. In contrast, the correlation coefficients between

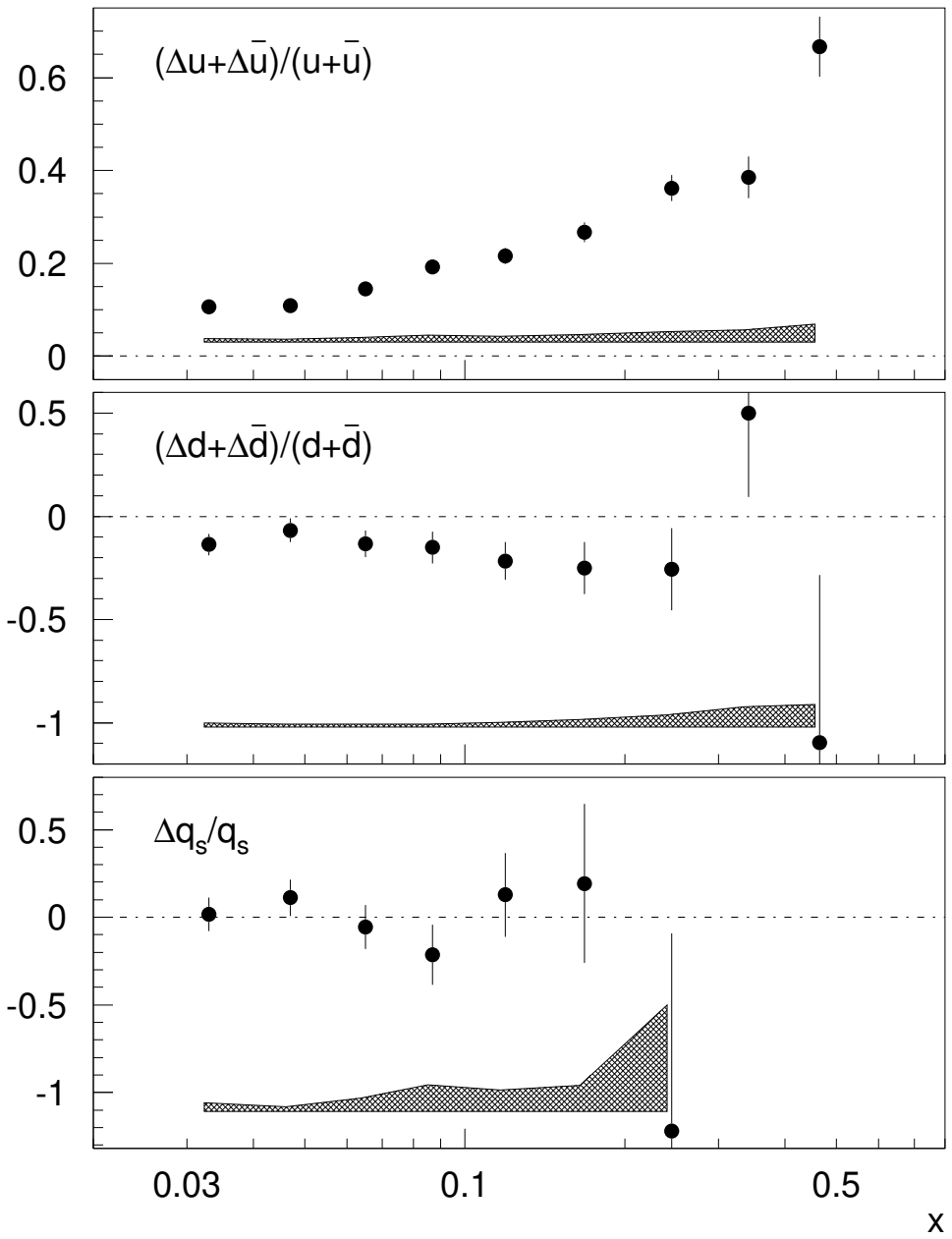

Figure 5.4.: The flavour decomposition $(\Delta u + \Delta\bar{u})/(u + \bar{u})$, $(\Delta d + \Delta\bar{d})/(d + \bar{d})$ and $\Delta q_{\mathrm{s}}/q_{\mathrm{s}}$ of the quark polarisation as a function of x, derived from the HERMES inclusive and semi-inclusive asymmetries on the ^{3}He and proton targets. The sea polarisation is assumed to be flavour symmetric (Eq. 5.8) in this analysis. The error bars represent the statistical errors and the bands indicate the systematical uncertainties.

the up quark and the sea quark polarisation are small and about -0.1, and those between the down quark and the sea quark polarisation are about 0.4. The $\chi^2_{\mathrm{min}}/\mathrm{NDF}$ of the fit (where $\mathrm{NDF} = 6$) varies between 0.1 and 2.4 for the different x-bins with an average

value of 1.2.

The systematic uncertainties, shown by the shaded bands in Fig. 5.4, were determined from the systematic uncertainties of the measured asymmetries, the unpolarised quark distributions, the fragmentation functions and the sea assumption $\Delta q_{\rm s}/q_{\rm s} = 0$ for $x > 0.3$. The size of the different systematic error contributions will be discussed in section 5.5.3.

The uncertainty due to the symmetry assumption about the sea polarisation was derived by comparing the quark polarisations produced by Eqs. (5.8) and (5.7). The quark polarisations are compared in Fig. 5.5 and change by typically less than 1% when the assumption Eq. (5.8) is replaced by (5.7).

Polarised quark distributions $\Delta q_f(x)$ were determined by multiplying the extracted quark polarisations $\Delta q_f(x)/q_f(x)$ with the known unpolarised distributions at $Q^2 = 2.5$ GeV^2 which were taken from the *CTEQ4LQ* parametrisation. It was assumed that the quark polarisations are independent of Q^2 within the x and Q^2-range of this measurement. The *CTEQ4LQ* parametrisations are compared to other parametrisations of unpolarised parton distributions in appendix A.3.

The results for the up, $x[\Delta u(x) + \Delta\bar{u}(x)]$, and down, $x[\Delta d(x) + \Delta\bar{d}(x)]$, distributions are shown in Fig. 5.6 and are compared with different sets of parametrisations of world data in LO QCD: *Glück et al.* (Standard Scenario, LO) [Glu 96], *Gehrmann and Stirling* (Gluon A, LO) [Ger 96] and *De Florian et al.* ($0.1 < \Delta g < 0.8$, LO) [Flo 98]. These parametrisations have been obtained from fits of expression (2.56) to the measured values of the inclusive spin structure functions g_1 ([Ger 96]), or from a fit of the LO QCD expression $\sum_f e_f^2\ \Delta q_f(x,Q^2) / \sum_f e_f^2\ q_f(x,Q^2)$ to the measured inclusive spin asymmetries $A_1(x,Q^2)$ assuming that $R = 0$ ([Glu 96, Flo 98]). The parametrisation from Ref. [Flo 98] includes as input to the fit the semi-inclusive charged hadron asymmetries from SMC [Ade 98a] in addition to the inclusive asymmetries.

Parametrisations that were fitted to spin asymmetries A_1 under the assumption $R = 0$ do not fit the polarised up quark distribution extracted from the HERMES data, while the parametrisation of *Gehrmann* is in agreement. The parametrisations from *Glück* and *De Florian* can be brought into agreement with the HERMES results by dividing by $[1 + R(x)]$. Fig. 5.6 demonstrates the size of the effect for the parametrisation by *Glück*. The *Gehrmann* parametrisation, which is derived from fits to g_1 instead of A_1, does not need this correction. The explanation for the observed difference is that the ratio R of the longitudinal to transverse absorption cross section is set to zero in the LO fits. On the other hand, in the extraction of g_1 from experiment, the measured values of R are used which are non-zero. The result of the fit then depends on the input for the fit, either A_1 (as in Ref. [Glu 96, Flo 98]) or g_1 (as in Ref. [Ger 96]). From the relation $A_1 = 2xg_1(1+R)/F_2(1+\gamma^2)$, which is quoted here for the assumption that $g_2 = 0$, it follows directly that the two choices lead to different results (see also appendix A.4).

In LO QCD the isospin triplet combination $\Delta q_3(x) = \Delta u(x) + \Delta\bar{u}(x) - \Delta d(x) - \Delta\bar{d}(x)$ is related to the spin structure functions according to $\Delta q_3(x) = 6[g_1^{\rm p}(x) - g_1^{\rm n}(x)]$. Fig. 5.7 illustrates that the semi-inclusive result for $\Delta q_3(x)$ is in good agreement with the parametrisations from *Glück* and from *Gehrmann* which were obtained from inclusive

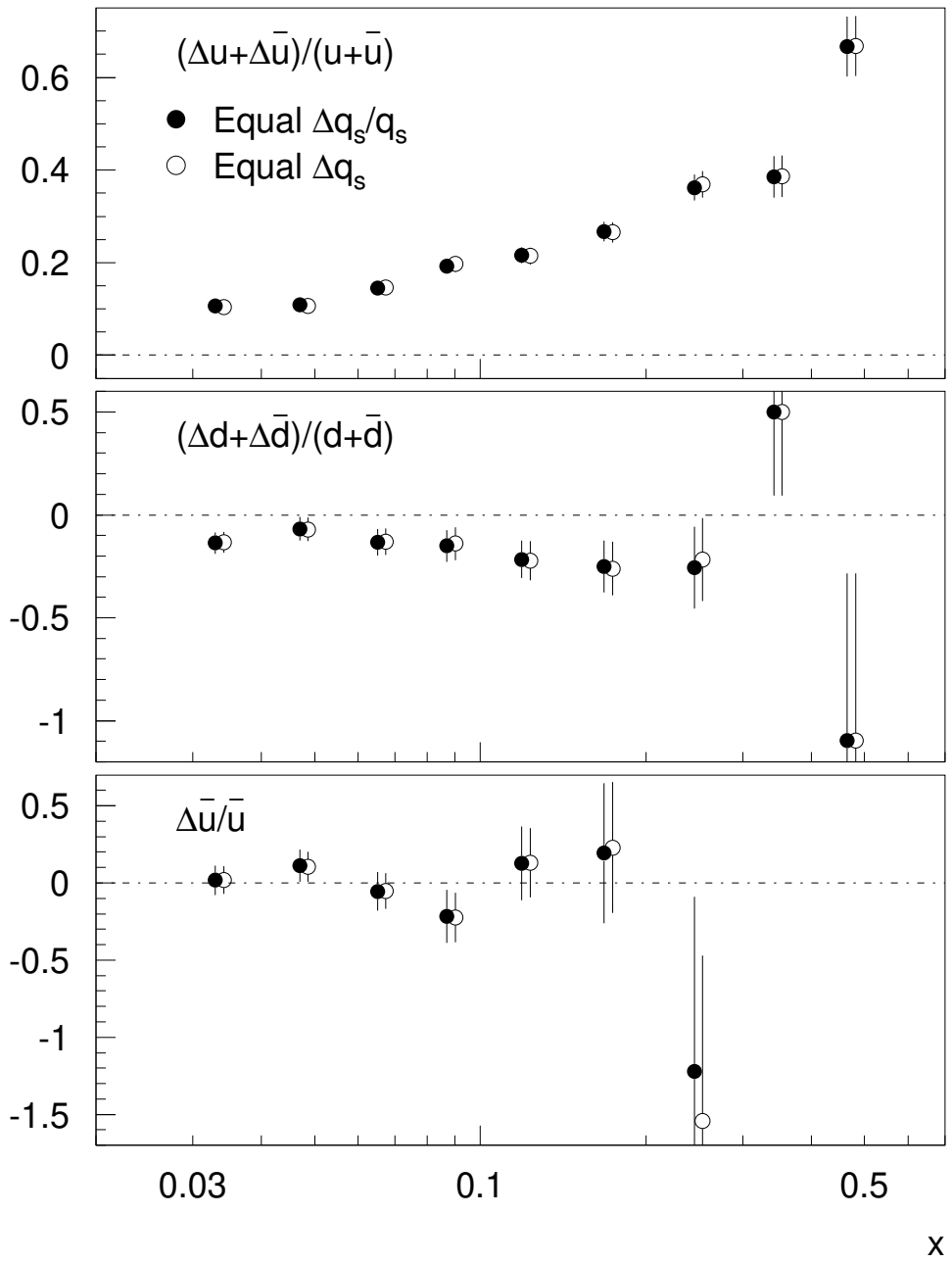

Figure 5.5.: The flavour decomposition of the quark polarisations for a SU(3)$_f$ symmetric sea (Eq. (5.7), open circles) and a polarisation symmetric sea (Eq. (5.8), closed circles). The closed circles are identical to those shown in Fig. 5.4. All error bars are statistical. To allow a direct comparison with the results for a polarisation symmetric sea, the quantity $\Delta\bar{u}/\bar{u} = \Delta q_{\mathrm{s}}/\bar{u}$ is shown for the results based on a SU(3)$_f$ symmetric sea, where $\Delta q_s \equiv \Delta u_s = \Delta d_s = \Delta s = \Delta\bar{u} = \Delta\bar{d} = \Delta\bar{s}$. The difference between the up or down quark polarisations obtained for the two sea assumptions vanishes for $x > 0.3$ since the polarised sea quark distributions are fixed to zero in this x-range.

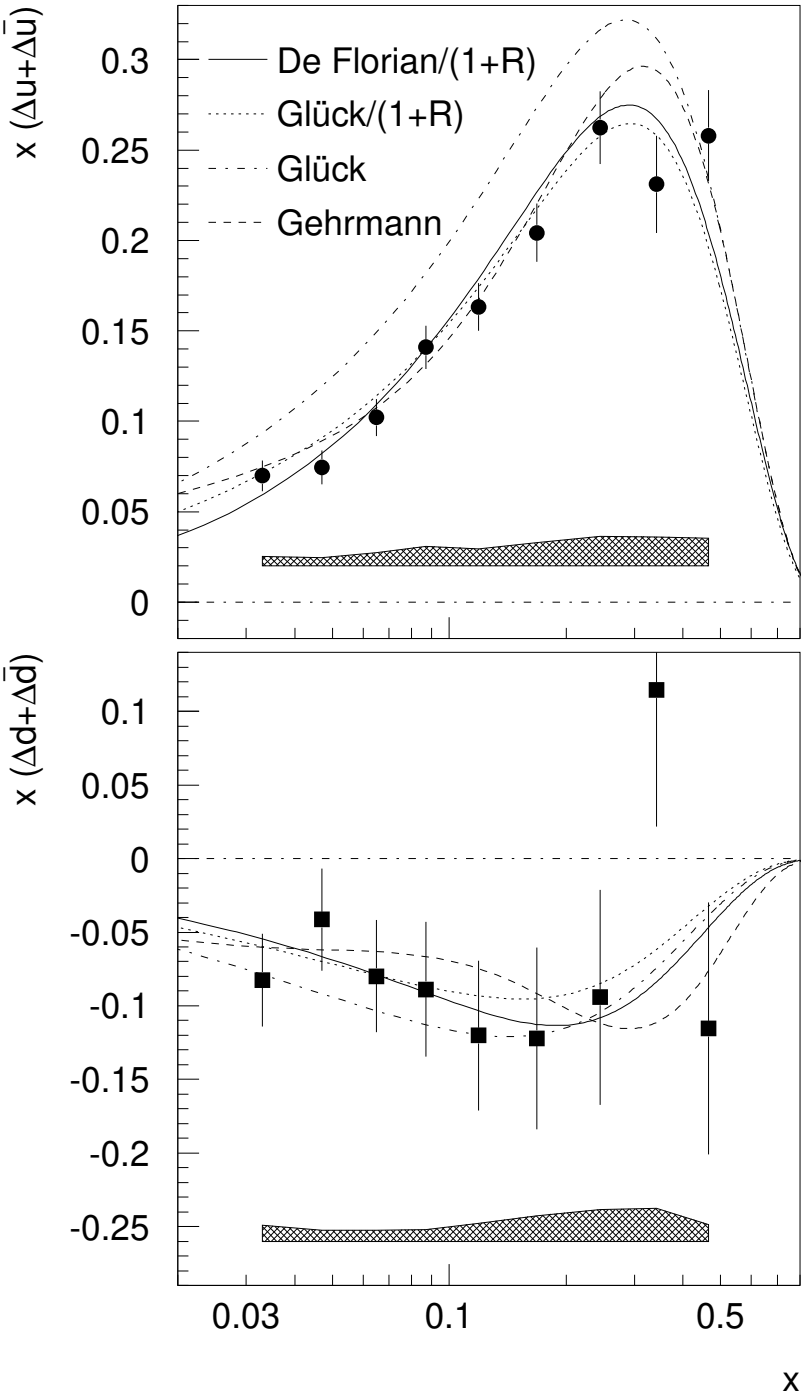

Figure 5.6.: The polarised quark distributions at $Q^2 = 2.5$ GeV^2 separately for $x(\Delta u + \Delta\bar{u})$ and $x(\Delta d + \Delta\bar{d})$ as a function of x. The experimental results are compared to different sets of LO parametrisations (see text for references). The *De Florian* and *Glück* parametrisations are divided by $(1 + R)$ to allow a direct comparison. The error bars shown are the statistical uncertainties and the bands indicate the systematical uncertainties of the HERMES data.

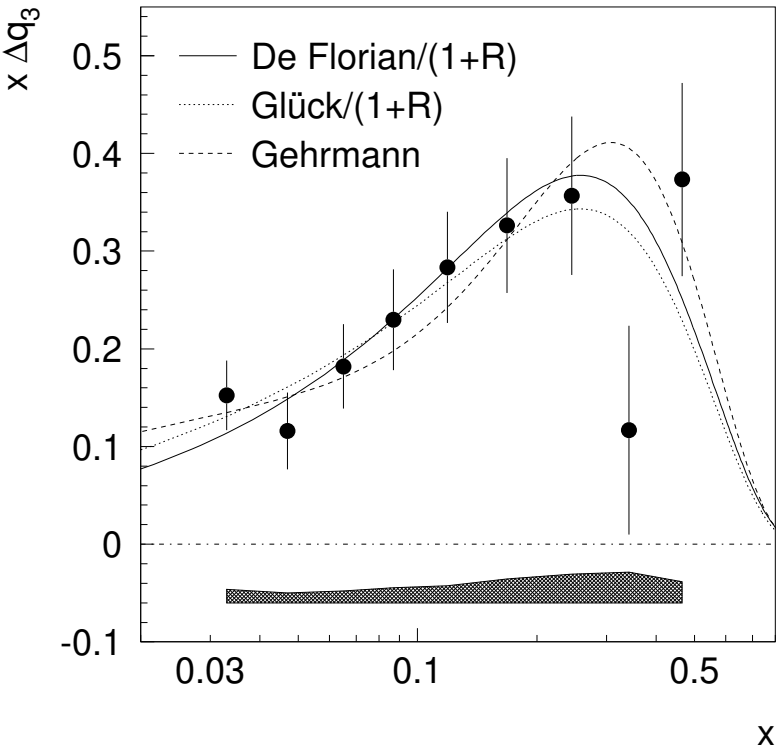

Figure 5.7.: The triplet combination $x\Delta q_3(x)$ at $Q^2 = 2.5$ GeV^2. The result is compared to the same sets of parametrisations as in Fig. 5.6. The error bars represent the statistical uncertainties and the band indicates the systematical uncertainties of the HERMES data.

measurements alone, as well as with the *De Florian* parametrisation which includes as input in addition the semi-inclusive charged hadron asymmetries from SMC.

5.5.2. Valence decomposition

Instead of separating the polarisations of quarks and anti-quarks of the same flavour, in the valence decomposition the valence quark polarisations are separated from the sea quark polarisation as discussed in section 5.1.2. The fitted sea polarisation $\Delta q_{\rm s}/q_{\rm s}$ is identical for the valence and for the flavour decomposition. As in case of the flavour decomposition, the sea distribution was set to zero for $x > 0.3$ in the valence decomposition and the effect on the results of the valence distributions was included in their systematic errors. The results for the quark polarisations $\Delta u_{\rm v}(x)/u_{\rm v}(x)$, $\Delta d_{\rm v}(x)/d_{\rm v}(x)$ and $\Delta q_{\rm s}(x)/q_{\rm s}(x)$ are given in table B.11 and were extracted assuming a flavour independent sea quark polarisation (Eq. (5.8)).

The statistical precision of the total up $(u + \bar{u})$ and down $(d + \bar{d})$ quark polarisations is superior to that of the valence up and down quark polarisations because of the strong correlations with the sea polarisation in the latter case. The correlation coefficients for the

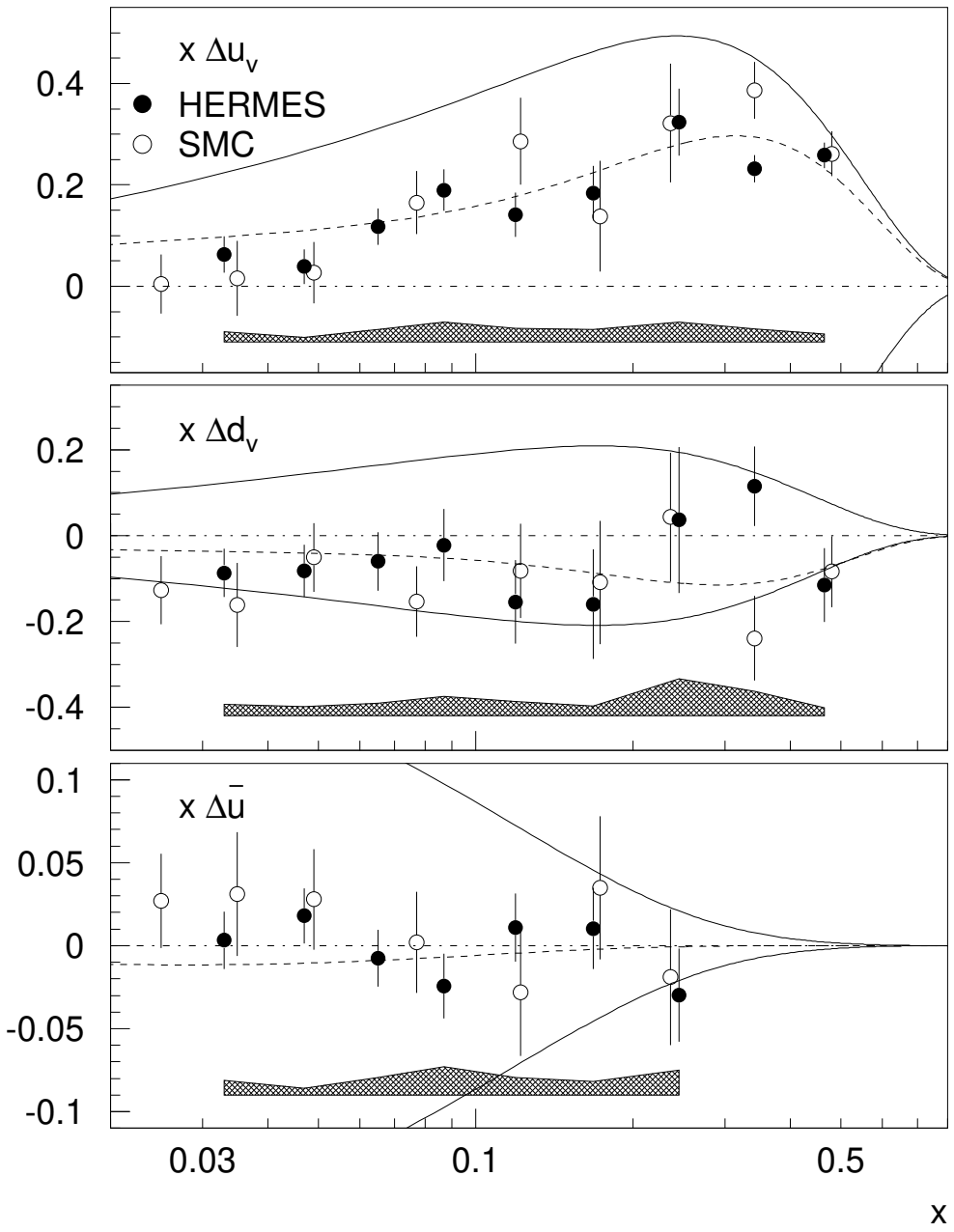

Figure 5.8.: The polarised valence quark $[x\Delta u_{\rm v}(x)$, $x\Delta d_{\rm v}(x)]$ and sea quark $[x\Delta\bar{u}(x)]$ distributions at $Q^2 = 2.5\,\mathrm{GeV}^2$. The HERMES error bars represent the statistical and the bands the HERMES systematic uncertainties. The distributions are compared to the results from SMC extrapolated to $Q^2 = 2.5\,\mathrm{GeV}^2$. The SMC error bars correspond to the total uncertainty of the experiment and were obtained by adding the statistical and systematical errors quadratically. The solid lines indicate the positivity limit and the dashed lines are the parametrisations from *Gehrmann* (Gluon A, LO). Note that some of the SMC data points were shifted slightly in x to make them clearly visible.

valence decomposition are given in table B.12. For the valence up and down quark polarisations the correlation coefficients are about $+0.7$ for $x < 0.3$ whereas they change sign to -0.7 in the region of $x > 0.3$ where the sea polarisation is fixed to zero. The up quark and the sea quark polarisations are strongly anti-correlated (-0.94). This correlation coefficient is significantly larger than the value of -0.1 obtained for the flavour decomposition. A similar effect is observed for the correlation between $\Delta d_{\rm v}(x)/d_{\rm v}(x)$ and $\Delta q_{\rm s}(x)/q_{\rm s}(x)$. The $\chi^2_{\rm min}$ of the fit does not depend on whether the quark polarisations are combined into distributions of the same flavour or into valence and sea quarks. Therefore, the goodness of the fit is the same for the valence and for the flavour decomposition.

The polarised valence distributions $\Delta u_{\rm v}(x)$, $\Delta d_{\rm v}(x)$ and $\Delta q_{\rm s}(x)$ were calculated from the quark polarisations by multiplying with the *CTEQ4LQ* parametrisation of unpolarised quark distributions at $Q^2 = 2.5$ GeV^2. The upper plots in Fig. 5.8 show the results for the x-weighted polarised valence quark distributions $x\Delta u_{\rm v}(x)$ and $x\Delta d_{\rm v}(x)$ at $Q^2 = 2.5$ GeV^2. Since for scattering off sea quarks the contribution from quarks and anti-quarks with flavour u dominates, the lower plot shows the polarised $x\Delta\bar{u}(x) = x\Delta u_{\rm s}(x)$ sea distribution. The polarised valence up quark distribution is positive over the measured range of x and the polarisation increases with increasing values of x. The polarised valence down quark distribution is negative. Fig. 5.8 includes the results from SMC [Ade 98a] obtained at $Q^2 = 10$ GeV^2, which were extrapolated to $Q^2 = 2.5$ GeV^2 by assuming a Q^2-independent quark polarisation, and are shown here for the HERMES x-range. The SMC results were derived under the sea assumption presented in Eq. (5.7). The positivity limit and the parametrisation of polarised quark distributions from *Gehrmann* are included in Fig. 5.8. The parametrisation and the SMC results are consistent with the HERMES results within the statistical and systematic uncertainties. The experimental uncertainty of $\Delta u_{\rm v}(x)$ and $\Delta\bar{u}(x)$ is significantly reduced compared to the results from SMC, while the experimental precision of the two experiments is similar for $\Delta d_{\rm v}(x)$.

5.5.3. Systematic error of polarised quark distributions

The systematic error of the polarised quark distributions was determined from the systematic error of the measured asymmetries, the uncertainties in the fragmentation functions and unpolarised quark distributions, and from the assumption $\Delta q_{\rm s}/q_{\rm s} = 0$ for $x > 0.3$.

The calculation of the systematic error of the polarised quark distributions due to the systematic error of the measured asymmetries is presented in appendix A.6.

The *CTEQ4LQ* [Lai 97] parametrisation of unpolarised quark distributions $q_f(x, Q^2)$ has been used as input to Eq. (5.5) to extract the polarised quark distributions. The systematic uncertainty of the *CTEQ4LQ* parametrisation was determined from the difference between the *CTEQ4LQ* and the LO *GRV* parametrisation [Glu 95]. The resulting systematic error of the polarised distributions was calculated from the difference of the results obtained for using the *GRV* instead of the *CTEQ4LQ* parametrisation of unpolarised distributions as input to Eq. (5.5).

The LUND fragmentation model fitted to HERMES hadron distributions (SF1) has

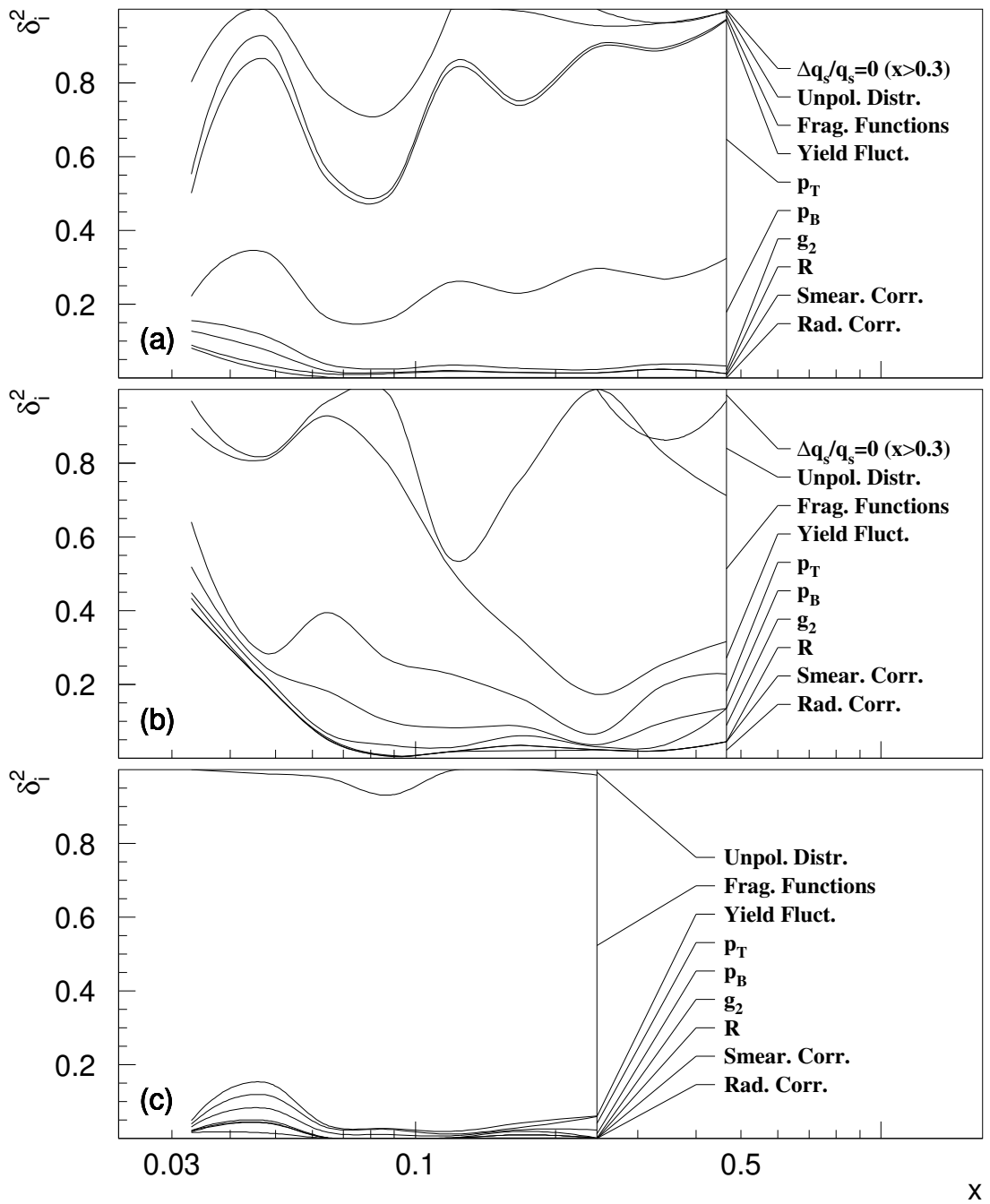

Figure 5.9.: Systematic error decomposition of (a): $(\Delta u + \Delta\bar{u})/(u + \bar{u})$, (b): $(\Delta d + \Delta\bar{d})/(d + \bar{d})$ and (c): $\Delta q_s/q_s$, shown as a function of x. In each figure, the vertical distance between two adjacent lines represents the fractional systematic error contribution $\delta_i^2 \equiv \sigma_i^2/\sigma_{\mathrm{TOT}}^2$, where σ_i is the systematic error of the quark polarisations related to a given source i and $\sigma_{\mathrm{TOT}} = \sqrt{\sum_i \sigma_i^2}$ is the total systematic error. By definition of δ_i^2 the different contributions add up to one: $\sum_i \delta_i^2 = 1$.

been used to determine the fragmentation functions (see section 5.2). The systematic uncertainty of the fragmentation functions has been derived from comparing different fragmentation models and varying the model parameters in JETSET. The systematic uncertainty of the polarised quark distributions due to the uncertainty in the fragmentation functions was derived from the maximum deviation of the results obtained from either of the alternative models IF and SF2 to those extracted from SF1.

For $x > 0.3$ the sea polarisation $\Delta q_{\rm s}/q_{\rm s}$ was fixed to zero and the corresponding effect on the results for the non-sea polarisations was included in their systematic uncertainties. To determine this systematic uncertainty, the up and down quark polarisations have been extracted in the region $x > 0.3$ for setting $\Delta q_{\rm s}/q_{\rm s}$ to the upper $(+[1+\gamma^2]/[1+R])$ and lower $(-[1+\gamma^2]/[1+R])$ positivity bound. The systematic error of the up and down quark polarisation was then calculated from the average deviation of these results to the values obtained for setting $\Delta q_{\rm s}/q_{\rm s}$ to zero.

The decomposition of the systematic error of the polarised quark distributions is presented in table B.10 for the flavour decomposition and in table B.13 for the valence decomposition. Fig. 5.9 shows the fractional error contributions $\delta_i^2 \equiv \sigma_i^2/\sigma_{\rm TOT}^2$, where σ_i is the systematic error of the quark distributions related to a given source i and $\sigma_{\rm TOT} = \sqrt{\sum_i \sigma_i^2}$ is the total systematic error. One can see from the figure that the dominating sources of the systematic error of $(\Delta u+\Delta\bar{u})/(u+\bar{u})$ are the uncertainties of the target and the beam polarisation measurements which amount to about 70% of the total uncertainty, depending on x, and the uncertainty in the fragmentation functions which contributes about 15%. For $(\Delta d + \Delta\bar{d})/(d+\bar{d})$ there are major contributions to the systematic error from the yield fluctuations ($\simeq 30\%$), the fragmentation functions ($10-70\%$) and somewhat smaller ones from the beam and target polarisation measurements ($\simeq 10\%$). The systematic uncertainty of $\Delta q_{\rm s}/q_{\rm s}$ is entirely controlled by the uncertainty in the fragmentation functions. For the valence quark polarisation $\Delta u_{\rm v}/u_{\rm v}$ ($\Delta d_{\rm v}/d_{\rm v}$) the assumption $\Delta q_{\rm s}/q_{\rm s} = 0$ for $x > 0.3$ accounts for about 40% (80%) of the systematic error in the region $x > 0.3$. For $x < 0.3$ the dominating sources of systematic errors of the valence distributions are the uncertainties of the fragmentation functions ($50-70\%$) and of the target and beam polarisation measurements ($10-20\%$).

5.5.4. Moments of polarised quark distributions

The moment $\Delta^{(n)}q_f(Q_0^2)$ of the polarised quark distribution $\Delta q_f(x,Q_0^2)$ is defined as

$$\Delta^{(n)}q_f(Q_0^2) \equiv \int_0^1 x^n\ \Delta q_f(x,Q_0^2)\ {\rm d}x\ . \tag{5.20}$$

The first $(n=0)$ and second moments $(n=1)$ of the polarised quark distributions have been calculated at $Q_0^2 = 2.5$ GeV^2 and are compared to other experimental data and to model predictions.

In the measured x-range of $0.023 < x < 0.6$ the integral $\Delta^{(n)}q_f$ was obtained as

$$\Delta^{(n)}q_f(Q_0^2) = \sum_i \left(\left.\frac{\Delta q_f}{q_f}\right|_i \int_{x_i}^{x_{i+1}} x^n \; q_f(x, Q_0^2)\, \mathrm{d}x \right), \tag{5.21}$$

where $(\Delta q_f/q_f)|_i$ was assumed to be constant within each bin (x_i, x_{i+1}) and independent of Q^2. The unpolarised distributions $q_f(x, Q_0^2)$ were taken from the *CTEQ4LQ* parametrisation. The statistical (systematical) error of the integral over the measured range was calculated by adding the point to point statistical (systematical) errors quadratically (linearly).

Outside the measured x-region extrapolations are required. There is no clear prediction for the low-x extrapolation (see e.g. [Abe 97b] for a discussion of different predictions). For comparison with previous measurements the low-x extrapolation has been obtained from a Regge extrapolation [Hei 73, Ell 88] according to $\Delta q_f(x) \propto x^{-\alpha}$. Here, the exponent $-\alpha$ is the intercept of the axial vector Regge trajectory, which is expected to lie between 0 and -0.5 [Ell 96]. As the simplest case $\Delta q_f(x) \propto x^{-\alpha}$ with $\alpha = 0$ was fitted to the data for $x < 0.075$. The statistical error of the Regge extrapolation was derived from the statistical error of the fit. For comparison, the extrapolation to $x = 0$ was determined using the parametrisations from *Glück* and from *Gehrmann*. In this second approach, the low-x contribution was estimated from the average of the results obtained from the two parametrisations and its uncertainty was taken to be half of the difference between both values. An upper limit for the low-x contribution to the integrals of the polarised quark distributions is given by the unpolarised distributions. For the valence distributions this limit is $\int_0^{0.023} \mathrm{d}x \; u_\mathrm{v}(x) = 0.40$ and $\int_0^{0.023} \mathrm{d}x \; d_\mathrm{v}(x) = 0.26$ at $Q^2 = 2.5\,\mathrm{GeV}^2$, while one obtains values greater than 2.5 for the flavour distributions due to the contributions from sea quarks.

The extrapolation to $x = 1$ was derived from the *Glück* and from the *Gehrmann* parametrisations in the same way as for the low-x extrapolation. The systematic uncertainty of the high-x extrapolation (which was derived from comparing the results obtained with the two parametrisations) is small and was included in the quoted uncertainty of the total integral. The upper limit for the high-x extrapolation as obtained from the unpolarised distributions is given by $\int_{0.6}^1 \mathrm{d}x \; [u(x) + \bar{u}(x)] = 0.025$, $\int_{0.6}^1 \mathrm{d}x \; [d(x) + \bar{d}(x)] = 0.004$ at $Q^2 = 2.5\,\mathrm{GeV}^2$, and similarly for the valence distributions since the contribution from sea quarks is negligible for $x > 0.6$.

The first and second moments in the range $0 < x < 1$ are given in table 5.1 for various combinations of polarised quark distributions. The total integral was calculated from the sum of the integral over the measured region, the Regge type low-x extrapolation and the high-x extrapolation as obtained from the parametrisations. The statistical error of the low-x extrapolation was included into the statistical error of the total integral. A model dependent uncertainty of the Regge extrapolation at low-x was not included in the quoted systematic error of the total integral.

The spin carried by up, down and strange quarks is found to be[5] $\Delta u + \Delta\bar{u} = 0.58 \pm$

[5]For simplicity the first moment $\Delta^{(0)}q_f$ is referred to as Δq_f.

Table 5.1.: First and second moments of various spin distributions. The results are given for the measured region $0.023 < x < 0.6$, for the low-x and the high-x extrapolation, and for the total integral. The low-x contribution to the integral was calculated assuming a Regge type low-x behaviour. The values for the low-x and the high-x contributions given in brackets $[\ldots]$ were derived from the *Gehrmann* and the *Glück* parametrisations. The total integral was calculated from the sum of the integral over the measured x-range, the Regge type low-x extrapolation, and the high-x extrapolation as obtained from the parametrisations. The items $\Delta^{(1)}u_{\mathrm{v}}$ and $\Delta^{(1)}d_{\mathrm{v}}$ denote the second moments of the respective valence quark distribution. The octet combination Δq_8^* was extracted assuming SU(3)$_f$ symmetric sea distributions whereas all other quantities are based on the assumption of a polarisation symmetric sea. Note that the entry for $\Delta s + \Delta\bar{s}$ does not represent a direct measurement of the strange sea (see text). All integrals are given for $Q^2 = 2.5\,\mathrm{GeV}^2$.

	measured region	low-x	high-x	total integral
$\Delta u + \Delta\bar{u}$	$0.52 \pm 0.02 \pm 0.03$	0.04 ± 0.00 $[\ 0.13 \pm 0.01]$	$[\ 0.02 \pm 0.00]$	$0.58 \pm 0.02 \pm 0.03$
$\Delta d + \Delta\bar{d}$	$-0.24 \pm 0.06 \pm 0.04$	-0.03 ± 0.01 $[-0.14 \pm 0.00]$	$[-0.00 \pm 0.00]$	$-0.27 \pm 0.06 \pm 0.04$
$\Delta s + \Delta\bar{s}$	$-0.01 \pm 0.03 \pm 0.04$	0.00 ± 0.01 $[-0.05 \pm 0.01]$	$[-0.00 \pm 0.00]$	$-0.01 \pm 0.03 \pm 0.04$
$\Delta\bar{u}$	$-0.01 \pm 0.02 \pm 0.03$	0.00 ± 0.01 $[-0.03 \pm 0.00]$	$[-0.00 \pm 0.00]$	$-0.01 \pm 0.02 \pm 0.03$
$\Delta\bar{d}$	$-0.02 \pm 0.04 \pm 0.04$	0.00 ± 0.01 $[-0.03 \pm 0.00]$	$[-0.00 \pm 0.00]$	$-0.02 \pm 0.04 \pm 0.04$
$\Delta\Sigma$	$0.27 \pm 0.06 \pm 0.06$	0.01 ± 0.01 $[-0.06 \pm 0.01]$	$[\ 0.02 \pm 0.00]$	$0.30 \pm 0.06 \pm 0.06$
Δq_3	$0.76 \pm 0.07 \pm 0.06$	0.07 ± 0.01 $[\ 0.26 \pm 0.01]$	$[\ 0.02 \pm 0.00]$	$0.85 \pm 0.07 \pm 0.06$
Δq_8	$0.31 \pm 0.09 \pm 0.10$	0.00 ± 0.02 $[\ 0.09 \pm 0.03]$	$[\ 0.02 \pm 0.00]$	$0.33 \pm 0.09 \pm 0.10$
Δq_8^*	$0.31 \pm 0.08 \pm 0.08$	0.00 ± 0.02 $[\ 0.09 \pm 0.03]$	$[\ 0.02 \pm 0.00]$	$0.33 \pm 0.08 \pm 0.08$
Δu_{v}	$0.54 \pm 0.05 \pm 0.08$	0.03 ± 0.01 $[\ 0.18 \pm 0.02]$	$[\ 0.02 \pm 0.00]$	$0.59 \pm 0.05 \pm 0.08$
Δd_{v}	$-0.20 \pm 0.11 \pm 0.12$	-0.03 ± 0.02 $[\ 0.09 \pm 0.01]$	$[-0.00 \pm 0.00]$	$-0.23 \pm 0.11 \pm 0.12$
$\Delta^{(1)}u_{\mathrm{v}}$	$0.124 \pm 0.009 \pm 0.014$	0.002 ± 0.001 $[\ 0.002 \pm 0.001]$	$[\ 0.013 \pm 0.000]$	$0.139 \pm 0.009 \pm 0.014$
$\Delta^{(1)}d_{\mathrm{v}}$	$-0.024 \pm 0.025 \pm 0.022$	-0.002 ± 0.001 $[\ 0.001 \pm 0.000]$	$[-0.002 \pm 0.001]$	$-0.028 \pm 0.025 \pm 0.022$

$0.02(\text{stat.}) \pm 0.03(\text{syst.})$, $\Delta d + \Delta\bar{d} = -0.27 \pm 0.06 \pm 0.04$ and $\Delta s + \Delta\bar{s} = -0.01 \pm 0.03 \pm 0.04$, and the total faction of the nucleon spin carried by quark spins is $\Delta\Sigma = 0.30 \pm 0.06 \pm 0.06$. When separating the flavour distributions into SU(3)$_f$ triplet (Δq_3) and octet (Δq_8) contributions, the results are $\Delta q_3 = 0.85 \pm 0.07 \pm 0.06$ and $\Delta q_8 = 0.33 \pm 0.09 \pm 0.10$. The first (second) moment of $\Delta u_\text{v}(x)$ is $0.59 \pm 0.05 \pm 0.08$ ($0.139 \pm 0.009 \pm 0.014$) and for the first (second) moment of $\Delta d_\text{v}(x)$ one obtains $-0.23 \pm 0.11 \pm 0.12$ ($-0.028 \pm 0.025 \pm 0.022$).

The triplet contribution Δq_3 is directly related to the Bjørken sum rule according to

$$\Delta q_3(Q^2) = \left| \frac{g_\text{A}}{g_\text{V}} \right| \Delta C^\text{NS}(Q^2) \,, \tag{5.22}$$

where the first moment of the non-singlet coefficient function $\Delta C^\text{NS}(Q^2)$ is given by Eq. (2.61). Higher twist corrections are expected to be small [Ste 95, Mey 96, Ji 97, Bal 98] and have been neglected. The semi-inclusive result agrees with the prediction 1.00 ± 0.06 of the Bjørken sum rule obtained in an estimate of $\Delta C^\text{NS}(Q^2)$ in 4$^\text{th}$ order in α_s for $Q^2 = 2.5$ GeV^2. The large theoretical error of the Bjørken sum rule prediction comes from the uncertainty in α_s which is magnified in 4$^\text{th}$ order. The numerical values for ΔC^NS at $Q^2 = 2.5$ GeV^2 are computed in appendix A.7.

In the following section the HERMES results for the first and second moments are compared to other experimental results and to model predictions.

5.6. Comparison of results

5.6.1. Results from semi-inclusive measurements

The only other measurement of polarised quark distributions from semi-inclusive DIS has been performed by the SMC Collaboration. The HERMES and SMC results for the x-dependence of the valence and sea quark distributions were shown in Fig. 5.8. In this section the integrals of the polarised quark distributions are compared. To allow a direct comparison of the HERMES and SMC results, the integrals of the polarised quark distributions were determined in the range $0.023 < x < 0.6$, in which both experimental data sets overlap. For this comparison, the polarised quark distributions from SMC were extrapolated to $Q^2 = 2.5$ GeV^2 (assuming Q^2-independent quark polarisations) and integrated according to Eq. (5.21). For the integration of the SMC results, the LO *GRV* parametrisation was used as input for the unpolarised distributions since the latter had been originally used in the analysis by SMC. The HERMES and SMC results are compared in table 5.2. There is good agreement of the two experiments.

The published SMC values for the integrals of the valence and sea quark distributions $\int_{0.003}^{0.7} \mathrm{d}x\, \Delta u_\text{v}(x) = 0.73 \pm 0.10 \pm 0.07$, $\int_{0.003}^{0.7} \mathrm{d}x\, \Delta d_\text{v}(x) = -0.47 \pm 0.14 \pm 0.08$, and $\int_{0.003}^{0.7} \mathrm{d}x\, \Delta\bar{u}(x) = 0.01 \pm 0.04 \pm 0.03$ [Ade 98a] differ from the values given in table 5.2. This is due to the following two reasons. Firstly, the integrals of both experiments have

Table 5.2.: Comparison of the HERMES and SMC integrals of polarised valence and sea quark distributions in the HERMES x-range of $0.023 < x < 0.6$. The SMC integrals shown in the table were extrapolated to $Q^2 = 2.5$ GeV^2 and integrated over the HERMES x-range.

	HERMES	SMC
$\Delta\bar{u}$	$-0.01 \pm 0.02 \pm 0.03$	$0.02 \pm 0.03 \pm 0.02$
$\Delta\bar{d}$	$-0.02 \pm 0.04 \pm 0.04$	$0.02 \pm 0.03 \pm 0.02$
$\Delta\bar{s}$	$-0.01 \pm 0.02 \pm 0.02$	$0.01 \pm 0.03 \pm 0.02$
$\Delta u_{\rm v}$	$0.54 \pm 0.05 \pm 0.08$	$0.59 \pm 0.08 \pm 0.07$
$\Delta d_{\rm v}$	$-0.20 \pm 0.11 \pm 0.12$	$-0.33 \pm 0.11 \pm 0.09$
$\Delta^{(1)} u_{\rm v}$	$0.124 \pm 0.009 \pm 0.014$	$0.146 \pm 0.016 \pm 0.012$
$\Delta^{(1)} d_{\rm v}$	$-0.024 \pm 0.025 \pm 0.022$	$-0.053 \pm 0.024 \pm 0.015$

been extracted in different x-ranges and at different scales. If the SMC values are integrated according to Eq. (5.21) over the total SMC x-range of $0.003 \leq x \leq 0.7$ and at $Q^2 = 10$ GeV^2 the results are $\int_{0.003}^{0.7} \mathrm{d}x\, \Delta u_{\rm v}(x) = 0.68 \pm 0.10 \pm 0.10$, $\int_{0.003}^{0.7} \mathrm{d}x\, \Delta d_{\rm v}(x) = -0.45 \pm 0.13 \pm 0.13$ and $\int_{0.003}^{0.7} \mathrm{d}x\, \Delta\bar{u}(x) = 0.01 \pm 0.04 \pm 0.04$. Secondly, the two experiments prefer different intergration methods: Eq. (5.21) used to integrate the HERMES polarised quark distributions differs from the formula

$$\Delta^{(n)} q_f = \sum_i (x_i)^n \, \Delta q_f(x_i) \, \Delta x_i \, , \tag{5.23}$$

used by SMC [Pre 97]. In Eq. (5.23), x_i denotes the mean x value of bin i and Δx_i is the bin width. Eq. (5.23) produces a significantly larger value for the integral of $\Delta u_{\rm v}(x)$ than Eq. (5.21). However, the integration according to Eq. (5.23) might be questionable since the average value of $\Delta u_{\rm v}(x)$ measured by SMC in the last x-bin of $0.4 < x < 0.7$ exceeds the positivity limit at the upper bin boundary of $x = 0.7$ (see Fig. 5.8). Therefore, the integration by Eq. (5.23) causes an unphysical contribution to the integral of $\Delta u_{\rm v}(x)$. The same effect is present for the calculation of the second moment of $\Delta u_{\rm v}(x)$.

5.6.2. Constituent and relativistic quark models

In the Constituent Quark Model (CQM) the spin and flavour part of the wave function for a proton with spin up is given by [Gri 87]

$$\begin{aligned} |p^{\uparrow}\rangle \;=\; & \frac{1}{\sqrt{18}} \big(2|u^{\uparrow}u^{\uparrow}d^{\downarrow}\rangle + 2|u^{\uparrow}d^{\downarrow}u^{\uparrow}\rangle + 2|d^{\downarrow}u^{\uparrow}u^{\uparrow}\rangle - |u^{\uparrow}u^{\downarrow}d^{\uparrow}\rangle - |u^{\downarrow}u^{\uparrow}d^{\uparrow}\rangle - |u^{\downarrow}d^{\uparrow}u^{\uparrow}\rangle \\ & - |u^{\uparrow}d^{\uparrow}u^{\downarrow}\rangle - |d^{\uparrow}u^{\uparrow}u^{\downarrow}\rangle - |d^{\uparrow}u^{\downarrow}u^{\uparrow}\rangle \big) \, . \end{aligned} \tag{5.24}$$

The wave function $|n^{\uparrow}\rangle$ of the neutron is obtained from Eq. (5.24) by exchanging u with d quarks. These wave functions can be used to calculate the static properties of baryons.

The CQM describes with good accuracy the static magnetic moments of baryons. For a baryon in the ground state, the magnetic moment must be the sum of the magnetic moments of the quarks since there is no orbital angular momentum. The magnetic moment of the baryon is then simply the vector sum of the magnetic moments of its constituent quarks. The operator for the magnetic moment of the proton can be written as

$$\boldsymbol{\mu}_{\mathrm{p}} = \boldsymbol{\mu}_u + \boldsymbol{\mu}_u + \boldsymbol{\mu}_d = 2\mu_u \boldsymbol{\sigma}_u + \mu_d \boldsymbol{\sigma}_d \,, \tag{5.25}$$

where μ_f is the magneton of a quark with flavour f

$$\mu_f = \frac{e_f\, e}{2m_f} \tag{5.26}$$

and $\boldsymbol{\sigma}$ is the vector of Pauli matrices. The magnetic moments of the proton and the neutron are found to be

$$\mu_{\mathrm{p}} = \langle p^{\uparrow}|(\boldsymbol{\mu}_{\mathrm{p}})_z|p^{\uparrow}\rangle = \frac{1}{3}\left(4\mu_u - \mu_d\right) \,, \tag{5.27}$$

$$\mu_{\mathrm{n}} = \langle n^{\uparrow}|(\boldsymbol{\mu}_{\mathrm{n}})_z|n^{\uparrow}\rangle = \frac{1}{3}\left(4\mu_d - \mu_u\right) \,, \tag{5.28}$$

which leads for $m_u = m_d$ to the prediction

$$\frac{\mu_{\mathrm{n}}}{\mu_{\mathrm{p}}} = -\frac{2}{3} \,, \tag{5.29}$$

in very good agreement with the experimental value of -0.685. For the first moment of the polarised quark distributions the model predicts[6]

$$\Delta u = +\frac{4}{3} \,, \tag{5.30}$$

$$\Delta d = -\frac{1}{3} \,, \tag{5.31}$$

and $\Delta\Sigma = \Delta u + \Delta d = 1$. The CQM therefore overestimates the measured value of Δu by a factor of about 2, whereas the model prediction for Δd is compatible with the results from semi-inclusive measurements within relatively large experimental errors.

In relativistic quarks models like the MIT Bag model [Gre 89] the contribution of quarks spins to the nucleon spin is reduced to $\Delta\Sigma \approx 0.65$ [Jaf 90] and the remaining contribution is accounted for by quark orbital angular momenta. The semi-inclusive result of $\Delta\Sigma = 0.30 \pm 0.06 \pm 0.06$ amounts to about 40% of the value expected from relativistic quark models.

[6] In the CQM one has $\Delta s = 0$ (since $s = 0$) and thus $\Delta\Sigma = \Delta u + \Delta d$.

5.6.3. Baryon decays and inclusive spin structure functions

The spin carried by up, down and strange quarks can be obtained from inclusive structure function measurements in combination with results from weak baryon decays.

The axial charge matrix element a_0 is related to the first moment Γ_1 of the spin structure function g_1 by Eq. (2.58). Assuming isospin ($a_3 = |g_\mathrm{A}/g_\mathrm{V}|$) and SU(3)$_f$ symmetry ($a_8 = 3F - D$), Eq. (2.58) can be written as

$$\Gamma_1^{\mathrm{p(n)}}(Q^2) = \frac{1}{12}\left[+(-)\left|\frac{g_\mathrm{A}}{g_\mathrm{V}}\right| + \frac{1}{3}(3F-D)\right]\,\Delta C^{\mathrm{NS}}(Q^2) + \frac{1}{9}a_0(Q^2)\,\Delta C^{\mathrm{S}}(Q^2)\,. \tag{5.32}$$

In the $\overline{\mathrm{MS}}$ factorisation scheme the value of $a_0(Q^2)$ equals the value of $\Delta\Sigma(Q^2)$, so that $\Delta\Sigma$ can be extracted from the measured integrals Γ_1 using Eq. (5.32). Combining the result for $\Delta\Sigma = \Delta u + \Delta\bar{u} + \Delta d + \Delta\bar{d} + \Delta s + \Delta\bar{s}$ with Eqs. (2.63), (2.65) and (2.66) which can be expressed as

$$\begin{aligned}
\Delta u + \Delta\bar{u} - \Delta d - \Delta\bar{d} &= \left|\frac{g_\mathrm{A}}{g_\mathrm{V}}\right|\,\Delta C^{\mathrm{NS}}\,,\\
\Delta u + \Delta\bar{u} + \Delta d + \Delta\bar{d} - 2(\Delta s + \Delta\bar{s}) &= (3F-D)\,\Delta C^{\mathrm{NS}}\,,
\end{aligned}$$

one obtains a set of three linear equations for the three unknowns $\Delta u + \Delta\bar{u}$, $\Delta d + \Delta\bar{d}$ and $\Delta s + \Delta\bar{s}$. A recent global fit to world data yields [Ell 96]

$$\Delta u + \Delta\bar{u} = 0.66 \pm 0.03 \pm \ldots\,, \tag{5.33}$$

$$\Delta d + \Delta\bar{d} = -0.35 \pm 0.03 \pm \ldots\,, \tag{5.34}$$

$$\Delta s + \Delta\bar{s} = -0.08 \pm 0.03 \pm \ldots\,, \tag{5.35}$$

and $\Delta\Sigma = 0.23 \pm 0.04 \pm \ldots$ at $Q^2 = 2.5$ GeV^2. To compare with the semi-inclusive result the QCD corrections applied in [Ell 96] have been removed (see appendix A.7). The symbol $+\ldots$ represents further theoretical and systematic uncertainties from higher twist effects, the low-x extrapolation and a possible Q^2-dependence of A_1. These uncertainties are estimated to be of the same magnitude than the quoted errors.

The results (5.33) to (5.35) can be compared to the first moments of the quark spin distributions as extracted from semi-inclusive measurements. The semi-inclusive result for $\Delta u + \Delta\bar{u} = 0.58 \pm 0.02 \pm 0.03$ and $\Delta d + \Delta\bar{d} = -0.27 \pm 0.06 \pm 0.04$ differs from the inclusive analysis by 1.7 and 1.0 standard deviations, respectively, so that the results are consistent. The value of $\Delta s + \Delta\bar{s}$ is found to be close to zero in this semi-inclusive analysis whereas it is significantly negative in the inclusive analysis. Neither result represents a direct measurement of $\Delta s + \Delta\bar{s}$ but rather depends on the assumption of SU(3)$_f$ symmetry for the inclusive case and on the sea symmetry condition (Eq. (5.8)) for the semi-inclusive case. The total spin integral $\Delta\Sigma = \int_0^1 (\Delta u(x) + \Delta\bar{u}(x) + \Delta d(x) + \Delta\bar{d}(x) + \Delta s(x) + \Delta\bar{s}(x))\,\mathrm{d}x = 0.30 \pm 0.06 \pm 0.06$ agrees well with the inclusive result of

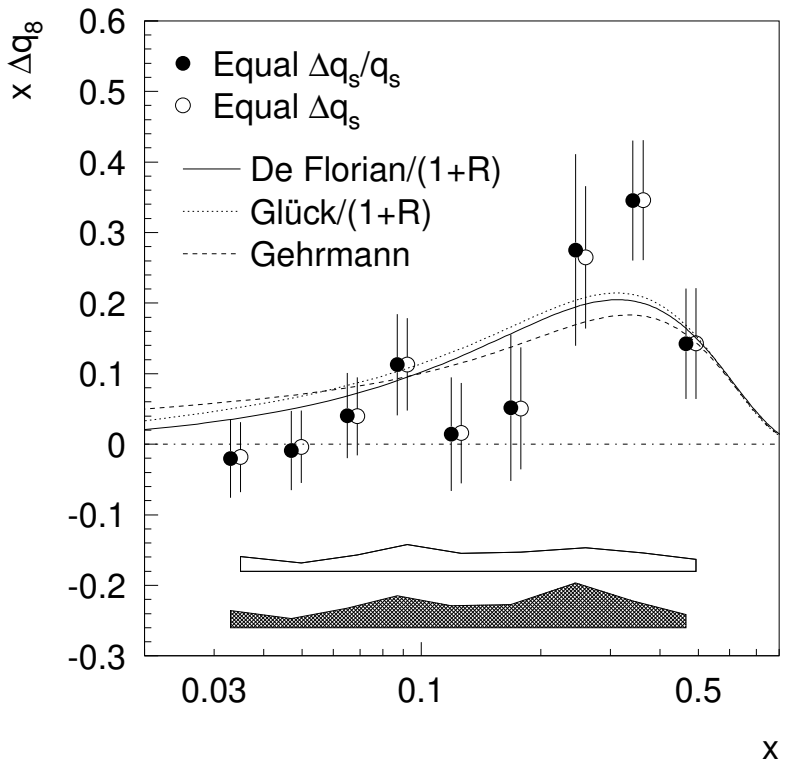

Figure 5.10.: The SU(3)$_f$ octet combination $x\Delta q_8(x)$ at $Q^2 = 2.5$ GeV^2 assuming SU(3)$_f$ symmetric sea distributions (open circles) or flavour independent sea polarisations (full circles). The data are compared to the same sets of parametrisations as in Fig. 5.6. The error bars indicate the statistical errors and the upper (lower) band shows the systematic uncertainties which correspond to the open (full) circles.

0.23 ± 0.04. The large theoretical uncertainty of the extrapolation at low-x is not included in the quoted errors.

The Ellis-Jaffe sum rule, which is based on SU(3)$_f$ symmetry and on the assumption of a zero polarisation of strange quarks, has been found to be violated (see section 2.5.2). Models to explain this discrepancy invoke either SU(3)$_f$ symmetry breaking, a large negative strange quark polarisation, or SU(3)$_f$ *asymmetric* polarised sea distributions. Semi-inclusive data provide an excellent test of such models. This is illustrated for two examples: (i) a model with symmetric sea (Eq. (5.7)) and unbroken SU(3)$_f$ and (ii) a model which is not SU(3)$_f$ symmetric combined with a flavour asymmetric sea according to Eq. (5.8). In the first case the octet combination $\Delta q_8 = \int_0^1 (\Delta u(x) + \Delta\bar{u}(x) + \Delta d(x) + \Delta\bar{d}(x) - 2(\Delta s(x) + \Delta\bar{s}(x)))\,\mathrm{d}x$ can be related to the hyperon decay constants F and D according to $\Delta q_8 = (3F - D)\,\Delta C^{\mathrm{NS}} = 0.46 \pm 0.04$ at $Q^2 = 2.5$ GeV^2. The semi-inclusive result yields $\Delta q_8 = 0.33 \pm 0.08 \pm 0.08$ which is lower than the prediction, but still consistent. A similar deviation shows up at low-x in the comparison of the

semi-inclusive result of $\Delta q_8(x)$ with the fits from Ref. [Flo 98, Ger 96, Glu 96] which are dominated by inclusive data (see Fig. 5.10). In the second case we assume a flavour asymmetric polarised sea according to Eq. (5.8) and obtain from the semi-inclusive analysis the result $\Delta q_8 = 0.33 \pm 0.09 \pm 0.10$. Following Ref. [Lic 95] Δq_8 can be calculated according to

$$\Delta q_8 = \frac{2\lambda\Delta q_0 + 3(3F - D)\,\Delta C^{\mathrm{NS}}}{3 + 2\lambda}\,, \tag{5.36}$$

where λ is estimated from the averaged ratio of the *CTEQ4LQ* unpolarised distribution functions according to $1 + \lambda = \langle \Delta\bar{d}(x)/\Delta\bar{s}(x)\rangle = \langle \bar{d}(x)/\bar{s}(x)\rangle = 4.8 \pm 0.4$. The model yields $\Delta q_8 = 0.35 \pm 0.07$. The results are compatible with both assumptions and do not allow a definite statement about the question whether the polarised quark distributions violate SU(3)$_f$ symmetry. A direct measurement of the strange sea is required for a final conclusion about the reason for the violation of the Ellis-Jaffe sum rule.

5.6.4. Lattice QCD calculations

The measured first and second moments of $\Delta u_{\mathrm{v}}(x)$ and $\Delta d_{\mathrm{v}}(x)$ can be compared to predictions from a quenched lattice QCD calculation [Goe 97a]. In this calculation the first moments of the valence distributions are

$$\Delta u_{\mathrm{v}} = 0.84 \pm 0.05, \quad \Delta d_{\mathrm{v}} = -0.25 \pm 0.02 \tag{5.37}$$

at $Q^2 = 5$ GeV^2 compared to the semi-inclusive result of $\Delta u_{\mathrm{v}} = 0.57 \pm 0.05 \pm 0.08$ and $\Delta d_{\mathrm{v}} = -0.23 \pm 0.11 \pm 0.12$ when evolved to the same scale. While the values for Δd_{v} agree within relatively large experimental errors, the first moment Δu_{v} obtained in this analysis is significantly lower than the lattice calculation. Note, however, that the error quoted for the semi-inclusive result does not include the uncertainty related to low-x extrapolation. This uncertainty is significantly diminished for the second moments where it is much smaller than the experimental errors related to the integral over the measured range. The lattice QCD calculation of the second moments yields

$$\Delta^{(1)} u_{\mathrm{v}} = 0.198 \pm 0.008, \quad \Delta^{(1)} d_{\mathrm{v}} = -0.048 \pm 0.003 \tag{5.38}$$

at $Q^2 = 4$ GeV^2 compared to the HERMES value of $\Delta^{(1)} u_{\mathrm{v}} = 0.131 \pm 0.009 \pm 0.013$ and $\Delta^{(1)} d_{\mathrm{v}} = -0.027 \pm 0.024 \pm 0.021$ at the same scale. The deviation observed for the first moment Δu_{v} is also present for the second moment $\Delta^{(1)} u_{\mathrm{v}}$, where the deviation corresponds to 3.8 standard deviations. The relative factors between the measured results and the lattice predictions for the first and second moments of $\Delta u_{\mathrm{v}}(x)$ are similar to those observed in the unpolarised case [Goe 97b].

It has been shown in section 5.5.4 that the SMC results are consistent with the HERMES results. However, the value for the second moment $\Delta^{(1)} u_{\mathrm{v}} = 0.155 \pm 0.017 \pm 0.010$ quoted by SMC at a scale of $Q^2 = 10$ GeV^2 [Ade 98a] is in agreement with the lattice prediction of $\Delta^{(1)} u_{\mathrm{v}} = 0.189 \pm 0.008$ at the same scale whereas the HERMES value does not agree with the lattice calculation.

6. Summary

The major aim of the HERMES experiment at HERA/DESY is to investigate the spin structure of the nucleon by polarised deep inelastic lepton-nucleon scattering.

In this thesis, spin asymmetries of the inclusive and semi-inclusive cross sections for the production of positively and negatively charged hadrons have been extracted in deep inelastic scattering of longitudinally polarised positrons from longitudinally polarised pure atomic hydrogen and ^{3}He gas targets. The data cover a kinematic range of $0.023 < x < 0.6$ and $1\ \text{GeV}^2 < Q^2 < 10\ \text{GeV}^2$. The inclusive asymmetries on both targets are in agreement with measurements at SLAC and CERN. The semi-inclusive asymmetries on ^{3}He were first measured by HERMES and no data exist for comparison. The semi-inclusive asymmetries on the proton are in agreement with the results from the SMC experiment at CERN. The experimental uncertainty of the world data on semi-inclusive charged hadron asymmetries on the proton was significantly reduced by the addition of the HERMES data from 1996 and 1997.

The measured inclusive asymmetries and semi-inclusive charged hadron asymmetries on the hydrogen and ^{3}He target were used to determine the polarised quark distributions of the nucleon. The extraction was based on a leading order QCD formalism whereby the LUND string fragmentation model was used to unfold the quark to hadron fragmentation process. Polarised quark distributions were extracted for the up $[\Delta u(x) + \Delta\bar{u}(x)]$ and down $[\Delta d(x) + \Delta\bar{d}(x)]$ flavours, and for valence $[\Delta u_{\text{v}}(x),\ \Delta d_{\text{v}}(x)]$ and sea quarks. In order to reduce the statistical error of the measured sea quark distributions, it was assumed that the polarisation of sea quarks is independent of flavour.

The up quark polarisation is found to be positive and the down quark polarisation is negative over the measured range of x. Their absolute values increase with increasing values of x and remain different from zero within the full x-range of the measurement. The sea polarisation is compatible with zero over the measured x-range. The HERMES results for the valence and sea quark polarisations are in agreement with the only other measurement by SMC [Ade 98a]. The experimental errors of the up quark and the sea quark polarisations are significantly smaller than those quoted by SMC, while the precision is similar for the down quark polarisation.

The first and second moments of the polarised quark distributions have been determined at $Q^2 = 2.5\ \text{GeV}^2$. The fraction of the nucleon spin carried by up, down and sea quarks is found to be $\Delta u + \Delta\bar{u} = 0.58 \pm 0.02 \pm 0.03$, $\Delta d + \Delta\bar{d} = -0.27 \pm 0.06 \pm 0.04$ and $\Delta s + \Delta\bar{s} = -0.01 \pm 0.03 \pm 0.04$, and the total faction of the nucleon spin carried

by quark spins is $\Delta\Sigma = \Delta u + \Delta\bar{u} + \Delta d + \Delta\bar{d} + \Delta s + \Delta\bar{s} = 0.30 \pm 0.06 \pm 0.06$. The first moment of the flavour triplet combination of the polarised quark distributions $\Delta q_3 = \Delta u + \Delta\bar{u} - \Delta d - \Delta\bar{d} = 0.85 \pm 0.07 \pm 0.06$ agrees with the prediction 1.00 ± 0.06 from the Bjørken sum rule at $Q^2 = 2.5$ GeV^2. The measured value of the flavour octet combination $\Delta q_8 = \Delta u + \Delta\bar{u} + \Delta d + \Delta\bar{d} - 2(\Delta s + \Delta\bar{s}) = 0.33 \pm 0.09 \pm 0.10$ is consistent with results from weak baryon decays using SU(3) flavour symmetry arguments. Predictions from a quenched lattice QCD calculation overestimate the HERMES results for the first and second moments of the polarised valence up quark distribution.

Since 1998 the HERMES experiment has been taking data on a polarised deuteron target and has been equipped with a ring-imaging Čerenkov detector. The high statistics data from HERMES on polarised deuterium will complement the high statistics data on the proton and ^{3}He, and will improve the precision with which the polarised quark distributions can be extracted. The ring-imaging Čerenkov detector provides hadron identification over the full momentum range and thus enables the measurement of semi-inclusive kaon and pion spin asymmetries which are expected to provide a first direct measurement of the strange and light sea quark polarisations.

This analysis contributed to the publication of the HERMES results on the *Flavour Decomposition of the Polarised Quark Distributions in the Nucleon from Inclusive and Semi-inclusive Deep-inelastic Scattering* [Ack 99].

A. Formalism of the analysis

A.1. Extraction formalism for polarisation symmetric sea distributions

For polarisation symmetric sea distributions the quark polarisations $\Delta q_f/q_f(x)$ were related to the measured inclusive and semi-inclusive spin asymmetries by Eq. (5.5). For the flavour decomposition the asymmetries $A_1^{(h)}$ are written in terms of three independent quark polarisations

$$p_u = \frac{\Delta u + \Delta\bar{u}}{u + \bar{u}}, \tag{A.1}$$

$$p_d = \frac{\Delta d + \Delta\bar{d}}{d + \bar{d}}, \tag{A.2}$$

$$p_{q_\mathrm{s}} = \frac{\Delta q_\mathrm{s}}{q_\mathrm{s}}, \tag{A.3}$$

where the assumption given in Eq. (5.8) is used to express the polarisations of the individual sea quark flavours in terms of a single function $\Delta q_\mathrm{s}/q_\mathrm{s}$. In order to determine the parameters $p_u,\ p_d$ and p_{q_s} the numerator of Eq. (5.5) is rearranged in the following way

$$\begin{aligned} A_1^{(h)}(x_i) \;\propto\; & e_u^2 \sum_{j,k} \underbrace{\left\{p_u\ \left[u+\bar{u}\right](x_i,Q_j^2) - p_{q_\mathrm{s}}\ \bar{u}(x_i,Q_j^2)\right\}}_{\Delta u(x_i,Q_j)}\ \tilde{D}_u^{(h)}(x_i,Q_j^2,z_k)\,\Delta Q_j^2\,\Delta z_k \\ + \;& e_d^2 \sum_{j,k} \underbrace{\left\{p_d\ \left[d+\bar{d}\right](x_i,Q_j^2) - p_{q_\mathrm{s}}\ \bar{d}(x_i,Q_j^2)\right\}}_{\Delta d(x_i,Q_j^2)}\ \tilde{D}_d^{(h)}(x_i,Q_j^2,z_k)\,\Delta Q_j^2\,\Delta z_k \\ + \;& e_s^2 \sum_{j,k} \underbrace{p_{q_\mathrm{s}}\ s(x_i,Q_j^2)}_{\Delta s(x_i,Q_j^2)}\ \tilde{D}_s^{(h)}(x_i,Q_j^2,z_k)\,\Delta Q_j^2\,\Delta z_k \\ + \;& \ldots\,, \end{aligned} \tag{A.4}$$

where the symbol $+\ldots$ represents the additional terms from the remaining sea quark distributions which are rewritten in the same way as the Δs term. The variable x_i denotes the mean x value of bin i which is determined by averaging x over collected events within each bin. Owing to Eq. (A.4) the quark polarisations $p_u,\ p_d$ and p_{q_s} are obtained at the mean x and Q^2 value of each x-bin.

The valence decomposition is obtained similarly by isolating the valence quark polarisations $\Delta u_{\rm v}/u_{\rm v}$ and $\Delta d_{\rm v}/d_{\rm v}$ instead of the flavour combinations $(\Delta u + \Delta\bar{u})/(u + \bar{u})$ and $(\Delta d + \Delta\bar{d})/(d + \bar{d})$. The sea polarisation $\Delta q_{\rm s}/q_{\rm s}$ is treated identically in both schemes.

Based on the expression (A.4) for $A_1^{(h)}$, Eq. (5.6) is solved in each x-bin for the respective quark polarisations using the program MINUIT (Version 94.1) [Jam 94] for function minimisation and error analysis. MINUIT offers a choice of different algorithms for function minimisation from which the standard MIGRAD algorithm was chosen.

A.2. Extraction formalism for SU(3)$_f$ symmetric sea distributions

The extraction of the quark polarisations assuming SU(3)$_f$ symmetric sea distributions (Eq. 5.7) instead of polarisation symmetric sea distributions (Eq. 5.8) requires a technical modification of the formalism. This modification is outlined in this paragraph.

Provided the quark polarisations $\Delta q_f/q_f$ are independent of Q^2 in the limited x and Q^2-range of the experiment the polarised quark distributions can be written as

$$\Delta q_f(x_i, Q_j^2) \;=\; \frac{\Delta q_f(x_i, Q_j^2)}{q_f(x_i, Q_j^2)} q_f(x_i, Q_j^2) \approx \frac{\Delta q_f(x_i, Q_0^2)}{q_f(x_i, Q_0^2)} q_f(x_i, Q_j^2)\;, \qquad \text{(A.5)}$$

where Q_0^2 is chosen as the average $Q^2 = 2.5$ GeV^2 of the experiment. To obtain the polarised quark distributions $\Delta q_f(x_i, Q_0^2)$ the expression (5.3) is expressed as

$$A_1^{(h)}(x_i) \propto \sum_f e_f^2 \left[\sum_{j,k} \Delta q_f(x_i, Q_0^2) \left[\frac{q_f(x_i, Q_j^2)}{q_f(x_i, Q_0^2)} \right] \tilde{D}_f^{(h)}(x_i, Q_j^2, z_k)\, \Delta Q_j^2 \Delta z_k \right] , \qquad \text{(A.6)}$$

where the ratio $q_f(x_i, Q_j^2)/q_f(x_i, Q_0^2)$ is taken from parametrisations of unpolarised quark distributions. For the flavour decomposition the asymmetries are written in terms of three independent polarised quark distributions

$$p_u \;=\; \Delta u + \Delta\bar{u}\;, \qquad \text{(A.7)}$$

$$p_d \;=\; \Delta d + \Delta\bar{d}\;, \qquad \text{(A.8)}$$

$$p_{q_{\rm s}} \;=\; \Delta q_{\rm s}\;, \qquad \text{(A.9)}$$

where Eq. (5.7) is used to express the polarised sea distributions of the individual flavours in terms of a single function $\Delta q_{\rm s}$. In order to determine the parameters $p_u,\ p_d$ and $p_{q_{\rm s}}$

Eq. (A.6) is rearranged in the following way

$$\begin{aligned} A_1^{(h)}(x_i) \;\propto\; & e_u^2 \sum_{j,k} \underbrace{\left\{ (p_u - p_{q_s}) \left[\frac{u(x_i,Q_j^2)}{u(x_i,Q_0^2)} \right] \right\}}_{\Delta u(x_i,Q_j)} \tilde{D}_u^{(h)}(x_i,Q_j^2,z_k)\,\Delta Q_j^2\,\Delta z_k \\ + \;& e_d^2 \sum_{j,k} \underbrace{\left\{ (p_d - p_{q_s}) \left[\frac{d(x_i,Q_j^2)}{d(x_i,Q_0^2)} \right] \right\}}_{\Delta d(x_i,Q_j)} \tilde{D}_d^{(h)}(x_i,Q_j^2,z_k)\,\Delta Q_j^2\,\Delta z_k \\ + \;& e_s^2 \sum_{j,k} \underbrace{\left\{ p_{q_s} \left[\frac{s(x_i,Q_j^2)}{s(x_i,Q_0^2)} \right] \right\}}_{\Delta s(x_i,Q_j)} \tilde{D}_s^{(h)}(x_i,Q_j^2,z_k)\,\Delta Q_j^2\,\Delta z_k \\ + \;& \ldots\,, \end{aligned} \tag{A.10}$$

where the symbol $+\ldots$ represents the contributions from the remaining sea quarks. This way, the polarised quark distributions are obtained at $Q_0^2 = 2.5$ GeV^2. The quark polarisations are then determined by dividing by the polarised quark distributions by the respective unpolarised distributions at $Q_0^2 = 2.5$ GeV^2.

The valence decomposition is obtained similarly by isolating the valence quark distributions $\Delta u_{\rm v}$ and $\Delta d_{\rm v}$ instead of the flavour combinations $\Delta u + \Delta\bar{u}$ and $\Delta d + \Delta\bar{d}$. The sea distribution $\Delta q_{\rm s}$ is treated identically in both schemes.

A.3. Parametrisations of unpolarised quark distributions and A_1

The polarised and unpolarised quark distributions Δq_f and q_f were defined in section 2.3 and are related to the structure functions g_1 and F_1 in LO QCD by Eqs. (2.49) and (2.50). Following Eq. (2.18) the inclusive asymmetry A_1 can be expressed in terms of the spin structure function g_1, the unpolarised structure function F_2 and the ratio $R = \sigma_{\rm L}/\sigma_{\rm T}$ by

$$A_1(x,Q^2) \overset{g_2=0}{=} \frac{g_1(x,Q^2)}{F_1(x,Q^2)} = \frac{g_1(x,Q^2)}{(1+\gamma^2)F_2(x,Q^2)/\left[2x(1+R(x,Q^2))\right]}\,. \tag{A.11}$$

The parametrisations of unpolarised quark distributions used in this analysis were taken from *CTEQ4LQ* (NLO) [Lai 97] and alternatively from *GRV* (LO) [Glu 95]. The LO parametrisations were obtained from a fit of the expression

$$F_2(x,Q^2) = \sum_f e_f^2\; x\; \tilde{q}_f(x,Q^2) \tag{A.12}$$

to world data on $F_2(x,Q^2)$ which were extracted from cross sections using non-zero values of R and γ^2.

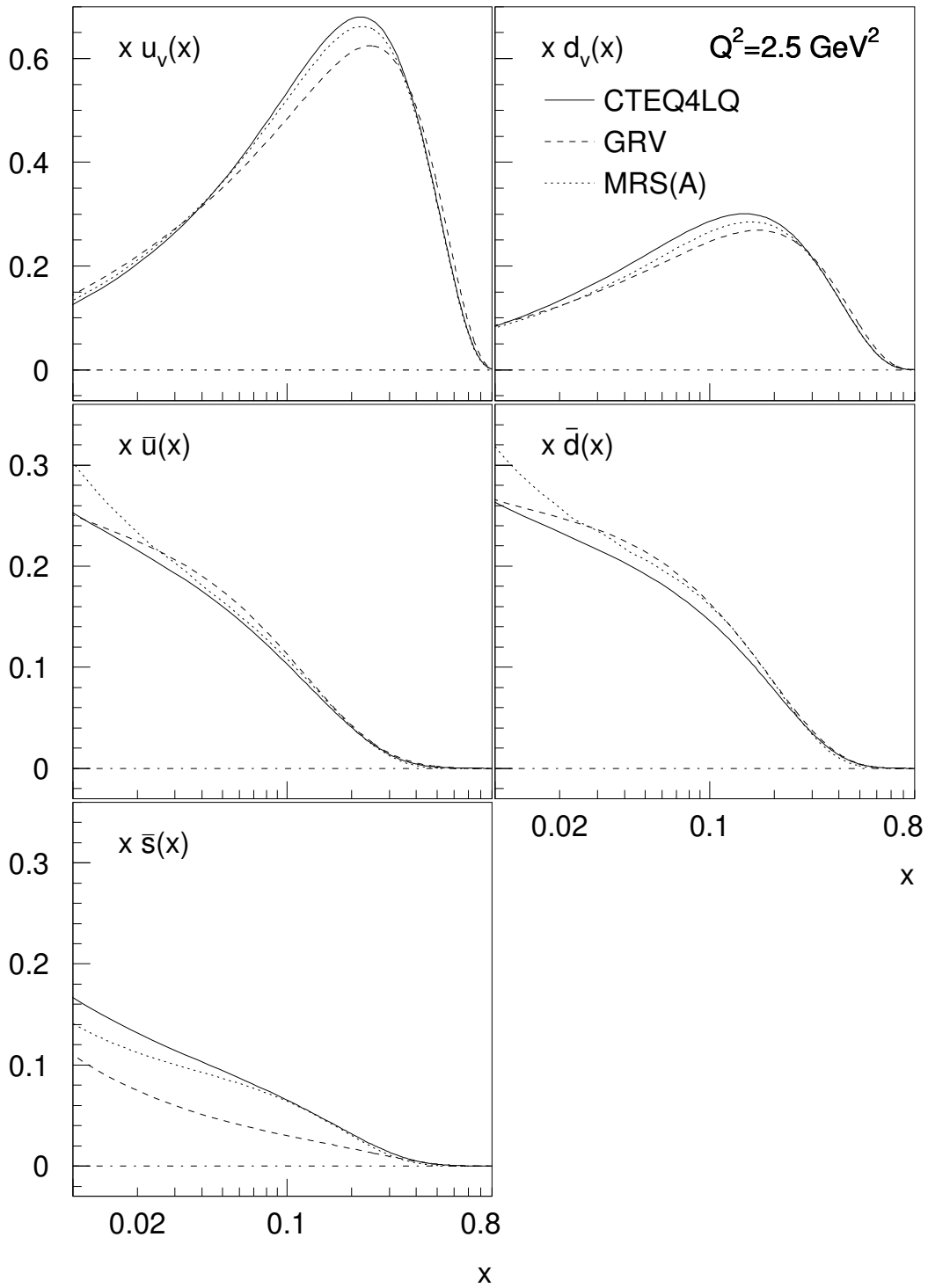

Figure A.1.: Parametrisations of unpolarised valence and sea quark distributions at $Q^2 = 2.5\,\mathrm{GeV}^2$. The different sets of parametrisations correspond to the following publications: *CTEQ4LQ* (NLO) [Lai 97], *GRV* (LO) [Glu 95] and *MRS(A)* (NLO) [Mar 95]. Note the different scales on the vertical axes for valence and sea quark distributions.

Following Eq. (2.56) for g_1 and Eqs. (A.11) and (A.12), the inclusive asymmetry A_1 is given as a function of the polarised quark distributions Δq_f and unpolarised quark distributions $\tilde{q}_f$ by

$$A_1(x,Q^2) = \left[\frac{1+R(x,Q^2)}{1+\gamma^2}\right] \frac{\sum_f e_f^2\, \Delta q_f(x,Q^2)}{\sum_f e_f^2\, \tilde{q}_f(x,Q^2)}\,. \tag{A.13}$$

The unpolarised quark distributions $\tilde{q}_f$ are simply called q_f in Eq. (5.1) and everywhere else in this text except for this section and section A.4. The distributions q_f as defined by F_1 in Eq. (2.55) are related to $\tilde{q}_f$ by $q_f = \tilde{q}_f\ (1+\gamma^2)/(1+R)$. Relation (A.13), which was derived for the inclusive asymmetry A_1, applies in the same way to the semi-inclusive hadron asymmetries A_1^h. The quark polarisations extracted in this analysis correspond to the ratio $\Delta q_f/\tilde{q}_f$. In terms of Δq_f and $\tilde{q}_f$ the positivity limit $|A_1| \leq 1$ writes[1] $|\Delta q_f/\tilde{q}_f| \leq (1+\gamma^2)/(1+R)$.

The correction factor $(1+R)/(1+\gamma^2)$ is given in table B.1 at the average value of x and Q^2 of each x-bin. It decreases from $1.34\ (1.34)$ at $x = 0.033$ to $0.97\ (1.00)$ at $x = 0.46$ for the inclusive (semi-inclusive) asymmetries. Consequently, $\tilde{q}_f \approx 1.34\ q_f$ at the lowest value of x while $\tilde{q}_f \approx q_f$ at the highest x-value.

Fig. A.1 compares different parametrisations of unpolarised valence and sea quark distributions which correspond to the following publications: *CTEQ4LQ* (NLO) [Lai 97], *GRV* (LO) [Glu 95] and *MRS(A)* (NLO) [Mar 95]. Despite of the fact that the *CTEQ4LQ* parametrisation is NLO, it was prefered to the LO *GRV* parametrisation because it is superior to *GRV* in describing the F_2 data in the relatively low Q^2-range of the HERMES experiment. The difference of both parametrisations was included in the systematic error of the extracted quark polarisations.

A.4. Parametrisations of polarised quark distributions

In Fig. 5.6 the measured polarised quark distributions are compared to the LO parametrisations from *De Florian et al.* ($0.1 < \Delta g < 0.8$, LO) [Flo 98], *Gehrmann and Stirling* (Gluon A, LO) [Ger 96] and *Glück et al.* (Standard Scenario, LO) [Glu 96]. This section outlines the corrections which have to be applied to these parametrisations to allow a direct comparison with the results presented in this analysis.

The parametrisations of polarised quark distributions were obtained from fits to the measured spin asymmetries A_1 or spin structure functions g_1. In these fits, constraints were imposed on the first moments of the spin distributions to fulfil the Bjørken sum rule

[1] For the extraction of polarised quark distributions the SMC Collaboration used the *GRV* LO parametrisation for the unpolarised quark distributions. However, they assumed that $A_2 = 0$ instead of $g_2 = 0$. Assuming $A_2 = 0$ the $(1+\gamma^2)$ factor does not appear in Eq. (A.13) since in this case $A_1 = (1+\gamma^2)\, g_1/F_1$ (instead of $A_1 = g_1/F_1$ for $g_2 = 0$) so that the $1+\gamma^2$ factor cancels.

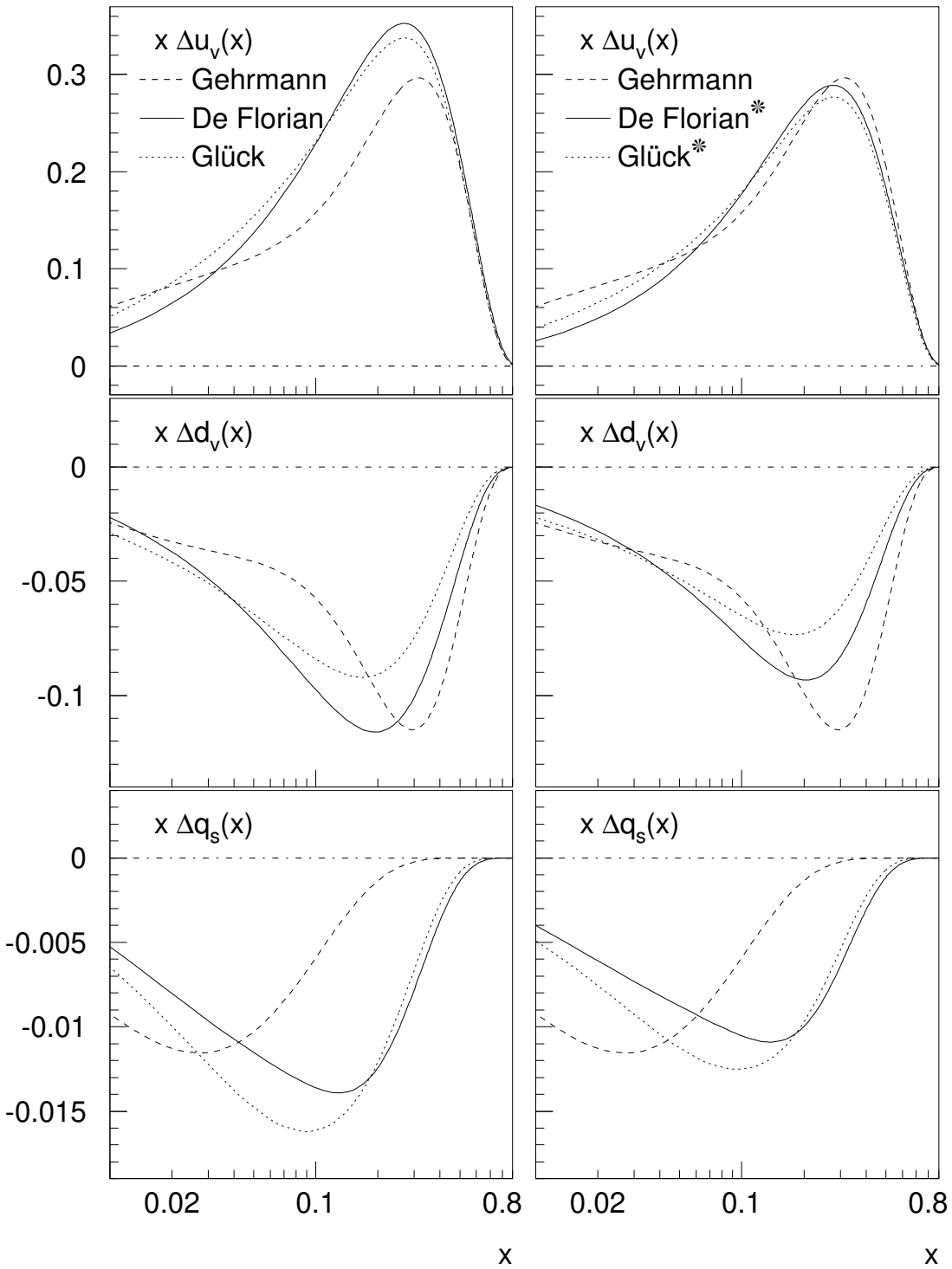

Figure A.2.: LO parametrisations of $x\Delta u_{\mathrm{v}}(x)$, $x\Delta d_{\mathrm{v}}(x)$ and $x\Delta q_{\mathrm{s}}(x)$ at $Q^2 = 2.5\,\mathrm{GeV}^2$. (See text for references.) The left-hand figures show the published distributions. The right-hand figures show the parametrisations *Glück** and *De Florian** which were corrected by $(1+R)$ to allow a direct comparison with *Gehrmann*. All sea quark distributions are SU(3)$_f$ symmetric.

$\Delta q_3(Q^2) = |g_A/g_V|\ \Delta C^{NS}(Q^2)$ and the relation $\Delta q_8(Q^2) = (3F-D)\ \Delta C^{NS}(Q^2)$ which is based on the assumption of SU(3)$_f$ symmetry.

The LO parametrisations introduced above can be subdivided in two classes. The first class, represented by *Glück* and *De Florian*, obtained $\Delta q_f(x,Q^2)$ from a fit of the expression

$$A_1(x,Q^2) \simeq \frac{1}{1+\gamma^2}\ \frac{\sum_f\ e_f^2\ \Delta q_f(x,Q^2)}{\sum_f\ e_f^2\ \tilde{q}_f(x,Q^2)} \tag{A.14}$$

to the measured asymmetries $A_1(x,Q^2)$. In these fits, the LO *GRV* parametrisation was used as input for the unpolarised distributions $\tilde{q}_f$ which were extracted in the way described in the previous section. It follows from the comparison of Eq. (A.14) with Eq. (A.13) that the *Glück* and *De Florian* parametrisations of Δq_f have to be divided by $(1+R)$ to allow a direct comparison with the results of this analysis.

The second class of parametrisations is represented by the one from *Gehrmann* who fits the expression

$$g_1(x,Q^2) = \frac{1}{2}\sum_f\ e_f^2\ \Delta q_f(x,Q^2) \tag{A.15}$$

to the measured values of $g_1(x,Q^2)$. In the analyses from experimental data g_1 is usually derived from the measured A_1 according to $g_1 \simeq A_1 F_1$ with $F_1 = (1+\gamma^2)F_2/\left[2x(1+R)\right]$. It follows that

$$A_1(x,Q^2) \simeq \left[\frac{1+R(x,Q^2)}{1+\gamma^2}\right]\ \frac{2x\ g_1(x,Q^2)}{F_2(x,Q^2)} = \left[\frac{1+R(x,Q^2)}{1+\gamma^2}\right]\ \frac{\sum_f e_f^2\ \Delta q_f(x,Q^2)}{\sum_f e_f^2\ \tilde{q}_f(x,Q^2)}\,, \tag{A.16}$$

which is consistent with Eq. (A.13). Consequently, the *Gehrmann* parametrisation can be directly compared to the polarised quark distributions extracted in this analysis.

Fig. A.2 displays the LO polarised quark distributions from *Glück*, *De Florian* and *Gehrmann*. The figure shows both the published and the corrected *Glück* and *De Florian* distributions. The latter were obtained from the published ones by dividing by $(1+R)$. All parametrisations shown in the figure are characterised by SU(3)$_f$ symmetric sea distributions, i.e. $\Delta q_s \equiv \Delta u_s = \Delta d_s = \Delta s = \Delta\bar{u} = \Delta\bar{d} = \Delta\bar{s}$.

A.5. Construction of the covariance matrix $\mathcal{V}_A$

The statistical covariance $\mathcal{V}(A_i,A_j)$ of two types of asymmetries A_i and A_j is defined as

$$\mathcal{V}(A_i,A_j) \ \equiv\ \langle\ (A_i - \langle A_i\rangle)\ (A_j - \langle A_j\rangle)\ \rangle\,, \tag{A.17}$$

where the symbol $\langle f\rangle$ denotes the expectation value of the quantity f.

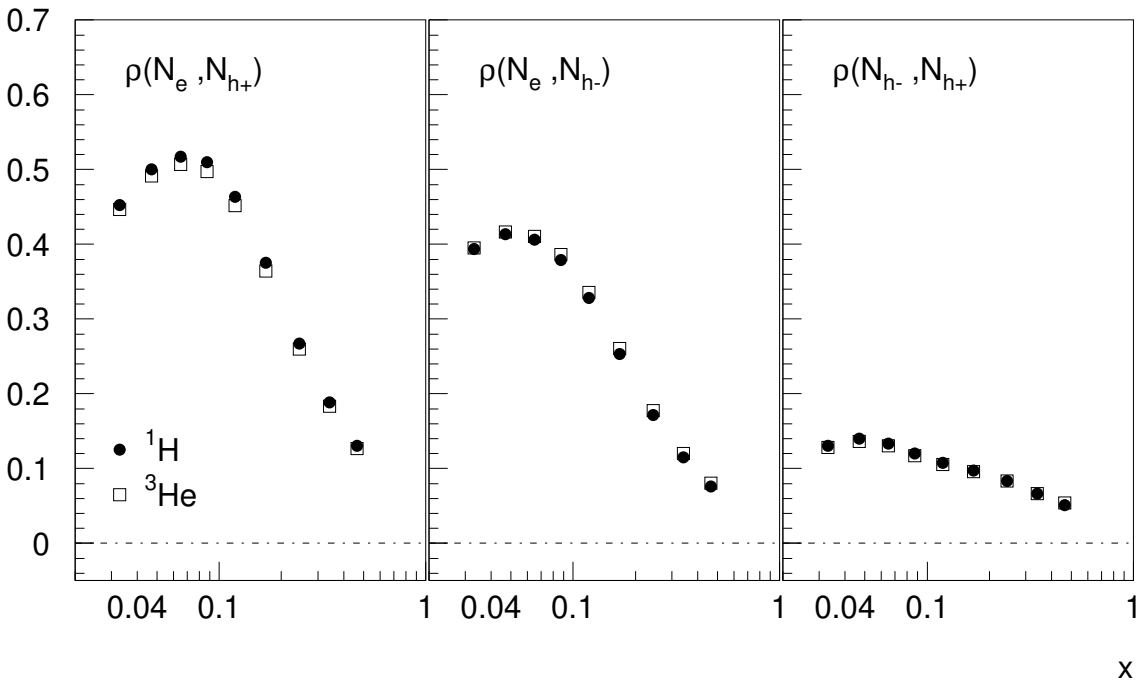

Figure A.3.: Correlation coefficients ρ of count rates for inclusive and semi-inclusive DIS events for a proton and ^{3}He target.

The covariances $\mathcal{V}(A_i, A_j)$ of the different types of asymmetries can be related to the covariances $\mathcal{V}(N_i, N_j)$ of the respective particle count rates by

$$\begin{aligned}
\mathcal{V}(A_i, A_j) &= \sum_{\mu,\nu} \frac{\partial A_i}{\partial N_\mu} \frac{\partial A_j}{\partial N_\nu} \, \mathcal{V}(N_\mu, N_\nu) \\
&= \frac{\partial A_i}{\partial N_{i^+}} \frac{\partial A_j}{\partial N_{j^+}} \, \mathcal{V}(N_{i^+}, N_{j^+}) + \frac{\partial A_i}{\partial N_{i^-}} \frac{\partial A_j}{\partial N_{j^-}} \, \mathcal{V}(N_{i^-}, N_{j^-}) \\
&\simeq \frac{1}{2} \left[\frac{\partial A_i}{\partial N_{i^+}} \frac{\partial A_j}{\partial N_{j^+}} + \frac{\partial A_i}{\partial N_{i^-}} \frac{\partial A_j}{\partial N_{j^-}} \right] \, \mathcal{V}(N_i, N_j) \\
&\simeq \frac{\partial A_i}{\partial N_{i^\pm}} \frac{\partial A_j}{\partial N_{j^\pm}} \, \mathcal{V}(N_i, N_j), \qquad \text{(A.18)}
\end{aligned}$$

where Greek indices run over both spin states. In Eq. (A.18) it was made use of the fact that the asymmetry A_i for a given particle type only depends on the count rates for this particle in both spin states (denoted as N_{i^+} and N_{i^-}) and that the two spin states are statistically uncorrelated ($\mathcal{V}(N_{j^+}, N_{i^-}) = 0$). Furthermore, the approximations $N_{i^\pm} \simeq N_i/2$ and consequently $|\partial A_i/\partial N_{i^+}| \simeq |\partial A_i/\partial N_{i^-}|$ were used. Under the same assumptions the errors of the asymmetries become $\sigma_{A_i} = |\partial A_i/\partial N_{i^\pm}| \, \sigma_{N_i}$ and hence

$$\mathcal{V}(A_i, A_j) \simeq \frac{\sigma_{A_i} \, \sigma_{A_j}}{\sigma_{N_i} \, \sigma_{N_j}} \, \mathcal{V}(N_i, N_j), \qquad \text{(A.19)}$$

so that the correlations $\rho(A_i, A_j) \equiv \mathcal{V}(A_i, A_j)/(\sigma_{A_i} \, \sigma_{A_j})$ of the different types of asym-

Table A.1.: Correlation coefficients ρ of count rates for inclusive and semi-inclusive DIS events for a proton and ^{3}He target [Tip 99].

	Proton			**Helium-3**		
x	$\rho(N_e, N_{h^+})$	$\rho(N_e, N_{h^-})$	$\rho(N_{h^-}, N_{h^+})$	$\rho(N_e, N_{h^+})$	$\rho(N_e, N_{h^-})$	$\rho(N_{h^-}, N_{h^+})$
0.033	0.452	0.394	0.130	0.446	0.395	0.128
0.047	0.500	0.414	0.140	0.492	0.417	0.137
0.065	0.517	0.406	0.134	0.507	0.411	0.130
0.087	0.509	0.379	0.120	0.497	0.386	0.118
0.119	0.464	0.328	0.107	0.451	0.336	0.105
0.168	0.375	0.253	0.098	0.364	0.260	0.096
0.245	0.267	0.171	0.083	0.260	0.177	0.083
0.342	0.188	0.115	0.067	0.183	0.120	0.067
0.465	0.130	0.076	0.051	0.127	0.081	0.054

metries equal the correlations $\rho(N_i, N_j) \equiv \mathcal{V}(N_i, N_j)/(\sigma_{N_i}\,\sigma_{N_j})$ of the respective particle count rates:

$$\rho(A_i, A_j) \;\simeq\; \rho(N_i, N_j)\,. \tag{A.20}$$

The correlations $\rho(N_i, N_j)$ are shown in Fig. A.3 and are given in table A.1 for the count rates of inclusive and semi-inclusive DIS events. They were calculated from the measured hadron multiplicities $\langle n_h\rangle = \langle N_h\rangle/\langle N_e\rangle$ according to [Tip 99]

$$\rho(N_e, N_h) \;=\; \frac{\langle n_h\rangle}{\sqrt{\langle n_h^2\rangle}}\,, \tag{A.21}$$

$$\rho(N_{h_1}, N_{h_2}) \;=\; \frac{\langle n_{h_1}\, n_{h_2}\rangle}{\sqrt{\langle n_{h_1}^2\rangle\langle n_{h_2}^2\rangle}}\,. \tag{A.22}$$

In addition, the asymmetry correlations $\rho(A_i, A_j)$ have been determined directly from PEPSI by generating a random sample of about 500 inclusive and semi-inclusive asymmetries on both targets, each based on $5 \cdot 10^5$ DIS events per spin state. The correlations $\rho(A_i, A_j)$ extracted from the generated asymmetries are found to be in agreement with the correlations $\rho(N_i, N_j)$ of the particle count rates. However, the statistical error[2] of $\rho(A_i, A_j)$ was significantly larger than the error of $\rho(N_i, N_j)$ so that the covariance matrix $\mathcal{V}_{\boldsymbol{A}}$ was constructed from the covariances of the particle numbers using Eq. (A.20).

A.6. Systematic error calculation

This section describes the calculation of the systematic error of the extracted quark polarisations due to the systematic uncertainties of the measured asymmetries. The systematic

[2]The statistical error of the correlation coefficient $\rho(A_i, A_j)$ decreases with the number M of asymmetries like $1/\sqrt{M}$.

uncertainties of the asymmetries were discussed in section 4.6.1. The systematic error of the extracted quark polarisations $\Delta q_f/q_f$ due to the systematic error of the asymmetries is calculated using the techniques of the covariance matrix [Bar 89], where a covariance matrix $\mathcal{V}^{\mathrm{SYS}}_{\boldsymbol{A}_\mathrm{m}}$ is constructed which contains the systematic error of the asymmetry vector $\boldsymbol{A}_\mathrm{m}$. This covariance matrix is then added to the covariance matrix $\mathcal{V}^{\mathrm{STAT}}_{\boldsymbol{A}_\mathrm{m}}$ which contains the statistical covariances of $\boldsymbol{A}_\mathrm{m}$:

$$\mathcal{V}^{\mathrm{TOT}}_{\boldsymbol{A}_\mathrm{m}} = \mathcal{V}^{\mathrm{SYS}}_{\boldsymbol{A}_\mathrm{m}} + \mathcal{V}^{\mathrm{STAT}}_{\boldsymbol{A}_\mathrm{m}} \,, \tag{A.23}$$

and Eq. (5.6) is solved using the full covariance matrix given by Eq. (A.23). The systematic error σ_{SYS} of the quark polarisations is defined by

$$\sigma_{\mathrm{SYS}} = \sqrt{\sigma^2_{\mathrm{TOT}} - \sigma^2_{\mathrm{STAT}}} \,, \tag{A.24}$$

where σ_{TOT} is the error of the extracted quark polarisations using the full covariance matrix $\mathcal{V}^{\mathrm{TOT}}_{\boldsymbol{A}_\mathrm{m}}$, and σ_{STAT} is the error obtained for $\mathcal{V}^{\mathrm{STAT}}_{\boldsymbol{A}_\mathrm{m}}$. In the following the construction of $\mathcal{V}^{\mathrm{SYS},i}_{\boldsymbol{A}_\mathrm{m}}$ for each systematic error source i is discussed. The full covariance matrix is then obtained from the sum $\mathcal{V}^{\mathrm{SYS}}_{\boldsymbol{A}_\mathrm{m}} = \sum_i \mathcal{V}^{\mathrm{SYS},i}_{\boldsymbol{A}_\mathrm{m}}$.

Beam polarisation The contribution of the fractional beam polarisation error to the covariance matrix $\mathcal{V}^{\mathrm{SYS}}_{\boldsymbol{A}_\mathrm{m}}$ was calculated by[3]

$$\left[\mathcal{V}^{p_\mathrm{B}}\right]_{ij} = \left[\left(\frac{\delta p_\mathrm{B}}{p_\mathrm{B}}\right)^2_{\mathrm{RISE}} + \left[\rho^{p_\mathrm{B}}\right]_{ij} \left(\frac{\delta p_\mathrm{B}}{p_\mathrm{B}}\right)_{\mathrm{COR},i} \left(\frac{\delta p_\mathrm{B}}{p_\mathrm{B}}\right)_{\mathrm{COR},j} \right] A_j \, A_j \,, \tag{A.25}$$

where the correlation coefficient $\left[\rho^{p_\mathrm{B}}\right]_{ij}$ was taken to be one for asymmetries of the same year and zero for asymmetries of different years. Here, $(\delta p_\mathrm{B}/p_\mathrm{B})_{\mathrm{RISE}}$ denotes the systematic error obtained from the rise time calibration of the polarimeter and $(\delta p_\mathrm{B}/p_\mathrm{B})_{\mathrm{COR}}$ refers to the systematic error due to the corrections which are applied to the measured raw polarisation. The values of $(\delta p_\mathrm{B}/p_\mathrm{B})_{\mathrm{COR}}$ are given for each year of data taking in section 4.6.1.

Target polarisation The fractional systematic error of the target polarisation was given in section 4.6.1 for each year of data taking. Its contribution to the covariance matrix can be written as

$$\left[\mathcal{V}^{p_\mathrm{T}}\right]_{ij} = \left[\rho^{p_\mathrm{T}}\right]_{ij} \left(\frac{\delta p_\mathrm{T}}{p_\mathrm{T}}\right)_i \left(\frac{\delta p_\mathrm{T}}{p_\mathrm{T}}\right)_j A_i \, A_j \,, \tag{A.26}$$

where $\left[\rho^{p_\mathrm{T}}\right]_{ij}$ is one for asymmetries of the same target and zero for different targets.

[3] To reduce the number of subscripts, in this section the notation A is used for the photon-nucleon asymmetry A_1. The symbol $\left[\mathcal{V}^{p_\mathrm{B}}\right]_{ij} \equiv \left[\mathcal{V}^{\mathrm{SYS},p_\mathrm{B}}_{\boldsymbol{A}_\mathrm{m}}\right]_{ij}$ refers to the element of the covariance matrix $\mathcal{V}^{\mathrm{SYS},p_\mathrm{B}}_{\boldsymbol{A}_\mathrm{m}}$ in row i and column j, where the indices i and j run from 1 to 9.

Cross section ratio R There are two contributions from R to the systematic error of the quark polarisations. The first one arises from the depolarisation factor D which depends on R and the second one from the $(1 + R)$ factor in Eq. (5.1). It follows from Eqs. (2.33), (4.23) and (5.1) that $\delta A_1/A_1 = \delta R\ (1 - \varepsilon)/[(1 + R)(1 + \varepsilon R)]$. The contribution to the covariance matrix then writes

$$\left[\mathcal{V}^R\right]_{ij} = \left[\frac{1-\varepsilon}{(1+R)(1+\varepsilon R)}\,\delta R\right]^2 A_i\, A_j\,, \tag{A.27}$$

where both R and δR were taken from [Whi 90].

Yield Fluctuations The systematic uncertainties of the inclusive and semi-inclusive helium asymmetries due to the yield fluctuations observed for the 1995 data were discussed in section 4.6.1. They were included into the helium part of the covariance matrix according to

$$\left[\mathcal{V}^{\mathrm{YIELD}}\right]_{ij} = [\delta A_i]^{\mathrm{YIELD}}\ [\delta A_j]^{\mathrm{YIELD}}\ . \tag{A.28}$$

Radiative corrections The systematic error $\delta(\Delta A_{\parallel}^{\mathrm{RC}})$ of the radiative correction term $\Delta A_{\parallel}^{\mathrm{RC}}$ is given in table 4.3 for the inclusive proton and the helium asymmetries. It was included into the covariance matrix according to

$$\left[\mathcal{V}^{\mathrm{RC}}\right]_{ij} = \left[\rho^{\mathrm{RC}}\right]_{ij}\ \delta(\Delta A_i^{\mathrm{RC}})\ \delta(\Delta A_j^{\mathrm{RC}})\,, \tag{A.29}$$

where $\delta(\Delta A^{\mathrm{RC}}) = \delta(\Delta A_{\parallel}^{\mathrm{RC}})/[D(1 + \eta\gamma)]$ and $\left[\rho^{\mathrm{RC}}\right]_{ij}$ is one for inclusive asymmetries of the same target and zero otherwise.

Smearing corrections Smearing corrections were applied to the proton asymmetries. For the smearing corrections the statistical uncertainty $\delta\eta_{\mathrm{SM}}$ of the correction factor η_{SM} was used as its systematic error. The systematic errors of the smearing correction factors were included into the proton part of the covariance matrix according to

$$\left[\mathcal{V}^{\mathrm{SM}}\right]_{ij} = \left[\rho^{\mathrm{SM}}\right]_{ij}\ \delta\eta_{\mathrm{SM}}^i A_i\ \delta\eta_{\mathrm{SM}}^j A_j\,, \tag{A.30}$$

where $\left[\rho^{\mathrm{SM}}\right]_{ij}$ is one for proton asymmetries which were obtained from the same reconstruction method (1996: NOVC, 1997: STD) and zero otherwise.

Spin structure function g_2 The systematic error $\delta(g_1/F_1)^{g_2}$ of the structure function ratio g_1/F_1 due to the experimental uncertainty of g_2 was discussed in section 4.6.1. The uncertainty of g_2 is the only systematic error source which contributes differently to the systematic error of A_1 and g_1/F_1. As discussed in section 4.6.1 it is the systematic of g_1/F_1 and not A_1 which determines the systematic error of the quark polarisations. The contribution of the uncertainty in g_2 to the covariance matrix is given by

$$\left[\mathcal{V}^{g2}\right]_{ij} = [\rho^{g_2}]_{ij}\ \delta(g_1/F_1)_i^{g_2}\ \delta(g_1/F_1)_j^{g_2}\,, \tag{A.31}$$

where $\left[\rho^{g_2}\right]_{ij}$ is one for asymmetries of the same target and zero otherwise.

A.7. QCD corrections

In this section numerical values are derived for the first moments of the singlet and non-singlet coefficient functions $\Delta C^{\rm S}(Q^2)$ and $\Delta C^{\rm NS}(Q^2)$ at $Q^2 = 2.5\,{\rm GeV}^2$. The coefficient functions were used to calculate the Bjørken sum rule prediction for Δq_3 and the SU(3)$_f$ prediction for Δq_8 at the HERMES scale. Furthermore, the correction factors were used to evolve the values for $\Delta u + \Delta\bar{u}$, $\Delta d + \Delta\bar{d}$ and $\Delta s + \Delta\bar{s}$ given in Ref. [Ell 96] to the scale of $Q^2 = 2.5\,{\rm GeV}^2$.

The scale dependence of the strong coupling constant is controlled by the renormalisation-group equation [Cas 98]

$$Q^2\frac{\partial}{\partial Q^2}\alpha_{\rm s}(Q^2) = -\frac{\beta_0}{2\pi}\alpha_{\rm s}^2(Q^2) - \frac{\beta_1}{4\pi^2}\alpha_{\rm s}^3(Q^2) - \frac{\beta_2}{64\pi^3}\alpha_{\rm s}^4(Q^2) - \ldots\,, \tag{A.32}$$

where

$$\begin{aligned}\beta_0 &= 11 - \frac{2}{3}n_f\,,\\ \beta_1 &= 51 - \frac{19}{3}n_f\,,\\ \beta_2 &= 2857 - \frac{5033}{9}n_f + \frac{325}{27}n_f^2\,,\end{aligned} \tag{A.33}$$

and n_f is the number of quarks with mass less than the energy scale Q^2. When solving the differential equation (A.32) for $\alpha_{\rm s}(Q^2)$ the dimensional scale parameter Λ is introduced as a constant of integration. Taking into account terms up to order $\alpha_{\rm s}^4$ in Eq. (A.32) the scale dependence of the strong coupling constant reads[4]

$$\begin{aligned}\alpha_{\rm s}(Q^2) &= \frac{4\pi}{\beta_0\ln(Q^2/\Lambda^2)}\\ &\times\left\{1 - \frac{2\beta_1}{\beta_0^2}\frac{\ln\left[\ln(Q^2/\Lambda^2)\right]}{\ln(Q^2/\Lambda^2)} + \frac{4\beta_1^2}{\beta_0^4\ln^2(Q^2/\Lambda^2)}\left[\left(\ln\left[\ln(Q^2/\Lambda^2)\right] - \frac{1}{2}\right)^2 + \frac{\beta_2\beta_0}{8\beta_1^2} - \frac{5}{4}\right]\right\}.\end{aligned} \tag{A.34}$$

For $n_f = 4$ the combined deep inelastic scattering data on the scale dependence of α_s yield $\Lambda_{\overline{\rm MS}}^{(n_f=4)} = 305 \pm 56$ MeV in the $\overline{\rm MS}$ renormalisation scheme which corresponds to $\alpha_s^{(5)}(m_Z) = 0.117 \pm 0.004$ [Cas 98]. Throughout this work $n_f = 3$ is used as relevant for the Q^2-range of the HERMES experiment [Ell 96]. The procedure to calculate $\Lambda_{\overline{\rm MS}}^{(3)}$ from $\Lambda_{\overline{\rm MS}}^{(4)}$ is described in [Mar 84] where the following approximate relationship is derived

$$\Lambda_{\overline{\rm MS}}^{(3)} \simeq \Lambda_{\overline{\rm MS}}^{(4)}\left(\frac{m_c}{\Lambda_{\overline{\rm MS}}^{(4)}}\right)^{2/27}\left[\ln\left(\frac{m_c}{\Lambda_{\overline{\rm MS}}^{(4)}}\right)^2\right]^{107/2025}. \tag{A.35}$$

[4] The expression (2.45) for $\alpha_s(Q^2)$ corresponds to the solution of Eq. (A.32) for $\beta_i = 0$ for $i \geq 1$.

For a charm quark mass $m_c = 1.25 \pm 0.15$ GeV [Cas 98] the result for $\Lambda^{(3)}_{\overline{\rm MS}}$ is 358 ± 66 MeV and thus $\Lambda^{(3)}_{\overline{\rm MS}}/\Lambda^{(4)}_{\overline{\rm MS}} \simeq 1.17$. With this value for $\Lambda^{(3)}_{\overline{\rm MS}}$ it follows[5] from Eq. (A.34)

$$\alpha_{\rm s}^{(3)}(2.5\ {\rm GeV}^2) = 0.351 \pm 0.040 \tag{A.36}$$

which corresponds to $\alpha_{\rm s}^{(3)}(m_Z) = 0.107 \pm 0.003$.

For $n_f = 3$ the first moments of the non-singlet and singlet coefficient functions are given by Eqs. (2.61) and (2.62). For $\alpha_{\rm s}^{(3)} = 0.351 \pm 0.040$ the numerical results are

$$\Delta C^{\rm S}(2.5\ {\rm GeV}^2) = 0.869 \pm 0.018\ , \tag{A.37}$$

$$\Delta C^{\rm NS}(2.5\ {\rm GeV}^2) = 0.795 \pm 0.045\ , \tag{A.38}$$

where the error of $\Delta C^{\rm S}$ and $\Delta C^{\rm NS}$ was calculated from the error of $\alpha_{\rm s}^{(3)}$.

In the analysis from Ref. [Ell 96], which is based on the assumption of SU(3)$_f$ symmetry, predictions are made for the first moments of the polarised quark distributions

$$\begin{aligned} \Delta u + \Delta\bar{u} &= 0.82 \pm 0.03\ , \\ \Delta d + \Delta\bar{d} &= -0.44 \pm 0.03\ , \\ \Delta s + \Delta\bar{s} &= -0.11 \pm 0.03\ , \end{aligned} \tag{A.39}$$

which refer to an evolution scale of $Q^2 = \infty$. These values were derived from $\Delta\Sigma(\infty) = 0.27$, $\Delta q_3(\infty) = |g_{\rm A}/g_{\rm V}|$ and $\Delta q_8(\infty) = 3F - D$. When the values for $\Delta\Sigma$, Δq_3 and Δq_8 are evolved to $Q^2 = 2.5$ GeV^2 according to

$$\begin{aligned} \Delta\Sigma(2.5\ {\rm GeV}^2) &= \Delta\Sigma(\infty)\ \Delta C^{\rm S}\ \ (2.5\ {\rm GeV}^2)\ , \\ \Delta q_3(2.5\ {\rm GeV}^2) &= \Delta q_3(\infty)\ \Delta C^{\rm NS}(2.5\ {\rm GeV}^2)\ , \\ \Delta q_8(2.5\ {\rm GeV}^2) &= \Delta q_8(\infty)\ \Delta C^{\rm NS}(2.5\ {\rm GeV}^2)\ , \end{aligned} \tag{A.40}$$

the results for the first moments of the polarised quark distributions at $Q^2 = 2.5$ GeV^2 are

$$\Delta u + \Delta\bar{u} = 0.66 \pm 0.03\ , \tag{A.41}$$

$$\Delta d + \Delta\bar{d} = -0.35 \pm 0.03\ , \tag{A.42}$$

$$\Delta s + \Delta\bar{s} = -0.08 \pm 0.02\ , \tag{A.43}$$

and $\Delta\Sigma = 0.23 \pm 0.04$. Furthermore, using Eq. (A.38), the value for the Bjørken sum rule prediction at $Q^2 = 2.5$ GeV^2 is

$$\Delta q_3(2.5\ {\rm GeV}^2) = \left|\frac{g_{\rm A}}{g_{\rm V}}\right|\ \Delta C^{\rm NS}(2.5\ {\rm GeV}^2) = 1.00 \pm 0.06 \tag{A.44}$$

and the SU(3)$_f$ prediction for Δq_8 becomes

$$\Delta q_8(2.5\ {\rm GeV}^2) = (3F - D)\ \Delta C^{\rm NS}(2.5\ {\rm GeV}^2) = 0.46 \pm 0.04\ . \tag{A.45}$$

[5] For $n_f = 4$ one obtains $\alpha_{\rm s}^{(4)}(2.5\ {\rm GeV}^2) = 0.347 \pm 0.035$ and $\alpha_{\rm s}^{(4)}(m_Z) = 0.114 \pm 0.004$.

B. Tables of results

Table B.1.: Kinematical factors on the proton target and R-parametrisation. For each x-bin the table shows the mean value of x and Q^2 for inclusive and semi-inclusive DIS events averaged over both spin states. The values of $R(x, Q^2)$ were taken from the parametrisation of [Whi 90]. The kinematical factors ε, η, γ, and D shown in the table were calculated from the mean values of x, Q^2 and R (where necessary).

Bin	x	Q^2	ε	η	γ	D	R	$1/(1+\eta\gamma)$	$(1+R)/(1+\gamma^2)$
Inclusive DIS events									
1	0.033	1.212	0.534	0.025	0.056	0.715	0.341	0.999	1.336
2	0.047	1.467	0.684	0.041	0.073	0.593	0.334	0.997	1.327
3	0.065	1.717	0.788	0.061	0.093	0.490	0.323	0.994	1.312
4	0.087	1.991	0.849	0.083	0.116	0.417	0.308	0.991	1.291
5	0.119	2.303	0.897	0.113	0.147	0.349	0.287	0.984	1.259
6	0.168	2.660	0.934	0.157	0.193	0.285	0.250	0.971	1.205
7	0.245	3.056	0.961	0.225	0.263	0.227	0.202	0.944	1.124
8	0.342	3.743	0.969	0.289	0.332	0.204	0.158	0.913	1.044
9	0.465	5.164	0.967	0.332	0.384	0.216	0.116	0.887	0.973
Semi-inclusive DIS events with positively charged hadrons									
1	0.033	1.207	0.538	0.025	0.056	0.712	0.341	0.999	1.336
2	0.047	1.455	0.690	0.042	0.073	0.587	0.335	0.997	1.327
3	0.065	1.752	0.777	0.059	0.092	0.502	0.322	0.995	1.311
4	0.087	2.142	0.820	0.076	0.112	0.456	0.305	0.992	1.289
5	0.118	2.703	0.848	0.096	0.135	0.428	0.275	0.987	1.252
6	0.165	3.672	0.857	0.116	0.162	0.433	0.211	0.982	1.180
7	0.238	5.161	0.864	0.143	0.197	0.444	0.143	0.973	1.100
8	0.339	7.228	0.867	0.172	0.237	0.452	0.098	0.961	1.040
9	0.447	9.749	0.858	0.193	0.269	0.474	0.072	0.951	1.000
Semi-inclusive DIS events with negatively charged hadrons									
1	0.033	1.207	0.538	0.025	0.056	0.712	0.341	0.999	1.336
2	0.047	1.455	0.690	0.042	0.073	0.587	0.335	0.997	1.327
3	0.065	1.752	0.777	0.059	0.092	0.502	0.322	0.995	1.311
4	0.087	2.142	0.820	0.076	0.112	0.456	0.305	0.992	1.289
5	0.118	2.703	0.848	0.096	0.135	0.428	0.275	0.987	1.252
6	0.165	3.672	0.857	0.116	0.162	0.433	0.211	0.982	1.180
7	0.238	5.161	0.864	0.143	0.197	0.444	0.143	0.973	1.100
8	0.339	7.228	0.867	0.172	0.237	0.452	0.098	0.961	1.040
9	0.447	9.749	0.858	0.193	0.269	0.474	0.072	0.951	1.000

Table B.2.: The 1997 proton asymmetries $A_1^{(h)} = A_{||}^{(h)} / [D(1+\eta\gamma)]$.

Bin	x	Q^2	$A_1 \pm$ stat.$\pm$ syst.
1	0.033	1.21	$0.0749 \pm 0.0076 \pm 0.0050$
2	0.047	1.47	$0.1070 \pm 0.0088 \pm 0.0070$
3	0.065	1.72	$0.1160 \pm 0.0097 \pm 0.0090$
4	0.087	1.99	$0.1620 \pm 0.0105 \pm 0.0116$
5	0.119	2.30	$0.1910 \pm 0.0112 \pm 0.0151$
6	0.168	2.66	$0.2520 \pm 0.0140 \pm 0.0211$
7	0.245	3.06	$0.3250 \pm 0.0177 \pm 0.0271$
8	0.342	3.74	$0.4860 \pm 0.0299 \pm 0.0342$
9	0.465	5.16	$0.6400 \pm 0.0415 \pm 0.0449$

Bin	x	Q^2	$A_1^{h^+} \pm$ stat.$\pm$ syst.
1	0.033	1.21	$0.0887 \pm 0.0183 \pm 0.0067$
2	0.047	1.46	$0.1160 \pm 0.0196 \pm 0.0092$
3	0.065	1.75	$0.1330 \pm 0.0196 \pm 0.0112$
4	0.087	2.14	$0.1850 \pm 0.0223 \pm 0.0139$
5	0.118	2.70	$0.2500 \pm 0.0242 \pm 0.0170$
6	0.165	3.67	$0.2580 \pm 0.0286 \pm 0.0235$
7	0.238	5.16	$0.4000 \pm 0.0400 \pm 0.0278$
8	0.339	7.23	$0.4900 \pm 0.0805 \pm 0.0355$
9	0.447	9.75	$0.5560 \pm 0.1640 \pm 0.0468$

Bin	x	Q^2	$A_1^{h^-} \pm$ stat.$\pm$ syst.
1	0.033	1.21	$0.0335 \pm 0.0236 \pm 0.0031$
2	0.047	1.46	$0.0902 \pm 0.0252 \pm 0.0038$
3	0.065	1.75	$0.0672 \pm 0.0265 \pm 0.0049$
4	0.087	2.14	$0.0214 \pm 0.0298 \pm 0.0068$
5	0.118	2.70	$0.1550 \pm 0.0325 \pm 0.0097$
6	0.165	3.67	$0.1660 \pm 0.0408 \pm 0.0147$
7	0.238	5.16	$0.1970 \pm 0.0587 \pm 0.0214$
8	0.339	7.23	$0.6560 \pm 0.1220 \pm 0.0302$
9	0.447	9.75	$0.1200 \pm 0.2490 \pm 0.0448$

Table B.3.: Systematic error of the 1997 proton asymmetries. The table shows the total systematic error of $A_1^{(h)}$ and the contributions from each systematic error source: Target (p_{T}) and beam (p_{B}) polarisation measurements, cross section ratio R (R), radiative corrections (Rad. Corr.), combined acceptance and smearing corrections (Smear. Corr.), yield fluctuations (Yield Fluct.) and structure function g_2 (g_2).

Inclusive asymmetry A_1								
Bin	Total	p_{T}	p_{B}	R	Rad. Corr.	Smear. Corr.	Yield Fluct.	g_2
1	0.0050	0.0033	0.0025	0.0027	0.0001	0.0007	0.0000	0.0006
2	0.0070	0.0044	0.0033	0.0041	0.0000	0.0009	0.0000	0.0011
3	0.0090	0.0057	0.0043	0.0050	0.0000	0.0011	0.0000	0.0018
4	0.0116	0.0073	0.0055	0.0063	0.0000	0.0015	0.0000	0.0028
5	0.0151	0.0097	0.0073	0.0077	0.0000	0.0018	0.0000	0.0043
6	0.0211	0.0130	0.0098	0.0112	0.0000	0.0022	0.0000	0.0069
7	0.0271	0.0168	0.0127	0.0120	0.0001	0.0026	0.0000	0.0119
8	0.0342	0.0200	0.0150	0.0132	0.0001	0.0035	0.0000	0.0189
9	0.0449	0.0225	0.0170	0.0157	0.0001	0.0027	0.0000	0.0310

Semi-inclusive asymmetry $A_1^{h^+}$								
Bin	Total	p_{T}	p_{B}	R	Rad. Corr.	Smear. Corr.	Yield Fluct.	g_2
1	0.0067	0.0044	0.0033	0.0036	0.0000	0.0007	0.0000	0.0006
2	0.0092	0.0058	0.0044	0.0054	0.0000	0.0009	0.0000	0.0011
3	0.0112	0.0072	0.0054	0.0063	0.0000	0.0011	0.0000	0.0018
4	0.0139	0.0090	0.0067	0.0076	0.0000	0.0012	0.0000	0.0028
5	0.0170	0.0111	0.0084	0.0088	0.0000	0.0011	0.0000	0.0043
6	0.0235	0.0147	0.0111	0.0127	0.0000	0.0012	0.0000	0.0069
7	0.0278	0.0174	0.0131	0.0124	0.0000	0.0011	0.0000	0.0119
8	0.0355	0.0212	0.0160	0.0140	0.0000	0.0013	0.0000	0.0189
9	0.0468	0.0244	0.0184	0.0170	0.0000	0.0017	0.0000	0.0310

Semi-inclusive asymmetry $A_1^{h^-}$								
Bin	Total	p_{T}	p_{B}	R	Rad. Corr.	Smear. Corr.	Yield Fluct.	g_2
1	0.0031	0.0020	0.0015	0.0016	0.0000	0.0008	0.0000	0.0006
2	0.0038	0.0023	0.0017	0.0021	0.0000	0.0009	0.0000	0.0011
3	0.0049	0.0029	0.0022	0.0026	0.0000	0.0009	0.0000	0.0018
4	0.0068	0.0040	0.0031	0.0034	0.0000	0.0010	0.0000	0.0028
5	0.0097	0.0058	0.0044	0.0046	0.0000	0.0009	0.0000	0.0043
6	0.0147	0.0085	0.0064	0.0073	0.0000	0.0010	0.0000	0.0069
7	0.0214	0.0123	0.0093	0.0088	0.0000	0.0010	0.0000	0.0119
8	0.0302	0.0166	0.0125	0.0109	0.0000	0.0012	0.0000	0.0189
9	0.0448	0.0225	0.0170	0.0157	0.0000	0.0018	0.0000	0.0310

Table B.4.: The 1996 proton asymmetries $A_1^{(h)} = A_{||}^{(h)} / [D(1+\eta\gamma)]$.

Bin	x	Q^2	$A_1 \pm$ stat.$\pm$ syst.
1	0.033	1.21	$0.0863 \pm 0.0123 \pm 0.0059$
2	0.047	1.47	$0.0967 \pm 0.0146 \pm 0.0082$
3	0.065	1.72	$0.1210 \pm 0.0155 \pm 0.0105$
4	0.087	2.00	$0.1690 \pm 0.0172 \pm 0.0135$
5	0.119	2.31	$0.2140 \pm 0.0187 \pm 0.0177$
6	0.168	2.66	$0.2340 \pm 0.0223 \pm 0.0245$
7	0.244	3.08	$0.3260 \pm 0.0280 \pm 0.0315$
8	0.342	3.77	$0.3750 \pm 0.0483 \pm 0.0391$
9	0.465	5.25	$0.5740 \pm 0.0682 \pm 0.0497$

Bin	x	Q^2	$A_1^{h^+} \pm$ stat.$\pm$ syst.
1	0.033	1.20	$0.0825 \pm 0.0312 \pm 0.0079$
2	0.047	1.45	$0.0999 \pm 0.0318 \pm 0.0107$
3	0.065	1.75	$0.1490 \pm 0.0336 \pm 0.0132$
4	0.087	2.14	$0.1720 \pm 0.0363 \pm 0.0163$
5	0.118	2.72	$0.2510 \pm 0.0384 \pm 0.0200$
6	0.166	3.68	$0.2270 \pm 0.0469 \pm 0.0273$
7	0.239	5.18	$0.4800 \pm 0.0635 \pm 0.0323$
8	0.338	7.26	$0.2340 \pm 0.1300 \pm 0.0408$
9	0.449	9.81	$0.8910 \pm 0.2610 \pm 0.0521$

Bin	x	Q^2	$A_1^{h^-} \pm$ stat.$\pm$ syst.
1	0.033	1.20	$0.0905 \pm 0.0394 \pm 0.0036$
2	0.047	1.45	$0.1060 \pm 0.0415 \pm 0.0043$
3	0.065	1.75	$0.0644 \pm 0.0426 \pm 0.0056$
4	0.087	2.14	$0.1650 \pm 0.0485 \pm 0.0078$
5	0.118	2.72	$0.2560 \pm 0.0523 \pm 0.0111$
6	0.166	3.68	$0.2840 \pm 0.0679 \pm 0.0167$
7	0.239	5.18	$0.2760 \pm 0.0929 \pm 0.0244$
8	0.338	7.26	$0.4380 \pm 0.1970 \pm 0.0340$
9	0.449	9.81	$0.1080 \pm 0.4130 \pm 0.0496$

Table B.5.: Systematic error of the 1996 proton asymmetries. The table shows the total systematic error of $A_1^{(h)}$ and the contributions from each systematic error source: Target (p_{T}) and beam (p_{B}) polarisation measurements, cross section ratio R (R), radiative corrections (Rad. Corr.), combined acceptance and smearing corrections (Smear. Corr.), yield fluctuations (Yield Fluct.) and structure function g_2 (g_2).

Inclusive asymmetry A_1								
Bin	Total	p_{T}	p_{B}	R	Rad. Corr.	Smear. Corr.	Yield Fluct.	g_2
1	0.0059	0.0046	0.0025	0.0027	0.0001	0.0007	0.0000	0.0006
2	0.0082	0.0061	0.0033	0.0041	0.0000	0.0009	0.0000	0.0011
3	0.0105	0.0079	0.0043	0.0050	0.0000	0.0011	0.0000	0.0018
4	0.0135	0.0101	0.0055	0.0063	0.0000	0.0015	0.0000	0.0028
5	0.0177	0.0134	0.0073	0.0077	0.0000	0.0018	0.0000	0.0043
6	0.0245	0.0180	0.0098	0.0112	0.0000	0.0022	0.0000	0.0069
7	0.0315	0.0232	0.0127	0.0120	0.0001	0.0026	0.0000	0.0119
8	0.0391	0.0275	0.0150	0.0132	0.0001	0.0035	0.0000	0.0189
9	0.0497	0.0310	0.0170	0.0157	0.0001	0.0027	0.0000	0.0310

Semi-inclusive asymmetry $A_1^{h^+}$								
Bin	Total	p_{T}	p_{B}	R	Rad. Corr.	Smear. Corr.	Yield Fluct.	g_2
1	0.0079	0.0061	0.0033	0.0036	0.0000	0.0007	0.0000	0.0006
2	0.0107	0.0080	0.0044	0.0054	0.0000	0.0009	0.0000	0.0011
3	0.0132	0.0100	0.0054	0.0063	0.0000	0.0011	0.0000	0.0018
4	0.0163	0.0123	0.0067	0.0076	0.0000	0.0012	0.0000	0.0028
5	0.0200	0.0153	0.0084	0.0088	0.0000	0.0013	0.0000	0.0043
6	0.0273	0.0203	0.0111	0.0127	0.0000	0.0011	0.0000	0.0069
7	0.0323	0.0239	0.0131	0.0124	0.0000	0.0011	0.0000	0.0119
8	0.0408	0.0292	0.0160	0.0140	0.0000	0.0015	0.0000	0.0189
9	0.0521	0.0336	0.0184	0.0170	0.0000	0.0019	0.0000	0.0310

Semi-inclusive asymmetry $A_1^{h^-}$								
Bin	Total	p_{T}	p_{B}	R	Rad. Corr.	Smear. Corr.	Yield Fluct.	g_2
1	0.0036	0.0027	0.0015	0.0016	0.0000	0.0008	0.0000	0.0006
2	0.0043	0.0031	0.0017	0.0021	0.0000	0.0009	0.0000	0.0011
3	0.0056	0.0040	0.0022	0.0026	0.0000	0.0009	0.0000	0.0018
4	0.0078	0.0056	0.0031	0.0034	0.0000	0.0010	0.0000	0.0028
5	0.0111	0.0080	0.0044	0.0046	0.0000	0.0009	0.0000	0.0043
6	0.0167	0.0117	0.0064	0.0073	0.0000	0.0010	0.0000	0.0069
7	0.0244	0.0170	0.0093	0.0088	0.0000	0.0010	0.0000	0.0119
8	0.0340	0.0228	0.0125	0.0109	0.0000	0.0014	0.0000	0.0189
9	0.0496	0.0310	0.0170	0.0157	0.0000	0.0019	0.0000	0.0310

Table B.6.: The 1995 ^{3}He asymmetries $A_1^{(h)} = A_{\parallel}^{(h)} / [D(1+\eta\gamma)]$.

Bin	x	Q^2	$A_1 \pm$ stat.$\pm$ syst.
1	0.033	1.22	$-0.0357 \pm 0.0134 \pm 0.0043$
2	0.048	1.47	$-0.0086 \pm 0.0144 \pm 0.0035$
3	0.065	1.73	$-0.0275 \pm 0.0155 \pm 0.0037$
4	0.087	2.00	$-0.0248 \pm 0.0180 \pm 0.0037$
5	0.118	2.31	$-0.0337 \pm 0.0194 \pm 0.0043$
6	0.166	2.66	$-0.0381 \pm 0.0234 \pm 0.0055$
7	0.239	3.07	$-0.0064 \pm 0.0299 \pm 0.0078$
8	0.338	3.79	$0.0783 \pm 0.0514 \pm 0.0116$
9	0.450	5.25	$-0.0236 \pm 0.0737 \pm 0.0187$

Bin	x	Q^2	$A_1^{h^+} \pm$ stat.$\pm$ syst.
1	0.033	1.21	$-0.0510 \pm 0.0320 \pm 0.0061$
2	0.048	1.45	$-0.0110 \pm 0.0330 \pm 0.0065$
3	0.065	1.75	$-0.0300 \pm 0.0340 \pm 0.0065$
4	0.087	2.14	$-0.0350 \pm 0.0390 \pm 0.0065$
5	0.118	2.71	$-0.0240 \pm 0.0410 \pm 0.0069$
6	0.165	3.68	$0.0060 \pm 0.0490 \pm 0.0076$
7	0.238	5.18	$-0.1550 \pm 0.0670 \pm 0.0095$
8	0.337	7.21	$-0.0920 \pm 0.1380 \pm 0.0128$
9	0.447	9.81	$-0.1100 \pm 0.2890 \pm 0.0198$

Bin	x	Q^2	$A_1^{h^-} \pm$ stat.$\pm$ syst.
1	0.033	1.21	$-0.0790 \pm 0.0370 \pm 0.0058$
2	0.048	1.45	$0.0210 \pm 0.0390 \pm 0.0057$
3	0.065	1.75	$-0.0210 \pm 0.0420 \pm 0.0059$
4	0.087	2.14	$0.0270 \pm 0.0490 \pm 0.0058$
5	0.118	2.71	$0.0090 \pm 0.0530 \pm 0.0061$
6	0.165	3.68	$-0.0220 \pm 0.0660 \pm 0.0068$
7	0.238	5.18	$0.0640 \pm 0.0920 \pm 0.0089$
8	0.337	7.21	$-0.2290 \pm 0.1990 \pm 0.0124$
9	0.447	9.81	$0.3080 \pm 0.6480 \pm 0.0192$

Table B.7.: Systematic error of the 1995 proton asymmetries. The table shows the total systematic error of $A_1^{(h)}$ and the contributions from each systematic error source: Target (p_{T}) and beam (p_{B}) polarisation measurements, cross section ratio R (R), radiative corrections (Rad. Corr.), combined acceptance and smearing corrections (Smear. Corr.), yield fluctuations (Yield Fluct.) and structure function g_2 (g_2).

Inclusive asymmetry A_1								
Bin	Total	p_{T}	p_{B}	R	Rad. Corr.	Smear. Corr.	Yield Fluct.	g_2
1	0.0043	0.0012	0.0010	0.0009	0.0029	0.0000	0.0026	0.0003
2	0.0035	0.0012	0.0010	0.0010	0.0013	0.0000	0.0026	0.0006
3	0.0037	0.0015	0.0012	0.0012	0.0006	0.0000	0.0026	0.0010
4	0.0037	0.0014	0.0011	0.0011	0.0002	0.0000	0.0026	0.0016
5	0.0043	0.0016	0.0013	0.0011	0.0006	0.0000	0.0026	0.0025
6	0.0055	0.0017	0.0013	0.0013	0.0010	0.0000	0.0026	0.0040
7	0.0078	0.0017	0.0013	0.0011	0.0014	0.0000	0.0026	0.0069
8	0.0116	0.0015	0.0012	0.0009	0.0018	0.0000	0.0026	0.0110
9	0.0187	0.0012	0.0010	0.0008	0.0020	0.0000	0.0026	0.0183

Semi-inclusive asymmetry $A_1^{h^+}$								
Bin	Total	p_{T}	p_{B}	R	Rad. Corr.	Smear. Corr.	Yield Fluct.	g_2
1	0.0061	0.0013	0.0010	0.0010	0.0000	0.0000	0.0057	0.0003
2	0.0065	0.0019	0.0015	0.0016	0.0000	0.0000	0.0057	0.0006
3	0.0065	0.0019	0.0015	0.0015	0.0000	0.0000	0.0057	0.0010
4	0.0065	0.0017	0.0013	0.0013	0.0000	0.0000	0.0057	0.0016
5	0.0069	0.0019	0.0015	0.0014	0.0000	0.0000	0.0057	0.0025
6	0.0076	0.0020	0.0016	0.0015	0.0000	0.0000	0.0057	0.0040
7	0.0095	0.0023	0.0018	0.0015	0.0000	0.0000	0.0057	0.0069
8	0.0128	0.0022	0.0018	0.0014	0.0000	0.0000	0.0057	0.0110
9	0.0198	0.0034	0.0027	0.0022	0.0000	0.0000	0.0057	0.0183

Semi-inclusive asymmetry $A_1^{h^-}$								
Bin	Total	p_{T}	p_{B}	R	Rad. Corr.	Smear. Corr.	Yield Fluct.	g_2
1	0.0058	0.0012	0.0010	0.0009	0.0000	0.0000	0.0055	0.0003
2	0.0057	0.0010	0.0008	0.0008	0.0000	0.0000	0.0055	0.0006
3	0.0059	0.0012	0.0010	0.0010	0.0000	0.0000	0.0055	0.0010
4	0.0058	0.0007	0.0006	0.0006	0.0000	0.0000	0.0055	0.0016
5	0.0061	0.0007	0.0006	0.0005	0.0000	0.0000	0.0055	0.0025
6	0.0068	0.0007	0.0005	0.0005	0.0000	0.0000	0.0055	0.0040
7	0.0089	0.0009	0.0007	0.0006	0.0000	0.0000	0.0055	0.0069
8	0.0124	0.0012	0.0010	0.0007	0.0000	0.0000	0.0055	0.0110
9	0.0192	0.0016	0.0013	0.0010	0.0000	0.0000	0.0055	0.0183

Table B.8.: The **flavour decomposition** $(\Delta u + \Delta\bar{u})/(u + \bar{u})$, $(\Delta d + \Delta\bar{d})/(d + \bar{d})$, and $\Delta q_{\mathrm{s}}/q_{\mathrm{s}}$ of the quark polarisation as a function of x derived from the HERMES inclusive and semi-inclusive asymmetries on the ^{3}He and proton targets. The sea polarisation is assumed to be flavour symmetric in this analysis.

Bin	$\frac{\Delta u+\Delta\bar{u}}{u+\bar{u}} \pm$ stat.$\pm$ syst.	$\frac{\Delta d+\Delta\bar{d}}{d+\bar{d}} \pm$ stat.$\pm$ syst.	$\Delta q_{\mathrm{s}}/q_{\mathrm{s}} \pm$ stat.$\pm$ syst.
1	$0.106 \pm 0.013 \pm 0.008$	$-0.137 \pm 0.052 \pm 0.018$	$0.017 \pm 0.095 \pm 0.048$
2	$0.109 \pm 0.014 \pm 0.007$	$-0.068 \pm 0.057 \pm 0.012$	$0.112 \pm 0.104 \pm 0.026$
3	$0.144 \pm 0.015 \pm 0.010$	$-0.133 \pm 0.063 \pm 0.012$	$-0.056 \pm 0.125 \pm 0.077$
4	$0.193 \pm 0.016 \pm 0.015$	$-0.151 \pm 0.078 \pm 0.014$	$-0.215 \pm 0.172 \pm 0.151$
5	$0.216 \pm 0.018 \pm 0.013$	$-0.216 \pm 0.092 \pm 0.022$	$0.128 \pm 0.240 \pm 0.121$
6	$0.267 \pm 0.021 \pm 0.017$	$-0.250 \pm 0.126 \pm 0.036$	$0.193 \pm 0.453 \pm 0.149$
7	$0.362 \pm 0.028 \pm 0.023$	$-0.256 \pm 0.198 \pm 0.059$	$-1.222 \pm 1.131 \pm 0.607$
8	$0.386 \pm 0.045 \pm 0.027$	$0.499 \pm 0.405 \pm 0.097$	$0.000 \pm 0.000 \pm 0.958$
9	$0.667 \pm 0.065 \pm 0.040$	$-1.096 \pm 0.813 \pm 0.109$	$0.000 \pm 0.000 \pm 1.024$

Table B.9.: Correlation coefficients of the quark polarisations $(\Delta u+\Delta\bar{u})/(u+\bar{u})$, $(\Delta d+\Delta\bar{d})/(d+\bar{d})$, and $\Delta q_{\mathrm{s}}/q_{\mathrm{s}}$ in each x-bin. Also shown is the χ^2_{min}/NDF of the fit.

	Correlation coefficients			
Bin	$\left(\frac{\Delta u+\Delta\bar{u}}{u+\bar{u}}, \frac{\Delta d+\Delta\bar{d}}{d+\bar{d}}\right)$	$\left(\frac{\Delta u+\Delta\bar{u}}{u+\bar{u}}, \frac{\Delta q_{\mathrm{s}}}{q_{\mathrm{s}}}\right)$	$\left(\frac{\Delta d+\Delta\bar{d}}{d+\bar{d}}, \frac{\Delta q_{\mathrm{s}}}{q_{\mathrm{s}}}\right)$	χ^2_{min}/NDF
1	-0.718	-0.081	-0.390	0.89
2	-0.708	-0.008	-0.405	0.18
3	-0.673	-0.047	-0.423	0.09
4	-0.639	-0.084	-0.438	1.92
5	-0.619	-0.055	-0.455	1.38
6	-0.584	-0.090	-0.459	0.84
7	-0.487	-0.298	-0.435	2.35
8	-0.724	0.000	0.000	2.03
9	-0.756	0.000	0.000	0.94

Table B.10.: Systematic error of $(\Delta u + \Delta\bar{u})/(u + \bar{u})$, $(\Delta d + \Delta\bar{d})/(d + \bar{d})$, and $\Delta q_s/q_s$ as a function of x. The table shows the total systematic error and the contributions from the different systematic error sources.

Bin	Total	Rad. Corr.	Smear. Corr.	R	g_2	p_B	p_T	Yield Fluc.	Frag. Model	Unpol. Distr.	$\Delta q_s/q_s = 0$ $(x > 0.3)$
$(\Delta u + \Delta\bar{u})/(u + \bar{u})$											
1	0.008	0.002	0.001	0.002	0.001	0.002	0.004	0.002	0.004	0.004	0.000
2	0.007	0.001	0.001	0.001	0.001	0.003	0.005	0.002	0.002	0.000	0.000
3	0.010	0.000	0.001	0.001	0.001	0.004	0.006	0.002	0.005	0.005	0.000
4	0.015	0.000	0.002	0.001	0.001	0.006	0.009	0.002	0.007	0.008	0.000
5	0.013	0.000	0.002	0.001	0.002	0.006	0.010	0.002	0.005	0.000	0.000
6	0.017	0.001	0.002	0.001	0.002	0.008	0.012	0.002	0.008	0.001	0.000
7	0.023	0.001	0.003	0.000	0.002	0.012	0.018	0.002	0.005	0.005	0.000
8	0.027	0.001	0.004	0.001	0.003	0.013	0.021	0.002	0.007	0.001	0.005
9	0.040	0.002	0.004	0.001	0.006	0.021	0.032	0.002	0.006	0.002	0.003
$(\Delta d + \Delta\bar{d})/(d + \bar{d})$											
1	0.018	0.012	0.000	0.003	0.002	0.005	0.006	0.009	0.005	0.003	0.000
2	0.012	0.006	0.000	0.000	0.002	0.002	0.002	0.009	0.001	0.005	0.000
3	0.012	0.003	0.000	0.001	0.001	0.004	0.006	0.009	0.003	0.002	0.000
4	0.014	0.001	0.000	0.001	0.002	0.004	0.006	0.010	0.006	0.001	0.000
5	0.022	0.003	0.000	0.000	0.002	0.005	0.008	0.012	0.004	0.015	0.000
6	0.036	0.005	0.005	0.000	0.006	0.006	0.010	0.015	0.024	0.018	0.000
7	0.059	0.009	0.001	0.000	0.005	0.004	0.010	0.019	0.054	0.001	0.000
8	0.097	0.014	0.000	0.002	0.012	0.024	0.031	0.023	0.073	0.019	0.036
9	0.109	0.023	0.000	0.000	0.032	0.000	0.033	0.032	0.068	0.055	0.019
$\Delta q_s/q_s$											
1	0.048	0.006	0.002	0.002	0.002	0.005	0.004	0.005	0.047	0.001	0.000
2	0.026	0.003	0.004	0.001	0.002	0.005	0.005	0.005	0.024	0.003	0.000
3	0.077	0.002	0.002	0.002	0.002	0.009	0.009	0.006	0.075	0.012	0.000
4	0.151	0.001	0.000	0.002	0.003	0.015	0.018	0.007	0.144	0.040	0.000
5	0.121	0.003	0.004	0.001	0.003	0.009	0.008	0.010	0.120	0.007	0.000
6	0.149	0.007	0.014	0.000	0.015	0.010	0.012	0.017	0.147	0.002	0.000
7	0.607	0.017	0.011	0.004	0.013	0.090	0.116	0.028	0.586	0.074	0.000
8	0.958	0.000	0.000	0.000	0.000	0.000	0.000	0.000	0.000	0.000	0.958
9	1.024	0.000	0.000	0.000	0.000	0.000	0.000	0.000	0.000	0.000	1.024

Table B.11.: The **valence decomposition** $\Delta u_{\rm v}/u_{\rm v}, \Delta d_{\rm v}/d_{\rm v}$ and $\Delta q_{\rm s}/q_{\rm s}$ of the quark polarisation as a function of x, derived from the HERMES inclusive and semi-inclusive asymmetries on the ^{3}He and proton targets. The sea polarisation is assumed to be flavour symmetric in this analysis.

Bin	$\Delta u_{\rm v}/u_{\rm v} \pm$ stat.$\pm$ syst.	$\Delta d_{\rm v}/d_{\rm v} \pm$ stat.$\pm$ syst.	$\Delta q_{\rm s}/q_{\rm s} \pm$ stat.$\pm$ syst.
1	$0.214 \pm 0.122 \pm 0.067$	$-0.468 \pm 0.306 \pm 0.148$	$0.018 \pm 0.095 \pm 0.048$
2	$0.107 \pm 0.096 \pm 0.026$	$-0.376 \pm 0.278 \pm 0.098$	$0.112 \pm 0.103 \pm 0.026$
3	$0.271 \pm 0.083 \pm 0.058$	$-0.239 \pm 0.272 \pm 0.116$	$-0.055 \pm 0.125 \pm 0.077$
4	$0.376 \pm 0.081 \pm 0.079$	$-0.080 \pm 0.303 \pm 0.163$	$-0.215 \pm 0.171 \pm 0.149$
5	$0.241 \pm 0.075 \pm 0.045$	$-0.520 \pm 0.326 \pm 0.114$	$0.129 \pm 0.240 \pm 0.122$
6	$0.279 \pm 0.082 \pm 0.038$	$-0.536 \pm 0.430 \pm 0.077$	$0.192 \pm 0.452 \pm 0.149$
7	$0.480 \pm 0.099 \pm 0.057$	$0.141 \pm 0.659 \pm 0.334$	$-1.191 \pm 1.127 \pm 0.595$
8	$0.398 \pm 0.046 \pm 0.044$	$0.629 \pm 0.510 \pm 0.316$	$0.000 \pm 0.000 \pm 0.958$
9	$0.674 \pm 0.066 \pm 0.042$	$-1.247 \pm 0.925 \pm 0.204$	$0.000 \pm 0.000 \pm 1.024$

Table B.12.: Correlation coefficients of the quark polarisations $\Delta u_{\rm v}/u_{\rm v}, \Delta d_{\rm v}/d_{\rm v}$ and $\Delta q_{\rm s}/q_{\rm s}$ in each x-bin. Also shown is the $\chi^2_{\rm min}$/NDF of the fit.

	Correlation coefficients			
Bin	$(\Delta u_{\rm v}/u_{\rm v}, \Delta d_{\rm v}/d_{\rm v})$	$(\Delta u_{\rm v}/u_{\rm v}, \Delta q_{\rm s}/q_{\rm s})$	$(\Delta d_{\rm v}/d_{\rm v}, \Delta q_{\rm s}/q_{\rm s})$	$\chi^2_{\rm min}$/NDF
1	0.729	-0.967	-0.863	0.89
2	0.700	-0.955	-0.858	0.18
3	0.696	-0.949	-0.863	0.09
4	0.699	-0.943	-0.871	1.92
5	0.705	-0.936	-0.882	1.38
6	0.734	-0.935	-0.902	0.84
7	0.768	-0.938	-0.922	2.35
8	-0.724	0.000	0.000	2.03
9	-0.756	0.000	0.000	0.94

Table B.13.: Systematic error of $\Delta u_\mathrm{v}/u_\mathrm{v}$, $\Delta d_\mathrm{v}/d_\mathrm{v}$, and $\Delta q_\mathrm{s}/q_\mathrm{s}$ as a function of x. The table shows the total systematic error and the contributions from the different systematic error sources.

Bin	Total	Rad. Corr.	Smear. Corr.	R	g_2	p_B	p_T	Yield Fluc.	Frag. Model	Unpol. Distr.	$\Delta q_\mathrm{s}/q_\mathrm{s} = 0$ $(x > 0.3)$
$\Delta u_\mathrm{v}/u_\mathrm{v}$											
1	0.067	0.002	0.002	0.006	0.001	0.008	0.010	0.002	0.066	0.001	0.000
2	0.026	0.008	0.002	0.002	0.001	0.004	0.006	0.001	0.025	0.002	0.000
3	0.058	0.000	0.000	0.002	0.001	0.010	0.014	0.001	0.055	0.008	0.000
4	0.079	0.000	0.002	0.002	0.001	0.015	0.019	0.001	0.074	0.007	0.000
5	0.045	0.002	0.000	0.000	0.001	0.010	0.013	0.000	0.041	0.010	0.000
6	0.038	0.000	0.002	0.001	0.001	0.010	0.013	0.001	0.034	0.003	0.000
7	0.057	0.000	0.003	0.000	0.002	0.019	0.027	0.000	0.046	0.005	0.000
8	0.044	0.001	0.004	0.000	0.004	0.013	0.022	0.003	0.007	0.002	0.035
9	0.042	0.002	0.002	0.000	0.005	0.021	0.032	0.002	0.006	0.004	0.014
$\Delta d_\mathrm{v}/d_\mathrm{v}$											
1	0.148	0.050	0.003	0.014	0.010	0.021	0.025	0.039	0.090	0.092	0.000
2	0.098	0.030	0.009	0.000	0.007	0.004	0.011	0.032	0.039	0.079	0.000
3	0.116	0.009	0.003	0.004	0.006	0.019	0.021	0.030	0.097	0.048	0.000
4	0.163	0.003	0.002	0.003	0.008	0.022	0.020	0.029	0.154	0.032	0.000
5	0.114	0.003	0.004	0.009	0.006	0.014	0.020	0.032	0.100	0.033	0.000
6	0.077	0.013	0.003	0.000	0.009	0.018	0.025	0.035	0.056	0.024	0.000
7	0.334	0.020	0.000	0.000	0.012	0.038	0.041	0.039	0.322	0.033	0.000
8	0.316	0.018	0.002	0.000	0.021	0.032	0.040	0.033	0.092	0.023	0.295
9	0.204	0.026	0.018	0.016	0.041	0.000	0.030	0.036	0.077	0.074	0.162
$\Delta q_\mathrm{s}/q_\mathrm{s}$											
1	0.048	0.006	0.002	0.002	0.002	0.003	0.003	0.005	0.047	0.001	0.000
2	0.026	0.009	0.004	0.001	0.002	0.002	0.004	0.005	0.024	0.003	0.000
3	0.077	0.002	0.002	0.002	0.002	0.007	0.008	0.006	0.075	0.011	0.000
4	0.149	0.001	0.000	0.002	0.003	0.015	0.015	0.007	0.143	0.038	0.000
5	0.122	0.005	0.004	0.005	0.003	0.009	0.008	0.011	0.120	0.012	0.000
6	0.149	0.007	0.004	0.001	0.006	0.011	0.012	0.016	0.147	0.003	0.000
7	0.595	0.016	0.000	0.000	0.009	0.085	0.105	0.027	0.574	0.020	0.000
8	0.958	0.000	0.000	0.000	0.000	0.000	0.000	0.000	0.000	0.000	0.958
9	1.024	0.000	0.000	0.000	0.000	0.000	0.000	0.000	0.000	0.000	1.024

Table B.14.: Non-default JETSET-7.4 parameters of the tuned LUND string fragmentation model and of the tuned independent fragmentation model as used to generate the fragmentation functions. The quark polarisations have been extracted using the fragmentation functions generated by the tuned LUND model with parameter settings from [Gei 98a] (SF1). To estimate the systematic uncertainty of SF1, the fragmentation functions were constructed from an alternative fit of the LUND model [Gei 98b] (SF2), and from the tuned independent fragmentation model [Gei 98b] (IF). In the table, the symbol – indicates that the parameter was set to the default value.
The parameters shown in the table have the following meanings [Sjö 94]: `PARJ(1)`: Suppression factor of diquark-antidiquark pair production in the colour field, compared with quark-antiquark production. `PARJ(14)`: Probability that a spin 0 meson is produced with an orbital angular momentum 1. `PARJ(21)`: Width $\langle p_\perp \rangle$ of the transverse momentum distributions for primary hadrons (see Eq. (2.81)). `PARJ(41)` `[PARJ(42)]`: Parameter a $[b]$ of the symmetric LUND fragmentation function (see Eq. (2.82)). `MSTJ(1)`: Choice of the fragmentation scheme (1: String fragmentation, 2: Independent fragmentation). `MSTJ(2)`: Gluon jet fragmentation scheme in independent fragmentation (3: A gluon is assumed to fragment like a pair of a u, d, or s quark and its anti-quark, sharing the gluon energy according to the Altarelli-Parisi splitting function, 1: A gluon is assumed to fragment like a random u, d, or s quark or anti-quark). `MSTJ(3)`: Energy, momentum and flavour conservation options in independent fragmentation (0: No explicit conservation of any kind, 1: Particles share momentum imbalance compensation according to their energy. Roughly equivalent to boosting event to the centre of mass frame). `MSTJ(42)`: Type of branching allowed in shower (1: QCD type branchings of quarks and gluons, 2: Coherent branching, i.e. with angular ordering).

Name in JETSET	Default value	SF1	SF2	IF
`PARJ(1)`	0.10	–	0.01	–
`PARJ(14)`	0.00	–	–	0.23
`PARJ(21)` [GeV]	0.36	0.34	0.40	0.31
`PARJ(41)`	0.30	0.82	0.15	1.38
`PARJ(42)` [GeV^{-2}]	0.58	0.24	0.35	1.16
`MSTJ(1)`	1	–	–	2
`MSTJ(2)`	3	–	–	1
`MSTJ(3)`	0	–	–	1
`MSTJ(42)`	2	–	–	1

List of Figures

2.1. Feynman diagram of deep inelastic charged lepton-nucleon scattering in lowest order QED . . . 3
2.2. The spin-independent proton structure function F_2^{p} . . . 6
2.3. Definition of scattering angles in polarised deep inelastic scattering . . . 8
2.4. The spin-dependent proton structure function g_1^{p} . . . 9
2.5. Schematical representation of the Q^2-dependence of quark distributions . 14
2.6. Experimental results on the Bjørken and Ellis-Jaffe sum rules . . . 18
2.7. Scaling and factorisation breaking of fragmentation functions . . . 22

3.1. The HERA storage ring . . . 27
3.2. Schematic diagram of the target region . . . 32
3.3. Schematic diagram of the hydrogen target . . . 34
3.4. Schematic diagram of the experimental apparatus . . . 35
3.5. Response of the lead-glass calorimeter . . . 37
3.6. Response of the pre-shower detector . . . 37
3.7. Response of the transition radiation detector . . . 38
3.8. Response of the threshold Čerenkov detector . . . 39
3.9. Schematic diagram of the luminosity monitor . . . 40

4.1. Likelihood distributions for particle identification . . . 47
4.2. Distribution of inclusive DIS events in the x versus Q^2 plane . . . 49
4.3. Asymmetries $A_{\parallel}^{(h)}$ for the ^{3}He and the proton target . . . 52
4.4. Feynman diagrams of higher order QED processes in deep inelastic lepton-nucleon scattering . . . 55
4.5. The virtual photon depolarisation factor D . . . 58
4.6. Asymmetries $A_1^{(h)}$ for the ^{3}He and the proton target . . . 59
4.7. The spin-dependent structure function g_2 of the proton and the neutron . . 63
4.8. Systematic error of the inclusive asymmetries A_1 for the ^{3}He and the proton target . . . 64
4.9. Systematic error of the structure function ratios g_1/F_1 for the ^{3}He and the proton target . . . 65

5.1. Quark flavour purities for a proton target . . . 73

5.2. Quark flavour purities for a neutron target 74
5.3. Test of the extraction formalism with Monte Carlo 76
5.4. The flavour decomposition of the quark polarisations 79
5.5. The flavour decomposition of the quark polarisations for two different sea assumptions 81
5.6. The polarised quark distributions $x\left(\Delta u + \Delta\bar{u}\right)$ and $x\left(\Delta d + \Delta\bar{d}\right)$ compared to parametrisations 82
5.7. The triplet combination $x\Delta q_3(x)$ compared parametrisations 83
5.8. The polarised valence and sea quark distributions as a function of x . . . 84
5.9. Systematic error of the quark polarisations for the flavour decomposition . 86
5.10. The SU(3)$_f$ octet combination $x\Delta q_8(x)$ compared to parametrisations . . 94

A.1. Parametrisations of unpolarised quark distributions 102
A.2. Parametrisations of polarised quark distributions 104
A.3. Correlation coefficients of count rates for inclusive and semi-inclusive DIS events 106

List of Tables

4.1. Overview of the event selection 45
4.2. Corrections to asymmetries for detector acceptance and kinematical smearing 55
4.3. QED Radiative corrections to the inclusive ^{3}He and proton asymmetries . 56

5.1. First and second moments of various spin distributions 89
5.2. Comparison of the HERMES and SMC integrals of polarised valence and sea quark distributions in the range $0.023 < x < 0.6$ 91

A.1. Correlation coefficients of count rates for inclusive and semi-inclusive DIS events 107

B.1. Kinematical factors and R-parametrisation 113
B.2. The 1997 proton asymmetries $A_1^{(h)}$ 114
B.3. Systematic error of the 1997 proton asymmetries $A_1^{(h)}$ 115
B.4. The 1996 proton asymmetries $A_1^{(h)}$ 116
B.5. Systematic error of the 1996 proton asymmetries $A_1^{(h)}$ 117
B.6. The 1995 ^{3}He asymmetries $A_1^{(h)}$ 118
B.7. Systematic error of the 1995 ^{3}He asymmetries $A_1^{(h)}$ 119
B.8. The flavour decomposition of the quark polarisations 120
B.9. Correlations and goodness of the fit for the flavour decomposition 120
B.10. Systematic error of the quark polarisations for the flavour decomposition . 121
B.11. The valence decomposition of the quark polarisations 122
B.12. Correlations and goodness of the fit for the valence decomposition 122
B.13. Systematic error of the quuark polarisations for the valence decomposition 123
B.14. Non-default JETSET parameters of fragmentation models 124

Bibliography

[Abe 95a] K. Abe et al. (E143-Collaboration), Phys. Rev. Lett. **74** (1995) 346.

[Abe 95b] K. Abe et al. (E143-Collaboration), Phys. Rev. Lett. **75** (1995) 25.

[Abe 96] K. Abe et al. (E143-Collaboration), Phys. Rev. Lett. **76** (1996) 587.

[Abe 97a] K. Abe et al. (E154-Collaboration), Phys. Lett. **B404** (1997) 377; Phys. Lett. **B405** (1997) 180.

[Abe 97b] K. Abe et al. (E154-Collaboration), Phys. Rev. Lett. **79** (1997) 26.

[Abe 98] K. Abe et al. (E143-Collaboration), Phys. Rev. **D58** (1998) 112003.

[Abe 99] K. Abe et al. (E143-Collaboration), Phys. Lett. **B452** (1999) 194.

[Abr 96] P. Abreu et al. (DELPHI-Collaboration), Z. Phys. **C73** (1996) 11.

[Ack 97] K. Ackerstaff et al. (HERMES-Collaboration), Phys. Lett. **B404** (1997) 383.

[Ack 98] K. Ackerstaff et al. (HERMES-Collaboration), Nucl. Instr. Meth. **A417** (1998) 230.

[Ack 99] K. Ackerstaff et al. (HERMES-Collaboration), Preprint hep-ex/9906035 (1999), accepted by Phys. Lett. **B**.

[Ada 97] D. Adams et al. (SMC-Collaboration), Phys. Lett. **B396** (1997) 338.

[Ade 98a] B. Adeva et al. (SMC-Collaboration), Phys. Lett. **B420** (1998) 180.

[Ade 98b] B. Adeva et al. (SMC-Collaboration), Phys. Rev. **D58** (1998) 112002.

[Adl 69a] S.I. Adler, Phys. Rev. **177** (1969) 2426.

[Adl 69b] S.I. Adler and W. Bardeen, Phys. Rev. **182** (1969) 1517.

[Adl 97] C. Adloff et al. (H1-Collaboration), Phys. Lett. **B406** (1997) 256.

[Air 98] A. Airapetian et al. (HERMES-Collaboration), Phys. Lett. **B442** (1998) 484.

[Ako 97] N. Akopov et al., *Determination of the 1995 Data Quality and the Extraction of the Spin Structure Function of the Neutron.* HERMES Internal Note 97-007 (1997).

[Aku 94] I.V. Akushevich and N.M. Shumeiko, J. Phys. G: Nucl. Part. Phys. **20** (1994) 513.

[Aku 97] I.V. Akushevich et al., Comp. Phys. Comm. **104** (1997) 201.

[Aku 98a] I.V. Akushevich and A. Nagaitsev, J. Phys. **G24** (1998) 2235.

[Aku 98b] I.V. Akushevich, Private communication.

[Alt 77] G. Altarelli and G. Parisi, Nucl. Phys. **B126** (1977) 298.

[Alt 82] G. Altarelli, Phys. Rep. **81** (1982) 1.

[Alt 88] G. Altarelli and G.G. Ross, Phys. Lett. **B212** (1988) 391.

[Alt 94] G. Altarelli et al., Phys. Lett. **B334** (1994) 187.

[And 83] B. Andersson et al., Phys. Rep. **97** (1983) 31.

[Ans 95] M. Anselmino et al., Phys. Rep. **261** (1995) 1.
Erratum-ibid. **281** (1997) 399.

[Ant 99] P.L. Anthony et al. (E155-Collaboration), Preprint hep-ex/9901006 (1999).

[Arn 84] M. Arneodo et al. (EMC-Collaboration), Phys. Lett. **B145** (1984) 458.

[Arn 85a] M. Arneodo et al. (EMC-Collaboration), Nucl. Phys. **B258** (1985) 249.

[Arn 85b] M. Arneodo et al. (EMC-Collaboration), Phys. Lett. **B165** (1985) 222.

[Arn 86] M. Arneodo et al. (EMC-Collaboration), Z. Phys. **C31** (1986) 1.

[Arn 89] M. Arneodo et al. (EMC-Collaboration), Nucl. Phys. **B321** (1989) 541.

[Aub 82] J.J. Aubert et al. (EMC-Collaboration), Phys. Lett. **B114** (1982) 373.

[Ava 96] H. Avakian et al., Nucl. Instr. Meth. **A378** (1996) 155.

[Ava 98] H. Avakian et al., Nucl. Instr. Meth. **A417** (1998) 69.

[Bai 99] B. Bains et al., *Determination of the Charged Hadron Asymmetries from the 1997 Data.* HERMES Internal Note 99-015 (1999).

[Bal 95] R.D. Ball et al., Nucl. Phys. **B444** (1995) 287.

[Bal 98] J. Balla et al., Nucl. Phys. **B510** (1998) 327.

[Bar 89] R.J. Barlow, *Statistics: A Guide to the Use of Statistical Methods in the Physical Sciences*, John Wiley & Sons Ltd. (1989).

[Bar 93] D.P. Barber et al., Nucl. Instr. Meth. **A329** (1993) 79.

[Bar 94] D.P. Barber et al., Nucl. Instr. Meth. **A338** (1994) 166.

[Bar 95] D.P. Barber et al., Phys. Lett. **B343** (1995) 436.

[Bar 96] S. Barrow et al., *Interim Report on the Measurement of the Positron Beam Polarisation.* HERMES Internal Note 96-002 (1996).

[Bec 99] M. Beckmann, Dissertation, Universität Freiburg (1999).

[Bel 69] J.S. Bell and R. Jackiw, Nuovo Cim. **51A** (1969) 47.

[Bel 96] J.E. Belz, *Beam Polarisation Smoothing for the Analysis of 1995 Data*, HERMES Internal Note 96-051 (1996).

[Bin 95] J. Binnewies et al., Z. Phys. **C65** (1995) 471.

[Bjø 66] J.D. Bjørken, Phys. Rev. **148** (1966) 1467;
J.D. Bjørken, Phys. Rev. **D1** (1970) 1376.

[Bjø 69] J.D. Bjørken, Phys. Rev. **179** (1969) 1547;
J.D. Bjørken and E.A. Paschos, Phys. Rev. **185** (1969) 1975.

[Bra 97] B. Braun, Proceedings of the Workshop Polarised Gas Targets and Polarised Beams. Edited by R.J. Holt and M.A. Miller, Urbana-Champaign, USA, AIP Conf. Proc. **421** (1997) 156.

[Bre 99] J. Breitweg et al. (ZEUS-Collaboration), Preprint hep-ex/9903056 (1999).

[Bur 70] H. Burkhardt and W.N. Cottingham, Ann. Phys. **56** (1970) 453.

[Cal 68] C.G. Callan and D.G. Gross, Phys. Rev. Lett. **21** (1968) 311; Phys. Rev. Lett. **22** (1969) 156.

[Car 88] R.D. Carlitz et al., Phys. Lett. **B214** (1988) 229.

[Cas 98] C. Caso et al., Review of Particle Physics, Eur. Phys. J. **C3** (1998) 1.

[Cha 81] A.W. Chao, Nucl. Instr. Meth. **180** (1981) 29; *Physics of High Energy Particle Accelerators*, American Institute of Physics Proceedings **87** (1982) 395.

[Che 96] H.Y. Cheng, Int. J. Mod. Phys. **A11** (1996) 5109.

[Cow 94] G. Cowan et al., *Measurement of Scaling Violations e^+e^- Annihilation.* Proc. 27th Int. Conf. on High Energy Physics, Vol. 2, Glasgow, Scottland (1994).

[DeS 98] D. DeSchepper et al., Nucl. Instr. Meth. **A419** (1998) 16.

[Dia 96] D. Diakonov et al., Nucl. Phys. **B480** (1996) 341.

[GEA 94] Application Software Group, Computing and Networks Division, CERN, GEANT – *Detector Description and Simulation Tool.* (1994).

[Efr 88] A.V. Efremov and O.V. Teryaev, J.I.N.R. Preprint E2-88-287, Dubna (1988).

[Ell 74] J. Ellis and R.L. Jaffe, Phys. Rev. **D9** (1974) 1444.

[Ell 88] J. Ellis and M. Karliner, Phys. Lett. **B213** (1988) 73.

[Ell 96] J. Ellis and M. Karliner, Preprint hep-ph/9601280 (1996); Phys. Lett. **B341** (1995) 397.

[Fan 49] U. Fano, Opt. Soc. Amer. **39** (1949) 859.

[Fer 97] M. Ferstl, *Polarisierte tiefinelastische Streuung an einem ^{3}He-Target im* HERMES*-Experiment.* Dissertation, Universität Erlangen-Nürnberg (1997).

[Fey 72] R.P. Feynman, *Photon-Hadron Interactions*, Benjamin (1972).

[Fie 78] R.D. Field and R.P. Feynman, Nucl. Phys. **B136** (1978) 1.

[Flo 98] D. de Florian et al., Phys. Rev. D **57** (1998) 5803.

[Fun 98] M.A. Funk, *A Measurement of the Polarised Parton Densities of the Nucleon in Deep Inelastic Scattering at* HERMES. Dissertation, Universität Hamburg (1998), DESY-THESIS-1998-017.

[Fri 90] J.L. Friar et al., Phys. Rev. **C42** (1990) 2310.

[Fri 98] R. Fries and A. Schäfer, Phys. Lett. **B443** (1998) 40.

[Gei 98a] P. Geiger, *Measurement of Fragmentation Functions at* HERMES. Dissertation, Universität Heidelberg (1998).

[Gei 98b] P. Geiger, Private communication.

[Ger 95] T. Gehrmann and W.J. Stirling, Z. Phys. **C65**, 461 (1995).

[Ger 96] T. Gehrmann and W.J. Stirling, Phys. Rev. **D53** (1996) 6100.

[Glu 95] M. Glück et al., Z. Phys. **C67** (1995) 433.

[Glu 96] M. Glück et al., Phys. Rev. **D53** (1996) 4775.

[Goe 97a] M. Göckeler et al., Phys. Lett. **B414** (1997) 340.

[Goe 97b] M. Göckeler et al., Nucl. Phys. (Proc. Suppl.) **B53** (1997) 81.

[Gre 89] W. Greiner and A. Schäfer, *Quantenchromodynamik*, Verlag Harri Deutsch (1989).

[Gri 72] V.N. Gribov and L.N. Lipatov, Sov. J. Nucl. Phys. **15** (1972) 438;
Sov. J. Nucl. Phys. **15** (1972) 675.

[Gri 87] D. Griffith, *Introduction to Elementary Particles.* John Wiley & Sons (1987).

[Gut 99a] A. Gute, *Messung der polarisierten Strukturfunktion g_1^p des Protons im* HERMES *Experiment.* Dissertation, Universität Erlangen-Nürnberg (1999), DESY-THESIS-1999-017.

[Gut 99b] A. Gute, Private communication.

[Hal 84] F. Halzen and A.D. Martin, *Quarks & Leptons.* John Wiley & Sons (1984).

[Has 99] D. Hasch, *Messung der polarisierten Strukturfunktion $g_1(x, Q^2)$ des Protons mit dem* HERMES *Experiment.* Dissertation, Humboldt-Universität Berlin (1999).

[Haw 98] E.A. Hawker et al. (E866-Collaboration), Phys. Rev. Lett. **80** (1998) 3715;
J.C. Peng et al. (E866-Collaboration), Phys. Rev. **D58** (1998) 092004;
K. Ackerstaff et al. (HERMES-Collaboration), Phys. Rev. Lett. **81** (1998) 5519.

[Hei 73] R. Heimann, Nucl. Phys. **B64** (1973) 429.

[HER 93] The HERMES-Collaboration, *Technical Design Report.* DESY-PRC 93/06, MPIH-V20-1993 (1993).

[HER 95] The HERMES-Collaboration, *Proposal to DESY for a Longitudinal Electron Polarimeter at the* HERA *East Section.* HERMES Internal Polarimeter Report 95-03 (1995).

[Hug 99] E. Hughes, Proceedings of the 7th International Workshop on Deep Inelastic Scattering and QCD, Zeuthen (1999), to appear in Phys. Lett. **B** (Proc. Suppl.)

[Ing 97] G. Ingelmann et al., Comp. Phys. Comm. **101** (1997) 108.

[Jaf 90] R.L. Jaffe and A. Manohar, Nucl. Phys. **B337** (1990) 509.

[Jam 94] F. James, CERN Computing and Networks Divison, MINUIT *Function Minimization and Error Analysis*. Reference Manual, Version 94.1, CERN Program Library (1994).

[Ji 95] X. Ji, Proceedings of the 3rd International Workshop on Deep Inelastic Scattering and QCD, Paris (1995).

[Ji 97] X. Ji and W. Melnitchouk, Phys. Rev. **D56** (1997) 1.

[Jon 91] C.T. Jones et al. (WA21-Collaboration), Z. Phys. **C51** (1991) 11.

[Kai 97] R.B. Kaiser, *Measurement of the Spin Structure Function of the Neutron Using Polarised Deep Inelastic Scattering*. D. Phil. thesis (partial fulfillment), Simon Fraser University, Vancouver (1997).

[Kat 95] A.L. Kataev and V.V. Starshenko, Mod. Phys. Lett. **A10** (1995) 235.

[Kod 95] J. Kodaira et al., Phys. Lett. **B345** (1995) 527.

[Kol 99] Y.G. Kolomensky, Private communication.

[Kra 95] L.H. Kramer et al., Nucl. Instr. Meth. **A365** (1995) 49.

[Kuc 83] T.V. Kutcho and N.M. Shumeiko, Nucl. Phys. **B219** (1983) 412.

[Lac 98] W.A. Lachnit, *Die hinteren* HERMES*-Driftkammern und ihr Einfluß auf systematische Fehler von Asymmetriemessungen.* Dissertation, Universität Erlangen-Nürnberg (1998).

[Lai 97] H.L. Lai et al., Phys. Rev. **D55** (1997) 1280.

[Lar 91] S.A. Larin et al., Phys. Rev. Lett. **66** (1991) 862;
S.A. Larin and J.A.M. Vermaseren, Phys. Lett. **B259** (1991) 345.

[Lar 94] S.A. Larin, Phys. Lett. **B334** (1994) 192.

[Lee 93] K. Lee et al., Nucl. Instr. Meth. **A333** (1993) 303.

[Lic 95] J. Lichtenstadt and H.J. Lipkin, Phys. Lett. **B353** (1995) 119.

[Mar 84] W.J. Marciano, Phys. Rev. **D29** (1984) 580.

[Mar 95] A.D. Martin et al., Phys. Rev. **D51** (1995) 4756;
Phys. Rev. **D50** (1994) 6734.

[Men 98] F.M. Menden, *Measurement of the Valence Quark Spin Distributions of the Nucleon Using Deep Inelastic Scattering at* HERMES. Diplomarbeit, Universität Hamburg (1998).

[Men 99] F.M. Menden, Private communication.

[Mer 96] R. Mertig and W.L. van Neerven, Z. Phys. **C70** (1996) 637.

[Mey 96] M. Meyer-Hermann et al., Phys. Lett. **B383** (1996) 463; Erratum-ibid. **393** (1997) 487.

[Pre 97] J. Pretz, *Messung der polarisierten Quarkverteilungen in semi-inklusiver Myon-Nukleon Streuung.* Dissertation, Universität Mainz (1997).

[Rob 90] R.G. Roberts, *The Structure of the Proton.* Cambridge University Press, (1990).

[Rol 96] S. Rolli, Preprint hep-ph/9607480 (1996).

[Ruh 96] M. Ruh et al., *Signal Shifts in the Calorimeter of the Transverse Polarimeter at* HERA. HERMES Internal Note 96-017 (1996).

[Ruh 97] M. Ruh et al., *Construction and Beam Test of a Spare Calorimeter for the* HERA *Transverse Polarimeter.* HERMES Internal Polarimeter Note-97-05 (1997).

[Ryc 96] D. Ryckbosch et al., *Systematic Error from the Radiative Correction Procedure.* HERMES Internal Note 96-046 (1996).

[Sjö 94] T. Sjöstrand, Comp. Phys. Comm. **82** (1994) 74; PYTHIA-*5.7 and* JETSET-*7.4, Physics and Manual.* CERN-TH.7112/93 (1993).

[Sok 64] A.A. Sokolov and I.M. Ternov, Sov. Phys. Doklady **8** (1964) 1203.

[Ste 95] E. Stein et al., Phys. Lett. **B343** (1995) 369; Phys. Lett. **B353** (1995) 107.

[Sto 94] F. Stock et al., Nucl. Instr. Meth. **A343** (1994) 334.

[Tal 98] H.A.M. Tallini, *A Measurement of the Quark Spin Distributions of the Nucleon at* HERMES. Ph.D. thesis, University of Liverpool (1998).

[Tip 97] B. Tipton, *Analysis of Positron Beam Polarisation Measurements in 1996.* HERMES Internal Note 97-019 (1997).

[Tip 99] B. Tipton, Ph.D. thesis, Massachusetts Institute of Technology (1999).

[Vel 92] M. Veltri, *Polarised Quark Distributions from Semi-Inclusive Lepto-Production: Studies for the* HERMES *Experiment*. Dissertation, Universität Heidelberg, MPIH-V18-1992;
The PEPSI *Page - Polarised Electron-Proton Scattering Interactions*.
URL address: `http://hermes.desy.de/~ihssen/pepsi.html`

[Vog 96] W. Vogelsang, Phys. Rev. **D54** (1996) 2023.

[Wan 77] S. Wandzura and F. Wilczek, Phys. Lett. **B72** (1977) 195.

[Wan 96] W. Wander, *Rekonstruktion hochenergetischer Streuereignisse im* HERMES *Experiment*. Dissertation, Universität Erlangen-Nürnberg (1996).

[Whi 90] L.W. Whitlow et al., Phys. Lett. **B250** (1990) 193.

[You 97] C. Young, Proceedings of the Workshop on *Deep Inelastic Scattering off Polarised Targets: Theory Meets Experiment*. Edited by J. Blümlein, T. Gehrmann and W.-D. Nowak. Zeuthen, September (1997).

[Zij 94] E.B. Zijlstra and W.L. van Neerven, Nucl. Phys. **B417** (1994) 61.

Acknowledgements

During the completion of this thesis I have benefited from the help and advice of many colleagues.
I would like to take this opportunity to sincerely thank Prof. Kay Königsmann for his valuable advice and support, for giving me the freedom to pursue my own preferences and for supporting my fruitful stay at the DESY laboratory in Hamburg.
During my work at the Transverse Polarimeter I have learned a lot from Dr. Peter Schüler. Thanks to him for his patience in explaining things to me when I started working at DESY.
I would like to thank Dr. Holger Ihssen for introducing me to the physics analysis and Dr. Michael Düren for his encouragement and excellent guidance at the later stage.
Thanks also to Bryan Tipton, who did a similar analysis at MIT, for his patience and help in solving many problems.
I would like to thank Dr. Horst Fischer for his constant support and encouragement since I began this thesis.
Thanks to Marc Beckmann, Stephan Brauksiepe, Dr. Jürgen Franz, Dr. Fritz-Herbert Heinsius, Heiko Lacker, Felix Menden, Dr. Armand Simon and all other members of the Freiburg group for taking time-outs for numerous discussions at DESY and in Freiburg. I have enjoyed working in this inspiring and good-spirited group.
Thanks also to many colleagues in the HERMES Collaboration (too many to mention by name individually) for creating a friendly atmosphere in Hamburg which made work really agreeable and lead to many useful discussions.
Finally, I am indebted to Dr. Michael Düren, Dr. Andreas Gute and Dr. Armand Simon for careful reading of the manuscript and for suggestions for amendments and improvements.